MATERIALS PHYSICS AND MECHANICS

MATERIALS PHYSICS AND MECHANICS

International scientific journal "**Materials Physics and Mechanics**" is published by Peter the Great St. Petersburg Polytechnic University in collaboration with Institute for Problems for Mechanical Engineering in the Russian Academy of Sciences in both hard copy and electronic versions. The journal provides an international medium for the publication of reviews and original research papers written in English and focused on the following topics:

- Mechanics of composite and nanostructured materials.
- Physics of strength and plasticity of composite and nanostructured materials.
- Mechanics of deformation and fracture processes in conventional materials (solids).
- Physics of strength and plasticity of conventional materials (solids).
- Physics and mechanics of defects in composite, nanostructured, and conventional materials.
- Mechanics and physics of materials in coupled fields.

Owner organizations: Peter the Great St. Petersburg Polytechnic University; Institute of Problems of Mechanical Engineering RAS.

Materials Physics and Mechanics is indexed in Chemical Abstracts, Cambridge Scientific Abstracts,
Web of Science Emerging Sources Citation Index (ESCI) and Elsevier Bibliographic Databases (in particular, SCOPUS).

МЕХАНИКА И ФИЗИКА МАТЕРИАЛОВ

Materials Physics and Mechanics

Том 52, номер 6, 2024 год

Тематика журнала

Международный научный журнал "Materials Physics and Mechanics" издается Санкт-Петербургским политехническим университетом Петра Великого в сотрудничестве с Институтом проблем машиноведения Российской академии наук в печатном виде и электронной форме. Журнал публикует обзорные и оригинальные научные статьи на английском языке по следующим тематикам:

• Механика композиционных и наноструктурированных материалов.
• Физика прочности и пластичности композиционных и наноструктурированных материалов.
• Механика процессов деформации и разрушения в традиционных материалах (твердых телах).
• Физика прочности и пластичности традиционных материалов (твердых тел).
• Физика и механика дефектов в композиционных, наноструктурированных и традиционных материалах.
• Механика и физика материалов в связанных полях.

Редколлегия принимает статьи, которые нигде ранее не опубликованы и не направлены для опубликования в другие научные издания. Все представляемые в редакцию журнала "Механика и физика материалов" статьи рецензируются. Статьи могут отправляться авторам на доработку. Не принятые к опубликованию статьи авторам не возвращаются.

Журнал "Механика и физика материалов" ("Materials Physics and Mechanics") включен в систему цитирования Web of Science Emerging Sources Citation Index (ESCI), SCOPUS и РИНЦ.

Contents

Field dependences of the magnetization of the hybrid SiC/Si structure grown by the vacancy method of coordinated substitution of atoms

N.I. Rul [1] ✉ iD **, V.V. Romanov** [1] iD **, A.V. Korolev** [2] iD **, S.A. Kukushkin** [3] iD **, V.E. Gasumyants** [1] iD

[1] Peter the Great St. Petersburg Polytechnic University, St. Petersburg, Russia

[2] M.N. Mikheev Institute of Metal Physics of the Ural Branch of the Russian Academy of Sciences, Ekaterinburg, Russia

[3] Institute for Problems in Mechanical Engineering of the Russian Academy of Science, St. Petersburg, Russia

✉ rul_ni@spbstu.ru

ABSTRACT
The measurement data and a general approach to the analysis of the field dependencies of magnetization of the hybrid SiC/Si structure grown by the vacancy method of coordinated substitution of atoms (VMCSA) are presented. The experimental results can be interpreted as a set of additive contributions to the magnetization of the sample. The analysis of the field dependences of magnetization allowed us to identify a presence of paramagnetic impurities in the sample under study and an inclusion that demonstrates characteristic features of ferromagnetic ordering. It is shown than the value of the specific diamagnetic mass susceptibility of the main SiC/Si substance determined from experimental data cannot be described by the simple additive contribution of silicon and silicon carbide.

KEYWORDS
silicon carbide • VMCSA, hybrid structure • SQUID • external magnetic field • magnetization • diamagnetism impurity ferromagnetism

Introduction

Silicon carbide is a promising material for the development of semiconductor electronic and nanoelectronics devices [1–5], having advantages over devices based on pure silicon [6–12]. SiC thin films can become the basis for integrated circuits, complementing or replacing silicon [13]. In this regard, the study of the physical characteristics and properties of silicon carbide [14–20], grown by the developed original methods, is of particular interest. The presented research involved a sample of the hybrid SiC/Si structure grown at temperature 1360 °C by the vacancy method of coordinated substitution of atoms on the surface of n-type monocrystalline silicon (111).

The vacancy method of coordinated substitution of atoms (VMCSA) [21] is a natural development of the method of coordinated substitution of atoms (MCSA), first proposed and generalized in a series of articles and reviews [22–26], and the process of SiC/Si structures formation by this method differs significantly from the characteristic processes of SiC growth on Si surfaces provided by classical methods [27–30].

The use of the MCSA and VMCSA for growing hybrid structures makes it possible to create materials with bright magnetic [31,32] and other physical properties [33–35] and features [36,37]. The discovered superconductivity of silicon carbide structures at ultra-low temperatures [38,39], in particular, motivated the presented experimental work, devoted to the study and analysis of the field dependences of the magnetization of the hybrid SiC/Si structure grown by VMCSA, measured at various temperatures.

Materials and Methods

To study the magnetic properties of the sample, a superconducting quantum interferometer [40,41] Quantum Design MPMS XL SQUID of the M.N. Mikheev Institute of Metal Physics of the Ural Branch of the Russian Academy of Sciences was used.

The measurements of the magnetization field dependences of the studied *hybrid SiC/Si structure* sample were carried out in the SQUID experimental setup [42] in the range of external magnetic fields up to 25 kOe both direct and reverse polarity with different magnetic field variation at temperatures of 5, 100 and 350 K. During the measurement process, the surface of the SiC/Si structure was oriented perpendicular to the direction of the external magnetic field.

Results and Discussion

To interpret the experimental data shown in Fig. 1, the so-called mechanical mixture model of the main substances of the studied structure, namely silicon carbide and silicon, containing impurities in concentrations much lower than the main chemical elements that form the structure under study, was used. The analysis showed that the measured field dependences can be described assuming the presence of ferromagnetic inclusions in the sample and, at the same time, paramagnetic impurities, contribution of which to the measured magnetization should obey the Curie law.

Thus, we proceeded from the idea that the measured dependences for the hybrid SiC/Si structure represents the total contribution of the spontaneous magnetization of ferromagnetic inclusions, the orientational paramagnetism [43] of impurity ions, increasing as the temperature decreases, and the diamagnetism of the hybrid SiC/Si structure itself.

Within the framework of the proposed model, the magnetization of the studied structure can be represented as:

$$M = fM_f + pM_p + dM_{SiC/Si} = f\chi_f H + \chi_{pd}H, \qquad (1)$$

where

$$\chi_{pd} = p\chi_d + d\chi_{SiC/Si} = \frac{pC}{T} + (1 - p - f)\chi_{SiC/Si}, \qquad (2)$$

f and p correspond to the fraction (by mass) of the ferromagnetic and paramagnetic components ($f, p \ll 1$), C is the Curie constant for paramagnetic impurities in the sample

under study, and χ_f, χ_p and $\chi_{SiC/Si}$ are the corresponding specific ferro-, para- and diamagnetic susceptibilities.
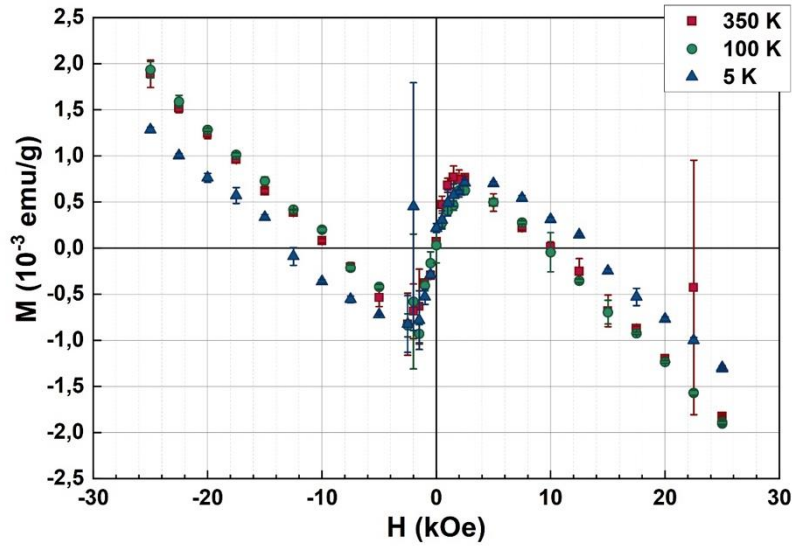
Fig. 1. Field dependences of the magnetization of the hybrid SiC/Si structure grown by the vacancy method of coordinated substitution of atoms at temperatures of 5, 100 and 350 K, respectively

In the region of strong magnetic fields determined from the condition $H > NM_s$, where M_s is the saturation magnetization of the ferromagnetic component, and N is the effective value of the demagnetizing factor, Eq. (1) for ferromagnetic component saturation can be rewritten as:

$$M = fM_s + \chi_{pd}H = fM_s + \left(\frac{pC}{T} + d\chi_{SiC/Si}\right)H, \tag{3}$$

which allows the analysis of the field dependencies using linear approximation. For the studied sample of the hybrid SiC/Si structure, the linear approximation was carried out in the fields with the strength higher than 15 kOe for the dependence measured at 5 K, and for the field dependences measured at 100 and 350 K in the external magnetic fields that exceeds 10 kOe. The results of the analysis of the field dependencies shown in Fig. 1 for the region of strong magnetic fields are given in Table 1.

Table 1. Properties of the sample under study in the region of strong magnetic fields

Temperature	Saturation magnetization, $f \cdot M_s$, 10^{-3} emu/g		Total para- and diamagnetic contributions to the magnetic susceptibility, χ_{pd}, 10^{-9} cm³/g	
	For opposite orientations of the external magnetic field		For opposite orientations of the external magnetic field	
5 K	1.33 ± 0.03	-1.07 ± 0.07	-105.3 ± 1.3	-93 ± 3
100 K	1.24 ± 0.04	-1.02 ± 0.03	-125.0 ± 1.9	-115.6 ± 2.3
350 K	1.32 ± 0.03	-1.08 ± 0.04	-126.2 ± 1.5	-115.5 ± 2.6

Impurity paramagnetism weakens with increasing temperature, which allows us to separate the paramagnetic contribution of the impurities and the diamagnetic

contribution of the main component SiC/Si on the field dependences in the region of strong magnetic fields by means of the linearization of the form:

$$T\chi_{pd} = pC + d\chi_{SiC/Si} \cdot T. \tag{4}$$

The results of processing the dependence shown in Fig. 2 using Eq. (4) are given in Table 2.

Table 2. Paramagnetic and diamagnetic contribution properties for the hybrid SiC/Si sample

Magnetic field region	Orientational paramagnetism, $p \cdot C$, 10^{-9} K·cm³/g	Diamagnetism of the main substance, $d \cdot \chi_{SiC/Si}$, 10^{-9} cm³/g
Direct magnetic field	105.2 ± 1.7	-126.33 ± 0.22
Reversed magnetic field	117 ± 5	-116.4 ± 0.4
Average value	110.6 ± 1.1	-121.28 ± 0.12
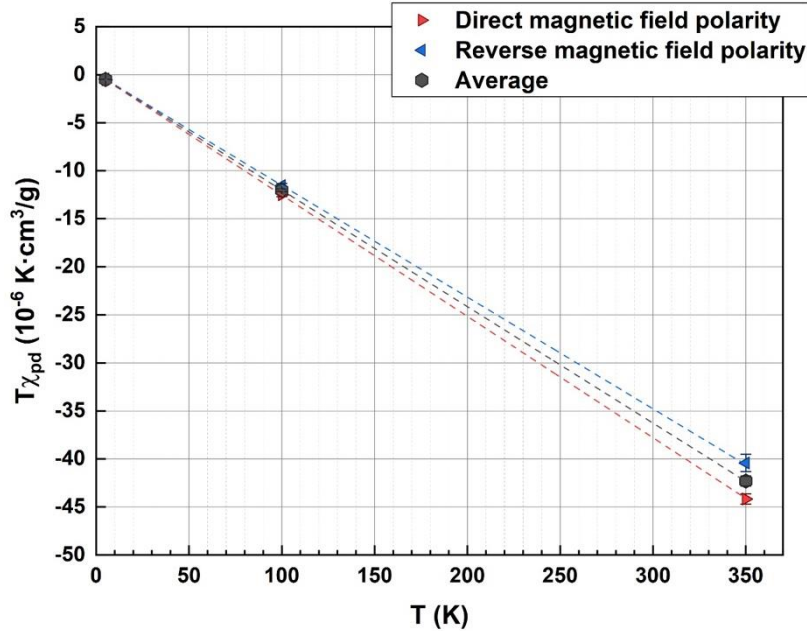
Fig. 2. Para- and diamagnetic contribution properties of the studied hybrid SiC/Si sample in the region of strong magnetic fields depending on temperature

It is obvious that the found specific diamagnetic susceptibility of the main SiC/Si component is less than the values $\chi_{Si} = -228 \cdot 10^{-9}$ cm³/g and $\chi_{SiC} = -265 \cdot 10^{-9}$ cm³/g for crystalline silicon [44,45] and silicon carbide [45,46] at room temperature, respectively, which makes it impossible to describe the diamagnetism of the hybrid structure under study by additive contribution of each component.

The experiment showed that in a weak external magnetic field the magnetization changes linearly. This observation indicates that the ferromagnetic inclusion found in the sample under study appears to saturate in relatively weak fields. Analysis of the experimental dependence in the region of weak magnetic fields corresponding to the condition $H < NM_s$, in the range from -1.5 to 1.5 kOe, allows us to identify the ferromagnetic contribution to the susceptibility of the studied sample and estimate the proportion of the ferromagnetic component as 10^{-3} wt. %.

The presented analysis made it possible to present the experimentally obtained magnetization field dependences of the hybrid SiC/Si structure as a set of contributions of various magnetic nature (Fig. 3).
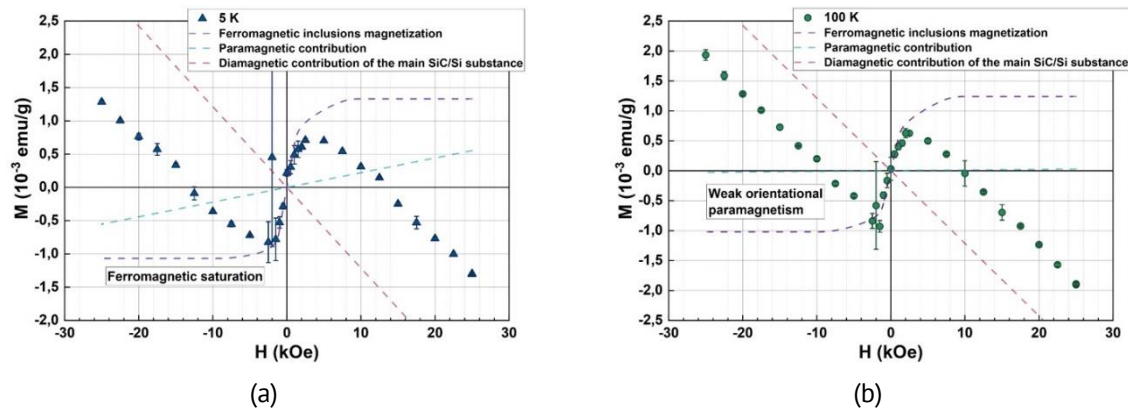
Fig. 3. The analysis of the field dependences of the hybrid SiC/Si structure measured at temperatures of (a) 5 and (b) 100 K performed within the framework of the proposed mechanical mixture model

Conclusions

The fields dependences of the magnetization of the hybrid SiC/Si structure grown by the vacancy method of coordinated substitution of atoms were measured on a superconducting quantum interferometer and studied.

The interpretation of the measured field dependences of magnetization within the framework of mechanical mixture model made it possible to identify a presence of paramagnetic impurities obeying Curie's law in the sample under study and a component that demonstrates characteristic features of ferromagnetic ordering, as well as to determine the value of the specific diamagnetic susceptibility of the main substance SiC/Si.

The field dependences of magnetization in relatively weak magnetic fields allow us to state with a certain degree of confidence that the observed ferromagnetic contribution is apparently due to the presence of a highly magnetic component in the sample under study, the weight fraction of which is significantly less than that of the main substance.

In addition, the measured value of the specific diamagnetic mass susceptibility of the main SiC/Si component cannot be described by the additive contribution of silicon and silicon carbide, requiring consideration of an additional paramagnetic contribution, which is, apparently, unable to reveal itself in the study of field dependences exclusively.

A joint analysis of both the field and temperature dependences of the magnetization of the studied structure may make it possible to clarify and supplement the proposed interpretation of the experimental results.

References

1. Li F, Roccaforte F, Greco G, Fiorenza P, La Via F, Pérez-Tomas A, Evans JE, Fisher CA, Monaghan FA, Mawby PA, Jennings M. Status and prospects of cubic silicon carbide power electronics device technology. *Materials*. 2021;14(19): 5831.
2. H Li, S Zhao, X Wang, L Ding, Mantooth HA. Parallel Connection of Silicon Carbide MOSFETs − Challenges, Mechanism, and Solutions. *IEEE Transactions on Power Electronics*. 2023;38(8): 9731−9749.

3. Langpoklakpam C, Liu AC, Chu KH, Hsu LH, Lee WC. Review of silicon carbide processing for power MOSFET. *Crystals.* 2022;12(2): 245.

4. Baliga BJ. Silicon carbide power devices: Progress and future outlook. *IEEE Journal of Emerging and Selected Topics in Power Electronics.* 2023;11(3): 2400–2411.

5. Di Paolo Emilio M. Silicon Carbide Devices. In: *GaN and SiC Power Devices. Synthesis Lectures on Engineering, Science, and Technology.* Cham: Springer; 2024. p.143–163.

6. Bhatnagar M, Baliga BJ. Comparison of 6H-SiC, 3C-SiC, and Si for power devices. *IEEE Transactions on Electron Devices.* 1993;40(3): 645–655.

7. Willardson RK, Weber ER. *SiC Materials and Devices.* Academic Press; 1998.

8. Y Su, Y Zhang, C Qiu, X Guo, Sun L. Silicon photonic platform for passive waveguide devices: materials, fabrication, and applications. *Advanced Materials Technologies.* 2020;5(8): 1901153.

9. Arjmand T, Legallais M, Nguyen TTT, Serre P, Vallejo-Perez M, Morisot F, Salem B, Ternon C. Functional devices from bottom-up Silicon nanowires: A review. *Nanomaterials*, 2022;12(7): 1043.

10. Wang S, Liu X, Zhou P. The road for 2D semiconductors in the silicon age. *Advanced Materials.* 2022;34(48): 2106886.

11. Zhou X, Yi D, Chan DWU, Tsang HK. Silicon photonics for high-speed communications and photonic signal processing. *npj Nanophoton.* 2024;1: 27.

12. Spreitzer M, Klement D, Parkelj Potočnik T, Trstenjak U, Jovanović Z, Duc Nguyen M, Yuan H, ten Elshof JE, Houwman E, Koster G, Rijnders G, Fompeyrine J, Kornblum L, Fenning DP, Liang Y, Tong WY, Ghosez P. Epitaxial ferroelectric oxides on silicon with perspectives for future device applications. *APL Materials.* 2021;9(4): 040701.

13. Yuan X, Laird I, Walder S. Opportunities, challenges, and potential solutions in the application of fast-switching SiC power devices and converters. *IEEE Transactions on Power Electronics.* 2021;36(4): 3925-3945.

14. Harris GL. *Properties of silicon carbide.* United Kingdom: IEE; 1995.

15. Tarasenko SA, Poshakinskiy AV, Simin D, Soltamov VA, Mokhov EN, Baranov PG, Dyakonov V, Astakhov GV. Spin and optical properties of silicon vacancies in silicon carbide− A review. *Status Solidi (b).* 2018;255(1): 1700258.

16. Abderrazak H, Hmida E. Silicon carbide: synthesis and properties. In: *Properties and applications of Silicon Carbide.* 2011. p.361–388.

17. Soltys LM, Mironyuk IF, Mykytyn IM, Hnylytsia ID, Turovska LV. Synthesis and Properties of Silicon Carbide. *Physics and Chemistry of Solid State.* 2023;24(1): 5-16.

18. Masri P. Silicon carbide and silicon carbide-based structures: The physics of epitaxy. *Surface science reports.* 2002;48(1-4): 1–51.

19. Chaussende D, Ohtani N. Silicon carbide. In: Fornari R. (ed.) *Single Crystals of Electronic Materials.* 2019. p. 129–179.

20. Pal M, Maity NP, Maity R. Silicon carbide membranes for micro-electro-mechanical-systems based CMUT with influence factors. *Materials Physics and Mechanics*. 2022;49(1): 85–96.

21. Grashchenko AS, Kukushkin SA, Osipov AV, Redkov AV. Vacancy growth of monocrystalline SiC from Si by the method of self-consistent substitution of atoms. *Catalysis Today.* 2021;397–399: 375–378.

22. Kukushkin SA, Osipov AV. Thin-film heteroepitaxy by the formation of the dilatation dipole ensemble. *Doklady Physics.* 2012;57(5): 217–220.

23. Kukushkin SA, Osipov AV. A new method for the synthesis of epitaxial layers of silicon carbide on silicon owing to formation of dilatation dipoles. *Journal of Applied Physics.* 2013;113(2): 4909.

24. Kukushkin SA, Osipov AV. Nanoscale single-crystal silicon carbide on silicon and unique properties of this material. *Inorganic Materials.* 2021;57(13): 1319–1329.

25. Kukushkin SA, Osipov AV. Epitaxial silicon carbide on silicon. Method of coordinated substitution of atoms (A Review). *Russian Journal of General Chemistry.* 2022;92: 584–610.

26. Kukushkin SA, Osipov AV. Thermodynamics, kinetics, and technology of synthesis of epitaxial layers of silicon carbide on silicon by coordinated substitution of atoms, and its unique properties. A Review. *Condensed Matter and Interphases.* 2022;24(4): 407–458.

27. Nishino S, Powell JA, Will HA. Production of large-area single-crystal wafers of cubic SiC for semiconductor devices. *Applied Physics Letters.* 1983;42(5): 460–462.

28. Severino A, Locke C, Anzalone R, Camarda M, Piluso N, La Magna A, Saddow S, Abbondanza G, D'Arrigo G, La Via F. 3C-SiC film growth on Si substrates. *ECS Transactions.* 2011;35(6): 99–116.

29. Kimoto T. Bulk and epitaxial growth of silicon carbide. *Progress in Crystal Growth and Characterization of Materials.* 2016;62(2): 329–351.

30. Via FL, Zimbone M, Bongiorno C, La Magna A, Fisicaro G, Deretzis I, et al. New approaches and understandings in the growth of cubic silicon carbide. *Materials.* 2021;14(18): 5348.

31. Bagraev NT, Kukushkin SA, Osipov AV, Khromov VS, Klyachkin LE, Malyarenko AM, Romanov VV. Magnetic properties of thin epitaxial SiC layers grown by the atom-substitution method on single-crystal silicon surfaces. *Semiconductors.* 2021;55(2): 137–145.

32. Bagraev NT, Kukushkin SA, Osipov AV, Romanov VV, Klyachkin LE, Malyarenko AM, Rul' NI. Room-temperature quantum oscillations of static magnetic susceptibility of silicon-carbide epitaxial layers grown on a silicon substrate by the method of the coordinated substitution of atoms. *Materials Physics and Mechanics.* 2022;50(1): 66–73.

33. Kukushkin SA, Osipov AV. Anomalous properties of the dislocation-free interface between Si (111) substrate and 3C-SiC (111) epitaxial layer. *Materials.* 2021;14(1): 1–12.

34. Kukushkin SA, Osipov AV, Osipova EV. Spintronic properties of the interface between Si(111) and 3C–SiC(111) grown by the method of coordinated substitution of atoms. *Technical Physics Letters.* 2022;48(10): 78–80.

35. Kukushkin SA, Osipov AV. Dielectric Function and Magnetic Moment of Silicon Carbide Containing Silicon Vacancies. *Materials.* 2022;(15): 4653.

36. Bagraev NT, Kukushkin SA, Osipov AV, Klyachkin LE, Malyarenko AM, Khromov VS. Terahertz emission from silicon carbide nanostructures. *Semiconductors.* 2022;56(13): 2050–2056.

37. Bagraev NT, Kukushkin SA, Osipov AV, Klyachkin LE, Malyarenko AM, Khromov VS. Registration of terahertz irradiation with silicon carbide nanostructures. *Semiconductors.* 2022;56(14): 2157–2163.

38. Muranaka T, Kikuchi Y, Yoshizawa T, Shirakawa N, Akimitsu J. Superconductivity in carrier-doped silicon carbide. *Science and Technology of Advanced Materials.* 2008;9: 044204.

39. Kriener M, Muranaka T, Kato J, Ren ZA, Akimitsu J. Superconductivity in carrier-doped silicon carbide. *Science and Technology of Advanced Materials.* 2008;9: 044205.

40. Anderson PW, Rowell JM. Probable observation of the Josephson superconducting tunneling effect. *Physical Review Letters.* 1963;10: 230.

41. Kleiner R, Koelle D, Ludwig F, Clarke J. Superconducting quantum interference devices: State of the art and applications. *Proceedings of the IEEE.* 2004;92(10): 1534–1548.

42. Clarke J. SQUIDs. *Scientific American.* 1994;271(2): 46–53.

43. Vonsovsky SV. Magnetism. Moscow: Science; 1971. (In Russian)

44. Weast R. *CRC, Handbook of Chemistry and Physics.* Boca Raton, Florida: Chemical Rubber Company Publishing; 1984.

45. Grigorieva IS, Meilikhova EZ. *Physical quantities. Directory.* Moscow: Energoatomizdat; 1991. (In Russian)

46. Haynes WM. *CRC Handbook of Chemistry and Physics.* 92nd ed. Boca Raton, FL: CRC Press; 2011.

About Authors

Nikolai I. Rul 🆔 Sc
Candidate of Physical and Mathematical Sciences
Assistant (Peter the Great St. Petersburg Polytechnic University, St. Petersburg, Russia)

Vladimir V. Romanov 🆔 Sc
Doctor of Physical and Mathematical Sciences
Professor (Peter the Great St. Petersburg Polytechnic University, St. Petersburg, Russia)

Aleksandr V. Korolev 🆔 Sc
Candidate of Physical and Mathematical Sciences
Lead Researcher (M.N. Mikheev Institute of Metal Physics of the Ural Branch of the Russian Academy of Sciences, Ekaterinburg, Russia)

Sergey A. Kukushkin 🆔 Sc
Doctor of Physical and Mathematical Sciences
Head of Laboratory (Institute of Problems of Mechanical Engineering of the Russian Academy of Sciences, St. Petersburg, Russia)

Vitaliy E. Gasumyants 🆔 Sc
Doctor of Physical and Mathematical Sciences
Professor (Peter the Great St. Petersburg Polytechnic University, St. Petersburg, Russia)

Formation of liquid-like inclusions near pores in amorphous intercrystalline layers in high-temperature ceramics

M.Yu. Gutkin (ID)**, S.A. Krasnitckii** (ID)**, N.V. Skiba** ✉ (ID)

Institute for Problems in Mechanical Engineering Russian Academy of Sciences, St. Petersburg, Russia

✉ nikolay.skiba@gmail.com

ABSTRACT
A theoretical model is suggested that describes a mechanism of plastic deformation in high-temperature ceramic materials containing amorphous intercrystalline layers (AILs) and pores in triple junctions of AILs. Within the model, the plastic deformation is realized through the generation of liquid-like inclusions on pore surfaces and their subsequent propagation along the AILs. In the exemplary case of high-temperature α-Al$_2$O$_3$ ceramics with AILs, the dependences of the critical values of the external shear stress for the formation of a liquid-like inclusion on deformation temperature in a wide range of the deformation temperatures from 300 to 1500 K are calculated. It is shown that the critical stress for the nucleation of a liquid-like inclusion strongly depends on the deformation temperature and weakly depends on the pore size.

KEYWORDS
high-temperature ceramics • amorphous intercrystalline layers • liquid-liked inclusions • pores • deformation temperature

Introduction

The unique mechanical properties of high-temperature ceramics, such as very high strength, hardness and wear resistance at elevated temperatures, make these materials extremely promising for practical use [1–3]. According to experiments [4–6] and computer modeling [7–10], these properties are largely determined by the state and behavior of intercrystallite boundaries. Typically, these intercrystallite boundaries are layers of amorphous material with covalent interatomic bonds. The outstanding mechanical properties of the ceramic composites with the amorphous intercrystalline layers (AILs) [11,12] has stimulated growing interest in this class of materials. However, the experimental investigations of the AIL evolution are extremely complicated and laborious due to their small size. A significant role is played by computer simulations [7–10] and analytical theoretical models [13–20].

In particular, Glezer and Pozdnyakov [13,14] proposed the concept of grain boundary microsliding (GBMS) modeling the GBMS region as an inclusion in the form of an oblate ellipsoid. Later, a number of works [8–10] appeared on computer modeling of the mechanisms of plastic behavior of the AILs in amorphous silicon as a typical amorphous covalent material. The authors of these works showed that the atomic structure of the amorphous silicon included liquid-like and solid-like regions. In this case, the area of the liquid-like phase increases with increasing mechanical load, which

indicates that the areas of the liquid-like phase are carriers of plastic deformation in the amorphous silicon.

With the help of the results of computer modeling [8–10], some theoretical models [17–20] were developed that describe micromechanisms of the formation of the liquid-like inclusions under the action of an external shear stress in the grain boundaries (GBs) between the adjacent triple junctions. In the framework of these theoretical models, the enhancement of the plastic deformation in the ceramic composites with AILs was realized due to the formation of the liquid-like inclusions near the triple junctions of the AILs [17], due to the nucleation of nanocracks on the liquid-like phase inclusions [18], due to the liquid-like inclusions overcoming the triple junctions of the AILs and the penetration into a neighboring AIL [19], and due to nucleation and the extension of the liquid-like inclusions in the AILs with the subsequent emission of lattice dislocations from the triple junctions of the AILs and the glide of these dislocations into the bulk of a neighboring grain [20]. In the models, the liquid-like inclusions and their elastic fields were modeled by gliding dislocation loops [17,18] and dislocation dipoles [19,20] with increasing Burgers vectors. It is worth noting that these models [17–20] considered the nucleation of the liquid-like inclusion at the triple junctions of the AILs that did not contain other defects.

However, it is well known that the most ceramic materials are characterized by high porosity, which significantly reduces their fracture toughness and ductility characteristics [21–25]. In these circumstances, it is important for the practical use to develop mechanisms for increasing the fracture toughness and the ductility of high-temperature ceramic composites with high porosity.

Thus, the main aim of this work is to develop a micromechanism of the enhancement of the plastic deformation in the high-temperature ceramics with AILs through the nucleation and the extension of the liquid-like inclusions near the triple junctions of the AILs containing pores.

Model

Consider a cylindrical pore of radius R_0 placed in an equilibrium triple-junction of GBs with amorphous structure in a ceramic sample of α-Al_2O_3. It is supposed that the stress disturbance in vicinity of the pore induced by the remote shear stress τ is responsible for the nucleation and the subsequent propagation of the liquid-like inclusion along the GB as it is shown in Fig. 1.

The analysis of critical conditions for the formation of the liquid-like nucleus can be provided in the framework of the quasi-equilibrium energetic approach. According to this approach, the energy change due to the formation of the liquid-like nucleus is determined as follows:

$$\Delta W = W_{st} + \Delta H - A, \tag{1}$$

where W_{st} is the strain energy of the liquid-like nucleus generated on the pore surface, ΔH is the enthalpy increment due to the transition from the liquid to the solid phase [20] and A is the work done by the external shear stress τ.

The analytical expression of the first term in Eq. (1) is derived in this study. In doing so, the plastic shear inherent to the liquid-like nucleus is modeled by the dipole of edge dislocations with the variable Burgers vectors $\pm \boldsymbol{s}$ ($\pm s$-dislocation dipole). Within the

model, the first dislocation is placed in the pore center while the second one is located at the distance L from the pore surface (see Fig. 1). The corresponding strain energy of this dipole can be determined as a virtual work done by its own stress field on the plastic sliding (see, for example [26]):

$$W_{st} = \frac{s}{2} \int_{R_0}^{R_0+L} [\sigma_{xy}^{(1)} + \sigma_{xy}^{(2)}] dx, \tag{2}$$

where $\sigma_{xy}^{(1)}$ and $\sigma_{xy}^{(2)}$ are the shear stresses of the dislocations forming the dipole (hereinafter the Cartesian coordinate system (x,y) with the origin in the pore center and the x-axis directed along the GB with the liquid-like nucleus is applied). Equation (2) can be rewritten in terms of the Airy stress functions so that:

$$W_{st} = \frac{s}{2} \left[\frac{\partial \chi_1}{\partial y} + \frac{\partial \chi_2}{\partial y} \right]_{x=R_0, \ y=0}^{x=R_0+L, \ y=0}, \tag{3}$$

where χ_1 and χ_2 are the Airy stress functions of the dislocations. It is worth noting that the Airy stress functions for linearly elastic and isotropic bodies containing dislocations are well-studied and widely referred in literature [27]. For instance, the Airy stress function of an edge dislocation symmetrically placed in the center of a cylindrical pore can be cast as:

$$\chi_1 = -\frac{sG}{2\pi(1-v)} y \left(\frac{1}{2} \frac{R_0^2}{r^2} + \ln r \right), \tag{4}$$

where G and v are the shear modulus and the Poisson ratio, respectively, r is the radial coordinate with respect to the pore center.
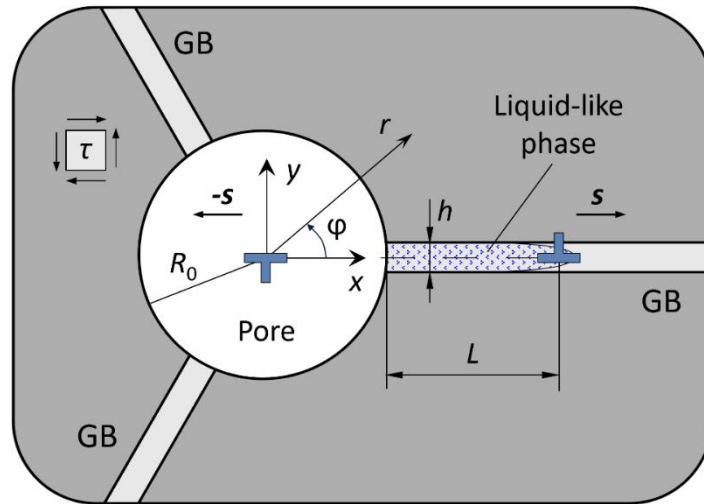
Fig. 1. A liquid-like inclusion emitted by the pore in a triple junction of the grain boundaries (GBs) under the external shear stress τ. The Cartesian (x, y) and polar (r, φ) coordinate systems associated with the pore center are shown

As for the dislocation located at a distance $d = R_0 + L$ from the pore center, the Airy stress function can be given by:

$$\chi_2 = \frac{sG}{2\pi(1-v)} y \left(\frac{1}{2} \frac{R_0^2}{r^2} \left(1 - \frac{r^2 r_1^2}{d^2 r_2^2} \right) + \ln \frac{r r_1}{r_2} \right), \tag{5}$$

where the following denotations are introduced:

$$r_1 = \sqrt{r^2 + d^2 - 2rd \cos \varphi}, \tag{6}$$

$$r_2 = \sqrt{r^2 + (R_0{}^2/d)^2 - 2rR_0{}^2/d \cos \varphi}. \tag{7}$$

Subsisting Eqs. (4) and (5) in Eq. (3), one can finally obtain the analytical expression of the strain energy of the $\pm s$-dislocation dipole ejected by the cylindrical pore in the form:

$$W_{st} = \frac{Gs^2}{8\pi(1-\nu)}\left(-1 + 2\ln\frac{L(2R_0+L)}{R_0 r_c}\right), \tag{8}$$

where r_c is the radius of the core of the second dislocation.

In further calculations, the parameter r_c is taken equal to the interatomic distance in α-Al$_2$O$_3$ ceramics: $a \approx 0.27$ nm [28]. It is worth mentioning that the effect of the decrease of the shear modulus G at elevated temperature can be incorporated into Eq. (8) by utilizing the experimental approximation for α-Al$_2$O$_3$ ceramic which is valid over a wide range of the temperatures [29]:

$$G(\text{GPa}) = 169 - 0.0229\,T, \tag{9}$$

where T is the temperature given in degrees Celsius. As for the Poisson ratio, it weakly depends on the temperature so that one can take $\nu = 0.23$.

Table 1. Temperature dependence of the specific enthalpy of α-Al$_2$O$_3$ ceramics

Temperature, K	300	400	500	600	700	800	900	1000	1100	1200	1300	1400	1500
Specific enthalpy of solid-like phase, kJ/mol	10.2	19.0	29.1	40.1	51.6	63.5	75.6	87.0	100.6	113.3	122.1	139.1	152.3
Increment of specific enthalpy from solid to liquid phase, kJ/mol	50.1	90.5	14.6	20.1	25.8	31.8	37.8	43.5	50.3	56.7	61.1	69.6	76.2

Turn now to the enthalpy term in Eq. (1). The experimental data on the enthalpy of solid-like phase H_m of α-Al$_2$O$_3$ ceramic are available in literature (see, for example, [30]), whereas the enthalpy of liquid-like phase H_i has not been thoroughly investigated. To avoid a lack of experimental research, one can estimate the unknown enthalpy of the liquid-like phase as $H_i \approx 1.5 H_m$, whence for the increment of enthalpy due to the transition from solid to liquid phase is valid $\Delta H = H_i - H_m \approx 0.5 H_m$. This approximation is in good agreement with experimental measures for Si ceramics in a wide range of temperatures [17]. The values of specific enthalpies of solid- and liquid-like phase, and increment of specific enthalpy in dependence of the temperature employed in the calculation below are given in Table 1. Finally, the enthalpy increment in Eq. (1) can be calculated in a similar way described in our previous work [20] with taking into account the data of Table 1 and the fact that the width of the liquid-like nucleus takes the average value $h \approx 4a$.

The last term in Eq. (1) is the work done by external forces on the formation of the liquid-like phase and can be defined as follows:

$$A = \tau s L. \tag{10}$$

Thus, all terms in Eq. (1) are defined. The section that follows moves on to the analysis of the energy change accompanying the formation of a liquid-like nucleus at the pore surface (Eq. (1)) under different temperature conditions.

Results

As mentioned above, the formation of the liquid-like inclusion is one of the effective mechanisms of plastic deformation in ceramics with the AILs such as α-Al$_2$O$_3$. Besides, it was noting that the porous structure of the sintered ceramics can significantly affect the initiation of the plastic deformation. In order to investigate the contribution of the latter factor to the nucleation of a liquid-like inclusion, the quasi-equilibrium energetic model is suggested.
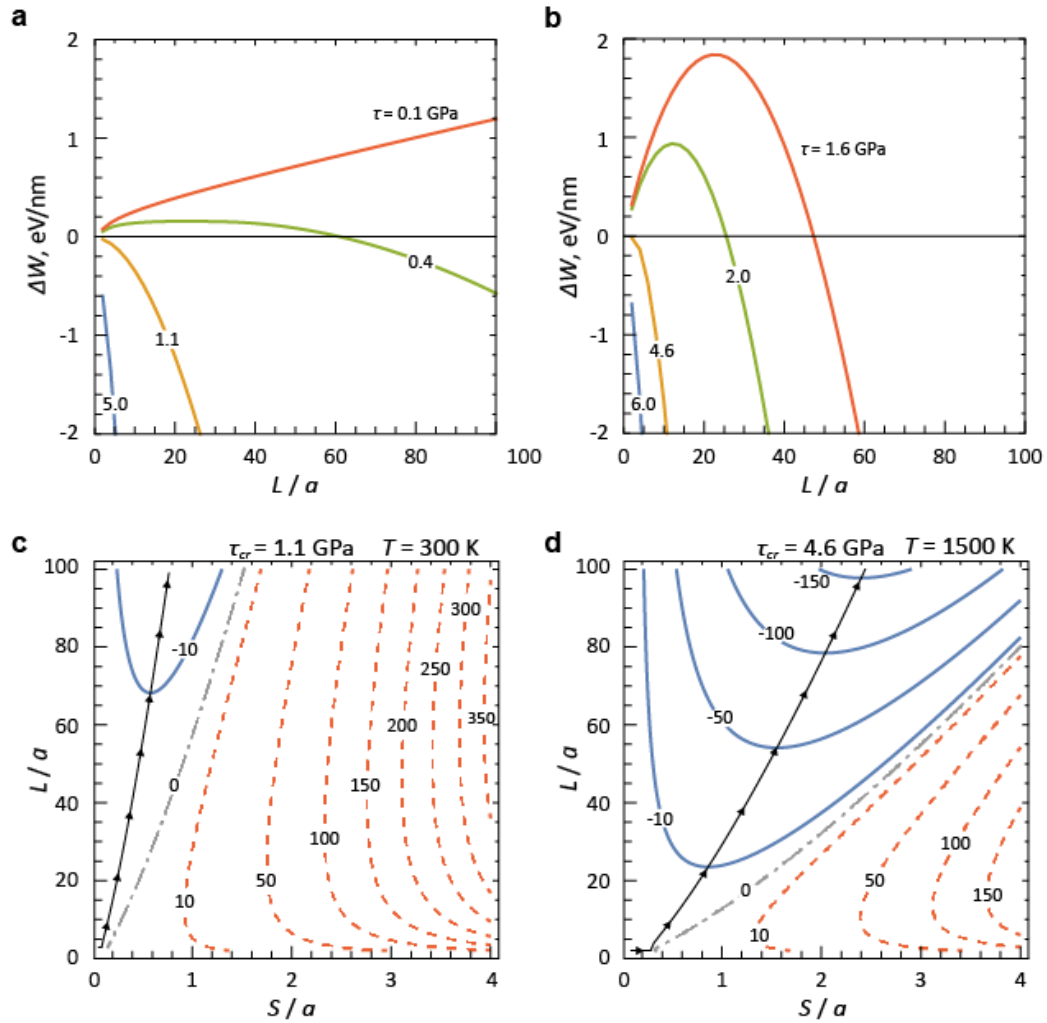
Fig. 2. The energy change accompanying the evolution of a liquid-like nucleous in vicinity of the pore of radius $R_0 = 100a$. The dependences of ΔW on the normalized length L/a are given for the plastic shear $s = 0.1a$ at different values of the remote stress τ for two temperatures: (a) $T = 300$ K and (b) $T = 1500$ K. Maps of ΔW in dependence on the normalized nucleus size L/a and its plastis shear s/a are given for two critical stress values: (c) $\tau_{cr}^{300\,K} \approx 1.1$ GPa and (d) $\tau_{cr}^{1500\,K} \approx 4.6$ GPa. The energy values on the maps are given in units of eV/nm for $v = 0.23$ and $a = 0.27$ nm

According to this model, the energy change due to the formation of the liquid-like nucleus at the cylindrical pore surface is determined by Eq. (1). Figures 2(a,b) illustrate the energy change $\Delta W(L)$ profiles obtained by Eq. (1) for quite low values of the plastic shear inherent to the liquid-like nucleus $s = 0.1a$. The curves $\Delta W(L)$ are given for pore size $R_0 = 100a$ and for different values of the remote shear stress τ in the cases of relatively

low temperatures (Fig. 2(a) for T = 300 K) and relatively high temperatures (Fig. 2(b) for T = 1500 K). As it is seen from the figures, the formation of the liquid-like inclusion is energetically favorable if the energy change becomes negative $W(L = 2a) < 0$ (hereinafter $L = 2a$ is taken as the smallest size of the nucleus). In other words, the shear stress τ should exceed some critical value τ_{cr} depending on the temperature conditions. For instance, the critical stress value $\tau_{cr} \approx 1.1$ GPa for T = 300 K, while $\tau_{cr} \approx 4.6$ GPa for T = 1500 K. It means that the formation of the liquid-like inclusion is inhibited at elevated temperatures. This fact can be elucidated by the intrinsic features of α-Al_2O_3 ceramic viz. The enthalpy contribution to the energy change of the process increases with the temperature growth.

The evolution of the liquid-like nucleus is demonstrated with the dependences of the energy change ΔW on the nucleus size L and its plastic shear s that are given for the critical stress values $\tau_{cr}^{300\,K}$ and $\tau_{cr}^{1500\,K}$ (see Fig. 2(c,d), respectively). The most preferable pathway of the nucleus evolution is depicted in the figures by the solid black line corresponding to the minimal values of the energy change starting from the initial values of parameters $L = 2a$ and $s = 0.1a$. What stands out from Figs. 2(c,d) is that, at the initial stage of the nucleus evolution, the nucleus has a tendency to accumulate the plastic shear until it reaches some value s_0 ($s_0 \approx 0.3a$ for T = 1500 K) conserving the size $L=2a$. At the next stage, the nucleus tends to evolve with increasing both the size L and the plastic shear s. It is worth mentioning that, at this stage, the size of the nucleus L almost linearly depends on the plastic shear s. The slope of these curves is strongly impacted by the temperature. For instance, for nucleus with $L = 100a$, the value of plastic shear is ~0.8a for T = 300 K while for T = 1500 K, the plastic shear is significantly bigger: ~2.4a. The slope value of the curve $L(s)$ is of great interest as an input for analyzing some more complicated mechanisms of the plastic deformation in ceramic materials such as the dislocation emission initiated by the liquid-like inclusion [20].
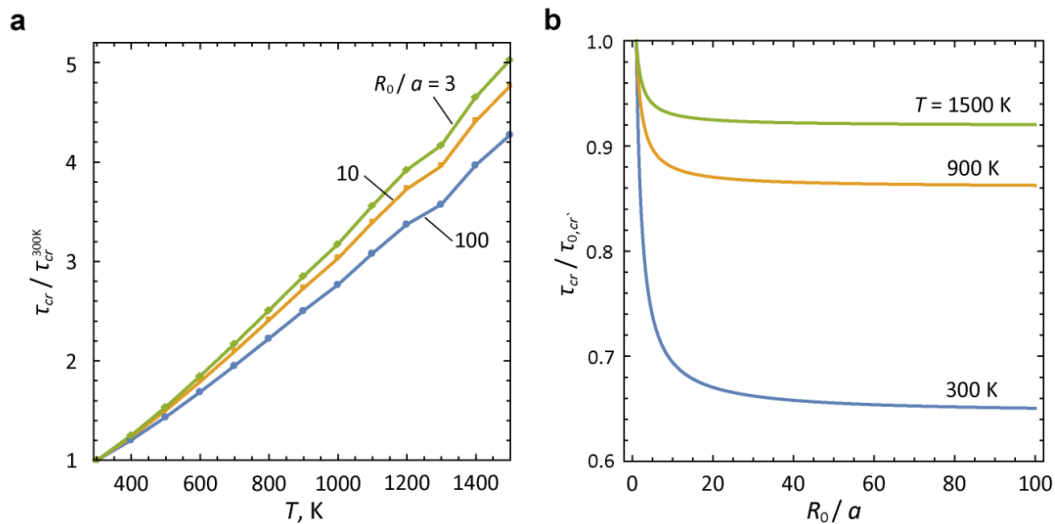
Fig. 3. The dependence of the critical stress τ_{cr} for the formation of a liquid-like nucleous on (a) the temperature T and (b) the pore radius R_0. The critical stress is given in units (a) of the critical stress $\tau_{cr}^{300\,K}$ determined for different values of the pore radius R_0 = 3a, 10a and 100a and (b) of the critical stress $\tau_{0,cr}$ for the pore-free case obtained for different values of the temperature T = 300, 900 and 1500 K

The effect of temperature on the critical shear stress of the formation of liquid-like inclusion is demonstrated in Fig. 3(a). The figure shows the dependences of $\tau_{cr}(T)$ for different values of the pore radius $R_0 = 3a$, $10a$ and $100a$. As is seen from the plots, the critical stress gradually increases with the temperature growth. Hence, the nucleation of the liquid-like inclusions probably occurs at relatively low temperatures rather than at high temperatures. Besides, one can note that the effect of the pore facilitates the formation of the liquid-like nuclei i.e. the bigger the pore size, the lower the critical stress for the liquid-like nuclei formation.

Figure 3(b) illustrates the ratio of the critical stress τ_{cr} for the case with the pore to that one $\tau_{0,cr}$ for the case without pore in dependence of the normalized pore radius R_0/a for three different temperatures: $T = 300$, 900 and 1500 K. The plots sharply drop in the interval of relatively small R_0/a ($R_0/a < 15$) and then tend to some constant values for bigger R_0/a ($R_0/a > 15$). These constant values estimate the reduction of the critical stress in the case of relatively big pores ($R_0/a > 15$) under different temperature conditions. For instance, the reduction of the critical stress reaches ~8 % at elevated temperatures ($T = 1500$ K), ~14 % at relatively middle temperatures ($T = 900$ K) and ~35 % at low temperatures ($T = 300$ K). Thus, the temperature of deformation significantly affects the decline of the critical stress τ_{cr} viz. the lower the temperature the bigger the stress falling.

Conclusions

In summary, a theoretical model of a new micromechanism of the plastic deformation in the high-temperature ceramic composites with pores in triple junctions of amorphous intercrystalline layers (AILs) is developed. Within the model, the plastic deformation of a ceramic sample occurs through the emission of nuclei of the liquid-like phase from the triple junction of the AILs containing a pore under the action of the external shear stress. The energy characteristics of the generation of liquid-like phase nuclei at the AIL triple junctions containing pores are calculated. In the exemplary case of a high-temperature α-Al_2O_3 nanoceramics, the critical stresses for the formation of a liquid-like inclusion at the cylindrical pore in the AIL triple junction for wide temperature range are determined. The temperature dependences of these critical stresses are plotted for different sizes of the pore.

Thus, the model shows that the plastic deformation in high-temperature ceramic composites with pores in the triple junctions of the AILs can effectively occur through the generation of liquid-like inclusions on the pore surfaces and their propagation along the AILs, thereby increasing the crack resistance and plasticity of these composites.

In addition, this model can serve as an effective basis for comparative analysis of the possibility of the implementing other mechanisms of the plastic deformation enhancement and the fracture, such as the emission of the lattice dislocations from the triple junctions of the GBs containing pores and the generation of nanocracks on pores. The development of models describing the action of these alternative mechanisms of the plasticity and the fracture in the high-temperature ceramic composites is the subject of our future research.

References

1. Koch CC, Ovid'ko IA, Seal S, Veprek S. *Structural Nanocrystalline Materials: Fundamentals and Applications.* Cambridge: Campridge University Press; 2007.

2. Zhang D, Yu R, Feng X, Guo X, Yang Y, Xu X. Enhanced mechanical properties of Al_2O_3 nanoceramics via low temperature spark plasma sintering of amorphous powders. *Materials.* 2023;16(16): 5652.

3. Wang LY, An L, Zhao J, Shimai S, Mao XJ, Zhang J, Liu J, Wang SW. High-strength porous alumina ceramics prepared from stable wet foams. *J. Adv. Ceram.* 2021;10: 852–859.

4. Zhang ZL, Sigle W, Koch CT. Dynamic behavior of nanometer-scale amorphous intergranular film in silicon nitride by in situ high-resolution transmission electron microscopy. *Journal of the European Ceramic Society.* 2011;31(9): 1835–1840.

5. Subramaniam A, Koch CT, Cannon RM, Rühle M. Intergranular glassy films: An overview. *Materials Science and Engineering A.* 2006;422(1-2): 3–18.

6. Kleebe HJ. Structure and chemistry of interfaces in Si_3N_4 ceramics studied by transmission electron microscopy. *Journal of the Ceramic Society of Japan.* 1997;105(1222): 453–475.

7. Mo YF, Szlufarska I. Simultaneous enhancement of toughness, ductility, and strength of nanocrystalline ceramics at high strain-rates. *Applied Physics Letters.* 2007;90(18): 181926.

8. Demkowicz MJ, Argon AS. High-density liquidlike component facilitates plastic flow in a model amorphous silicon system. *Physical Review Letters.* 2004;93(2): 025505.

9. Demkowicz MJ, Argon AS. Liquidlike atomic environments act as plasticity carriers in amorphous silicon. *Physical Review B.* 2005;72(24): 245205.

10. Demkowicz MJ, Argon AS, Farkas D, Frary M. Simulation of plasticity in nanocrystalline silicon. *Philosophical Magazine.* 2007;87(28): 4253–4271.

11. Hulbert DM, Jiang D, Kuntz JD. A low-temperature high-strain-rate formable nanocrystalline superplastic ceramic. *Scripta Materialia.* 2007;56(12): 1103–1106.

12. Xu X, Nishimura T, Hirosaki N. Superplastic deformation of nano-sized silicon nitride ceramics. *Acta Materialia.* 2006;54(1): 255–262.

13. Glezer A, Pozdnyakov V. Structural mechanism of plastic deformation of nanomaterials with amorphous intergranular layers. *Nanostructured Materials.* 1995;6(5-8): 767–769.

14. Pozdnyakov VA, Glezer AM. Anomalies of Hall-Petch dependence for nanocrystalline materials. *Technical Physics Letters.* 1995;21(1): 31–36.

15. Bobylev SV, Gutkin MYu, Ovid'ko IA. Plastic deformation transfer through the amorphous intercrystallite phase in nanoceramics. *Physics of the Solid* State. 2008;50(10): 1888–1894.

16. Bobylev SV, Ovid'ko IA. Dislocation nucleation at amorphous intergrain boundaries in deformed nanoceramics. *Physics of the Solid State.* 2008;50(4): 642–648.

17. Gutkin MYu, Ovid'ko IA. A composite model of the plastic flow of amorphous covalent materials. *Physics of the Solid State.* 2010;52(1): 58–64.

18. Gutkin MYu, Ovid'ko IA. Plastic flow and fracture of amorphous intercrystalline layers in ceramic nanocomposites. *Physics of the Solid State.* 2010;52(4): 718–727.

19. Gutkin MYu, Mikaelyan K.N. A model of strain hardening in nanoceramics with amorphous intercrystalline layers. *Physics of Complex Systems.* 2021;2(2): 51-60.

20. Gutkin MYu, Skiba NV. Emission of lattice dislocations from triple junctions of grain boundaries in high-temperature ceramics with amorphous intercrystalline layers. *Materials Physics and Mechanics.* 2024;52(1): 39-48.

21. Liu J, Huo W, Zhang X, Ren B, Li Y, Zhang Z, Yang J. Optimal design on the high-temperature mechanical properties of porous alumina ceramics based on fractal dimension analysis. *Journal of Advanced Ceramics.* 2018;7(2): 89–98.

22. Ovid'ko IA, Sheinerman AG. Micromechanisms for improved fracture toughness in nanoceramics. *Reviews on Advanced Materials Science.* 2011;29(2): 105–125.

23. Vakaeva AB, Krasnitckii SA, Smirnov A, Grekov, MA, Gutkin MY. Stress concentration and distribution at triple junction pores of three-fold symmetry in ceramics. *Reviews on Advanced Materials Science.* 2018;57(1): 63-71.

24. Vakaeva AB, Krasnitckii SA, Grekov MA, Gutkin MYu. Stress field in ceramic material containing threefold symmetry inhomogeneity. *Journal of Materials Science.* 2020;55(22): 9311-9321.

25. Krasnitckii SA, Sheinerman AG, Gutkin MYu. Brittle vs ductile fracture behavior in ceramic materials at elevated temperature. *Materials Physics and Mechanics.* 2024:52(2): 82-89.

26. Mura T. *Micromechanics of defects in solids.* Netherland: Martinus Nijhoff Publishers;1987.

27. Eshelby JD. Boundary problems. In: Nabarro FRN. (ed.) *Dislocation in solids, Vol. 1.* Amsterdam: North-Holland Publishing Company; 1979. p.167–221.

28. Lagerlöf KPD, Heuer AH, Castaing J, Rivière JP, Mitchell TE. Slip and twinning in sapphire (α-Al2O3). *Journal of the American Ceramic Society.* 1994;77(2): 385–397.

29. Munro RG. Evaluated material properties for a sintered alpha-alumina. *Journal of the American Ceramic Society.* 1997;80(8): 1919-1928.

30. Archer DG. Thermodynamic properties of synthetic sapphire (α-Al2O3), standard reference material 720 and the effect of temperature-scale differences on thermodynamic properties. *Journal of Physical and Chemical Reference Data.* 1993;22(6): 1441–1453.

About Authors

Mikhail Yu. Gutkin Sc

Doctor of Physical and Mathematical Sciences
Principal Researcher (Institute for Problems in Mechanical Engineering, Russian Academy of Sciences, St. Petersburg, Russia)

Stanislav A. Krasnitckii Sc

Candidate of Physical and Mathematical Sciences
Researcher (Institute for Problems in Mechanical Engineering, Russian Academy of Sciences, St. Petersburg, Russia)

Nikolai V. Skiba Sc

Doctor of Physical and Mathematical Sciences
Lead Researcher (Institute for Problems in Mechanical Engineering, Russian Academy of Sciences, St. Petersburg, Russia)

An influence of mechanical stresses on the phase state of spherulitic thin films of lead zirconate titanate

V.P. Pronin [1] ✉ iD, **I.V. Ryzhov** [1] iD, **M.V. Staritsyn** [2] iD, **S.V. Senkevich** [3] iD,

E.Yu. Kaptelov [3] iD, **I.P. Pronin** [3] iD

[1] Herzen State Pedagogical University of Russia, St. Petersburg, Russia

[2] National Research Centre "Kurchatov Institute" -Central Research Institute of Structural Materials

"Prometey", St. Petersburg, Russia

[3] Ioffe Institute, St. Petersburg, Russia

✉ pronin.v.p@yandex.ru

ABSTRACT
The influence of lateral mechanical stresses on the crystal structure, microstructure and dielectric properties of spherulitic thin films of lead zirconate titanate is studied. The composition of lead zirconate titanate corresponded to the region of the morphotropic phase boundary. In thin films, the perovskite phase was formed during high-temperature annealing of amorphous films deposited by RF magnetron sputtering of a ceramic target on a cold silicon substrate. The deformation of the crystal lattice caused by the change in density during crystallization of the perovskite phase in the films changed with an increase in the area of spherulitic blocks with a variation in the target-substrate distance during their deposition. An increase in mechanical stress led to a linear rotation of the crystal lattice and a change in its parameters, as well as to a change in the microstructure of thin films. Based on the temperature dependences of the reverse dielectric permittivity, changes in the temperature of structural phase transitions in the films were revealed.
KEYWORDS
lead zirconate titanate thin films • morphotropic phase boundary • spherulitic microstructure • mechanical stresses

Introduction

In recent years, an interest in thin films with spherulitic structure has been caused by both their increasing use in various practical applications and the development of multi-stage technologies based on the deposition of amorphous films at low temperatures and their subsequent multi-stage heat treatment. During heat treatment, crystallization of the films occurs through the formation of individual islands, which often take on a shape close to round, and are therefore called spherulites. The formation of a spherulitic microstructure is accompanied by an increase in the density of the films. The consequence of this is their shrinkage, which leads to a partial relaxation of lateral mechanical stresses acting from the amorphous or low-temperature intermediate phase. A similar situation is realized both in thin-film metals and alloys, and in semiconductor and dielectric films [1–8].

Since the change in the density of films during their crystallization can reach several percent, the formation of spherulites is accompanied by the appearance of strong lateral mechanical stresses and strain, Fig. 1. Thus, in hematite films (α-Fe_2O_3), the strain, estimated at ~ 0.5%, was accompanied by rotation of the growth axis, the rotation speed of which reached ~ 100 deg/µm [3]. In this regard, such crystal structures are often called transrotational [3,4] or simply rotational, when the rotation speed was lower and amounted to fractions or units of deg/µm [5−8].
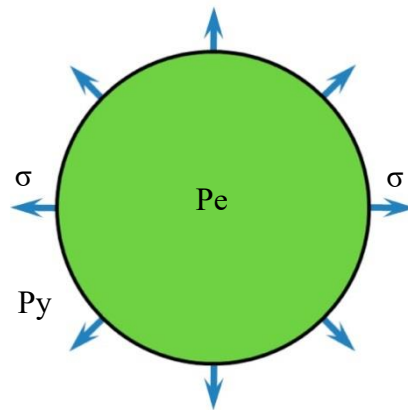
Fig. 1. Schematic representation of the effect of lateral mechanical stresses on a perovskite (Pe) two-dimensional island from the pyrochlore (Py) matrix

Until recently, the physical properties of rotational crystals have been practically unexplored, were mainly descriptive in nature and focused on the study of their microstructure features. There is even less information regarding thin ferroelectric films, primarily lead zirconate titanate (PZT) films, which are currently the main materials in microelectromechanics [9]. As a rule, everything was reduced to recording and describing the features of the spherulitic microstructure, without studying the nature of their formation and the role of mechanical stresses [10−14].

The development of new microscopic research methods, such as scanning electron microscopy, piezoresponse force microscopy, and second optical harmonic generation, have allowed a number of new results to be obtained in the study of thin-film spherulites. Thus, effects of lateral-radial self-polarization, an abnormally high second optical harmonic signal, and recrystallization of the perovskite phase were discovered in PZT thin films [15−17]. In addition, the phenomenon of electron channeling was discovered in InSiO and PZT films [7,18]. The objective of this work was to study the influence of mechanical stresses on the phase state of spherulitic thin PZT films, the composition of which corresponds to the region of the morphotropic phase boundary (MPB).

Interest in the phase state of PZT solid solutions in the region of coexistence of rhombohedral (R) and tetragonal (T) modifications of the ferroelectric phase (morphotropic phase boundary) is associated with anomalously high values of electromechanical and dielectric parameters, due to which ceramic materials based on PZT have remained the main materials of piezoelectric engineering over the past 70 years [19,20]. Thin PZT films find wider application both in microelectromechanics and in microwave electronics, non-volatile memory, photonics, IR technology, etc. [9,21−24]. At

the same time, the nature of the anomalously high technical parameters remains not entirely clear, and the phase diagram of PZT has been refined over the years and is becoming increasingly complex. Figure 2 reflects one of the most widespread modern concepts of the MPB, in the region of which the existence of an intermediate ferroelectric modification of the monoclinic phase (M-phase) at low temperature and its coexistence with the tetragonal modification above room temperature (shaded area in Fig. 2) are assumed. Significantly below room temperature, there is a phase boundary that is responsible for the phase transition associated with either parallel or antiparallel rotation of the octahedra along one or more orthogonal axes of the cube [19,25,26]. In a number of other works, for example in [27], a whole cascade of phase transformations of various modifications of the ferroelectric phase is assumed in the field of MPB.
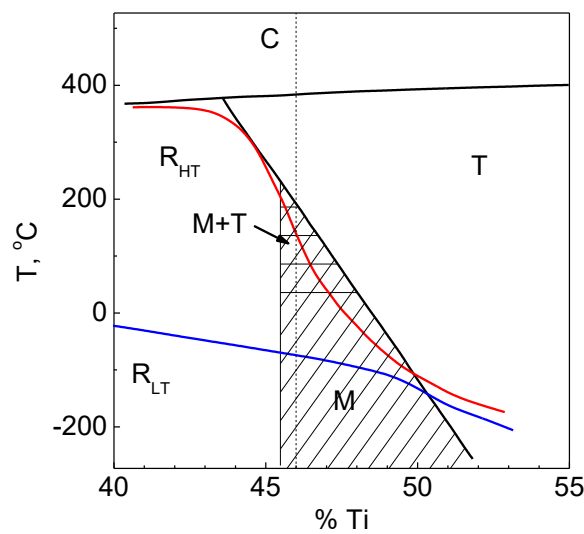
Fig. 2. Phase diagram of PZT solid solutions in the region of the morphotropic phase boundary, according to [19,24,25]

The phase diagram of thin PZT films in the MPB region can be even more complex, which is associated not only with the features of crystallization of the spherulitic structure of films from the amorphous phase, but also with the mechanical impact on the film from the substrate and intermediate sublayers [28,29]. According to theoretical calculations performed for epitaxial thin PZT films [30], mechanical stresses lead both to a shift toward an increase in the Curie temperature and to an expansion of the stable state of the monoclinic modification of the ferroelectric phase in the MPB region.

Materials and Methods

To identify the role of mechanical stresses associated with a decrease in their volume during the crystallization of the perovskite phase, thin films deposited from a ceramic target of the $PbZr_{0.54}Ti_{0.46}O_3$ composition corresponding to the region of the MPB using a two-stage method of RF magnetron sputtering were studied. Films with a thickness of about 500 nm were deposited at different target-substrate distances (D_{T-S}) in the range of 30–70 mm and, as a consequence, differed in the temperature of the substrate heated by

plasma (90–160 °C), as well as in the average size of spherulitic blocks (15–40 µm) formed by high-temperature annealing at 580 °C [16,31]. The films structure was studied using scanning electron microscopy in the electron backscatter mode and electron backscatter diffraction mode (Lira 3 Tescan, EVO-40 Zeiss), X-ray phase analysis θ-2θ (Rigaku Ultima IV), and optical microscopy (Nikon Eclipse LV150). An E7-20 immittance meter and a modified Sawyer-Tower scheme were used to study the dielectric properties.

Results and Discussion

Optical and phase analysis of the formed PZT films showed the absence of parasitic phases, and the presence of all the main reflections of the perovskite phase in the diffraction pattern indicated the polycrystalline nature of the crystalline structure (Fig. 3(a)). In the absence of reflection splitting, it was not possible to identify the symmetry of the ferroelectric phase. Figure 3(b) shows the dependence of the change in the lattice parameter of the perovskite structure under the assumption of pseudocubic symmetry, from which it is evident that the lattice parameter changes abruptly with a decrease in the target-substrate distance from 60 to 50 mm. Figure 3(c) demonstrates the change in the full width at half maximum (FWHM) of the (110) peak, which experiences a jump and correlates with the lattice parameter behavior.
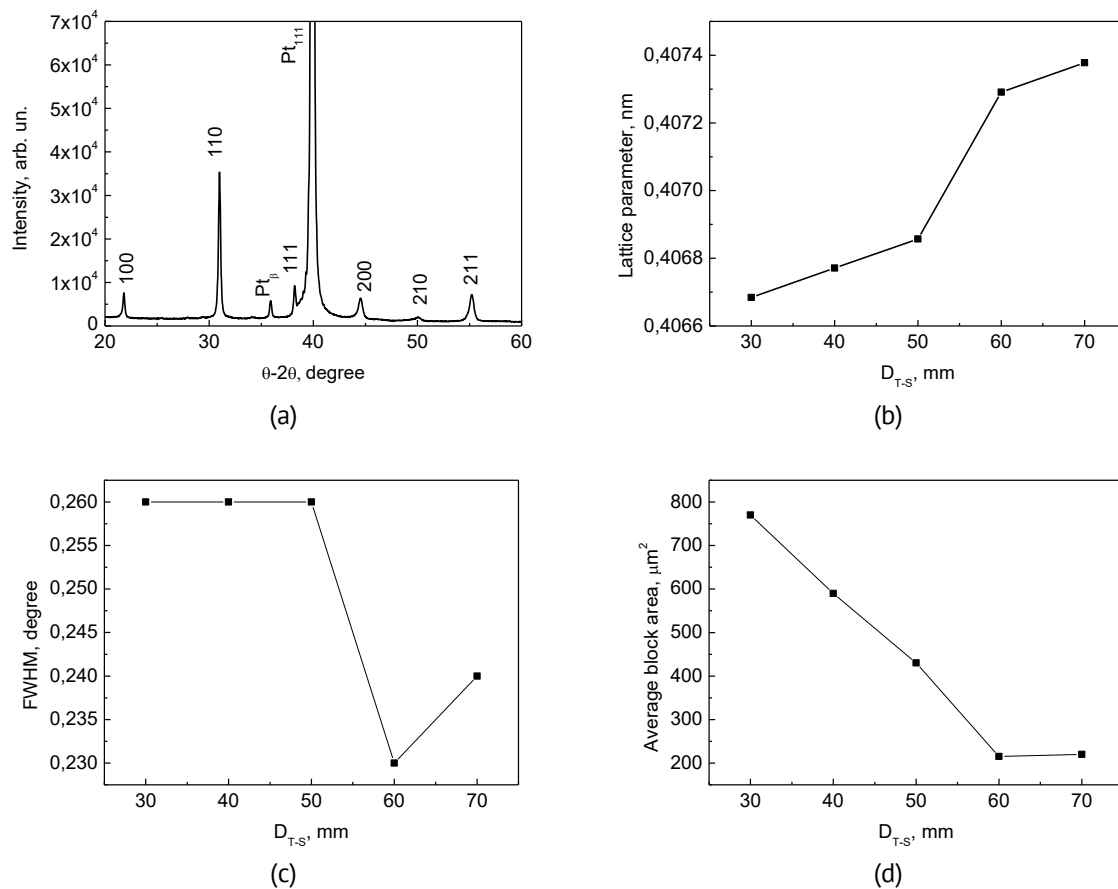
Fig. 3. Typical θ-2θ X-ray diffraction pattern of PZT thin films (a), change in the pseudocubic lattice parameter (b), change in the FWHM of the (110) reflex (c) and the average area of spherulitic blocks (d)
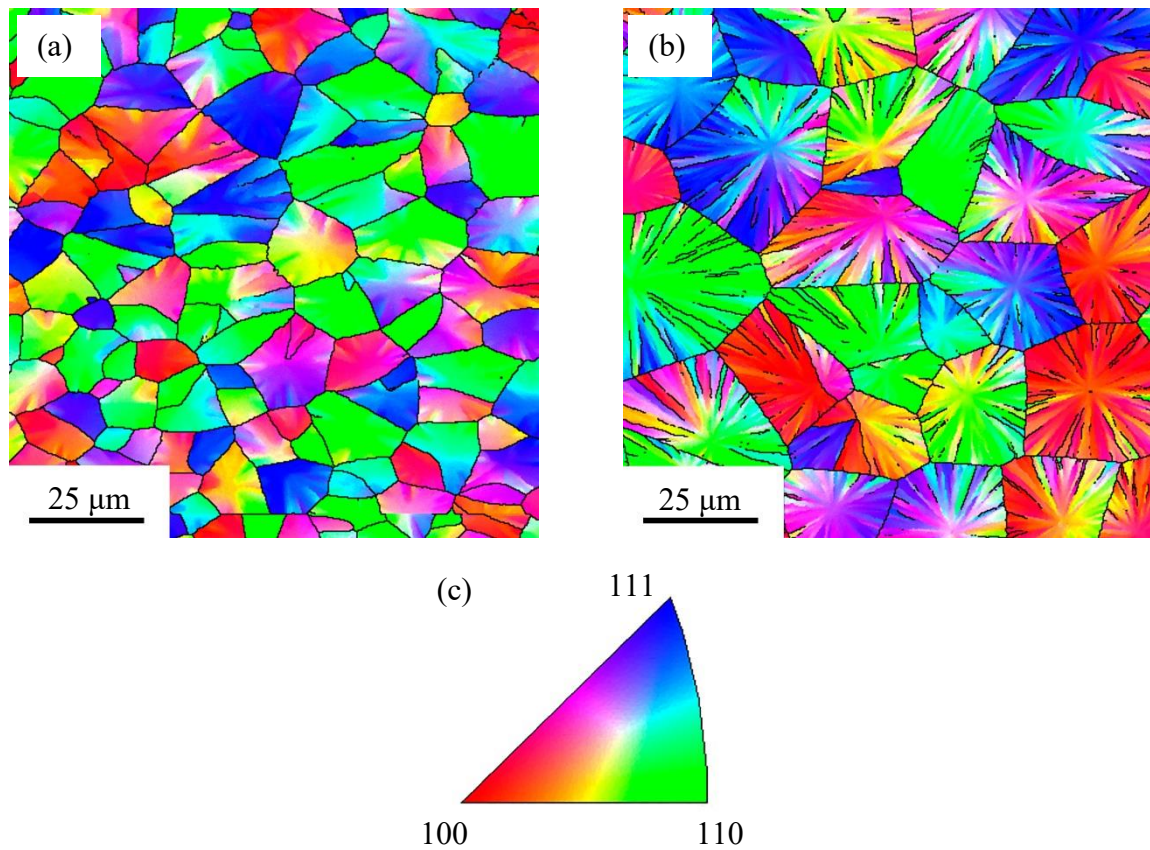
Fig. 4. Crystallographic orientation maps of growth axes of thin films deposited at D_{T-S} of 30 mm (a) and 60 mm (b), as well as color coding of growth axes orientations (c)
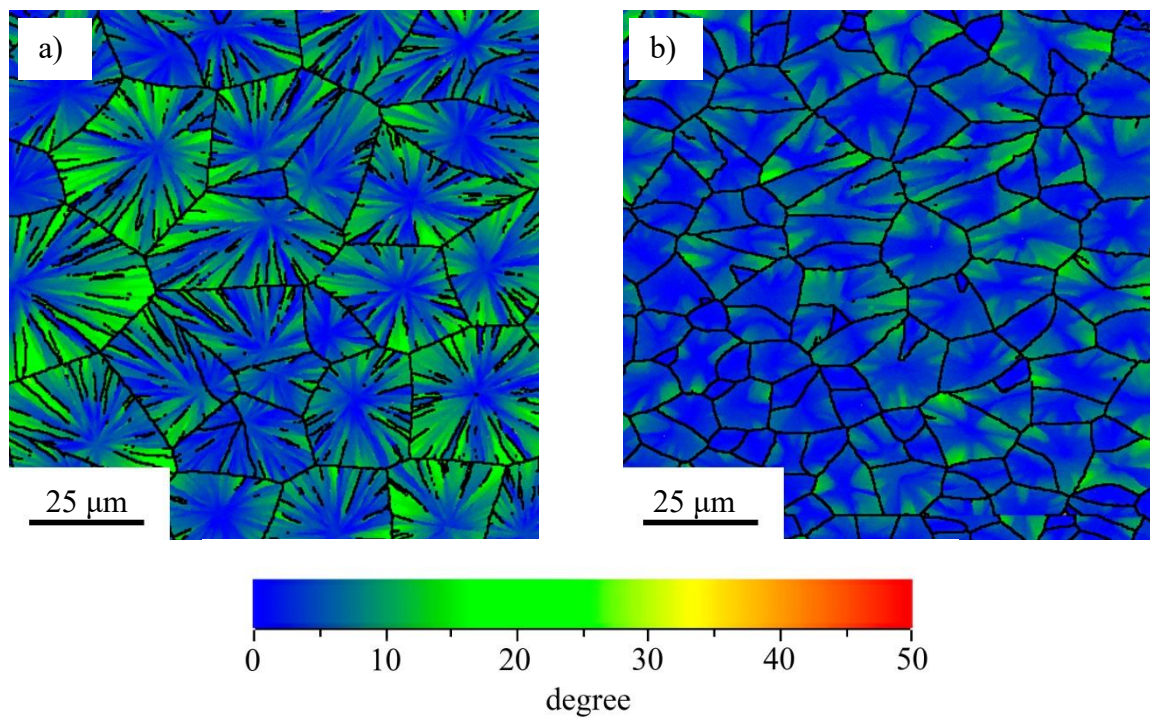
Fig. 5. GROD maps of thin spherulitic films deposited at target-substrate distances of 30 mm (a) and 60 mm (b)

High-temperature annealing of the deposited amorphous films resulted in the nucleation and growth of spherulitic islands of the perovskite phase, which formed a block structure during further growth. Electron images of spherulitic blocks, shown in Fig. 4(a,b), reflect a radially radiant microstructure. The block area increased with decreasing target-substrate distance, and this change correlated with the behavior of the lattice parameter (Fig. 3(d)). The electron backscatter diffraction maps confirm the polycrystalline nature of the spherulitic films, characterized by a predominant <110> growth texture.

Figure 5 shows GROD (Grain Reference Orientation Deviation) maps constructed based on the analysis of electron backscatter diffraction data, in which the change in color scale characterizes the rate of rotation of the crystal lattice.

Flowing radial color change within a single block or ray (Fig. 6(a)) indicates a monotonous and close to linear radial rotation of the crystal lattice from the center to its block periphery (Fig. 6(b)). The range of the rotation rate of crystal lattice of the samples studied was ~ 0.5 – 1.5 deg/µm. Thus, the obtained data indicate strain of the crystal lattice as a result of its rotation. Since the rotation of the crystal lattice occurs with the formation of dislocations, a partial relaxation of radial mechanical stresses takes place [5]. Similarly, partial relaxation of tangential component of mechanical stresses occurs with the appearance of radial boudaries (Fig. 4(b)).
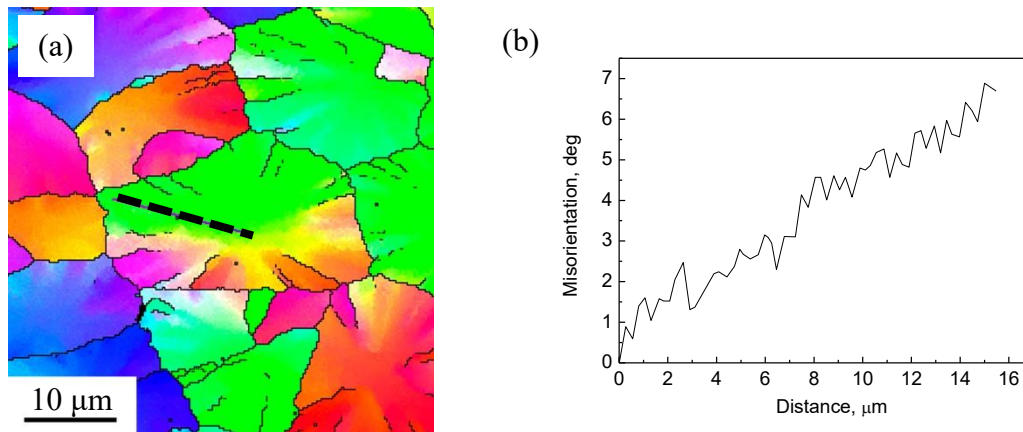
Fig. 6. Radial rotation of the crystal lattice in a spherulitic block in the direction indicated by the dotted line

As a first approximation, the maximum strain can be estimated using the equation for the strain of a flat cylinder:

$$\varepsilon = |\text{grad } \varphi| \, t/2, \tag{1}$$

where ε is the relative strain, t is the film thickness, φ is the rotation angle [2]. According to the obtained results, the estimate of the maximum value of ε varies in the range of 0.25 – 0.75 %.

The magnitude of mechanical stresses:

$$\sigma = E\varepsilon, \tag{2}$$

where E is Young's modulus (equal to 115 GPa [32]), lies in the range of ~ 300 – 900 MPa, while the elastic limit for thin PZT films, according to [33], is ~ 500 MPa. Since the rotation

of the crystal lattice occurs with partial relaxation of mechanical stresses [5], it is assumed that the actual residual stresses may be significantly less. However, for their accurate assessment, additional microscopic studies and an adequate model are necessary.

The study of the temperature dependences of the dielectric permittivity χ(T) made it possible to analyze and evaluate the phase state with a change in the target-substrate distance and the crystalline parameters of thin films. Figure 7 shows the temperature dependences of the reciprocal value of the permittivity (1/χ), a change in the slope of which may indicate a phase transformation from one modification of the ferroelectric phase to another [34]. As can be seen from the graphs, in the range of 20–300 °C (at the Curie temperature TC ~ 380–400 °C) in all the studied samples, two distinct changes in the slope on the $1/\chi(T)$ curve were observed - the phase transition PT-1 (curve 1) and the phase transition PT-2 (curve 2), the temperatures of which changed noticeably with variations in the target-substrate distance.
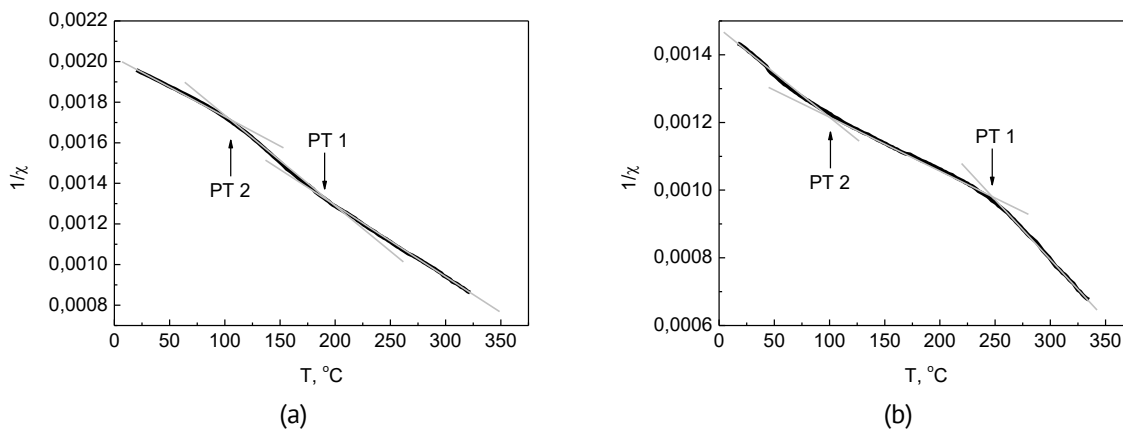
Fig. 7. Temperature dependences of the reciprocal dielectric permittivity (1/χ) for PZT thin films deposited at D_{S-T} of 30 mm (a) and 70 mm (b)
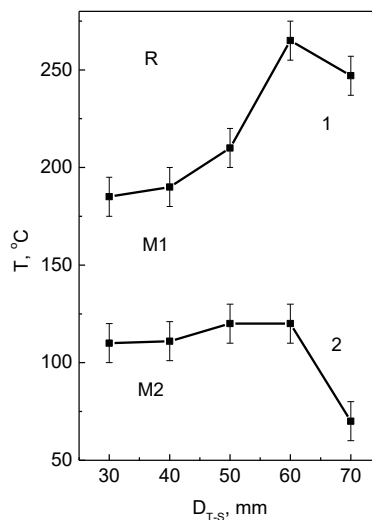
Fig. 8. Phase diagram of spherulitic thin films with changing target-substrate distance

These changes are reflected in Fig. 8. It is evident that with an increase in the size of the spherulitic blocks (and mechanical stresses), the temperature of PT-1 decreases noticeably, which correlates with the phase boundary on the *T-ε* phase diagram in thin PZT films, which reflects the phase transformation from the ferroelectric rhombohedral phase to the monoclinic (R→M1) ferroelectric phase with an increase in the deformation of the crystal lattice *ε* [29].

The interpretation of the low-temperature phase transition (M1→M2) (curve 2) in the films under study is associated with the presence of a phase transition associated with the rotation of oxygen octahedra. Such perovskite structures are observed in calcium titanate perovskite $CaTiO_3$ or in the low-temperature phase of strontium titanate $SrTiO_3$. In ceramic PZT solid solutions in the region of MPB, this phase transition is located below room temperature (Fig. 2). We believe the presence of strong mechanical stresses in PZT spherulitic films shifts this phase transition to the region toward higher temperatures by ~ 150 °C or more. To confirm the version, additional studies using highly sensitive X-ray equipment and a number of new structural methods are needed.

Conclusion

The paper studies spherulitic thin PZT films of composition corresponding to the morphotropic phase boundary, which were produced by a two-stage method, including RF magnetron sputtering of a ceramic target onto a platinized silicon substrate (1) and subsequent high-temperature annealing of the films in air (2). It is shown that a decrease in the target-substrate distance leads to an increase in the size of the spherulitic blocks, which in turn leads to a change in the parameters of the crystal lattice, a linear increase in its radial rotation, and an increase in the rotation rate.

The observed changes confirm the previously made assumptions about the role of tensile mechanical stresses in the plane of a spherulitic thin film, arising due to the difference in the densities of the amorphous and crystalline phases. In our case, in thin PZT films, the difference lies in the crystallization of the perovskite phase from the low-temperature intermediate pyrochlore phase. The values of mechanical stresses are estimated, the values of which either reach or exceed the elastic limit of thin PZT films.

Analysis of the slope changes in the temperature dependences of the reciprocal dielectric permittivity caused by a change in the phase state of thin films made it possible to reveal the relationship between mechanical stresses and temperature changes in structural phase transitions occurring in thin PZT films in the region of the morphotropic phase boundary.

References

1. Shtukenberg AG, Punin YO, Gunn E, Kahr B. Spherulites. *Chemical Reviews.* 2012;112(3): 1805–1838.

2. Kolosov VYu, Thölén AR. Transmission electron microscopy studies of the specific structure of crystals formed by phase transition in iron oxide amorphous films. *Acta Materialia.* 2000;48: 1829–1840.

3. Zhigalina OM, Khmelenin DN, Valieva YA, Kolosov VYu, Kuznetsov KA, Bokunyaeva AO, Vorotilov KA, Sigov AS. Structural features of PLZT films. *Crystallography Reports.* 2018;63(4): 646–655.

4. Kooi BJ, De Hosson JThM. On the crystallization of thin films composed of Sb3.6Te with Ge for rewritable data storage. *Journal of Applied Physics.* 2004;95(9): 4714–4721.

5. Lutjes NR, Zhou S, Antoja-Lleonart J, Noheda B, Ocelík V. Spherulitic and rotational crystal growth of Quartz thin films. *Scientific Reports.* 2021;11(1): 14888.

6. Musterman EJ, Dierolf V, Jain H. Curved lattices of crystals formed in glass. *International Journal of Applied Glass Science.* 2022;13(3): 402–419.

7. Da B, Cheng L, Liu X, Shigeto K, Tsukagoshi K, Nabatame T, Ding Z, Sun Y, Hu J, Liu J, Tang D, Zhang H, Gao Z, Guo H, Yoshikawa H, Tanuma S. Cylindrically symmetric rotating crystals observed in crystallization process of InSiO film. *Science and Technology of Advanced Materials: Methods.* 2023;3(1): 2230870.

8. Sun W, Zhou W. Growth mechanism and microstructures of Cu2O/PVP spherulites. *RSC Advances.* 2022;12: 20022.

9. Song L, Glinsek S, Defay E. Toward low-temperature processing of lead zirconate titanate thin films: Advances, strategies, and applications. *Applied Physics Reviews.* 2021;8(4): 041315.

10. Spierings GACM, Van Zon JBA, Larsen P K, Klee M. Influence of platinum-based electrodes on the microstructure of sol - gel and MOD prepared lead zirconate titanate films. *Integrated Ferroelectrics.* 1993;3(3): 283–292.

11. Nashimoto K, Nakamura S. Preparation and characterization of sol-gel derived epitaxial and oriented Pb(Zr0.52Ti0.48)O3 thin films. *Japanese Journal of Applied Physics.* 1994;33(9S): 5147–5150.

12. Chen S-Y, Chen I-W. Texture development, microstructure evolution, and crystallization of chemically derived PZT thin films. *Journal of American Ceramic Society.* 1998;81(1): 97–105.

13. Alkoy EM, Alkoy S, Shiosaki T. The effect of crystallographic orientation and solution aging on the electrical properties of sol-gel derived Pb(Zr0.45Ti0.55)O3 thin films. *Ceramic International.* 2007;33: 1455–1462.

14. Bretos I, Rodrigez-Castellon E, Tomczyk M, Jimenez R, Vilarinho PM, Calzada ML. Active layers of high-performance lead zirconate titanate at temperatures compatib le with silico-nano- and microelecrtonic devices. *Scientific Reports.* 2016;6: 20143.

15. Elshin AS, Pronin IP, Senkevich SV, Mishina ED. Nonlinear optical diagnostics of thin polycrystalline lead zirconate titanate films. *Technical Physics Letters.* 2020;46(4): 385–388.

16. Staritsyn MV, Pronin VP, Khinich II, Senkevich SV, Kaptelov EYu, Pronin IP, Elshin AS, Mishina ED. Microstructure of spherulitic lead zirconate titanate thin films. *Physics of the Solid State.* 2023;65(8): 1312–1318.

17. Kiselev DA, Staritsyn MV, Senkevich SV, Kaptelov EYu, Pronin IP, Pronin VP. Radially oriented lateral self-polarization in spherulitic lead zirconate titanate thin films. *Technical Physics Letters.* 2023;49(11): 45–47.

18. Staritsyn MV. Anomalous electron channeling in PZT thin films. *Condensed Matter and Interfaces.* 2023;25(4): 572–580.

19. Jaffe B, Cook W, Jaffe H. *Piezoelectric Ceramics*. London: Academic Press; 1971.

20. Xu Y. *Ferroelectric materials and their applications*. Amsterdam: North Holland; 1991.

21. Izyumskaya N, Alivov YI, Cho SJ, Morkoç H, Lee H, Kang YS. Processing, structure, properties, and applications of PZT thin films. *Critical Reviews in Solid State and Materials Sciences.* 2007;32: 111–202.

22. Balke N, Bdikin I, Kalinin SV, Kholkin AL. Electromechanical imaging and spectroscopy of ferroelectric and piezoelectric materials: state of the art and prospects for the future. *Journal of American Ceramic Society.* 2009;92(8): 1629–1647.

23. Selvamani R. Vibration of a hydrostatic stressed piezoelectric layer embedded on gravitating half space with sliding interface boundary. *Materials Physics and Mechanics.* 2020;44(2): 238–249.

24. Ma Y, Song J, Wang X, Liu Y, Zhou J. Synthesis, microstructure and properties of magnetron sputtered lead zirconate titanate (PZT) thin film. *Coatings.* 2021;11(8): 944.

25. Cox DE, Noheda B, Shirane G. Low-temperature phases in PbZr0.52Ti0.48O3: A neutron powder diffraction study. *Physics Review B.* 2005;71(13): 134110.

26. Cordero F. Elastic properties and enhanced piezoelectric response at morphotropic phase boundaries. *Materials.* 2015; 8(12): 8195–8245.

27. Reznichenko LA, Shilkina LA, Razumovskaya ON, Yaroslavtseva EA, Dudkina SI, Demchenko OA, Yurasov YuI, Esis AA, Andryushina IN. Phase formation in near-morphotropic region of the PbZr1−xTixO3 system, structural defects, and electromechanical properties of the solid solutions. *Physics of the Solid State.* 2009;51: 1010–1018.

28. Bruchhaus R, Pitzer D, Schreiter M, Wersing W. Optimized PZT thin films for pyroelectric IR detector arrays. *Journal of Electroceramics.* 1999;3(2): 151–162.

29. Pronin IP, Kaptelov EYu, Gol'tsev AV, Afanasjev VP. The effect of stresses on self-polarization of thin ferroelectric films. *Solid State Physics.* 2003;45(9): 1768–1773.

30. Pertsev NA, Kukhar VG, Kohlstedt H, Waser R. Phase diagrams and physical properties of single-domain epitaxial Pb(Zr1−xTix)O3 thin films. *Physical Review B.* 2003;67(5): 054107.

31. Pronin VP, Dolgintsev DM, Osipov VV, Pronin IP, Senkevich SV, Kaptelov EYu. The change in the phase state of thin PZT layers in the region of the morphotropic phase boundary obtained by the RF magnetron sputtering with varying target-substrate distance. 25th International Conference on Vacuum Technique and Technology. *IOP Conf. Series: Materials Science and Engineering.* 2018; 387(1): 012063.

32. Nazeer H, Nguyen MD, Sukas ÖS, Rijnders G, Abelmann L, Elwenspoek MC. Compositional dependence of the Young's modulus and piezoelectric coefficient of (110)-oriented pulsed laser deposited PZT thin films. *Journal of Microelectromechanical Systems.* 2015;24(1): 166–173.

33. Yagnamurthy S, Chasiotis I, Lambros J, Polcawich RG, Pulskamp JS, Dubey M. Mechanical and ferroelectric behavior of PZT-based thin films. *Journal of Microelectromechanical Systems.* 2011;20(6): 1250–1258.

34. Sheen D, Kim J-J. Dielectric and polarization switching anomalies near the morphotropic phase boundary in Pb(Zr1−xTix)O3 ferroelectric thin films. *Physical Review B.* 2003;67(14): 144102.

About Authors

Vladimir P. Pronin ⓘ Sc

Doctor of Physical and Mathematical Sciences
Professor (Herzen State Pedagogical University of Russia, St. Petersburg, Russia)

Igor V. Ryzhov ⓘ Sc

Candidate of Physical and Mathematical Sciences
Associate Professor (Herzen State Pedagogical University of Russia, St. Petersburg, Russia)

Mikhail V. Staritsyn ⓘ Sc

Engineer (National Research Centre "Kurchatov Institute" -Central Research Institute of Structural Materials "Prometey", St. Petersburg, Russia)

Stanislav V. Senkevich ⓘ Sc

Candidate of Physical and Mathematical Sciences
Researcher (Ioffe Institute, St. Petersburg, Russia)

Evgeny Yu. Kaptelov ⓘ Sc

Candidate of Physical and Mathematical Sciences
Senior Researcher (Ioffe Institute, St. Petersburg, Russia)

Igor P. Pronin ⓘ Sc

Doctor of Physical and Mathematical Sciences
Leading Researcher (Ioffe Institute, St. Petersburg, Russia)

Photoluminescent characteristics of solution-processed nanoscale copper oxide

S. Sachdeva ⓘD, I. Choudhary ✉ ⓘD

Maharishi Markandeshwar (Deemed to be University), Mullana-Ambala, Haryana, India

✉ ishan.phy@gmail.com

ABSTRACT

In the present work, pure CuO nanoparticles were synthesized using the co-precipitation method, and their properties such as structural, morphological, and optical were elucidated. The obtained X-ray diffraction (XRD) patterns confirm that the synthesized CuO powders crystalize to a monoclinic phase. In addition to that, the appearance of the broad XRD peaks reflects the confinement of the particle size to nonorange. The average particle size of the synthesized CuO nanoparticles measured using field emission scanning electron microscopy (FESEM) image is 36.8 nm. Due to the size confinement to the nanoscale, the synthesized CuO nanoparticles showed a high optical band gap of 2.84 eV. Further, the emission properties of CuO measured using photoluminescence (PL) spectroscopy at an excitation wavelength of 300 nm reflects that most of the emission lies in the ultraviolet (UV) range. However, upon close investigation of the emission spectra, the peak corresponding to the blue emission was also observed. The appearance of this blue emission was the consequence of the various defects present in CuO such as oxygen vacancies and copper interstitials. The Commission Internationale de l'Eclairage (CIE) color coordinates for the blue color emitted by CuO nanoparticles is (0.15, 0.13), which lies close to the ideal blue color. Further, the synthesized CuO nanoparticles showed a high color purity of 84.71 % for blue color.

KEYWORDS

CuO • nanoparticles • absorption • emission • defects

Introduction

In recent years, nanoscience and thin-film technology have led to the development of new technologically advanced devices. The major advantages of such devices include lightweight, non-toxic behavior, highly sensitive response, and high output performance with minimum losses [1]. Out of the various materials available, inorganic oxide semiconductors (IOS) are of great interest. IOS materials have a wide optical band gap range, large mobility values even in the amorphous phase, and serve as suitable host materials for various dopants [2–6]. Further, a notably enhanced performance of the devices has been observed for the devices fabricated using IOS nanostructures in comparison to their bulk counterparts. To date, due to the easy availability of the n-type metal oxide semiconductors such as zinc oxide (ZnO), titanium oxide (TiO_2), tin oxide (SnO_2), and tungsten oxide (WO_3), the nanostructures of n-type metal oxides semiconductors have been rigorously investigated worldwide. Numerous high-tech devices such as gas sensors [7–9], biosensors [10–12], nano thin film transistors [13–19], photo-voltaic [20–23], and memory devices [24,25] have been reported in the literature based upon the n-type metal oxide semiconductors. Despite this most of the electronic industry

is still dominated by silicon (Si) based devices. This happens because of the availability of only a few p-type metal oxide semiconductors in nature. To fully replace the silicon (Si) based electronic industry with oxides-based electronics, it is essential to identify a suitable p-type inorganic metal oxide semiconductor that has comparable performance with n-type metal oxide semiconductors and can be processed by cost-effective means. Given this, recent studies have shown that oxides of copper possess inherent p-type semiconducting behavior due to the presence of negatively charged copper vacancies [26,27]. In addition to that, the oxides of copper showed a narrow optical band gap ranging from 1.2 eV to 2.3 eV, which can be easily tuned either by doping or synthesizing its nanostructures [28–31]. This makes the oxides of copper an ideal candidate for various optoelectronic devices such as solar cells, heterojunction diodes, and inverters.

In nature, the oxides of copper exist in two phases namely cuprous oxide (Cu_2O) and Cupric oxide (CuO). However, out of these, CuO has been reported to be the most stable form of copper oxide, since obtaining the Cu_2O phase requires a fine tunability of oxygen partial pressures [29,32]. In addition to that, the Cu_2O phase has a large probability of getting oxidized and converted into a much more stable CuO phase. However, in comparison to the n-type metal oxide semiconductors, the conductivity in the CuO is dominated by the hole conduction. Due to the presence of highly directional localized 2p orbitals from oxygen in valence band maximum (VBM) and deep-level traps near VBM, the hole mobility of CuO is hindered significantly [33,34]. Thus, a band gap modification might improve the performance of CuO. Since, the optical band gap of the semiconductor material depends upon the particle size, in this work, an attempt has been made *a)* to synthesize the nanoparticles of p-type CuO using a cost-effective, and low-temperature solution-based co-precipitation method, and *b)* to study the optical properties of CuO nanoparticles.

Materials and Methods

To prepare CuO nanoparticles, the solution-processed co-precipitation method was adopted. 0.01 moles of copper acetate monohydrate [Cu $(CH_3COO)_2 \cdot H_2O$] from Sigma Aldrich with 99.9 % purity were mixed with 100 ml of laboratory absolute ethanol (99.9 % purity) in a round bottle flask. The flask was then subjected to an oil bath, which was well maintained at a temperature of 70 °C. The oil bath helps in maintaining a uniform and even temperature throughout the reaction. After a continuous vigorous stirring for 2 h, a transparent clear brown color solution with no segregation was obtained. At this point, 0.02 moles of sodium hydroxide (NaOH) were added to the reaction mixture. The addition of the NaOH increases the pH of the solution to 10.5, consequently, a co-precipitation reaction is forced and the solution turns slightly black in a few minutes indicating the formation of the pure copper oxide precipitates. The reaction mixture was then allowed to continuously stir for 2 h. The obtained precipitates were then separated from the solution using a centrifugation technique at 7000 rpm. However, the obtained precipitates were still wet and contained excess solvent. Hence, the obtained precipitates are placed in an oven for 4 h maintained at 100 °C. The dried precipitates were then ground in a mortar pastel and a fine black powder of CuO was obtained. The process flowchart of the synthesis has been presented in Fig. 1.
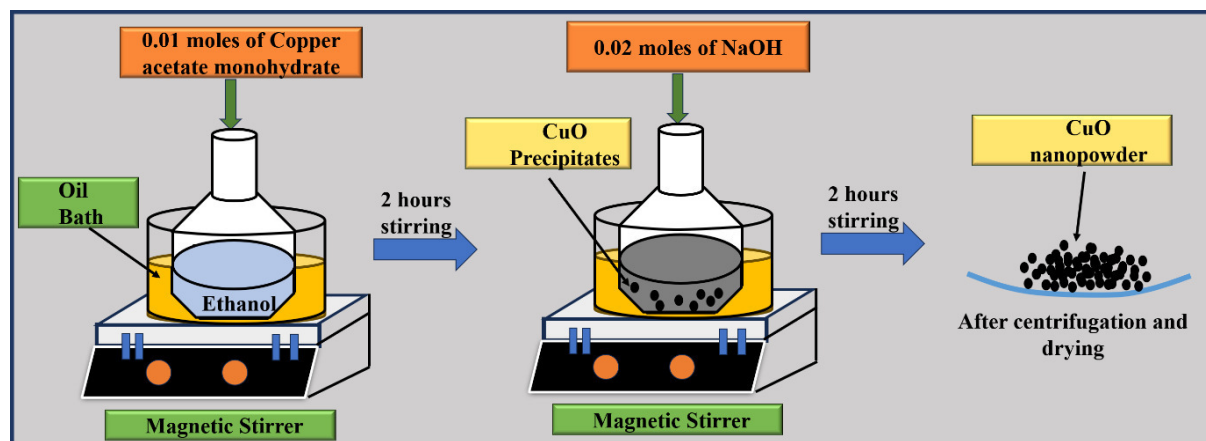
Fig. 1. Process flowchart of the CuO nanoparticles fabrication

Investigation of the structural, morphological, and optical properties of synthesized CuO powder was performed by various experimental techniques such as X-ray diffraction (XRD) (X'pert diffractometer of Philips), fourier infrared spectroscopy (FTIR) (Spectrum L1280130 FTIR spectrometer of Perkin Elmer), field emission scanning electron microscopy (FESEM), energy dispersive X-ray spectroscopy (EDS), UV visible spectroscopy (spectra max iD3), and spectroflurophotometer (Shimadzu RF-5301PC) were used. To perform XRD measurements the synthesized CuO powder was spread on a glass plate and X-rays were incident on the sample at a grazing angle of 2°. The diffraction angle 2θ was varied from 20° to 80° with a step size of 0.02. For the study of optical properties, samples for UV visible and photoluminescence (PL) measurements were prepared by dispersing CuO powder in a pure ethanol solution, which was filled inside a 96-well plate. The 96-well plate was then implanted inside the UV-visible spectrophotometer to obtain the absorbance spectra.

Results and Discussion

Structural analysis

The XRD pattern of the synthesized CuO powder using the co-precipitation technique has been depicted in Fig. 2. Appearance of the strong diffraction peaks reveals that the synthesized CuO particles are crystalline. Peak matching performed using X'pert high score software confirms that the synthesized CuO powders have been crystalized to a monoclinic phase, which corresponds to JCPDS card No. 48-1548. The diffraction peaks located at a diffraction angle (2θ) equal to 32.08°, 35.60°, 38.47°, 48.16°, 53.80°, 57.71°, 61.19°, 65.30°, 67.52°, 72.34°, and 74.60° belong to the (110), {(002), (11$\bar{1}$)}, {(111), (200)}, (20$\bar{2}$), (020), (202), (11$\bar{3}$), (31$\bar{1}$), (113), (331), and (004) respectively.

Next, we analyse the appearance of broad XRD patterns obtained for the synthesized pure CuO. According to the literature, smaller crystallite size (D) and microstrain (ε) are the two factors that lead to the broadening of the XRD peaks [29].
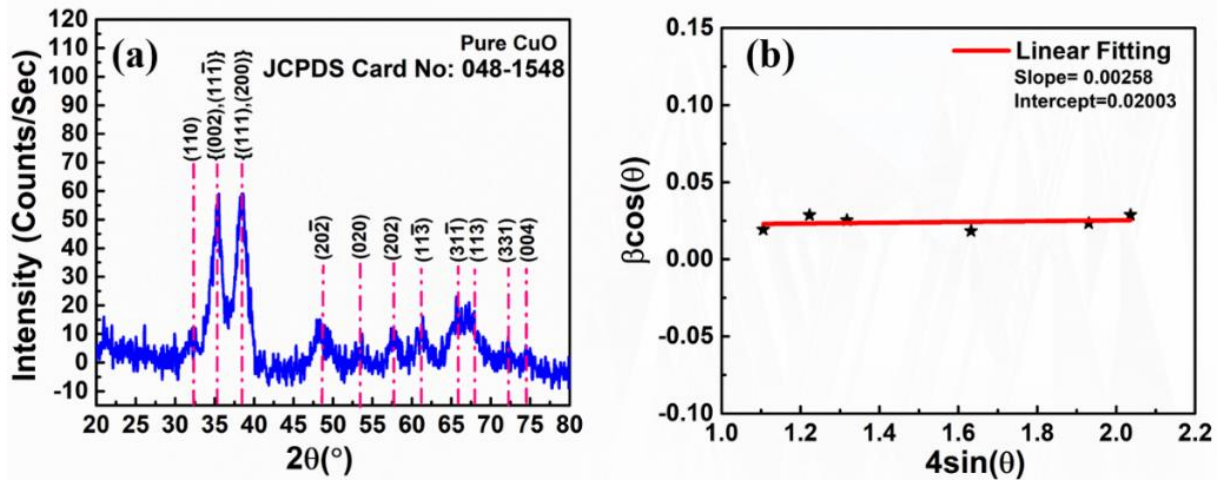
Fig. 2. (a) XRD pattern of synthesized pure CuO powder; (b) WHM plot of synthesized pure CuO

To quantify these factors simultaneously, the Williamson-Hall Method (WHM) can be adopted. According to this method, the total broadening of the XRD peak is given by:

$$(Broadening\ (\beta_T)\ )_{(Total)} = (Broadening)_{(Size)} + (Broadening)_{(microstrain)}, \qquad (1)$$

where β_T represents the full width at half maximum (FWHM) of the corresponding XRD peak. The broadening due to the crystallite size can be quantified using the Scherer formula as:

$$\beta_{Crystallite\ size} = \frac{K\lambda}{Dcos\theta}, \qquad (2)$$

where, K is shape factor, D is the crystallite size, λ is the X-ray wavelength, and θ is the diffraction angle. On the other hand, the microstrain broadening is quantified using:

$$\beta_{microstrain} = 4\varepsilon \cdot tan\,\theta. \qquad (3)$$

Upon substituting the Eqs. (2) and (3) in Eq. (1), a straight-line equation is obtained and is given as:

$$\beta_T cos\theta = \varepsilon(4\,sin\,\theta) + \frac{K\lambda}{D}. \qquad (4)$$

Hence, by plotting $\beta cos\theta$ along Y-axis and $4\,sin\,\theta$ along X-axis, the average values of crystallite size and the microstrain can be obtained. The value of the microstrain is governed by the slope of the curve, while the intercept governs the crystallite size. Figure 2(b) represents the corresponding WHM plot for the synthesize pure CuO powder. Thus, the calculated value of the microstrain is 0.00258 and the average crystallite size of the synthesized pure CuO powder is around 6.83 nm.

Next, we determine the lattice parameters and lattice volume of the CuO unit cell. For a monoclinic lattice the d-spacing is given by

$$\frac{1}{d^2} = \frac{1}{sin^2\beta}\left[\frac{h^2}{a^2} + \frac{k^2 sin^2\beta}{b^2} + \frac{l^2}{c^2} - \frac{2hl cos\beta}{ac}\right], \qquad (5)$$

where h, k, l are Miller indices of the plane, d is an interplanar spacing, a, b, c are lattice constants and β is the angle greater than 90°. The values of β, a, b, and c are calculated by considering (200), (002), (202), (20$\bar{2}$) and (020) lattice planes. The lattice volume of the monoclinic lattice then can be calculated using

$$V = abc \cdot sin\beta . \qquad (6)$$

All the lattice parameters and lattice volume has been listed in Table 1.

Table 1. Lattice parameters of synthesized pure CuO nanoparticles

Lattice Plane	d-spacing	β, °	Lattice constant *a*, Å	Lattice constant *b*, Å	Lattice constant *c*, Å	Lattice volume, Å³
(200)	2.3080					
(002)	2.5064					
(202)	1.5770	99.44	4.6794	3.4124	5.0817	80.0446
(20$\bar{2}$)	1.8599					
(020)	1.7062					

Morphological analysis: FESEM and EDS

The FESEM image of the synthesized pure CuO nanoparticles at a magnification of 30000x is shown in Fig. 3(a). The CuO nanoparticles showed an agglomerated spherical shape morphology. To determine the particle size using FESEM, the particle size of various nanoparticles distributed in the FESEM image was calculated with the help of Image-J software. The obtained data has been represented in Fig. 3(b) as a histogram. Using a normal distribution the calculated mean particle size of the synthesized CuO nanoparticles is 36.8 nm, with a standard deviation of 16.71 nm. The obtained result is also consistent with the crystallite size calculated using the XRD data.
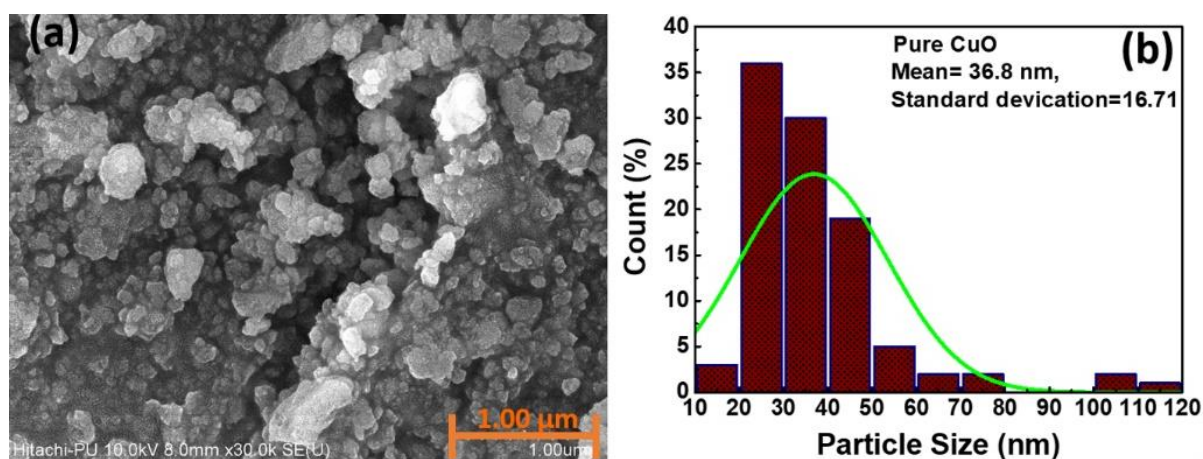
Fig. 3. (a) FESEM image of CuO nanoparticles at a magnification of 30000x;
(b) histogram and normal distribution of the CuO nanoparticles particle size

Element	Weight Percent	Atomic Percent
Copper	38.28%	71.13%
Oxygen	61.72%	28.87%
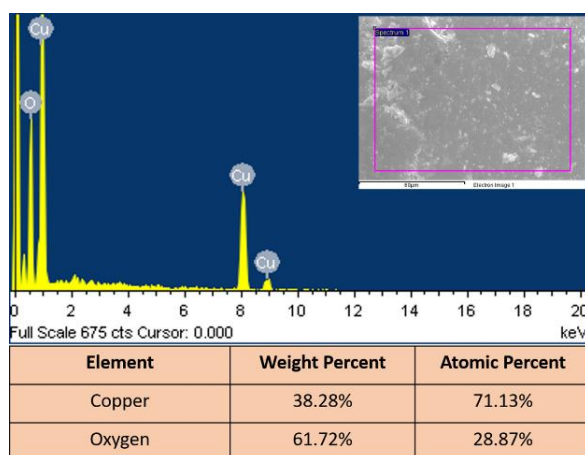
Fig. 4. EDS spectra of synthesized CuO nanoparticles

Next, we determine the elemental composition of the synthesized pure CuO nanoparticles using EDS spectroscopy, as shown in Fig. 4. The EDS spectra clearly show the peaks of copper (Cu) and oxygen (O), indicating the presence of both Cu and O ions.

The corresponding atomic percentages of Cu and O in synthesized CuO nanoparticles are 71.13 and 28.87 %, respectively. In terms of weight percentage, the Cu ion has 38.28 wt. %, and the O ion has a 61.72 wt. %.

Chemical Analysis

To identify the presence of various functional groups, stretching, and vibration modes present in the synthesized CuO nanoparticles, FTIR spectroscopy is performed. The obtained FTIR spectra have been presented in Fig. 5. According to the previous reports the peaks corresponding to the vibration and stretching of the CuO phase are located from 400 to 900 cm^{-1} band [35]. The obtained peak centred at 476.86 cm^{-1} corresponds to the A_u mode of vibration and is due to the stretching of Cu-O along [101] direction [36]. Further, the peaks at 745.46 and 856.01 cm^{-1} are associated with the Cu-O stretching mode along [$\bar{2}$02] direction [29]. In addition to that, the absence of any extra peak in the range of 600 to 650 cm^{-1} indicates the absence of IR active modes of the Cu_2O phase [36]. This eliminates the possibility of the formation of the secondary Cu_2O phase or complexes.
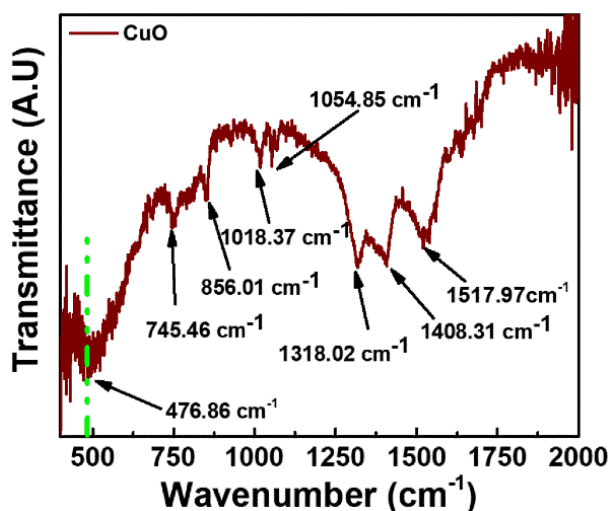
Fig. 5. FTIR spectra of synthesized CuO nanoparticles

The FTIR peaks that appear above 900 cm^{-1} are due to the presence of the functional groups attached to the CuO nanoparticles. The peaks appeared at 1318.02, 1408.31, and 1517.97 cm^{-1} are associated with the presence of cis-di substituted alkenes and amide (COO−) groups [29,37]. The peaks at 1018.37 and 1054.85 cm^{-1} are associated with the O−H bond stretching of the alkyl group [34,38].

Absorption properties

Figure 6(a) represents the absorption spectra of the synthesized pure CuO nanoparticles. The obtained spectra depict that pure CuO nanoparticles have an absorption edge located at 300.6 nm.
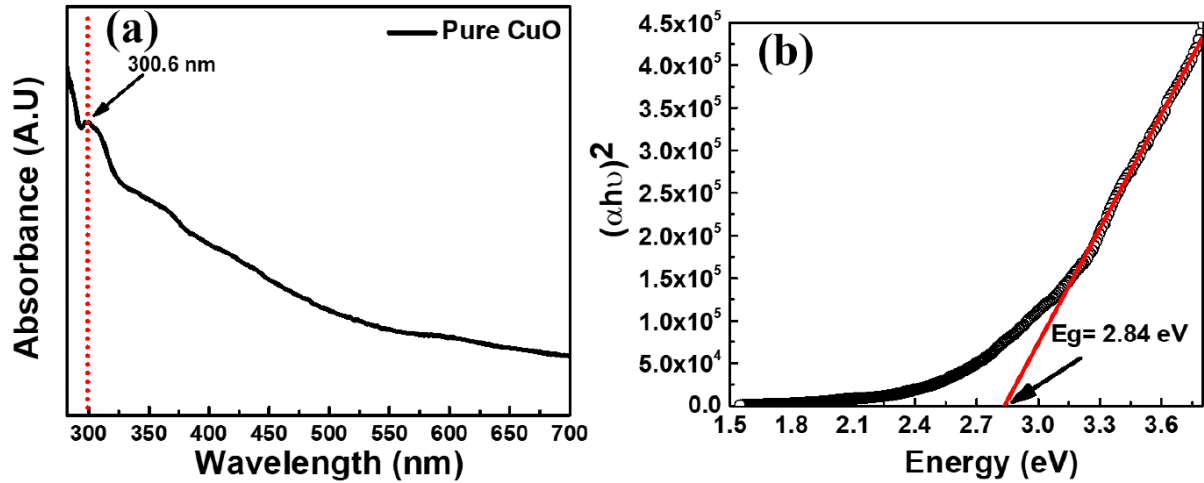
Fig. 6. (a) UV absorption spectra of synthesized pure CuO nanoparticles; (b) the ($\alpha h\nu$)2 vs $h\nu$ plot for synthesized pure CuO nanoparticles

To determine the optical band gap of the pure CuO, the well-known Tauc's method was adopted [39,40]. According to this method, the absorption coefficient α for a material can be given as:

$$\alpha h\nu = A(h\nu - E_g)^n, \tag{7}$$

where α represents the absorption coefficient, E_g represents the optical band gap, A is a constant, and exponent n can have values 0.5, 1.5, 2, or 3. The value of n determines the type of electronic transitions. In the case of direct electronic transitions, the value of n is equal to 0.5. The CuO is also a direct band gap semiconductor [41], hence we take n = 0.5 in our case also.

Figure 6(b) represents the ($\alpha h\nu$)^2 vs $h\nu$ plot for synthesized pure CuO nanoparticles. The optical band gap of 2.84 eV is determined using this approach for pure CuO nanoparticles. The obtained optical gap of synthesized pure CuO nanoparticles is quite higher in comparison to the bulk CuO, which is 1.2-1.9 eV [42]. This increase in the optical band gap might be due to the lower crystallite size of synthesized CuO nanoparticles. At the nanoscale level, the crystallite size becomes smaller than the Bohr radius of the exciton due to which the discrete energy level forms at the edges of the conduction and valence conduction band. Consequently. the band gap increases.

Emission properties

Figure 7(a,b) represents the PL spectra of the CuO nanoparticles at an excitation wavelength of 300 nm. The pure CuO nanoparticles showed a broad emission spectrum spreading from 320 to 600 nm.

To locate the exact peak positions, first, we removed the background using the b-spline interpolation method in Origin 9.0 software. The obtained emission spectra curve is then fitted using the Voigt function fitting. The Voigt function is a mixture of Gauss and Lorentz functions. According to the fitted curve the obtained emission spectra consists of 2 major emissions peaks positioned at 387.24 and 454.92 nm. The emission peak at 387.24 nm lies in the ultraviolet region and is of no interest. On the other hand, the emission peak at 454.92 nm corresponds to the blue region of the visible spectra, which is confirmed by plotting an XY chromaticity coordinate graph with the help of the

standard Commission Internationale de l'Eclairage (CIE) diagram, as depicted in Fig. 8. GOCIE software is used to prepare the CIE diagram. The obtained color coordinates corresponding to the emission wavelengths of 454.90 nm are (0.15; 0.13) and are marked as a black circle in Fig. 8.
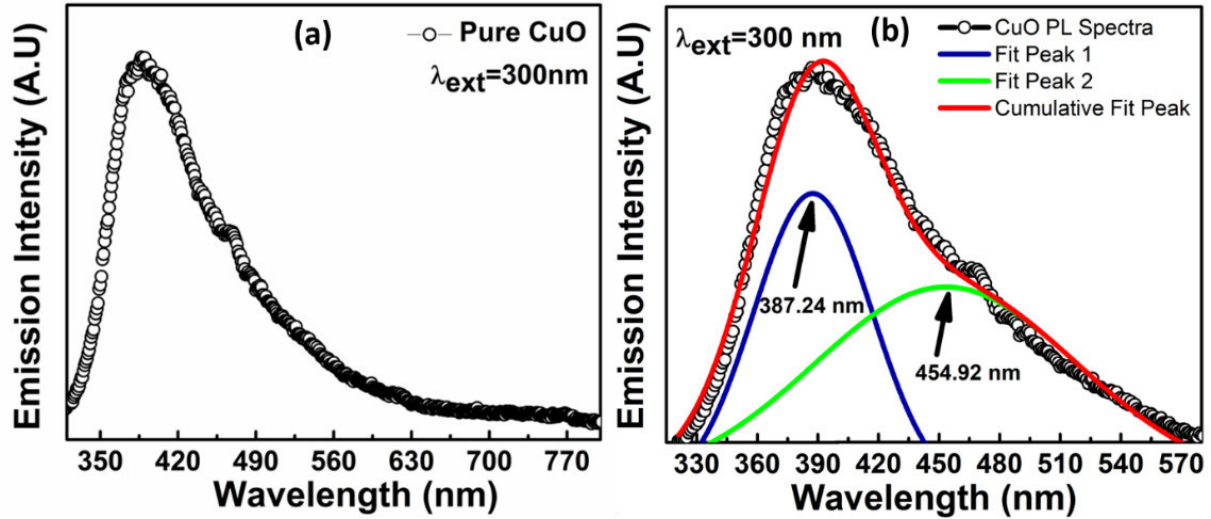
Fig. 7. (a) PL spectra of synthesized CuO nanoparticles at an excitation wavelength of 300 nm; (b) curve fitting of the emission peaks of synthesized CuO nanoparticles
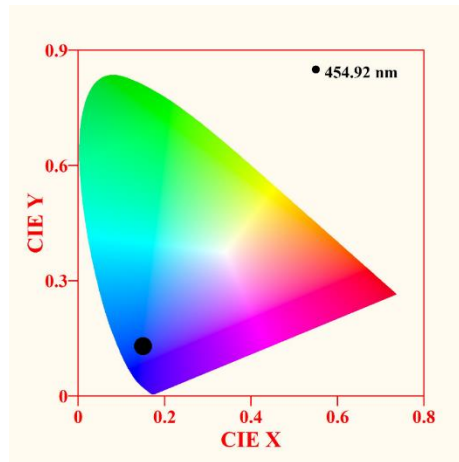
Fig. 8. CIE diagram of CuO nanoparticles at an excitation wavelength of 300 nm

Table 2. Defect reaction in synthesized CuO nanoparticles

$0.5O_2 \leftrightarrow \ddot{V}_O + 2e^-$	Formation of oxygen vacancies
$Cu_{Cu}^x \leftrightarrow V_{Cu}^{''} + \ddot{C}u_i$	Formation of negatively charged copper vacancies and copper interstitials

The emission peak at 387.24 nm appears due to the electron-hole pair recombination in free excitons. Since this peak lie in the UV region, it is of no interest. On the other hand, the emission peak centred at 454.92 nm lies in the blue region of the visible spectra. This blue emission peak is attributed to the defects present in the copper oxide such as surface states, oxygen vacancies, copper vacancies, and interstitial defects.

According to the reports of El-Trass et al. [43] the emission peak at 454.92 nm corresponds to the copper interstitial and oxygen vacancies. The corresponding Kroger-Vink defect reactions for the formation of these defects in CuO have been listed in Table 2.

Next, we determine the color purity of the blue colour emission corresponding to the emission wavelength of 454.92 nm using the expression:

$$Color\ purity = \frac{\sqrt{(Z_S - Z_I)^2 + (Y_S - Y_I)^2}}{\sqrt{(Z_D - Z_I)^2 + (Y_D - Y_I)^2}} \times 100\%, \tag{8}$$

where, $(Z_I; Y_I)$, $(Z_S; Y_S)$, and $(Z_D; Y_D)$ are the color coordinates of the standard illuminate point (0.3101; 0.3162), sample, and respective ideal blue color (0.14; 0.08). The calculated value of the color purity for the synthesized CuO nanoparticles is found to be 84.71 %.

In summary, it is established that synthesized CuO nanoparticles mostly emit in the UV range. However, the emission spectra also consist of the peak corresponding to the blue emission, which appeared due to the formation of oxygen vacancies and copper interstitial defects.

Conclusions

Pure CuO nanoparticles are synthesized using the co-precipitation method. The Broad XRD peaks suggest the particle size lies in the nano range and is confirmed using FESEM. The average particle size of the synthesized CuO nanoparticles is 36.8 nm. The synthesized CuO nanoparticles showed a high band gap of 2.84 eV due to the quantum size effect. Further, Blue emission from pure CuO nanoparticles at an excitation wavelength of 300 nm is demonstrated. The presence of the various defects in CuO such as oxygen vacancies and copper interstitials are the responsible factors for the appearance of this blue emission. The obtained CIE color co-ordinates for the blue color is (0.15, 0.13), and lies close to the ideal blue color co-ordinates (0.14, 0.08). Further, the synthesized CuO nanoparticles showed a high colour purity of 84.71 %.

References

1. Yu X, Marks TJ, Facchetti A. Metal oxides for optoelectronic applications. *Nat Mater.* 2016;15: 383–396.
2. Grundmann M, Klüpfel F, Karsthof R, Schlupp P, Schein FL, Splith D, Yang C, Bitter S, Wenckstern H. Oxide bipolar electronics: materials, devices and circuits. *Journal of Physics D: Applied Physics.* 2016;49(21): 213001.
3. Martins RFP, Ahnood A, Correia N, Pereira LMNP, Barros R, Barquinha PMCB, Costa R, Ferreira IMM, Nathan A, Fortunato EEMC. Recyclable, Flexible, Low-Power Oxide Electronics. *Advanced Functional Materials.* 2013;23: 2153–2161.
4. Petti L, Munzenrieder N, Vogt C, Faber H, Büthe L, Cantarella G, Bottacchi F, Anthopoulos TD, Tröster G. Metal oxide semiconductor thin-film transistors for flexible electronics. *Appl Phys Rev.* 2016; 3(2): 021303.
5. Hosono H, Yasukawa M, Kawazoe H. Novel oxide amorphous semiconductors: transparent conducting amorphous oxides. *Journal of Non-Crystalline Solids.* 1996;203: 334–344.
6. Hosono H, Kikuchi N, Ueda N, Kawazoe H. Working hypothesis to explore novel wide band gap electrically conducting amorphous oxides and examples. *Journal of Non-Crystalline Solids.* 1996;198–200(1): 165–169.
7. Nie L, Guo X, Gao C, Wu X, Chen J, Peng L. Fabrication and optical hydrogen gas sensing property of hierarchical WO3 Porous/Nanowires film. *Materials Letters.* 2022;314: 131805.
8. Franco MA, Conti PP, Andre RS, Correa DS. A review on chemiresistive ZnO gas sensors. *Sensors and Actuators Reports.* 2022;4: 100100.
9. Tian X, Cui X, Lai T, Ren J, Yang Z, Xiao M, Wang B, Xiao X, Wang Y. Gas sensors based on TiO$_2$ nanostructured materials for the detection of hazardous gases: A review. *Nano Materials Science.* 2021;3(4): 390–403.

10. Rafiee Z, Mosahebfard A, Sheikhi MH. High-performance ZnO nanowires-based glucose biosensor modified by graphene nanoplates. *Materials Science in Semiconductor Processing.* 2020;115: 105116.

11. Shetti NP, Bukkitgar SD, Reddy KR, Reddy CV, Aminabhavi TM. ZnO-based nanostructured electrodes for electrochemical sensors and biosensors in biomedical applications. *Biosensors and Bioelectronics.* 2019;141: 111417.

12. Pillai RR, Sreelekshmi PB, Meera AP. Enhanced biological performance of green sythesized copper oxide nanoparticles using Pimenta dioica leaf extract. *Materials Today: Proceedings.* 2022;50(2): 163–172.

13. Choudhary I, Deepak. Study on dielectric properties of PVP and Al_2O_3 thin films and their implementation in low-temperature solution-processed IGZO-based thin-film transistors. *Journal of Materials Science: Materials in Electronics.* 2021;32: 7875–7888.

14. Zhang L, Wei J, Zhou K, Wan C, Sun H. Highly transparent IGZO-TFTs uses IGZO source and drain electrodes with a composite insulation layer structure. *Optik.* 2020;204: 163654.

15. Kang M-S, Cho W-J. High-performance amorphous indium gallium zinc oxide thin-film transistors with sol-gel processed gate dielectric and channel layer fabricated using microwave irradiation. *Current Applied Physics.* 2018;18(9): 1080–1086.

16. Xue J, Song J, Dong Y, Xu L, Li J, Zeng H. Nanowire-based transparent conductors for flexible electronics and optoelectronics. *Science Bulletin.* 2017;62(2): 143–156.

17. Park S, Kim C-H, Lee W-J, Sung S, Yoon M-H. Sol-gel metal oxide dielectrics for all-solution-processed electronics. *Materials Science and Engineering: R: Reports.* 2017;114: 1–22.

18. Yu X, Marks TJ, Facchetti A. Metal oxides for optoelectronic applications. *Nature Materials.* 2016;15: 383–396.

19. Lorenz M, Ramachandra Rao MS, Venkatesan T, Fortunato E, Barquinha P, Branquinho R, Salgueiro D, Martins R, Carlos E, Liu A, Shan FK, Grundmann M, Boschker H, Mukherjee J, Priyadarshini M, DasGupta N, Rogers DJ, Teherani FH, Sandana EV, Bove P, Rietwyk K, Zaban A, Veziridis A, Weidenkaff A, Muralidhar M, Murakami M, Abel S, Fompeyrine J, Zuniga-Perez J, Ramesh R, Spaldin NA, Ostanin S, Borisov V, Mertig I, Lazenka V, Srinivasan G, Prellier W, Uchida M, Kawasaki M, Pentcheva R, Gegenwart P, Miletto Granozio F, Fontcuberta J, Pryds N. The 2016 oxide electronic materials and oxide interfaces roadmap. *Journal of Physics D: Applied Physics.* 2016;49: 433001.

20. Roa S, Sandoval M, Burgos MJC, Manidurai P, Suárez S. Potential photovoltaic properties of thin film solar cells based on chemically deposited ZnO/PbSe junctions. *Journal of Alloys and Compounds.* 2021;871: 159559.

21. Saleh Al-Khazali SM, Al-Salman HS, Hmood A. Low cost flexible ultraviolet photodetector based on ZnO nanorods prepared using chemical bath deposition. *Materials Letters.* 2020;277: 128177.

22. Aboulouard A, Gultekin B, Can M, Erol M, Jouaiti A, Elhadadi B, Zafer C, Demic S. Dye sensitized solar cells based on titanium dioxide nanoparticles synthesized by flame spray pyrolysis and hydrothermal sol-gel methods: a comparative study on photovoltaic performances. *Journal of Materials Research and Technology.* 2020;9(2): 1569–1577.

23. Kumar Rana A, Ban D-K, Patel M, Yun J-H, Kim J. A transparent photovoltaic device based on Cu_2O/ZnO/AZO for see-through applications. *Materials Letters.* 2019;255: 126517.

24. Hu L, Gao W, Xiao M, Li Z. Interfacial reaction induced digital-to-analog resistive switching in TiO_2-based memory devices. *Physica B: Condensed Matter.* 2022;632: 413730.

25. Yu Z, Sun T, Liu B, Zhang L, Chen H, Fan X, Sun Z. Self-rectifying and forming-free nonvolatile memory behavior in single-crystal TiO_2 nanowire memory device. *Journal of Alloys and Compounds.* 2021;858: 157749.

26. Meyer BK, Polity A, Reppin D, Becker M, Hering P, Klar PJ, Sander T, Reindl C, Benz J, Eickhoff M, Heiliger C, Heinemann M, Blasing J, Krost A, Shokovets S, Muller C, Ronning C. Binary copper oxide semiconductors: From materials towards devices. *Phys. Status Solidi B.* 2012;249(8): 1487–1509.

27. Li J, Tokumitsu E, Koyano M, Mitani T, Shimoda T. Highly conductive p-type amorphous oxides from low-temperature solution processing. *Applied Physics Letters.* 2012;101(13): 132104.

28. Usha V, Kalyanaraman S, Thangavel R, Vettumperumal R. Effect of catalysts on the synthesis of CuO nanoparticles: Structural and optical properties by sol–gel method. *Superlattices and Microstructures.* 2015;86: 203–210.

29. Kumar N, Parui SS, Limbu S, Mahato DK, Tiwari N, Chauhan RN. Structural and optical properties of sol–gel derived CuO and Cu_2O nanoparticles. *Materials Today: Proceedings.* 2021;41(2): 237–241.

30. Selvaraj SP. Enhanced surface morphology of copper oxide (CuO) nanoparticles and its antibacterial activities. *Materials Today: Proceedings.* 2022;50(7): 2865–2868.

31. Sivayogam D, Kartharinal Punithavathy I, Johnson Jayakumar S, Mahendran N. Study on structural, electro-optical and optoelectronics properties of CuO nanoparticles synthesis via sol gel method. *Materials Today: Proceedings.* 2022;48(2): 508–513.

32. Paul CA, Ranjith Kumar E, Suryakanth J, Abd El-Rehim AF. Analysis and characterization of structural, morphological, thermal properties and colloidal stability of CuO nanoparticles for various natural fuels. *Ceramics International.* 2023;49(19): 31193–31209.

33. Li BS, Akimoto K, Shen A. Growth of Cu_2O thin films with high hole mobility by introducing a low-temperature buffer layer. *J Cryst Growth.* 2009;311(4): 1102–1105.

34. Ghotbi MY, Rahmati Z. Nanostructured copper and copper oxide thin films fabricated by hydrothermal treatment of copper hydroxide nitrate. *Materials & Design.* 2015;85: 719–723.

35. Ethiraj AS, Kang DJ. Synthesis and characterization of CuO nanowires by a simple wet chemical method. *Nanoscale Research Letters.* 2012;7: 70.

36. Singh SJ, Chinnamuthu P. Highly efficient natural-sunlight-driven photodegradation of organic dyes with combustion derived Ce-doped CuO nanoparticles. *Colloids and Surfaces A: Physicochemical and Engineering Aspects.* 2021;625: 126864.

37. Choudhary I, Shukla R, Sharma A, Raina KK. Effect of excitation wavelength and europium doping on the optical properties of nanoscale zinc oxide. *Journal of Materials Science: Materials in Electronics.* 2020;31: 20033–20042.

38. Albert Manoharan A, Chandramohan R, David prabu R, Valanarasu S, Ganesh V, Shkir M, Kathalingam A, AlFaify S. Facile synthesis and characterization of undoped, Mn doped and Nd co-doped CuO nanoparticles for optoelectronic and magnetic applications. *Journal of Molecular Structure.* 2018;1171: 388–395.

39. Choudhary I, Sehrawat R, Mehta S, Mittal R, Dhawan R, Rana K, Suraj, Sachdeva S. Photoluminescent and magnetic characteristics of cobalt and manganese doped nanoscale zinc oxide. *Journal of Materials Science: Materials in Electronics.* 2023;34: 1505.

40. Tauc J. Optical properties and electronic structure of amorphous Ge and Si. *Materials Research Bulletin.* 1968;3(1): 37–46.

41. Dhineshbabu NR, Rajendran V, Nithyavathy N, Vetumperumal R. Study of structural and optical properties of cupric oxide nanoparticles. *Applied Nanoscience.* 2016;6: 933–939.

42. Xu L, Zheng G, Pei S, Wang J. Investigation of optical bandgap variation and photoluminescence behavior in nanocrystalline CuO thin films. *Optik.* 2018;158: 382–390.

43. El-Trass A, ElShamy H, El-Mehasseb I, El-Kemary M. CuO nanoparticles: Synthesis, characterization, optical properties and interaction with amino acids. *Applied Surface Science.* 2012;258(7): 2997–3001.

About Authors

Shubham Sachdeva iD Sc

M. Sc., Research Scholar (Maharishi Markandeshwar (Deemed to be University), Mullana-Ambala, Haryana, India)

Ishan Choudhary iD Sc

PhD, Assistant Professor (Maharishi Markandeshwar (Deemed to be University), Mullana-Ambala, Haryana, India)

Finite element analysis for prediction of femoral component strength in hip joint endoprosthesis made from meta-biomaterial

A.I. Borovkov [1] (ID) **, L.B. Maslov** [1,2] (ID) **, M.A. Zhmaylo** [1] ✉ (ID) **, F.D. Tarasenko** [1] (ID) **, L.S. Nezhinskaya** [1] (ID)

[1] Peter the Great St. Petersburg Polytechnic University, St. Petersburg, Russia

[2] Ivanovo State Power Engineering University, Ivanovo, Russia

✉ zhmaylo@compmechlab.com

ABSTRACT
A theoretical study on the structural strength of an endoprosthesis stem made from meta-biomaterial is presented. We considered six types of metamaterials based on a biocompatible titanium alloy comprised by unit cells of lattice and surface structures. The standard for testing femoral components of endoprostheses was used to develop virtual test benches for simulation of the loading process, followed by stress–strain analysis of meta-biomaterial implants. Our general findings confirm the load-bearing capacity of the structures, additionally pointing to potential issues that may arise if the manufacturing technology of metamaterial endoprostheses is insufficiently rigorous.

KEYWORDS
meta-biomaterial • lattice structures • surface structures • hip joint • endoprosthesis • finite element analysis • strength

Introduction

Metamaterials are understood as artificial macroscale structures composed from periodically repeated highly porous structural elements of the smallest size (micro-, meso-, nano-scale). The term 'metamaterials' reflects the fact that the complex internal structure of such materials at the mesoscale induces peculiar physical and mechanical properties at the macroscale, not observed in natural materials and alloys obtained by conventional methods or in other synthetic substances. A new approach, drawing on the physical principles and computational models to engineer materials with unique properties and advanced functionality, has become known as rational design (RD) [1]. The RD approach was first adopted to design the mechanical [2], electromagnetic [3], acoustic [4] and poroelastic [5] properties for modern functional metamaterials in various engineering fields other than biological and clinical medicine.

Specifically, meta-biomaterials [6] have gained attention in regenerative medicine as potential candidates for various medical and clinical applications, including tissue and organ repair. Key applications of meta-biomaterials in tissue engineering are engineering of three-dimensional structures, such as scaffolds, serving as temporary structural support for tissue regeneration, or such as implants and endoprostheses, which are artificial substitutes for individual organs or their parts, installed permanently in the

human body. Meta-biomaterials can be designed to mimic the biomechanical properties of natural tissues. For example, they may exhibit certain elastic stiffness properties, making them better suited to the mechanical requirements for repaired tissues and organs.

Importantly, the understanding of meta-biomaterials within the context of tissue engineering is rather more elaborate than the model of highly porous materials with complex internal structure, made from biocompatible metal or plastic. Meta-biomaterials are assumed to differ significantly from the vast majority of other metamaterials known today in that they are intended for simultaneously providing physical properties of dissimilar nature [6]. In this sense, meta-biomaterials can be regarded as multiphysical metamaterials in contrast to classical metamaterials designed to provide one type of physical properties, such as mechanical, acoustic or optical metamaterials. A crucial range of properties of a different physical nature are biophysical and biomechanical characteristics of living tissues (in particular, bone) that must be reproduced by meta-biomaterials. In addition to purely mechanical properties (elasticity, strength, stiffness), these include mass transport properties and topological characteristics necessary for functional and reparative regeneration of bone tissue [7]. Thus, a high level of porosity and an extensive network of pore channels in bone scaffolds and implants made from meta-biomaterials are the primary mechanobiological factors [8] deciding the efficiency of regenerative processes in the volume of artificial substitutes for human skeletal elements [9,10].

Endoprostheses with a developed porous surface based on biocompatible alloys are widely used in regenerative medicine to repair large bone defects of the human musculoskeletal system. Extensive bone defects resulting from injury, tumor or other pathological conditions require implants that can not only provide mechanical support but also promote restoration of the bone structure by stimulating osteogenesis (growth of new bone tissue), ensuring osseointegration (ingrowth of bone tissue into the pore space of the implant) and vascularization (growth of vessels in the defect site to improve blood supply) [11,12]. However, only the surface layer of limited thickness typically has a porous structure in most standard endoprostheses. Therefore, it is of utmost importance to carry out research into meta-biomaterials to develop new types of endoprostheses with through-porosity for major joints. Meta-biomaterials can help answer these biomedical challenges, thanks to their multiphysical nature.

Another critical problem occurring during deployment of all-metal endoprostheses and the patient's daily activities is the so-called stress shielding effect [13]. Due to high stiffness of the femoral stem in the hip endoprosthesis prepared by the standard procedure from a titanium alloy, stress redistribution occurs within the bone–implant system, since most of the load is taken by the metal structure. This results in a decreased stress level in the cortical bone tissue forming the medullary canal, where the bone is adjacent to the endoprosthesis. According to Wolff's law [14] and the main hypotheses of modern mechanobiology [15], this in turn leads to activation of specific bone cells (osteoclasts) responsible for the destruction of bone tissue, due to reduced stresses in the bone volume in the contact region between the bone and the endoprosthesis. Consequently, the processes of bone resorption are accelerated, becoming more prevalent than the processes of new bone tissue growth. Thus, the density and associated

strength characteristics of bone tissue decrease, leading over time to micro-destruction of bone at the interface with metal, weakening the fixation of the stem in the medullary canal, ultimately resulting in loosening or even complete dislocation.

Efforts to resolve this issue are underway in orthopedics, with alternative approaches adopting softer biocompatible polymers instead of metals [16]. Successful attempts to mitigate the stress-shielding effect include endoprosthesis components made of polyetheretherketone reinforced by carbon fibers (PEEK/CF) [17,18]. However, such approaches typically do not incorporate porous structures based on polymer materials due to a significant decrease in the strength of the implant, especially for highly loaded skeletal sites [19]. Therefore, another promising scenario explored in this study, reducing the integral stiffness of the structure while preserving the necessary strength, consists of using porous metamaterials based on biocompatible alloys with highly tunable effective elastic and strength properties [20,21].

The fundamental dependence of macroscopic properties of metamaterials on the microscale topology has sparked intense research into the characteristics of the internal structure determined by the geometry of the repeated unit cell [22,23]. The first types of meta-biomaterials, that is, metamaterials intended for tissue engineering, were designed based on unit cells that are strut microstructures, ranging from simple cube-like shapes to complex assemblies composed of multiple struts [24]. Unit cells of such beam-like metamaterials mimic the crystal lattices of metals, repeating their spatial symmetry groups [25]. Experimental clinical studies have confirmed that optimized lattice implants can be used in surgical procedures to partially replace the tubular bone with sufficiently long scaffolds [26]0. The proposed technique for developing a special type of metamaterial is based on a unit cell containing a pore of variable elliptical shape and orientation. The technique proved successful for the case of a hip endoprosthesis stem, reducing the weight of the structure by 9–11%, depending on the type of implant, while preserving structural strength [27]. Treatment of bone defects using open-pore scaffolds based on beam elements with strut diameters ranging from 200 to 500 µm is discussed in [28], detailing the structural optimization of a titanium scaffold to match its elastic properties to cortical bone tissue. The paper investigates the mechanical behavior of the constructed models of metamaterials, establishing the dependence of the elastic modulus on the characteristics of beam-type structures.

Metamaterials based on smooth surfaces in 3D space appeared later than structures based on beam elements. They offer an advantage over lattice-type metamaterials in specific applications necessitating a highly developed internal structure formed by a flow-through system of interconnected pore channels with curvature smoothing. A prominent class is metamaterials based on triply periodic minimal surfaces (TPMS) [29]0. TPMS are a family of periodically repeated implicit surfaces with zero mean curvature, i.e., local minimization of the surface area for a three-dimensional domain with a predefined interface. A metamaterial based on triply periodic minimal surfaces consists of infinite non-intersecting shells of a given thickness, repeating in the directions of three coordinate axes with a fixed or varying period. The internal surfaces of TPMS metamaterials have large specific area, making them good candidates for chemical microreactors, membrane devices, fuel elements, energy absorbers (for kinetic, thermal, acoustic wave energy, microwave electromagnetic waves) [29].

Much research is carried out into the biomedical applications of this family of metamaterials as bone scaffolds or implants. The reason for the attention that this topic has received is that effective osseointegration requires for artificial bone substitutes to have an extensive system of open-type pore channels for migration and transformation of active cells into bone matter, simultaneously providing sufficient strength to ensure the functionality of organs, especially the human musculoskeletal system. Metamaterials of this type offer potential advantages over the beam type due to larger area of internal surfaces, whose curvature is close to the curvature of trabecular bone tissue with its extensive system of pore channels. It was recently found that the surface curvature strongly affects tissue regeneration [30], and since the mean surface curvature of the trabecular bone is close to zero, meta-biomaterials based on TPMS should provide more efficient regeneration of biological tissue in the void space of the scaffold [31].

Even though additive technologies are becoming increasingly popular for manufacturing customized implants and endoprostheses, including those with an arbitrary porous [32] or periodic lattice structure [33–35], theoretical predictions of strength are still scarce, generally limited to studies of failure at the mesoscale level of the metamaterial unit cell [36] or using averaged models. A separate challenge is the construction of full-scale high-fidelity finite element models for endoprostheses made from meta-biomaterials and ab initio calculations of the stress–strain state of the endoprostheses, as these models must avoid simplifications and homogenization of elastoplastic properties [37].

Few papers are available for relatively small-sized lattice models of implants [26]0, [27,28] and endoprostheses [38,39], aimed at direct finite element analysis (FEA) of the stress distribution. Moreover, there are virtually no computational studies on the strength predictions for endoprostheses made of complex structural meta-biomaterials (in particular, surface-type) providing raw data without resorting to averaging procedures. The likely reason for this is that direct FEA simulation of the periodic internal spatial structure of lattice and, especially, surface metamaterials is very complex. On the other hand, it is crucial to obtain predictions of strength and fatigue resistance, as endoprostheses of major joints must be able to withstand substantial force during many loading cycles during the patient's normal motor activity after surgery.

This study is focused on designing the femoral stem for a human hip endoprosthesis made from a meta-biomaterial with through-porosity and a complex internal structure, which is one of the practical applications of metamaterials in tissue engineering. We characterized three configurations of meta-biomaterial based on lattice structures and three configurations based on triply periodic minimal surfaces. The main objective of the study is the theoretical evaluation of strength in an endoprosthesis stem, following the standard test procedure for biomedical products based on continuum mechanics.

Materials and Methods

Types of metamaterials

Meta-biomaterials based on Ti_6Al_4V titanium alloy were selected to develop models of candidate structures for the femoral component (stem) of hip endoprosthesis. This alloy is widely used in surgical procedures to replace bone structures with artificial

components due to its high strength properties, chemical stability and biocompatibility. This material can be used to manufacture components with thin elements and complex geometries and is also well-suited for products with requirements for minimal weight.

Three types of rod cells and three types of TPMS-based cells were taken as unit cells composing the metamaterials, while their geometry was tailored so that the bulk porosity and the content of the base material were the same for all types of cells. The overall dimensions of the cells were 3.7 × 3.7 × 3.7 mm^3, the porosity was 70 %, and the content of the base material 30 %.

Lattice metamaterials are represented in this study by the following structures: cubic with supports, diamond, double pyramid. Surface metamaterials were developed based on the following TPMS: Gyroid, Fischer–Koch, Schwarz D (Fig. 1). A detailed description of the procedure for constructing the unit cells of beam and surface-based metamaterials is provided in our previous studies [20,21].
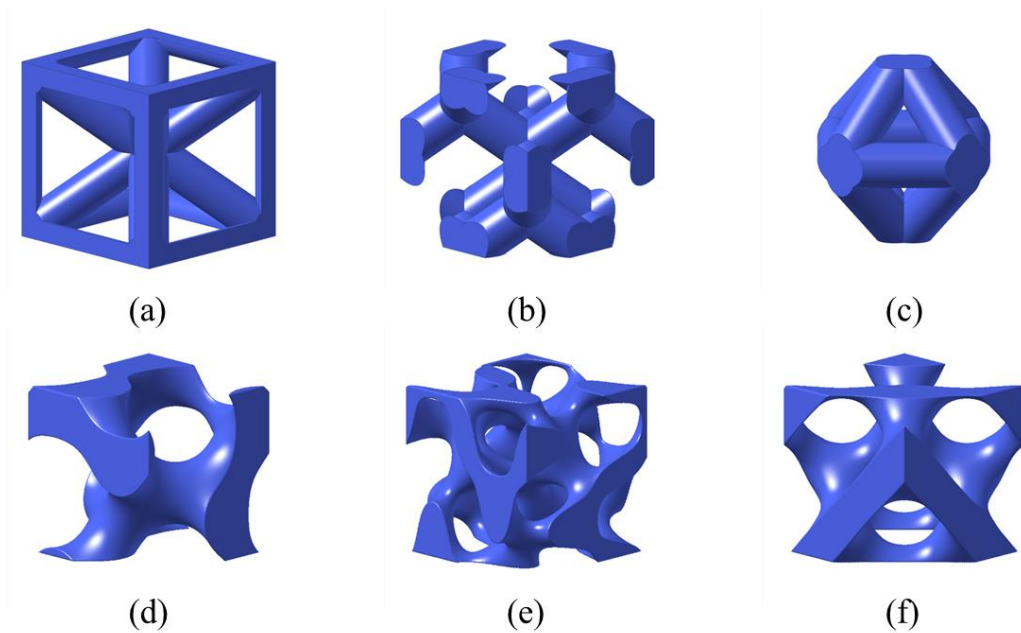
Fig. 1. Unit cells of six types of metamaterials: (a) Cubic with supports; (b) Diamond; (c) Double pyramid; (d) Gyroid; (e) Fischer–Koch; (f) Schwarz D

Model of endoprosthesis stem made from metamaterial

The external shape of the developed structure has a standard topology repeating the curvature of the proximal femur along the force lines, as described in an earlier study [40]. The overall dimensions of the stem were 176 × 66 × 15 mm^3. Figure 2 illustrates the construction of the three-dimensional model for the femoral component of the hip endoprosthesis made from meta-biomaterial. Three-dimensional geometric models of the stem based on lattice metamaterials were built in the ANSYS SpaceClaim module, and the models of the stem based on surface elements were built in the Altair Inspire software. The endoprosthesis stem based on the unit cells considered was developed in the following stages:

1. Construction of a parallelepiped or other shape closer to the target shape, circumscribed around the implant (Fig. 2(a)). This region is filled with metamaterial composed of 3.7 × 3.7 × 3.7 mm³ cells with a porosity of 70 %.

2. Export of the initial solid implant model from the STEP file format representing geometric data into the STL file format with a triangular surface mesh size of 0.2 mm (Fig. 2(b)).

3. Boolean intersection of the metamaterial preform with the target geometry of the solid implant in mesh format. The resulting implant is made from solid metamaterial without additional elements necessary for the femoral component of the hip endoprosthesis (Fig. 2(c)).

4. Completion of the stem model by replacing a part of the metamaterial in the proximal region of the implant with solid material for attaching the endoprosthesis head (Fig. 2(d)).
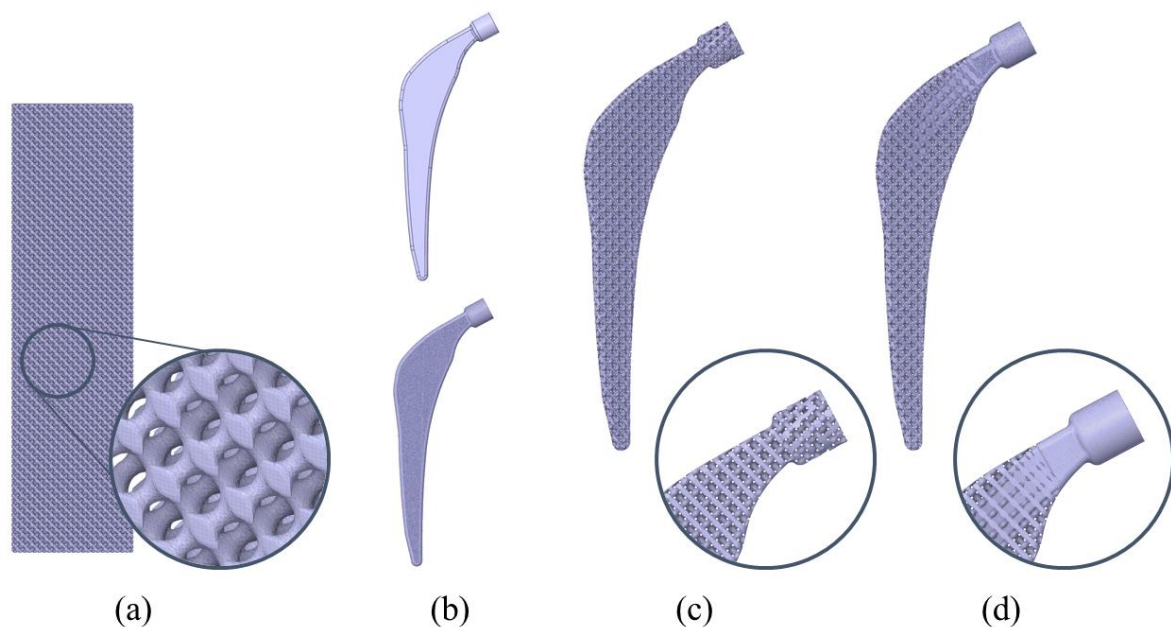
Fig. 2. Construction of model for femoral component of hip endoprosthesis manufactured from typical metamaterial: (a) metamaterial preform; (b) target geometry of stem in STEP and STL formats; (c) intermediate model of stem made entirely from metamaterial; (d) final model of femoral component made from metamaterial with solid head

A three-dimensional model of the structure built was saved in STL format and then exported to the Altair SimLab system for automatic construction of a three-dimensional mesh of tetrahedral finite elements. Because the surface of the implant composed of metamaterial cells has a very complex shape, the finite element mesh contains a large number of thin or self-intersecting elements along the outer edge. These low-quality elements need to be further modified to reliably obtain the stress fields in the structure. Small elements that do not meet the criteria for mesh quality are automatically detected in the Altair SimLab system, and subsequently corrected or deleted. The finite element model adjusted by this technique is again converted to neutral format of STL surface

mesh for subsequent steps. Figure 3 shows three-dimensional geometric models of the endoprosthesis stem made from all six types of metamaterials.

(a)   (b)   (c)

(d)   (e)   (f)
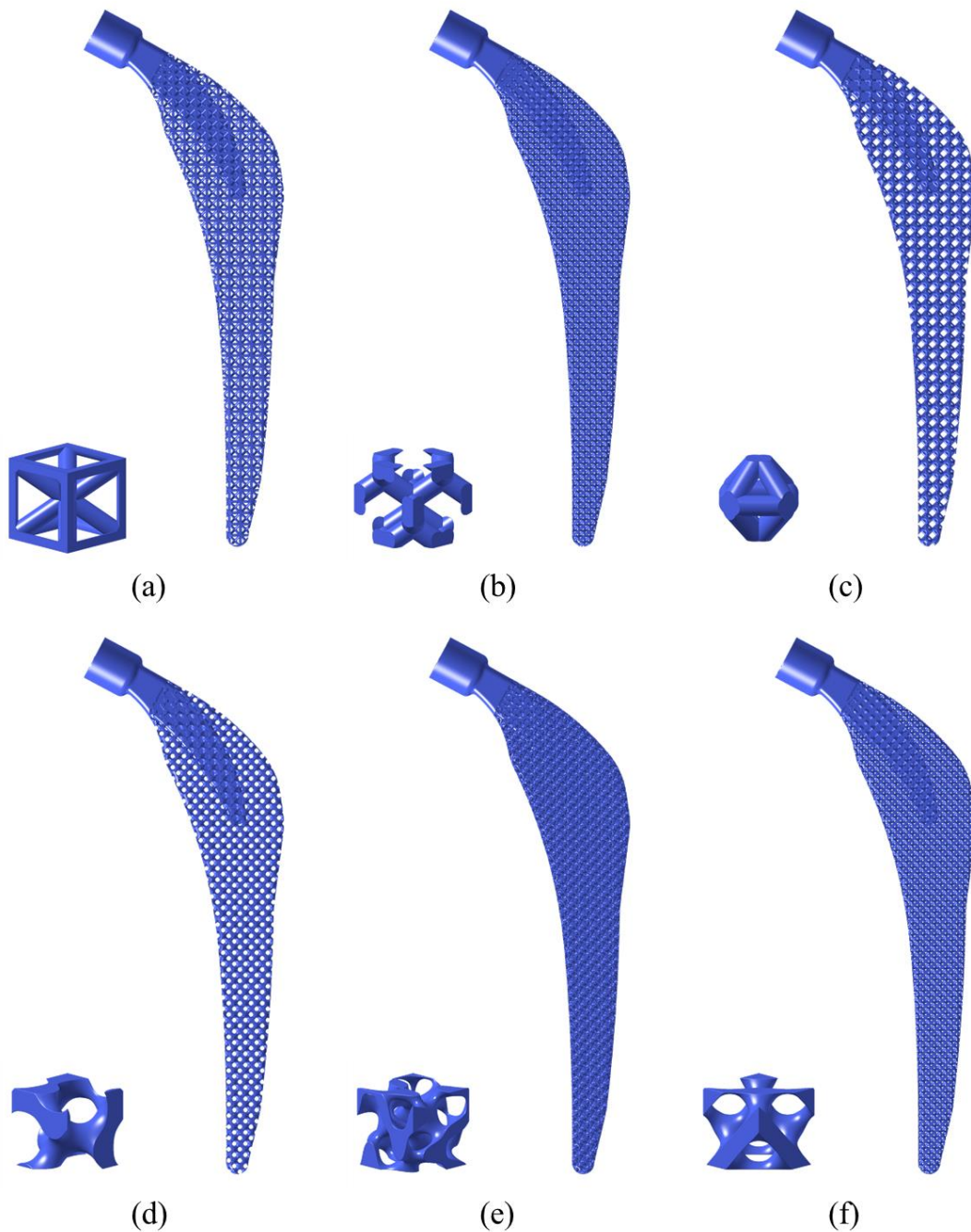
Fig. 3. 3D geometric models of endoprosthesis stem made of metamaterials based on following structures: (a) cubic with supports; (b) diamond; (c) double pyramid; (d) gyroid; (e) Fischer–Koch; (f) Schwarz D

Geometric model of test bench for endoprosthesis stem

A digital model of the virtual test bench intended for strength analysis of the femoral component of the hip endoprosthesis made from the selected metamaterials was developed following the procedure described in the GOST R ISO 7206-4-2012 standard

"Implants for surgery – Partial and total hip joint prostheses – Determination of endurance properties and performance of stemmed femoral components". This standard is aimed at strength predictions (including fatigue resistance under cyclic loads) of stemmed femoral components in total hip arthroplasty (THA), also used separately for partial hip prosthetics. The GOST standard is identical to the international standard ISO 7206-4:2010 "Implants for surgery — Partial and total hip joint prostheses — Part 4: Determination of endurance properties and performance of stemmed femoral components" [41]. According to the standard, the lower part of the test specimen is embedded into a solid medium; the head of the specimen is subjected to cyclic loading to produce axial compression, bending in two planes and torsion until failure occurs or the prescribed number of cycles are achieved.

Figure 4 shows the configuration of the medium-sized hip endoprosthesis stem (120–250 mm from the center of the femoral head to the most distal point of the stem) based on the GOST R ISO 7206-4-2012 standard. The implant is located in a cylindrical cup filled with solidifying bone cement at angles $\alpha = 10°$, $\beta = 9°$, determining the inclination of the stem axis in the frontal and sagittal planes. The height of the cup was not normalized; it was set to 120 mm in the digital model so as to preserve the key distance $D = 80$ mm from the center of the head to the level of stem fixation. The diameter of the cup was chosen equal to 60 mm to minimize the influence of rigid fixation of the cylinder surface formed.
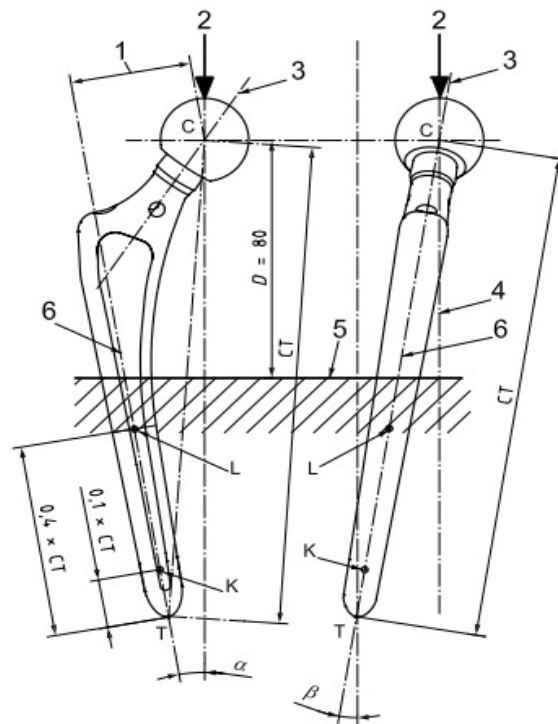
Fig. 4. Configuration of symmetrical endoprosthesis stems with CT distance of more than 120 mm, but less than or equal to 250 mm (based on GOST R ISO 7206-4-2012 (ISO 7206-4:2010)): arm *1* of head; load application point *2*; stem axis *3*; loading axis *4*; cement level *5*; stem axis KL *6*; T is the most distal point of the stem; C is the center of the head; D is the embedding level; K, L are points at certain distance from point T defining stem axis; α is the angle on the frontal plane CKL between loading axis *4* and stem axis *6*; β is the angle on sagittal plane perpendicular to CKL between loading axis *4* and stem axis *6*

The developed models of the metamaterial stem were combined in the Altair SimLab system with the constructed three-dimensional model of the cylinder made of bone cement using standard Boolean operations. The head of the femoral component was then added to the model as a truncated sphere.

This comprises a set of geometric models characterizing the biomechanical system, including the stem of the femoral component made from six types of metamaterials. A typical 3D numerical model of the implant–cement system is shown in Fig. 5.
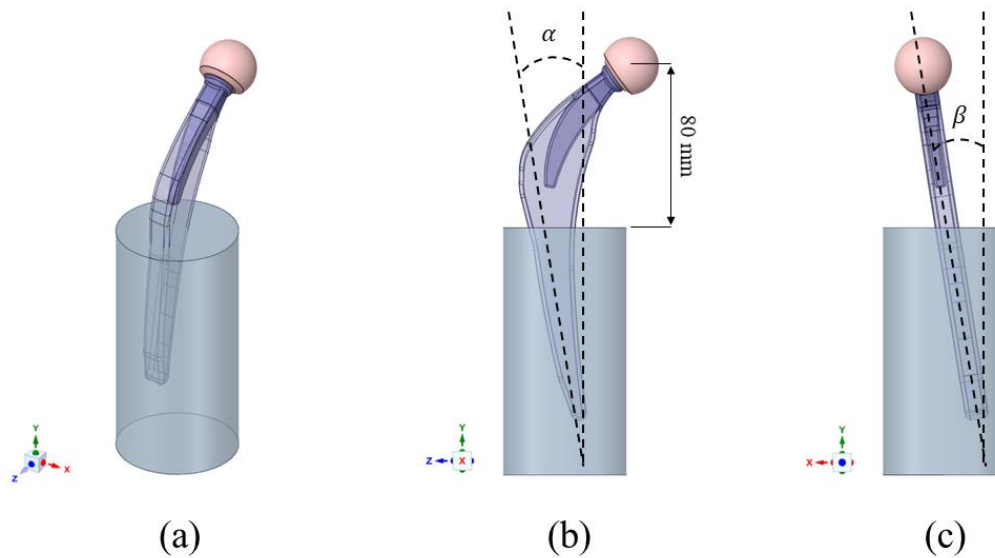
Fig. 5. Three-dimensional geometric model of implant–cement biomechanical system based on GOST R ISO 7206-4-2012 (ISO 7206-4:2010): (a) isometric view; (b) frontal view; (c) sagittal view

Finite element formulation for the problem on digital testing of the endoprosthesis stem

Three-dimensional geometric models of the virtual test bench (Fig. 5) were used to construct spatial finite element meshes with the tools of the Altair SimLab system. The developed numerical models are composed of tetrahedral finite elements with first-order displacement interpolation. The characteristic length of finite elements in the constructed mesh amounted to 0.2 mm for the stem, and to 1 mm for the ceramic head of the femoral component and the bone cement cylinder.

Finite element meshes characterizing the individual components of the system are constructed to have common nodes on adjacent surfaces of the components, with the exception of the interface between the implant and the ceramic head. The stem is rigidly fixed in bone cement in this approach, assuming no-slip, which is appropriate for both the given experimental setup following the standard guidelines and the developed porous structure of the metamaterial stem. From a computational standpoint, it is unnecessary to specify the contact interaction at the interfaces in this formulation (with the exception of the interface between the implant and the ceramic head, where the contact interaction is introduced into the model), yielding a faster and more stable solution.

The three-dimensional problem of elasticity theory describing the problem posed in the study is solved by the classical displacement-based finite element method using

the variational principle of minimum potential energy or generalization of the weighted residual method to three-dimensional problems [42].

The model (Fig. 5) is saved in INP format and exported to the Abaqus FEA suite to complete the finite element model and perform calculations of the stress-strain state for the fixed femoral component of the hip endoprosthesis as a system of solid deformable bodies. The formulation of the elasticity problem imposes the elastic properties of the materials used to manufacture the elements of the biomechanical system considered, the kinematic constraints and the acting forces.

According to the GOST R ISO 7206-4-2012 standard, a vertical load that is a total force of 2300 N is applied to the head of the femoral component (Fig. 4). Such a load is simulated in the finite element model by a concentrated force applied at a separate point (called Reference Point), mathematically connected to all nodes of the finite element mesh of the femoral head, ensuring a more uniform load distribution over the surface of the head (Fig. 6).

The kinematic constraints imposed assume that the outer surface of the cylinder is rigidly fixed, that is, all displacement components in the nodes of the finite element mesh on the outer surface are equal to zero (Fig. 6).
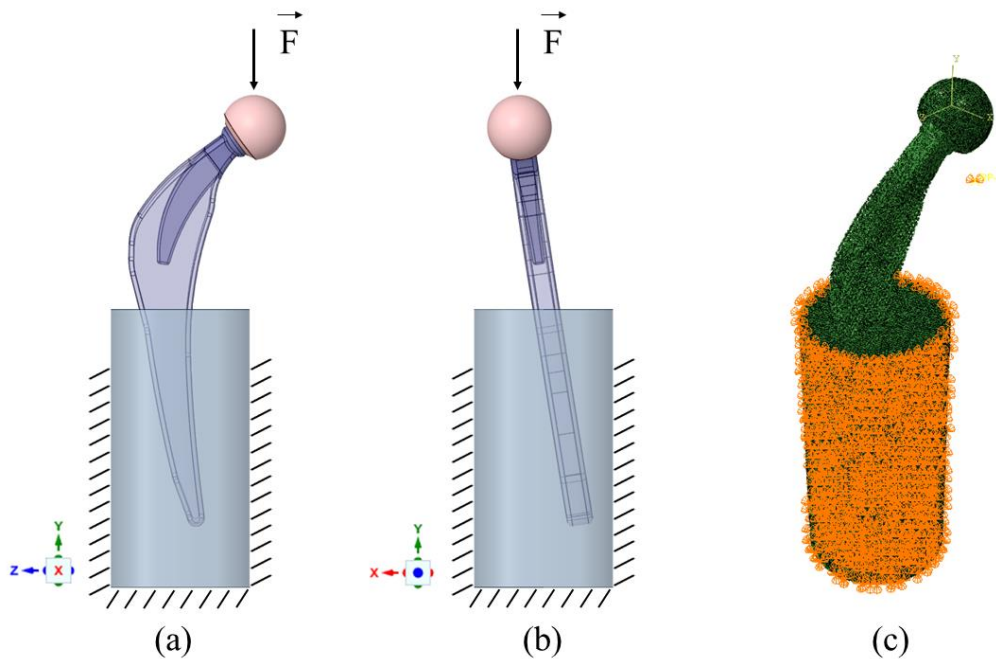
Fig. 6. Loading conditions for femoral component: (a) frontal view; (b)sagittal view; (c) isometric view of finite element model in Abaqus system

Setting the physical and mechanical properties of materials correctly is an extremely important factor for construction of high-fidelity digital models of virtual test environments. As mentioned above, the metamaterials in this paper are to be additively manufactured from the Ti_6Al_4V titanium alloy. The following parameter values were adopted for the mechanical properties of additive Ti_6Al_4V: density of 4.43 kg/m^3, Young's modulus of 113.8 GPa, Poisson's ratio of 0.342, yield strength of 950 MPa [43]. The fatigue properties of materials vary in a much wider range if different additive technologies and

subsequent surface treatments are introduced [44]. Analyzing the literature, we adopted a representative value of the fatigue limit equal to 350 MPa for the calculations with a symmetric loading cycle and a frequency of 10 Hz for Ti_6Al_4V titanium alloy obtained by the selective laser melting (SLM) technology [45,46].

The following mechanical characteristics were taken for the remaining components of the model: acrylic bone cement had a Young's modulus of 3.5 GPa, a Poisson's ratio of 0.3; the ceramic material of the femoral head had a Young's modulus of 0.43 GPa, a Poisson's ratio of 0.3 [47].

According to the GOST R ISO 7206-4-2012 standard, physical tests are aimed at evaluating the fatigue resistance of the endoprosthesis stem at a number of loading cycles set equal to $5 \cdot 10^6$. The system for inducing a quasi-static force to act on the head of the femoral component described in the standard functions with a pulsating loading cycle with a maximum force of 2300 N.

We determined the elastic displacements of the endoprosthesis stem, induced by the action of an applied force, and the integral stiffness of the structure with respect to the vertical displacements. Evaluating stiffness as a function of vertical displacements is of foremost interest, as it can provide deeper insights into the biomechanical behavior of the endoprosthesis The stiffness is calculated as follows: $k = \frac{F}{|U_2^{max}|}$, where is the k is the calculated stiffness of the endoprosthesis stem along the vertical direction; F is the magnitude of the vertical load; U_2^{max} is the maximum absolute value of the vertical component of the elastic displacement vector in the endoprosthesis stem.

Such a process was organized as follows for mathematical modeling of high-cycle fatigue strength using numerical analysis software:
1. Static elastic calculations of the stress–strain state of the biomechanical system under applied load (a force of 2300 N in our case) are carried out in Abaqus FEA software.
2. Computational results of the stress–strain state analysis, that is, the nodal values of displacements and components of the stress tensor, are exported to the Altair HyperLife system. Evaluation of the number of load cycles that the structure can withstand is then carried out based on the Wöhler curve set for the material used (in this case, Ti_6Al_4V titanium alloy) and the stresses in Gaussian nodes of finite elements.

The technique used in this study for evaluation of fatigue strength is incorporated in the Altair HyperLife software, using a well-known model for fatigue behavior of a material in the elastic range with a large number of symmetric loading cycles N_f, set by an exponential law within the range $N_1 < N_f < N_0$:

$$\sigma_a = S_f \left(N_f\right)^b, \tag{1}$$

where σ_a is the stress amplitude in a symmetric cycle , which the material can withstand at a given number of loading cycles N_f, S_f is the fatigue limit; b is the fatigue exponent calculated from the slope of the curve defined by Eq. (1) in logarithmic coordinates.

The parameters in Eq. (1) lie in the following ranges for common structural materials: $N_1 = 10^3 - 10^4$, $N_0 = 10^6 - 10^7$. It is assumed that the reference $S-N$ curve for the fatigue limit of the material at point N_0, described by Eq. (1), has an inflection, after which the failure process either slows down or stops. In the latter case, the curve is

believed to extend to a horizontal section with a characteristic ordinate taken as the fatigue limit of the material under symmetric cyclic loading.

This model follows from the formulation of the problem on evaluating the fatigue limit of the endoprosthesis stem under a significant number of loading cycles beyond the inflection point on the $S-N$ curve. Evaluating the fatigue parameters of the Ti$_6$Al$_4$V titanium alloy by Eq. (1) with the fatigue limit of 350 MPa at $N_0 = 1 \cdot 10^6$ and the ultimate tensile strength of 1230 MPa, conditionally corresponding to $N_1 = 10^3$, we obtain the values of the fatigue limit equal to $S_f = 4323$ MPa and the exponent equal to $b = -0.182$. Evaluating the fatigue parameters of the Ti$_6$Al$_4$V titanium alloy by Eq. (1) with the fatigue limit of 350 MPa at $N_0 = 1 \cdot 10^6$ and the ultimate tensile strength of 1233 MPa, conditionally corresponding to $N_1 = 1$, we obtain the values of the fatigue limit equal to $S_f = 1233$ MPa and the exponent equal to $b = -0.092$.

The influence of the constant component of the cyclic load in an asymmetric loading cycle is determined by the ratio between the mean value and the amplitude of the stress cycle that the material can withstand at a given number of loading cycles [48]:

$$\frac{\sigma_a}{\sigma_{-1}} + \frac{\sigma_m}{\sigma_\text{B}} = 1, \tag{2}$$

where σ_a and σ_m are the amplitude and mean stress in an asymmetric loading cycle that the material can withstand at a given number of loading cycles N_f; σ_{-1} is the fatigue limit of the material during a symmetric loading cycle; σ_B is the ultimate tensile strength of the material.

It follows from Eq. (2) that a linear decrease in the amplitude of the sustained stress cycle is observed with an increase in the constant component in the case of asymmetric loading:

$$\sigma_a = \sigma_{-1} - \varphi_\sigma \sigma_m, \text{ where } \varphi_\sigma = \frac{\sigma_{-1}}{\sigma_\text{B}} \tag{3}$$

Since the Wöhler curve is generally determined experimentally by uniaxial tensile testing, the stress tensor in the case of multiaxial yet in-phase loading is reduced to an equivalent nominal voltage at each point of the given structure and is used as the calculated parameter in Eq. (1). The maximum principal stress is taken as such nominal stress for brittle materials, and the von Mises equivalent stress with the sign corresponding to the sign of the maximum principal stress is taken for viscous materials.

The criterion for the critical state adopted in the fatigue calculations was the fatigue life, that is, the number of sustained cycles compared to the target value, selected as $5 \cdot 10^6$ cycles following the problem statement formulated in accordance with GOST R ISO 7206-4-2012. The Palmgren–Miner rule for damage accumulation was used for this purpose in the general case of a set of load scenarios, where failure occurs if the following inequality is satisfied:

$$\sum D_i = \sum \frac{n_i}{N_{if}} \geq 1.0 , \tag{4}$$

where D_i is the damage during n_i cycles with load i; n_i is the number of stress cycles under load i ; N_{if} is the number of cycles to failure, taken from the $S-N$ curve for the combination of stress amplitude and mean stress level i.

Therefore, the stress values calculated in the finite elements at a given static load simulating a pulsating loading cycle can be used to evaluate the number of cycles that the structure can withstand at the selected points of the material from Eqs. (1) and (3), and determine the degree of damage to the structure from Eq. (4).

Results and Discussion

Effective properties of metamaterials

The effective elastic moduli of the metamaterials are necessary for comparing their integral characteristics, even though the moduli are not directly related to the structures made from these materials. In addition, their analysis is valuable from a biomechanical standpoint, since the stiffness of the endoprosthesis stem directly affects the processes of bone resorption in the contact area with metal. Importantly, regeneration of tissue also occurs in the pore space of the metamaterial, which is necessary for reliable cementless fixation of the femoral component in the medullary canal of long tubular bones of the human skeleton.

A detailed description of the homogenization procedures applied to these types of metamaterials is presented in our earlier studies [20,21]. The effective elastic moduli found for the metamaterials based on the titanium alloy are given in Table 1.

Table 1. Effective elastic moduli for six types of metamaterials (MPa)

Elastic constants	Cubic w. supports	Diamond	Double pyramid	Gyroid	Fischer–Koch	Schwarz D
E_1, MPa	8850.8	6251.3	10237.0	8423.0	10997.7	8795.7
E_2, MPa	8850.7	6251.2	10237.0	8402.3	11002.4	8795.7
E_3, MPa	8850.6	6251.0	10237.0	8413.1	10996.2	8797.2
G_{12}, MPa	4557.9	5234.6	4632.6	5036.9	5107.8	6325.5
G_{23}, MPa	4557.9	5234.6	4632.6	5035.9	5107.6	6327.2
G_{31}, MPa	4557.9	5234.6	4632.6	5037.5	5107.3	6326.5
ν_{12}	0.301	0.364	0.275	0.338	0.321	0.343
ν_{13}	0.301	0.364	0.275	0.337	0.321	0.343
ν_{23}	0.301	0.364	0.275	0.337	0.321	0.343

As seen from Table 1, the metamaterials are symmetric with respect to 90-degree rotation around any axis of the Cartesian coordinate system coinciding with the principal axes of geometric symmetry. However, despite the same values of effective elastic constants along the principal axes and in the principal planes, the homogenized models of these metamaterials as continuous media are not isotropic. This is easily verified by calculating Poisson's ratio using the well-known formula for isotropic continuum: $\nu = \frac{E}{2G} - 1$. The values obtained by this formula, -0.03; -0.4; 0.1; -0.16; 0.076; -0.3, differ significantly from those in Table 1, which confirms the anisotropic nature of the governing equations of metamaterials, despite apparent full symmetry.

Notably, high porosity leads to a significant decrease in stiffness along the principal axes of material symmetry compared to a solid material. For example, Young's modulus of the lattice structures lies in the range of 6.25–10.2 GPa, while that of the surface structures lies in the range of 8.4–11.0 GPa. The shear modulus of lattice metamaterials

lies in the range of 4.56–5.23 GPa, and that of surface metamaterials lies in the range of 5.04–6.33 GPa. Double pyramid and Fischer–Koch cells exhibit the highest Young's moduli with moderate shear moduli.

According to experimental studies of the proximal femur [49], Young's moduli of compact tissue lie in the range of 7500–17500 MPa in the longitudinal direction and 4000–7000 MPa in the transversal direction, depending on the density of the tissue. Thus, the values obtained for Young's moduli of the meta-biomaterials at a porosity of 70 % are closer to the lower bound for elastic moduli in compact tissue in the longitudinal direction, but slightly higher than their values in the transversal direction. From a biomechanical standpoint, such a range of elastic properties of meta-biomaterials can allow the compact femoral tissue to accommodate the load sufficiently so that bone resorption does not occur due to reduced stress level near the metal implant.

On the other hand, from a mechanobiological standpoint, the through-porosity of the metamaterial implant ensures penetration of biological fluid and bone matter in both radial and axial direction of the medullary canal, which is impossible in an endoprosthesis made of solid material. The high through-porosity of the metamaterial used to manufacture the endoprosthesis allows filling the internal volume of the metamaterial with a large amount of bioactive substance with mesenchymal stem cells and growth factors at the stage of surgery, with subsequent free penetration of active progenitor cells into the implant. This can improve reparative regeneration in the volume of meta-biomaterial, ultimately ensuring reliable osseointegration of the implant [9,50].

Analysis of elastic displacements and stiffness

Elastic displacements induced by the applied load integrally characterize the stiffness of the structure, which is an important factor in the stability of the endoprosthesis in the medullary canal during operation. According to the GOST R ISO 7206-4-2012 standard, physical tests are carried out in such a way that the permissible deviation of the test specimen from the vertical axis does not exceed 0.2 mm. Thus, we analyzed both vertical displacements characterizing the bending and stiffness of the stem, and horizontal displacements characterizing the deviation of the stem from the vertical position, which is a requirement of the GOST standard.

Figure 7 shows the fields of components and magnitude for the vector of elastic displacements, induced by the applied vertical force of 2300 N, for the considered types of meta-biomaterials.

As evident from the displacement fields in Fig. 7, the picture of the displacement distribution is similar for different types of metamaterial, regardless of the topology class (lattice or surface). The upper point of the endoprosthesis stem, located on the cylindrical structural element of the stem, securing the head of the femoral component, exhibits the largest displacements. We can evaluate the integral stiffness of the structure by analyzing the maximum displacements of the endoprosthesis head under the action of the applied load. All components and the magnitude of the displacement vector of the upper point, as well as the stiffness of the endoprosthesis stem, are given in Table 2.
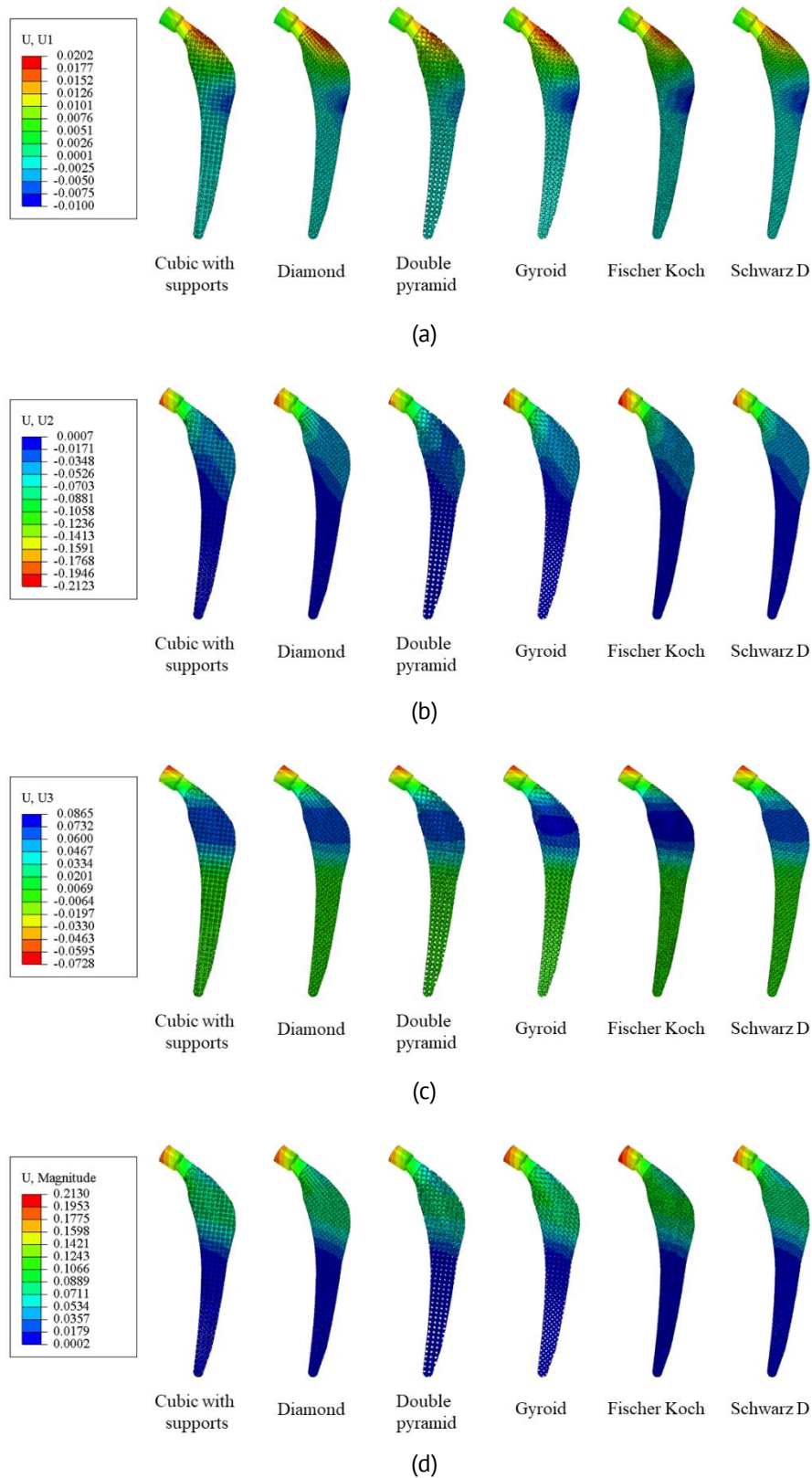
Fig. 7. Elastic displacement fields (in mm) in implant stem prepared from considered types of meta-biomaterial in the global coordinate system: (a) component along the X axis, in the median-sagittal plane; (b) component along the Y axis, in the vertical direction; (c) component along the Z axis, in the frontal plane; (d) displacement vector magnitude

Table 2. Displacements and stiffnesses for each type of implant stem

	Type of metamaterial cell					
	Cubic w. supports	Diamond	Double pyramid	Gyroid	Fischer–Koch	Schwarz D
U_1^{min}, mm	-0.008	-0.010	-0.006	-0.009	-0.010	-0.009
U_1^{max}, mm	0.019	0.020	0.017	0.020	0.018	0.018
U_2^{min}, mm	-0.0002	0.0003	-0.0003	-0.0003	0.0007	-0.0002
U_2^{max}, mm	-0.195	-0.198	-0.185	-0.203	-0.212	-0.195
U_3^{min}, mm	-0.071	-0.070	-0.069	-0.071	-0.073	-0.071
U_3^{max}, mm	0.074	0.073	0.069	0.080	0.087	0.072
U^{max}, mm	0.196	0.199	0.186	0.203	0.213	0.196
Stiffness, N/mm	11795	11616	12432	11330	10849	11795

The greatest contribution to the total displacement vector is expected to be made by the vertical component characterizing the elastic bending of the stem as a cantilever beam, fixed in the lower part and subjected to a bending moment at the end. The total displacements of the endoprosthesis head repeat the vertical displacements of the head with an accuracy to three significant digits. The maximum vertical displacement does not exceed 0.2 mm for such implants as Cubic w. supports, Diamond, Double pyramid and Schwarz D. The values of vertical displacements for the remaining implants, i.e., Gyroid and Fischer–Koch, are slightly higher than for the other implants, but by no more than 6 %.

Interestingly, small displacements are observed in the (XZ) plane of the middle part of the stem in the contact area between metal and bone cement. However, we believe that these displacements characterize the stiffness of the bone cement rather than the actual structure of the endoprosthesis stem and therefore are not of particular interest for this study. Nevertheless, it can be concluded that the endoprosthesis stem deviates from the vertical by less than 0.1 mm for all types of metamaterials, which is significantly less than the requirements in the GOST standard.

Multi-lattice structures designed to alleviate stress shielding were discussed in [51], with the weight of the implant reduced to 25 %. The elastic moduli of the lattice material cells varied in the range from 20 to 63 GPa with a porosity of 26–58%. The displacements of the model with the lattice structure exceed the displacements of the solid implant (4.04 and 3.81 mm, respectively), which is significantly higher than the displacements obtained in our study. Note that the model in [51] consisted of a femur with an implanted stem, and the load corresponded to a person with the weight of 700 N, walking at a normal speed, which could be the reason for the discrepancies with the results in our study.

An important mechanical factor affecting the biophysical processes in osteosynthesis with porous implants is the stiffness of the structure, which in the case of metamaterials is directly related to the internal structure, that is, the type and porosity of the unit cell. It was established in previous studies that the stiffness of the scaffold significantly affects the efficiency of the regeneration process in the pore space of the implant [9,15]. In particular, mathematical modeling of tissue regeneration in the scaffold volume with the porosity of 50 and 90 % [10,50] confirmed extensive osseointegration at lower amplitudes of the harmonic load in the case of greater porosity, which may be due a more pronounced effect of the mechanical stimulus deeper into the implant.

The stiffness of the metamaterial stem with a porosity of 70 %, calculated from vertical displacements, lies in the range of 11616–12432 N/mm for lattice structures and 10849–11795 N/mm for surface structures. Thus, lattice implants turn out to be stiffer than surface implants, which is extremely important from a mechanobiological standpoint. The stiffest metamaterial is the lattice type based on Double pyramid cell, and the least stiff is the surface type based on Fischer Koch cell, with the difference in stiffness amounting to almost 15 %, which is significant from a biomechanical standpoint.

A comparative analysis of experimental and computational data obtained in tests of the femoral component stem of the hip endoprosthesis following the ISO 7206-4:2010 requirements is presented in [32]. The bending stiffness was calculated for solid titanium and for a material with a random distribution of pore channels and an integral porosity of 33%, exhibiting a decrease by 47 % compared with the solid material in experimental measurements. The results were in good agreement with the full-scale test and the computational experiment for the solid implant and large discrepancies for the porous stem. However, despite the lower porosity, the stiffness of the porous endoprosthesis in [32] was only 1500 N/mm, which is significantly less than the stiffnesses obtained in our study. While there are some differences in the design of the stem at the macroscale, the main contribution to these discrepancies is probably made by the structure of the metamaterial compared to random porosity.

Stress and fatigue analysis

Analysis of the distribution of von Mises equivalent stresses indicates that the overall load on the implant is low (Fig. 8).
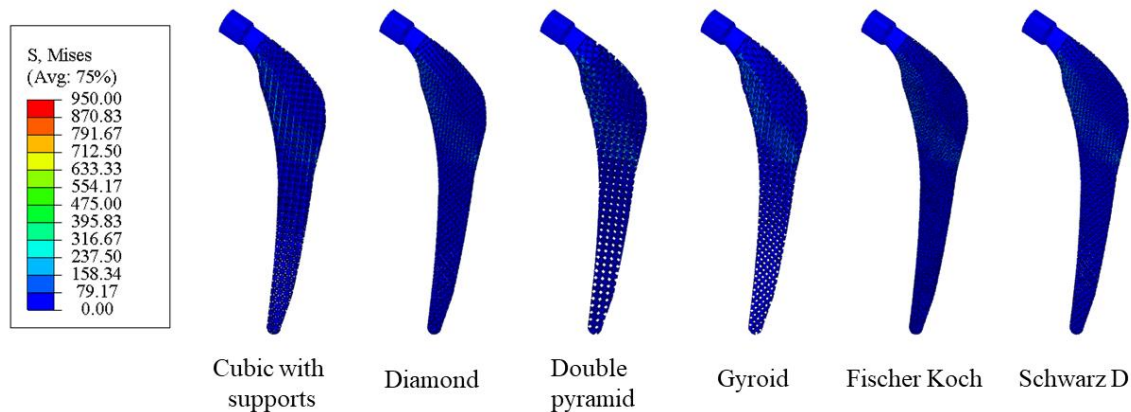
Fig. 8. Von Mises stress intensity (in MPa) in implant stems for each type of metamaterial

However, certain types of implants contain elements whose stress exceeds the yield strength of Ti_6Al_4V at 950 MPa. The maximum stresses are reached by thin elements appearing in the implant geometry due to its complex shape. As the unit cell does not fully fit into the endoprosthesis stem at its edge, there are regions where the strut comprising the metamaterial cell becomes geometrically thin and consequently capable of withstanding substantially lower loads. In view of this, the peak stress values are not a reliable indicator for assessing the applicability of the metamaterial in problems of this kind.

The stress distribution in the Diamond-type implant (Fig. 9) shows the most loaded zones, located along the lower (inner) edge of the stem and concentrated near the horizontal surface of bone cement.
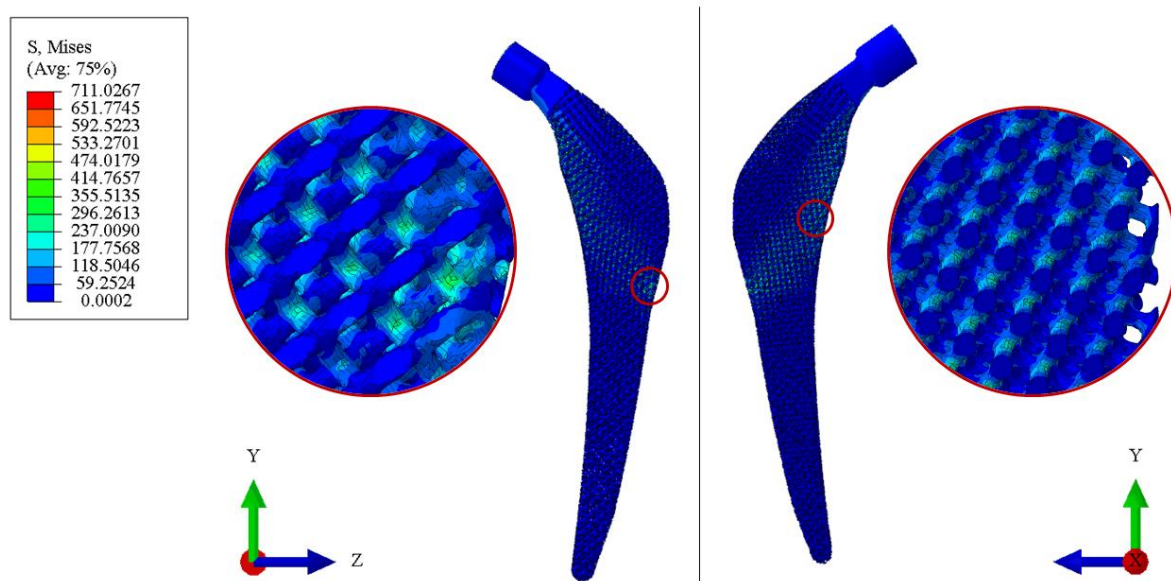
Fig. 9. Von Mises stress intensity (in MPa) in implant stem made of Diamond-type metamaterial

More detailed analysis of the stress state of the implant in each case can be carried out based on the histograms for the lattice (Fig. 10) and surface (Fig. 11) type metamaterials. The vertical axis characterizes the percentage of the implant volume located in the stress range plotted along the horizontal axis. More than 80 % of the implant volume for each type of metamaterial is in the stress range from 0 to 50, which does not exceed 5.3 % of the yield strength. More than 99 % of the volume does not exceed the fatigue limit of titanium alloy equal to 350 MPa. On average, implants made of lattice-type metamaterials have fewer stress concentrators, while Diamond and Double pyramid types do not exhibit regions where the yield strength of the titanium alloy is exceeded.

A small percentage of the implant volume is in the stress range exceeding the fatigue limit of 350 MPa. The number of elements reaching elevated stress values can be significantly reduced by refining the finite element model. Thin elements extending to the edge of the endoprosthesis stem often become stress concentrators and can be removed because they have no load-bearing capacity.

The distribution of stresses in the stem at the macroscale corresponds to both qualitative analytical predictions of the model describing bending in a cantilever beam subjected to a concentrated moment at the end, and studies by other authors evaluating the strength of hip endoprosthesis stems made of novel materials [18,39] The highest stresses occur on the inner surface of the leg in the bending region, reaching about 450 MPa in the case of the lattice gradient structure made from additive titanium alloy VT6 with a maximum vertical load of 2800 N described in [39]. Although the conditions of the numerical experiment and the porosity value of the considered metamaterials

differ, it can be argued that the stress values we calculated for this region (400–500 MPa) correspond to those presented in [39]. In general, the higher stress level in our case is due to the thinner beam or surface elements forming the metamaterial unit cells. Interestingly, a decrease in von Mises stresses was detected in [51] when part of the solid implant material was replaced with a multi-lattice structure.
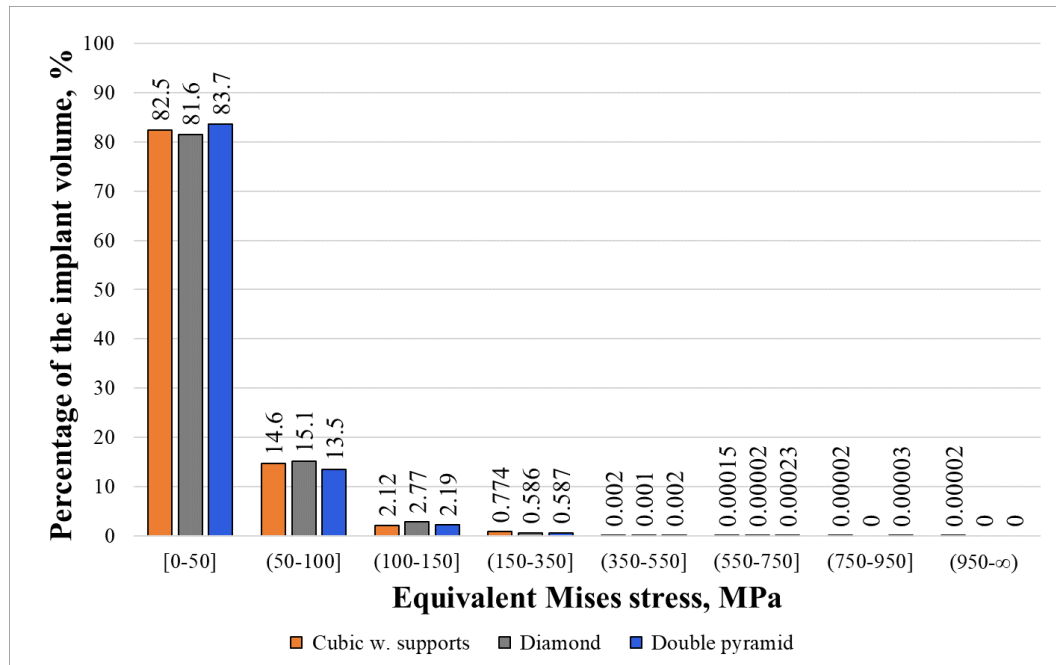
Fig. 10. Volume percentage in different stress ranges for implants based on lattice-type metamaterial
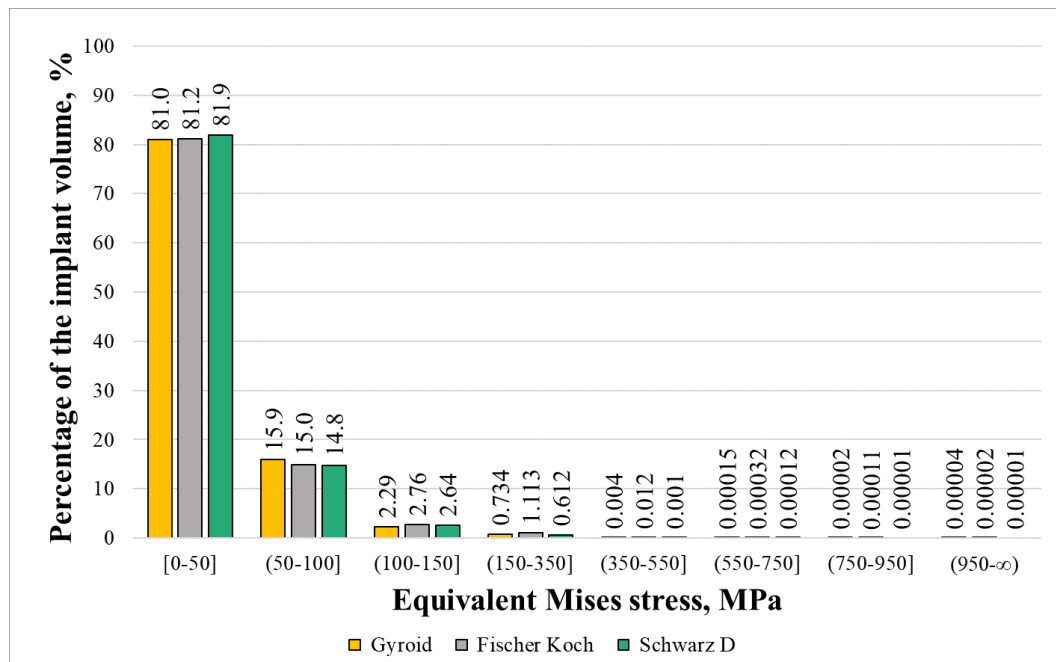
Fig. 11. Volume percentage in different stress ranges for implants based on surface-type metamaterial

Analysis of cyclic fatigue showed a general positive trend under high-cycle loading applied vertically to the surface of the implant head. The exception was a very insignificant fraction of the implant volume that could not withstand the number of cycles required by GOST (Table 3).

Table 3. Quantitative characteristics of fatigue in endoprosthesis stem

	Type of metamaterial cell					
	Cubic w. supports	**Diamond**	**Double pyramid**	**Gyroid**	**Fischer– Koch**	**Schwarz D**
Number of elements unable to withstand required number of cycles	27	1	32	39	40	32
Implant volume unable to withstand required number of cycles, %	$9.53 \cdot 10^{-5}$	$4.88 \cdot 10^{-6}$	$1.93 \cdot 10^{-4}$	$1.03 \cdot 10^{-4}$	$2.02 \cdot 10^{-4}$	$3.59 \cdot 10^{-5}$

Conclusion

Scaffolds and endoprostheses, that is, implants in a broad sense, manufactured from metamaterials are becoming increasingly widespread in tissue engineering and regenerative medicine, so it is of interest to determine the strength characteristics of such biomedical products. With this background in mind, we carried out a FEA-based theoretical study on the strength of a hip endoprosthesis stem manufactured entirely from highly porous meta-biomaterial, following the GOST R ISO 7206-4-2012 standard "Implants for surgery – Partial and total hip joint prostheses – Determination of endurance properties and performance of stemmed femoral components".

To design the endoprosthesis stem, we considered six configurations for the internal porous structure of the metamaterial based on biocompatible titanium alloy comprised by beam-type and TPMS unit cells. Digital 3D models of the hip endoprosthesis stem were constructed from elementary structural units. Evidently, the effective elastic moduli of the metamaterials lie in the range of physiological values of the cortical tissue in the femoral diaphysis, and the elastic moduli tensor has the property of material symmetry with respect to 90-degree rotation.

The standard procedure for testing the femoral components of endoprostheses was used to develop digital stands for simulating the loading process and calculate the stress–strain state of meta-biomaterial implants. The results obtained by finite element analysis of the structure prepared from various types of metamaterials generally confirm the load-bearing capacity of the given structures for the number of loading cycles set out by the standard.

We found potential issues that may arise if insufficient attention is paid to the complex shape of metamaterial implants and their additive manufacturing technology. In particular, replicating the smooth shape of the stem made of solid material with a lattice or surface meta-biomaterial can produce small regions of extremely low thickness, which

in turn leads to computational problems. Therefore, a direction we propose for future studies consists of developing new types of endoprostheses from meta-biomaterials, focusing closely on preserving the structure of the metamaterial near smooth surfaces with variable curvature.

We believe that digital tests can be used as a primary substitute for field experiments in developing new types of endoprostheses from meta-biomaterials.

References

1. Overvelde JT, Weaver JC, Hoberman C, Bertoldi K. Rational design of reconfigurable prismatic architected materials. *Nature.* 2017; 541: 347–352.

2. Bertoldi K, Vitelli V, Christensen J, van Hecke M. Flexible mechanical metamaterials. *Nature Reviews Materials.* 2017;2: 17066.

3. Watts CM, Liu X, Padilla WJ. Metamaterial electromagnetic wave absorbers. *Advanced Materials*. 2012;24: OP98–OP120.

4. Mei J, Ma G, Yang M, Yang Z, Wen W, Sheng P. Dark acoustic metamaterials as super absorbers for low-frequency sound. *Nature Communications.* 2012;3: 756.

5. Maslov LB. Study of vibrational characteristics of poroelastic mechanical systems. *Mechanics of Solids.* 2012;47(2): 221–233.

6. Zadpoor AA. Meta-biomaterials. *Biomaterials Science.* 2019;8(1): 18–38.

7. Cowin SC. (ed.) *Bone Mechanics Handbook*. 2nd ed. CRC Press; 2001.

8. van der Meulen MCH, Huiskes R. Why mechanobiology? A survey article. *Journal of Biomechanics.* 2002;35(4): 401–414.

9. Zadpoor AA. Bone tissue regeneration: the role of scaffold geometry. *Biomaterials Science*. 2015;3(2): 231–245.

10. Maslov LB. Biomechanical model and numerical analysis of tissue regeneration within a porous scaffold. *Mechanics of Solids.* 2020;55(7): 1115–1134.

11. Tonndorf R, Aibibu D, Cherif C. Isotropic and anisotropic scaffolds for tissue engineering: collagen, conventional, and textile fabrication technologies and properties. *Int. J. Mol. Sci.* 2021;22: 9561.

12. Hutmacher DW, Schantz J, Lam CX, Tan KC, Lim TC. State of the art and future directions of scaffold-based bone engineering from a biomaterials perspective. *J. Tissue Eng. Regen. Med.* 2007;1: 245–260.

13. Sumner DR, Turner TM, Igloria R, Urban RM, Galante JO. Functional adaptation and ingrowth of bone vary as a function of hip implant stiffness. *Journal of Biomechanics.* 1998;31; 909–917.

14. Wolff J. *Das Gesetz der Transformation der Knochen*. Berlin: A. Hirchwild; 1892.

15. Isaksson H. Recent advances in mechanobiological modeling of bone regeneration. *Mechanics Research Communications.* 2012;42: 22–31.

16. Ramakrishna S, Mayer J, Wintermantel E, Leong KW. Biomedical applications of polymer-composite materials: a review. *Composites Science and Technology*. 2001;61: 1189–1224.

17. Li CS, Vannabouathong C, Sprague S, Bhandari M. The use of carbon-fiber-reinforced (CFR) PEEK material in orthopedic implants: a systematic review. *Clin. Med. Insights Arthritis Musculoskelet. Disord.* 2015;8: 33–45.

18. Boudeau N, Liksonov D, Barriere T, Maslov L, Gelin JC. Composite based on polyetheretherketone reinforced with carbon fibres, an alternative to conventional materials for femoral implant: Manufacturing process and resulting structural behavior. *Materials & Design.* 2012;40(9): 148–156.

19. Maslov LB, Zhmaylo MA, Dmitryuk AYu, Kovalenko AN Study of the strength of a hip endoprosthesis made of polymeric material. *Russian Journal of Biomechanics.* 2022;4: 19-33.

20. Borovkov AI, Maslov LB, Zhmaylo MA, Tarasenko FD, Nezhinskaya LS. Elastic properties of additively produced metamaterials based on lattice structures. *Materials Physics and Mechanics.* 2023;51(7): 42-62.

21. Borovkov AI, Maslov LB, Zhmaylo MA, Tarasenko FD, Nezhinskaya LS. Finite element analysis of elastic properties of metamaterials based on triply periodic minimal surfaces. *Materials Physics and Mechanics.* 2024;52(2): 11–29.

22. Hanks B, Berthel J, Frecker M, Simpson TW. Mechanical properties of additively manufactured metal lattice structures: data review and design interface. *Addit. Manuf.* 2020;35: 101301.

23. Jia Z, Liu F, Jiang X, Wang L. Engineering lattice metamaterials for extreme property, programmability, and multifunctionality. *J. Appl. Phys.* 2020;127: 150901.

24. Feng J, Fu J, Lin Z, Shang C, Li B. A review of the design methods of complex topology structures for 3D printing. *Visual Computing for Industry, Biomedicine and Art.* 2018;1(1): 5.

25. Dong G, Tang Y, Zhao YF. A 149 line homogenization code for three-dimensional cellular materials written in MATLAB. *Journal of Engineering Materials and Technology.* 2019;141: 011005.

26. Bolshakov P, Raginov I, Egorov V, Kashapova R, Kashapov R, Baltina T, Sachenkov O. Design and optimization lattice endoprosthesis for long bones: Manufacturing and clinical experiment. *Materials.* 2020;13: 1185.

27. Bolshakov P, Kuchumov AG, Kharin N, Akifyev K, Statsenko E, Silberschmidt V. Method of computational design for additive manufacturing of hip endoprosthesis based on basic-cell concept. *Int. J. Numer. Meth. Biomed. Engng.* 2024;40(3): 3802.

28. Wieding J, Wolf A, Bader R. Numerical optimization of open-porous bone scaffold structures to match the elastic properties of human cortical bone. *J Mech Behav Biomed Mater.* 2014;37(9): 56-68.

29. Feng JW, Fu JZ, Yao XH, He Y. Triply periodic minimal surface (TPMS) porous structures: from multi-scale design, precise additive manufacturing to multidisciplinary applications. *Int. J. Extrem. Manuf.* 2022;4: 022001.

30. Gouveia RM, Koudouna E, Jester J, Figueiredo F, Connon CJ. Template curvature influences cell alignment to create improved human corneal tissue equivalents. *Adv. Biosyst.* 2017;1(12): 1700135.

31. Bobbert F, Zadpoor A. Effects of bone substitute architecture and surface properties on cell response, angiogenesis, and structure of new bone. *J. Mater. Chem. B.* 2017;5(31): 6175–6192.

32. Simoneau C, Terriault P, Jetté B, Dumas M, Brailovski V. Development of a porous metallic femoral stem: Design, manufacturing, simulation and mechanical testing. *Materials & Design.* 2017;114: 546–556.

33. Heinl P, Müller L, Körner C, Singer RF, Müller FA. Cellular Ti-6Al-4V structures with interconnected macro porosity for bone implants fabricated by selective electron beam melting. *Acta Biomater.* 2008;4: 1536–1544.

34. Parthasarathy J, Starly B, Raman S, Christensen A. Mechanical evaluation of porous titanium (Ti6Al4V) structures with electron beam melting (EBM). *J. Mech. Behav. Biomed. Mater.* 2010;3: 249–259.

35. Izri Z, Bijanzad A, Torabnia S, Lazoglu I. In silico evaluation of lattice designs for additively manufactured total hip implants. *Comput. Biol. Med.* 2022;144: 105353.

36. Shalimov AS, Tashkinov MA. Modeling of deformation and fracture of porous heterogeneous media taking into account their morphological composition. *PNRPU Mechanics Bulletin.* 2020;4: 175–187.

37. Zadpoor AA. Mechanical performance of additively manufactured meta-biomaterials. *Acta Biomater.* 2019;85: 41–59.

38. Tilton M, Lewis GS, Hast MW, Fox E, Manogharan G. Additively manufactured patient-specific prosthesis for tumor reconstruction: Design, process, and properties. *PLoS ONE.* 2021;16(7): e0253786.

39. Sufiiarov VSh, Orlov AV, Popovich AA, Chukovenkova MO, Soklakov AV, Mikhaluk DS. Numerical analysis of strength for an endoprosthesis made of a material with graded lattice structures. *Rus. J. Biomech.* 2021;25(1): 55–66.

40. Borovkov AI, Maslov LB, Zhmailo MA, Tarasenko FD, Nezhinskaya LS. Development of a gradient structure of the femoral component of a hip joint endoprosthesis based on a lattice-type metamaterial. In: *Collection of annotations of the 51st school-conference "Current problems of mechanics" in memory of D.A. Indianseva. Veliky Novgorod, June 19-21, 2024.* 2024. p.175–176. (In Russian)

41. International Standard. *ISO 7206-4:2010. Implants for surgery − Partial and total hip joint prostheses − Part 4: Determination of endurance properties and performance of stemmed femoral components (IDT).* OSO; 2010.

42. Maslov LB. *Finite element poroelastic models in biomechanics.* 2nd ed. St. Petersburg: Lan'; 2023. (In Russian)

43. Boyer R, Welsch G, Collings EW. *Materials properties handbook: titanium alloys.* ASM International; 1994.

44. Lewandowski JJ, Seifi M. Metal Additive Manufacturing: A Review of Mechanical Properties. *Annual Review of Materials Research.* 2016;46(1): 151–186.

45. Benedetti M, Cazzolli M, Fontanari V, Leoni M. Fatigue limit of Ti6Al4V alloy produced by Selective Laser Sintering. *Procedia Structural Integrity.* 2016;2: 3158–3167.

46. Günther J, Krewerth D, Lippmann T, Leuders S, Tröster T, Weidner A, Biermann H, Niendorf T. Fatigue life of additively manufactured Ti−6Al−4V in the very high cycle fatigue regime. *International Journal of Fatigue.* 2017;94: 236–245.

47. Kulmetyeva VB, Porozova SE. *Ceramic materials: production, properties, application.* Perm: Perm State Technical University Publishing House; 2009. (In Russian)

48. Birger IA, Mavlyutov RR. *Strength of materials.* Moscow: Nauka, 1986. (In Russian)

49. Wirtz DC, Schiffers N, Pandorf T, Radermacher K, Weichert D, Forst R. Critical evaluation of known bone material properties to realize anisotropic FE-simulation of the proximal femur. *J. Biomech.* 2000;33(10): 1325–1330.

50. Maslov LB. Mathematical model of bone regeneration in a porous implant. *Mechanics of Composite Materials.* 2017; 53(3): 399–414.

51. Gok MG. Creation and finite-element analysis of multi-lattice structure design in hip stem implant to reduce the stress-shielding effect. *Proceedings of the Institution of Mechanical Engineers, Part L: Journal of Materials: Design and Applications.* 2022;236(2): 429–439.

About Authors

Aleksey I. Borovkov ⓘ Sc

Candidate of Technical Sciences, Associate Professor
Vice-rector for digital transformation (Peter the Great St. Petersburg Polytechnic University, St. Petersburg, Russia)

Leonid B. Maslov ⓘ Sc

Doctor of Physical and Mathematical Sciences, Associate Professor
Lead Researcher (Peter the Great St. Petersburg Polytechnic University, St. Petersburg, Russia)
Lead Researcher (Ivanovo State Power Engineering University, Ivanovo, Russia)

Mikhail A. Zhmaylo ⓘ Sc

Master of Science
Lead Engineer (Peter the Great St. Petersburg Polytechnic University, St. Petersburg, Russia)

Fedor D. Tarasenko ⓘ Sc

Master of Science
Lead Engineer (Peter the Great St. Petersburg Polytechnic University, St. Petersburg, Russia)

Liliya S. Nezhinskaya ⓘ Sc

Bachelor of Science
Engineer (Peter the Great St. Petersburg Polytechnic University, St. Petersburg, Russia)

Heat exchanger and the influence of lattice structures on its strength

A.G. Pulin ✉ ⓘD, M.A. Laptev ⓘD, K.A. Alisov ⓘD, V.V. Barskov ⓘD, V.A. Rassokhin ⓘD,

B. Gong ⓘD, V.S. Kotov, G.A. Roshchenko ⓘD, A.M. Balakin ⓘD, M. Golubtsov ⓘD,

I.R. Nurkov ⓘD, M. Basati Panah ⓘD

Peter the Great St. Petersburg Polytechnic University, Saint-Petersburg, Russia

✉ pulin.anton.g@gmail.com

ABSTRACT
The heat exchanger is the main heat engineering equipment in various industries. The design of modern heat exchangers implies the presence of various turbulators. The purpose of turbulators is to increase the efficiency of heat exchange processes. Research of turbulators is limited to finding the optimal ratio between heat exchange parameters and hydraulic resistance of the system, without touching upon the issues of changing the strength characteristics of heat exchangers. Within the framework of this article, an analysis of a section of a tubular heat exchanger with a flow turbulator in the form of a lattice structure is carried out. Within the framework of this article, the method of comparative numerical modeling was chosen, consisting in the study of the stress-strain state and frequency response of the objects of study in the original and modernized formulations, under the action of thermal and gas-dynamic loads, modeled in heat-conjugate and mechanical analysis. The result of this study is the results of numerical modeling, reflecting the general change in the stress-strain state and frequency response of the heat exchanger. The analysis showed that the use of lattice structures reduces the average equivalent stresses in the heat exchanger by 10–20 % depending on the flow mode. In addition, frequency analysis showed a significant increase in the natural frequencies of the modified heat exchanger in the range from 86 % to 125 %. These results show that the use of flow turbulators allows increasing not only the efficiency of heat exchange processes, but also its strength.

KEYWORDS
mechanics • numerical investigation • structural analysis • modal analysis • physics of strength additive technologies • heat exchangers

Introduction

Given the importance of the energy industry in various spheres, its development is linked to the need to achieve high efficiency, cost-effectiveness, and environmental friendliness. Future energy plants should demonstrate higher efficiency than current technologies,

reduced fuel consumption, and minimal environmental impact. These requirements form the basis for shaping energy development strategies in different countries.

There are many ways to improve power plants, such as by optimizing elements and their parts, improving the efficiency of individual components of power plants, and using alternative working fluids. All approaches improve the characteristics of turbomachines to varying degrees but do not have a comprehensive approach, which has an impact on one of the parameters. A complex impact on all parameters of this concept can be provided by the use of high-efficiency heat exchangers. Thus, for example, the presence of a heat-exchange apparatus in the gas turbine unit (GTU) increases the efficiency of the power plant by reducing the amount of heat required for supplying to the thermodynamic cycle, increasing environmental friendliness owing to the effective utilization of thermal energy at the outlet from the turbine part of the GTU, and increasing efficiency by reducing the fuel consumption burned in the GTU.

A heat exchanger is auxiliary heat engineering equipment used to transfer heat energy from a heat carrier to a less heated body for the realization of various thermal processes. The heat transfer process occurs during the flow of these heat carriers through channels of various shapes. By analyzing the operating conditions of the heat exchangers, it can be established that they are significantly affected by these isolated flows. Thus, the heat exchanger apparatus is affected by:

1. Temperature loads. Temperature gradient: heat exchangers can be subjected to significant temperature variations that cause thermal expansion and contraction of the materials from which they are made. These variations can result in significant tensile/compression stresses and plastic deformations.

2. Aerodynamic impact. Pressure gradient: the heat exchanger must be able to withstand the operating pressure of the heat-transfer fluids, which can be significant depending on the intended use of the heat exchanger. Pressure effects led to the formation of various simple and combined bending stresses.

3. Mechanical loads. Vibrations: the presence of direct mechanical connections with other units of the power plant, as well as unbalanced aerodynamic flows, leads to the appearance of various vibrations in individual housing parts. The prolonged impact of vibrations on structures can lead to the formation of various fatigue cracks, which can lead to the violation of duct tightness and active mixing of coolants.

4. Chemical stress. Corrosion: interaction with aggressive chemicals can lead to the development of corrosion on the surface of heat exchangers, which can also lead to cracks and channel isolation failure. Deposition: Interaction with aggressive media leads to the deposition of various solid particles on the surface of the heat exchanger, the accumulation of which leads to the thickening and deterioration of the heat exchange efficiency.

Neglecting these loads can significantly affect the service life and reliability of heat exchangers. All of the above-mentioned influences must be considered in the design stage of heat exchangers. However, as diagnostics show, it is impossible to perform a comprehensive analysis of all loads because the heat exchange process is non-stationary and can change the magnitude of its impact on the design during its operation.

The durability of heat exchangers is one of the key factors that determine their longevity and performance. The strength depends on the material from which the heat

exchanger is constructed, as well as the operating conditions. The materials used to manufacture heat exchangers must be highly corrosion-resistant and resistant to high temperatures. The most common materials used are stainless steel, titanium, aluminum, and copper. Additionally, the strength of the heat exchanger depends on its design. For example, plate heat exchangers have a large surface area for heat exchange, which allows them to operate at high temperature and pressure. Certain elements of heat exchangers can act as stiffeners, increasing their strength. It is important to note that the strength of heat exchangers may decrease over time owing to exposure to aggressive media or mechanical damage. Therefore, regular inspection and maintenance of the heat exchangers should be performed to maintain their efficiency and safety.

By preventing possible defects in heat exchangers at the design stage, it is possible to increase their durability, which in turn will positively affect the efficiency and economy of the power plant itself. Thus, improving the efficiency and durability of heat exchangers will reduce the cost of energy production, which will ultimately reduce the price for consumers. Therefore, analyzing the defects of heat exchangers that occur during their operation and searching for methods to eliminate these defects (both at the design and operation stages) is an important direction of development in the energy industry.

For example, in [1], the process of describing the defects of heat exchangers, as well as the reasons that led to their formation, is shown. The authors conducted an all-sided analysis of the loads acting on the surface of the heat exchanger and found that the defect occurred as a result of thermal fatigue, caused by temperature fluctuations due to poor water circulation. Thermal stresses occurred which led to fatigue followed by water leakage.

According to the other authors, the defects on metal tube resulted from the high-temperature corrosion of the weld [2]. Scanning electron microscopy (SEM) analysis, metallographic, and electrochemical corrosion studies showed that the base metal has a higher corrosion potential than the weld under service conditions, which results in weld corrosion.

Other researchers have also performed diagnostics of heat exchangers, during which the development of corrosion on the surface of heat exchangers was observed [3]. The primary cause of corrosion development is the contact of the heat exchanger surface with a high-temperature chemically aggressive medium.

In [4], tube overheating and failure due to scale formation were studied. The failure samples in the field were obtained from the convection tube of the primary reforming. The object was a spiral ribbed tube. The tube exhibited a tear accompanied by bulging. The analysis performed using the finite element method in this study simulated real field conditions. It was found that prolonged overheating due to scaling both outside and inside the inner part of the tube prevents the smooth heat transfer process. Consequently, this leads to the deterioration of heat transfer and violates the original design concept. A metallurgical examination confirmed this conclusion. In addition, the finite element analysis confirmed this conclusion.

Summarizing, it can be seen that heat exchangers work in extremely aggressive environments, which negatively affects their strength and leads to destruction [5–7].

Preventing defects in heat exchangers is a critical aspect of their operation, because defects can lead to reduced efficiency, increased operating costs, and even accidents.

There are several methods for preventing defects in heat exchangers, which can be divided into several main categories:

1. Project measures. Optimal choice of materials: use of materials resistant to corrosion, erosion, and thermal deformation, such as stainless steel, nickel, or titanium-based alloys, especially in aggressive environments. Thermal expansion consideration: the heat exchanger is designed considering the thermal expansion of materials to avoid stresses and deformations that can lead to leakage or joint failure. Coatings and protective layers: application of protective coatings (e.g., anti-corrosion) on the internal surfaces of pipes and plates to prevent corrosion and reduce fouling. Design optimization: a proper fluid flow design to minimize stagnation zones and evenly distribute heat loads, thereby reducing the risks of localized overheating or corrosion.

2. Operational measures. Operating parameter monitoring: continuous monitoring of the temperature, pressure, flow rate, and other operating parameters to ensure that they are within the design values. Deviations can cause thermal shocks, erosion, or accelerated deposit formation. Filtration and cleaning: filters and separators are used to remove solids and contaminants from the media to reduce the risk of erosion and clogging of the heat exchanger pipes and ducts. Prevent thermal shocks: avoid sudden changes in temperature and pressure, which can cause thermal shocks and structural damage.

3. Preventive measures and maintenance.

In summary, it can be seen that the process of operation of heat exchangers produces the development of various types of defects, owing to the inability to take into account the various non-stationary processes occurring in heat exchangers, as well as technological inaccuracies. The level of impact from loads is a difficult task, and improvement of the technological process is a more affordable solution to extend the resources of heat exchangers. Based on this, the authors considered the option of improving the heat exchanger apparatus through design changes. It is worth noting that when designing heat exchangers, it is worth considering many factors besides durability: efficiency, material costs, production costs.

The most common method of manufacturing heat exchangers is the use of standard technological operations, such as casting, pressing, stamping, and rolling, as well as the active use of various types of welding to form channels through which the coolants move. However, additive technologies have been actively used for the manufacture of heat exchangers [8,9]. Additive technologies are the process of creating objects by applying a material layer-by-layer based on a three-dimensional model. Unlike traditional manufacturing methods, where materials are usually removed or specially deformed to create the shape of an object, in additive technologies, materials are added sequentially to create the final product. The principle of 3D metal printing has made it possible to create objects with highly complex geometries, with the possibility of integrating additional stiffeners (lattices) into the design, which will also absorb additional loads from the flow, thus reducing the overall stress concentration on the heat exchanger surface [10]. In addition to heat exchangers, additive technologies are also used in other energy machines. The technological process of additive manufacturing is also being actively studied [11]. Thus, the additive manufacturing process covers a wide variety of engineering industries. Technological features, designs and their mechanical properties

are being actively studied. Advances in additive manufacturing have led to the creation of three-dimensional periodic minimum surfaces (TPMS) for heat exchangers.

Another paper [12] reviewed different types of lattices, their properties and applications, where it was found that lattice infill has unique properties that often cannot be fully obtained using conventional fabrication methods. In addition, gratings effectively absorb energy and distribute stress evenly, and such structures are highly rigid, which will have a positive effect on vibration resistance. One of the most common types of such gratings is the gyroid, which is a triply periodic minimum surface (TPMS) that can be approximated by the following equation:

$$\sin x \cdot \cos y + \sin y \cdot \cos z + \sin z \cdot \cos z = 0. \tag{1}$$

The properties of these structures are actively studied by various authors. For example, in [13], a finite element analysis of the elastic properties of metamaterials based on three-fold periodic minimal surfaces was provided.

The use of lattice structures to improve the quality of heat and mass transfer processes is considered by the authors in another work [14]. There was a simulation of heat transfer with lattice structures. In this work, the effectiveness of their use has been proven. And the Nusselt number of a relatively smooth channel has increased from 2 to 5 times.

It is worth noting that, at present, the topic of increasing the strength of various objects through the introduction of lattice structures is very relevant, since this technology allows a significant increase in the strength properties of the object. Authors have conducted both numerical and experimental studies to investigate the strength properties of lattice structures.

In [15], compression and fall head tests of different types of lattices were performed. In this study, the optimal design was selected, which has a high pedigree, while being as durable as possible. In [16], the influence of the direction of the load on the compressive strength of additively manufactured three-period frames with a minimum surface was studied. Another article [17] examines the effect of porosity of various types of structures on strength properties. Based on [17], the Gyroid lattice type can be distinguished as one of the most durable types of gratings. In another study [18], the optimization of the TPMS structure for titanium dioxide composite ceramics was accelerated using finite element modeling (FEM) using a multi-purpose optimization algorithm. Quasi-static experiments and jackhammer experiments were conducted to study the mechanical response and deformation behavior of lattice structures in [19]. The global processes of structural deformation were recorded by a digital camera. In another article [20], the mechanical properties and energy absorption ability of printed TPMS samples with a gradient and a stepwise variable structure were studied. The difference between the homogeneous and stepped gyroid samples was negligible, and only one structural crack appeared during the compression test. Also, speaking about heat exchange properties, it is impossible not to consider the studies of heat transfer in these structures. The work [21] measured the heat transfer efficiency of a number of heat exchangers based on three times periodic minimum surfaces. The results showed that the TPMS sheet-gyroid design provides a high heat transfer rate and a moderate pressure drop. In [22], three new structures of mathematically controlled TPMS radiators were investigated using models based on computational fluid dynamics (CFD). The results showed that TPMS-based heat sinks

outperform conventional heat sinks by 48–61 % due to random flow disturbances and high packing density. This work demonstrates the potential of porous TPMS architectures as very promising heat sinks. Research has also been conducted on new methods to improve convective heat transfer based on precise control of the gyroid-type TPMS lattice structure in paperwork of other authors [23]. Some authors are already investigating real objects and conducting a comparative analysis of the influence of lattice structures on heat transfer. For example, in one of these works [24], a comparative analysis of the cooling system of the turbine blade with classical columns-intensifiers of heat exchange processes with a lattice structure was carried out. During this analysis, it was revealed that TPMS is a more effective intensifier than classical ones. The effectiveness of TPMS structures has also been proven in [25] on the design of a small-sized high-efficiency lattice heat exchanger. In recent years, various authors have analyzed new designs for heat exchangers manufactured using additive technologies [26,27]. In addition to studying the designs, technologies and mathematical modeling of such lattice structures, experimental studies are also being conducted that prove the high efficiency of these structures in heat exchangers [28,29].

Analyzing the above articles, it was found that a single assessment of heat exchange processes or strength characteristics of lattice structures is carried out. The main emphasis in heat exchangers is on the study of the optimal ratio of heat transfer parameters and hydraulic resistance coefficients, by varying the geometric parameters and types of lattice structures. The issues of changing the strength characteristics of heat exchangers during the integration of lattice structures remain unresolved, which does not allow for a full assessment of the acceptability of using lattice structures in heat exchangers to increase their efficiency and strength.

This paper is devoted to the study of the influence of lattice structures on the strength of heat exchangers manufactured using additive technologies. In this study, strength analysis of heat exchanger sections with and without a lattice structure was carried out for a wide range of Reynolds numbers. The aim of this work is to carry out a comparative analysis of the strength of a heat exchanger at different flow regimes realized in a heat exchanger using numerical simulation.

Thus, the research object of the study is a heat exchanger. The aim of the study is to conduct a comprehensive analysis of the influence of lattice structures on its operating parameters. The tasks of this study are geometric modeling, the results of gas dynamic, strength and vibration numerical studies, as well as comparison of results and impact assessment.

Methods

This study was conducted using computer-aided engineering software Ansys 19 R2. This calculation software has well proven the compliance of the output results for solving strength and dynamic gas computational problems, which is confirmed by validation studies. The temperature and pressure distribution data obtained as a result of gas dynamic numerical simulation in Ansys CFX were set as the acting load on the heat exchanger. The Steady State Thermal module was also used to account for heat transfer.

The strength calculation was performed in the Ansys Static Structural and Ansys Modal blocks.

The numerical study of the strength of the heat exchanger section described in this paper is based on the results of gas dynamic modeling obtained by the authors in the study [30]. This study investigated the efficiency enhancement of heat exchangers by introducing turbulent lattice structures fabricated using additive technologies into their design. The classical methodology for evaluating the efficiency of a lattice structure is used to evaluate the efficiency of the flow turbulators. However, this turbulizer is also a stiffener that can positively influence the strength characteristics of the structure, as verified in this study.

Because the present study is based on the results of previous gas-dynamic modeling, further analysis should include a comprehensive assessment of the effectiveness of the use of lattice structures, including both the impact on the intensification of heat transfer and the impact on the improvement of strength properties, which should be considered in continuity with each other. Figure 1 shows a combined flowchart of previous and current studies.
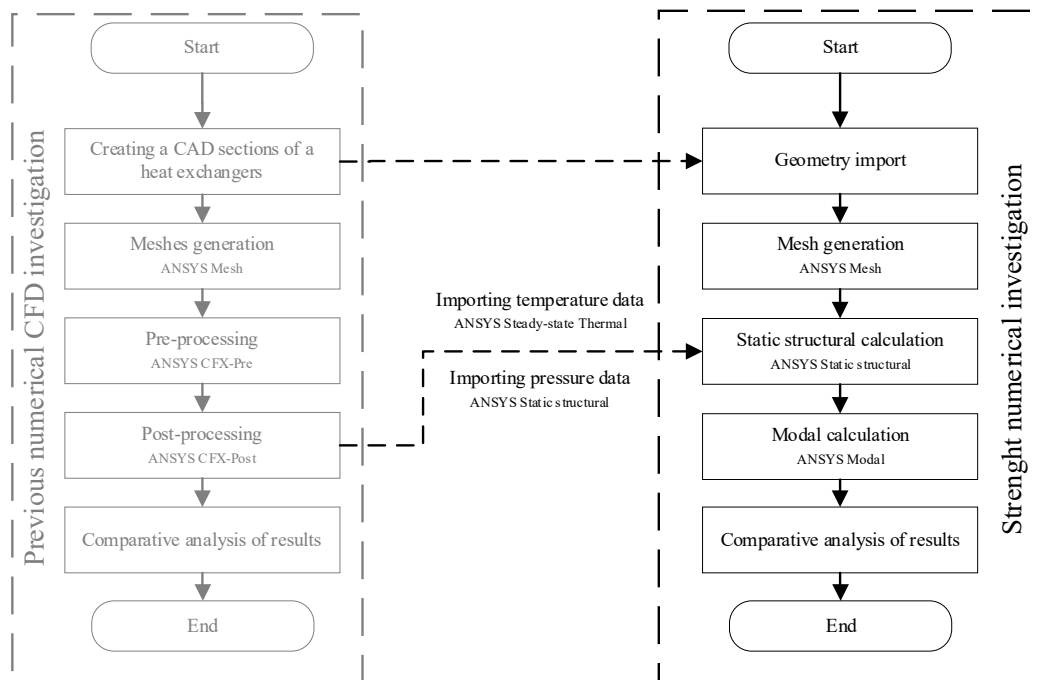
Fig. 1. Block diagram of studies

The previous study was performed by numerical modeling of the heat transfer process for two heat exchanger sections with and without the lattice structure inside. A small section of the tubular heat exchanger was selected as a reference. In this heat exchanger, one pipe of a smaller radius is located in a larger pipe. Hot liquid flows through the inner pipe, and cold liquid flows through the outer one. A section of a lattice gyroid structure was embedded in the center of one of the samples. The lattice structure was modeled using nTop software. Straight sections were specially modeled, since when setting boundary conditions, the flow parameters are averaged. At the entrance and exit

near the lattice structure, the results are greatly distorted, since the flow inside and near the lattice has a large spread of parameters, and averaging it, unreliable results are obtained.

Figure 2 shows the geometrical models of the heat exchanger sections, with and without a lattice structure. Table 1 lists the geometrical parameters of the investigated sections of the heat exchangers.
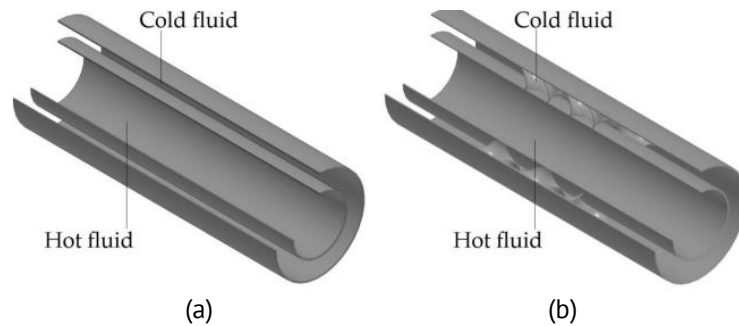
Fig. 2. Geometric models of the studied heat exchanger sections in cross-section:
(a) with and (b) without a lattice structure

Table 1. The geometric properties of the heat exchangers sections

Parameter	Unit	Value
Inner diameter of the pipe	mm	48
Outer diameter of the pipe	mm	80
Thickness of all walls	mm	1
Length of the heat exchangers sections	mm	240
Length of the lattice section	mm	80
Periodicity size of the gyroid lattice	mm	40

Using the results of the gas dynamic numerical study conducted earlier, static strength calculations and modal frequency analysis were also numerically performed in the present study. The calculation was also performed for the two heat exchanger sections presented earlier in a previous study under different flow regimes (Re=1000, Re=7500, Re=40000). Boundary conditions for CFD calculation are presented in Table 2.

Table 2. Boundary conditions

Parameter	Unit	Value	
		Cold fluid	Hot fluid
Inlet velocity	m/s	0.87 / 6.5 / 34.7	0.87 / 6.5 / 34.7
Inlet temperature	K	500	1000
Outlet static pressure	Pa	101325	101325

The strength calculation process involves several steps. First, previously created geometrical models of the heat exchanger sections were imported. Subsequently, the material (structural steel) is assigned. The source of the material properties of the heat exchanger is the Ansys material database. For this study, a standard structural steel was chosen since the main purpose of this work is a comparative analysis in which the influence of the lattice structure on changes in stresses and frequencies in the design of

the heat exchanger is investigated. In order to conduct a correct comparative analysis, it is necessary to adhere to equivalent research objects with the same properties and conditions. It should be noted that because this task is purely comparative, matching material properties to real properties with high accuracy is not necessary. In this case, for a correct comparison, the main point in setting up the solution to the problem is ensuring the same boundary conditions and corresponding loads.

Subsequently, a computational mesh was created by dividing the model into finite elements. Due to the fact that geometrically the gyroid is a complex surface, it is not possible to create a block-structured grid for this section of the heat exchanger. Therefore, the unstructured grid type was chosen. The mesh models of the two sectors differ quite significantly. In the case of a smooth heat exchanger, the mesh is significantly simpler and more uniform in length. In the sector with a lattice structure, the mesh thickens at the joints of the walls, as well as in geometrically complex parts of the heat exchanger. The total number of mesh elements for a heat exchanger without a lattice structure is 672188, and for a sector with it number of elements is 880470. The size of the meshes elements is 1 mm.
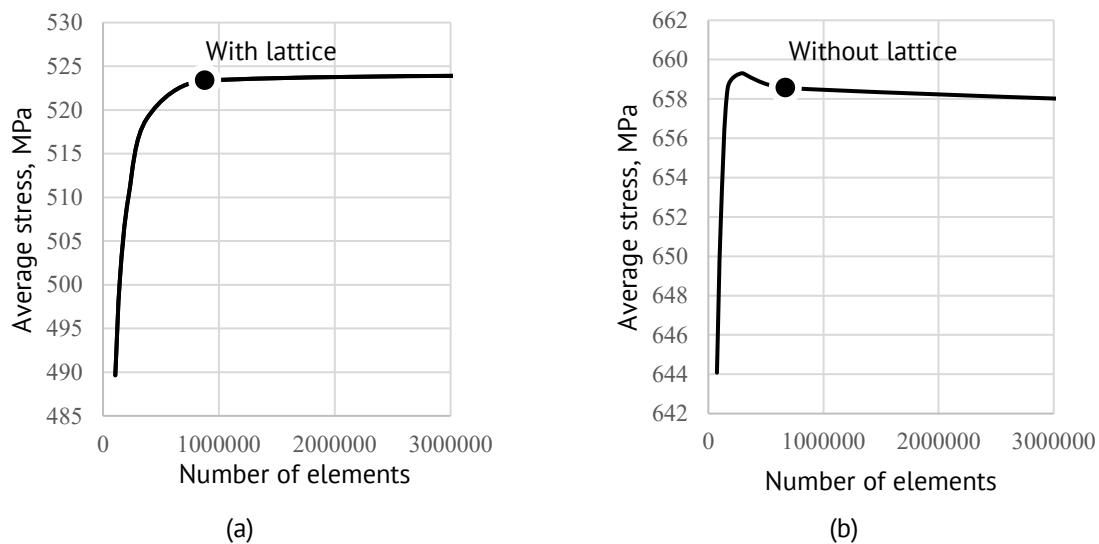
Fig. 3. Mesh independences analysis results: (a) with and (b) without lattice

When building a computational mesh, it is worth considering that the accuracy of the calculations and the time of analysis depend on its quality and mesh size. A finer mesh yields more accurate results but significantly increases the computational time. The choice of the mesh element size should be guided by the achievement of mesh independence. Mesh independence is a concept in numerical methods that denotes the state when the results of a numerical simulation become virtually independent of the size and structure of the mesh used for the computation. Thus, the optimal grid was selected based on the results of the analysis of grid independence. It was estimated by the average values of stress. Figure 3 shows mesh independent results. In these graphs, the values of the mesh model elements selected for further calculations are highlighted with dots.

After the mesh model was built, the static strength was calculated in the Static Structural module, which used the finite element method to determine the stress and

strain distributions.

The setup of the gas dynamic calculation was described in more detail in the previous article [30]. This strength calculation was solved within the framework of an elastic formulation and all stresses and deformations obtained in this study are described within the framework of Hooke's law.

When creating a computational model for strength calculation, the following boundary conditions were set:

1. the temperature distribution along the walls of the heat exchanger obtained during the gas dynamic calculation;

2. the pressure distribution along the walls of the heat exchanger obtained during the gas dynamic calculation;

3. pinning condition "Fixed Support" at the edges of heat exchangers.

Ansys used the finite element method (FEM) to calculate static strength. The equation used to determine the stresses and deformations in the elements is as follows:

$$K\Delta = F, \tag{2}$$

where K is the element stiffness matrix, Δ is the vector of nodal movements, F is the vector of external forces and moments.

This equation is solved by a system of equations using the Gaussian method or other methods of numerical linear algebra. As a result, we obtain the values of the nodal displacements Δ, which are then used to calculate the stresses in each element according to:

$$\begin{cases} \sigma_{xx} = E(\varepsilon_{xx} + \nu\varepsilon_{yy}), \\ \quad \sigma_{xy} = G\gamma_{xy}, \\ \quad \sigma_{yz} = G\gamma_{yz}, \\ \quad \sigma_{zx} = G\gamma_{zx}, \end{cases} \tag{3}$$

where σ is the stress vector, E is the Young's modulus, ν is Poisson's ratio, G is the shear modulus, γ is shear strain between the corresponding planes.

This was followed by modal analysis in the Ansys Modal, which allowed the determination of natural frequencies and vibration shapes.

Results and Discussion

In the earlier research process, it was found that the lattice structures intensified heat transfer by creating vortex flow structures, as well as by increasing the heat transfer area. Also, in the described article was carried out a comparative analysis of the obtained results of heat transfer intensification with the results of intensification by using classical turbulators, such as different types of fins. According to the results of the analysis, the investigated turbulizers were found to be more efficient than classical turbulizers. As a parameter to evaluate the effectiveness of the lattice structure as a heat exchange intensifier was used parameter Nu/Nu_{smooth} which shows the increase in the Nusselt number (the criterion of similarity of thermal processes, characterizing the relationship between the intensity of heat exchange due to convection and the intensity of heat exchange due to conduction) when using a flow turbulator relative to the smooth section of the heat exchanger. It should be noted that the study was conducted at different velocities of the working medium at the inlet to assess the effectiveness of this type of

turbulizer for different flow types (laminar and turbulent). Thus, it was possible to determine the most effective flow type for this type of turbulator. Figure 4 shows a graph of the dependence of the parameter *Nu/Nu$_{smooth}$* on the Reynolds number. The results obtained from the static strength calculations and modal analysis are presented in Table 3. Figures 5–8 show the results obtained during the strength calculation.
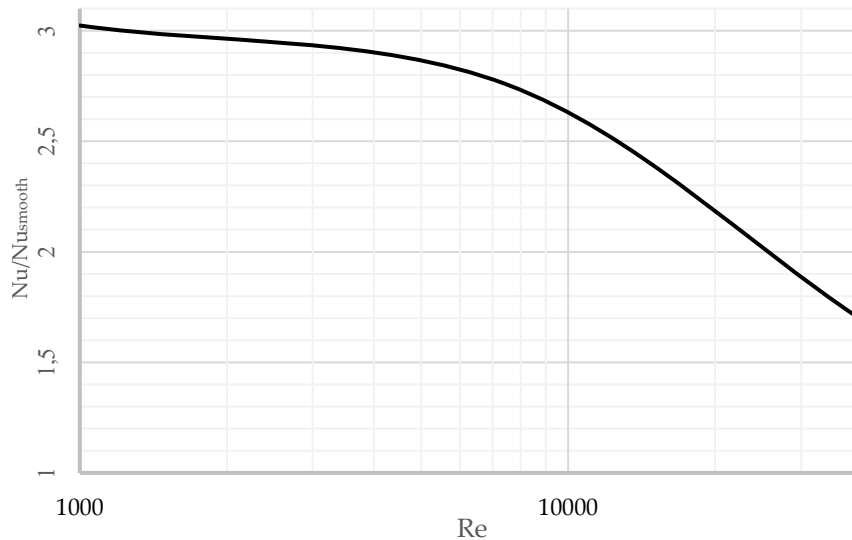
Fig. 4. Graph of dependence of the *Nu/Nu$_{smooth}$* parameter on Reynolds number

Table 3. Strength calculation results

Parameter	Unit	Value					
		Without lattice			With lattice		
		Re=1000	*Re*=7500	*Re*=40000	*Re*=1000	*Re*=7500	*Re*=40000
Average displacement ΔL_{avg}	mm	0.13375	0.13267	0.12458	0.13173	0.12459	0.12651
Average stress σ_{avg}	MPa	668.79	658.56	609.73	547.60	523.36	541.61
Average stress at inner wall $\sigma_{in\,avg}$	MPa	927.34	900.43	769.80	675.35	670.60	748.19
Average stress at external wall $\sigma_{ext\,avg}$	MPa	516.20	516.04	517.03	577.61	583.43	528.18
Average stress value at lattice $\sigma_{lattice\,avg}$	MPa	–	–	–	280.32	260.22	277.41
1st natural frequency ω_1	Hz	1554.6			3493.1		
2nd natural frequency ω_2	Hz	1554.7			3496.9		
3rd natural frequency ω_3	Hz	1738.7			3747.2		
4th natural frequency ω_4	Hz	1738.8			3797.0		
5th natural frequency ω_5	Hz	2044.2			3807.8		
6th natural frequency ω_6	Hz	2044.3			3818.0		
Mass m	kg	0.7694			0.8665		
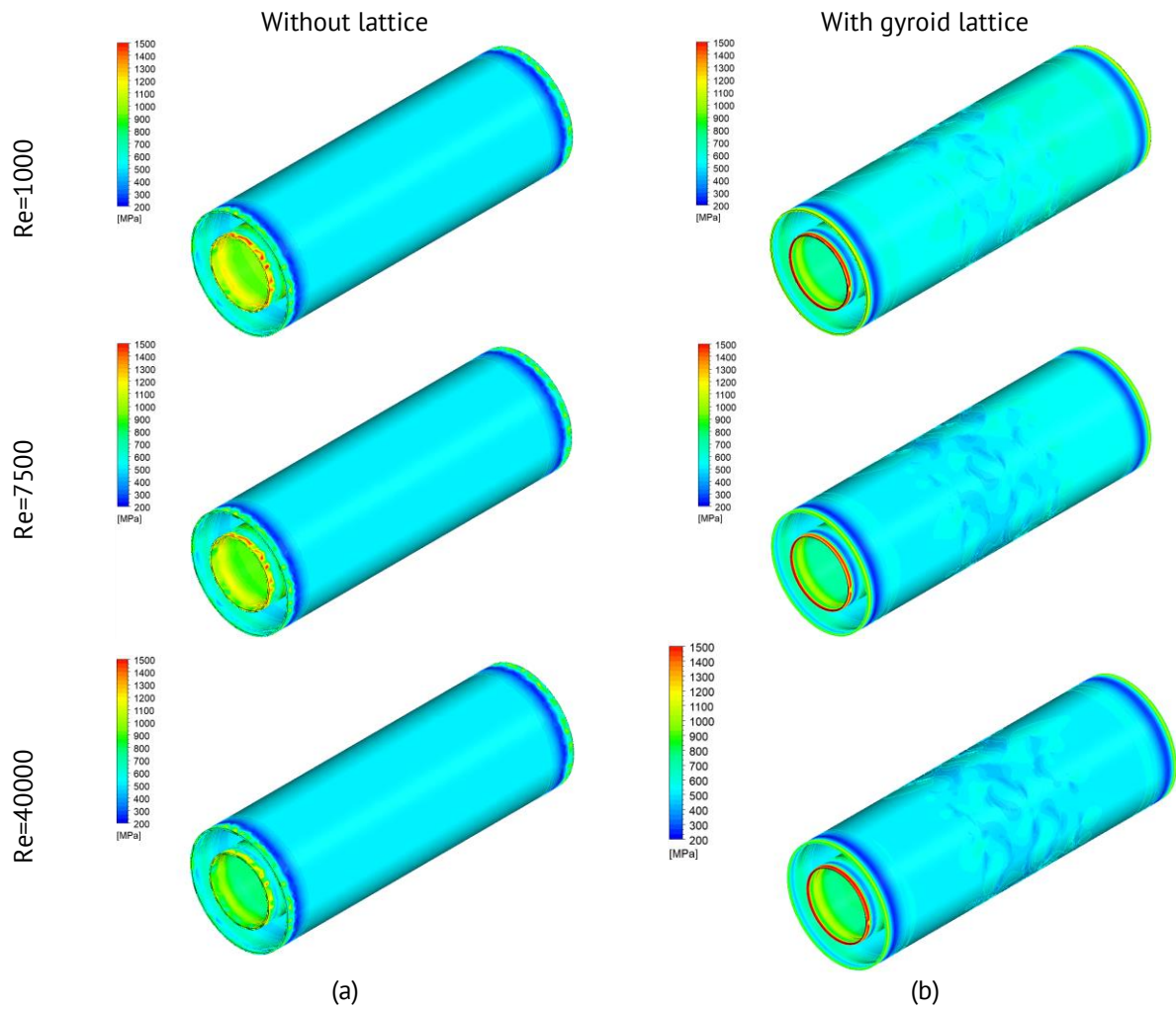
Fig. 5. Diagrams of stress values in the heat exchanger sections for different flows:
(a) without and (b) with gyroid lattice
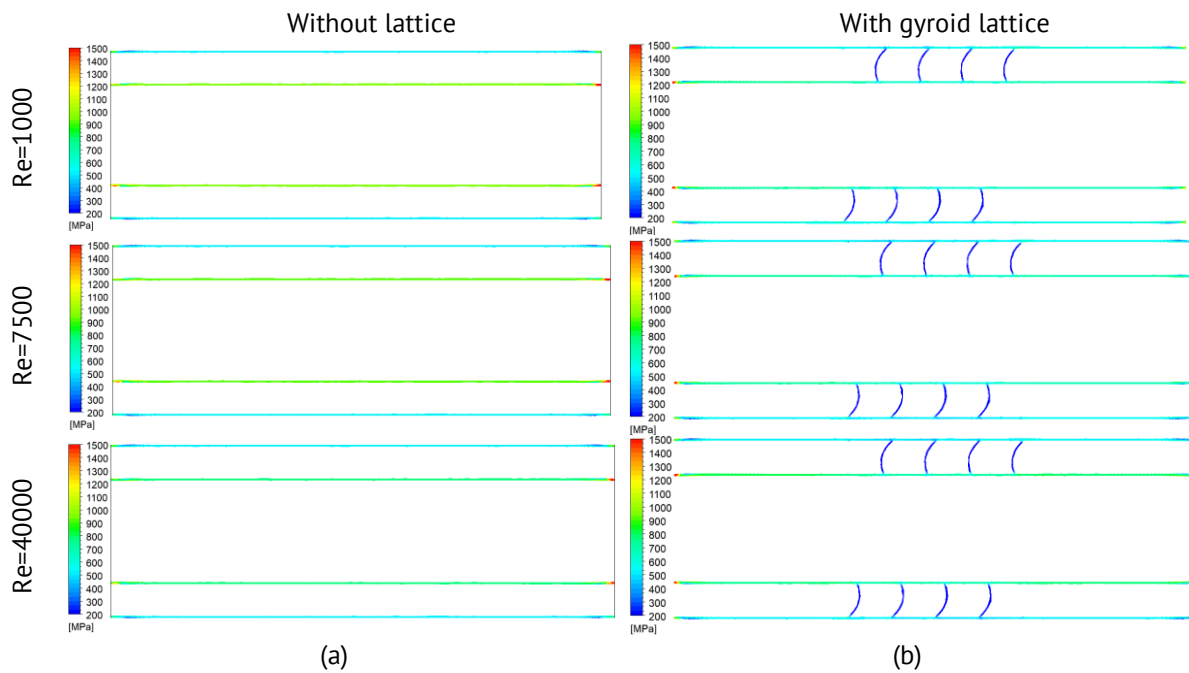
Fig. 6. Diagrams of stress values in the heat exchanger sections for different flows (cross-section):
(a) without and (b) with gyroid lattice
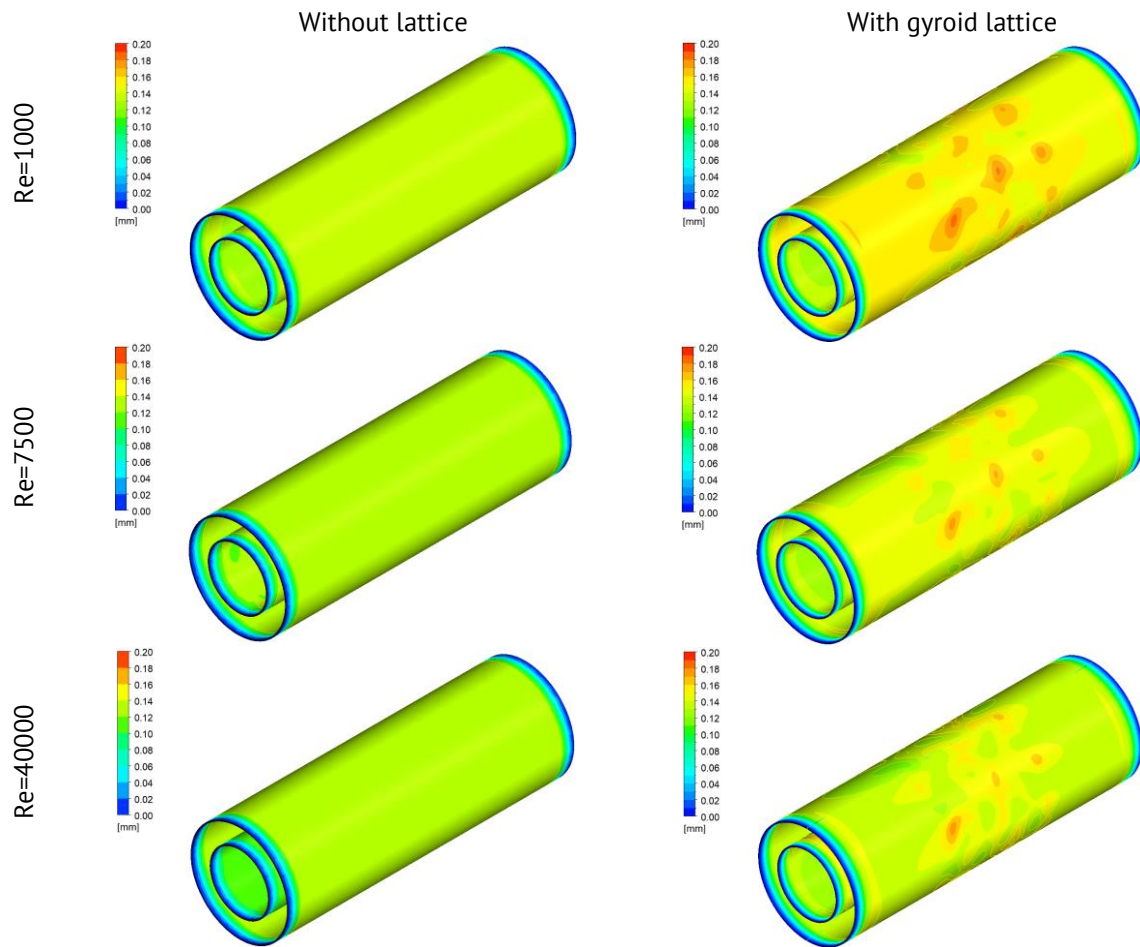
Fig. 7. Diagrams of the total displacement in the heat exchanger sections for different flows: (a) without and (b) with gyroid lattice
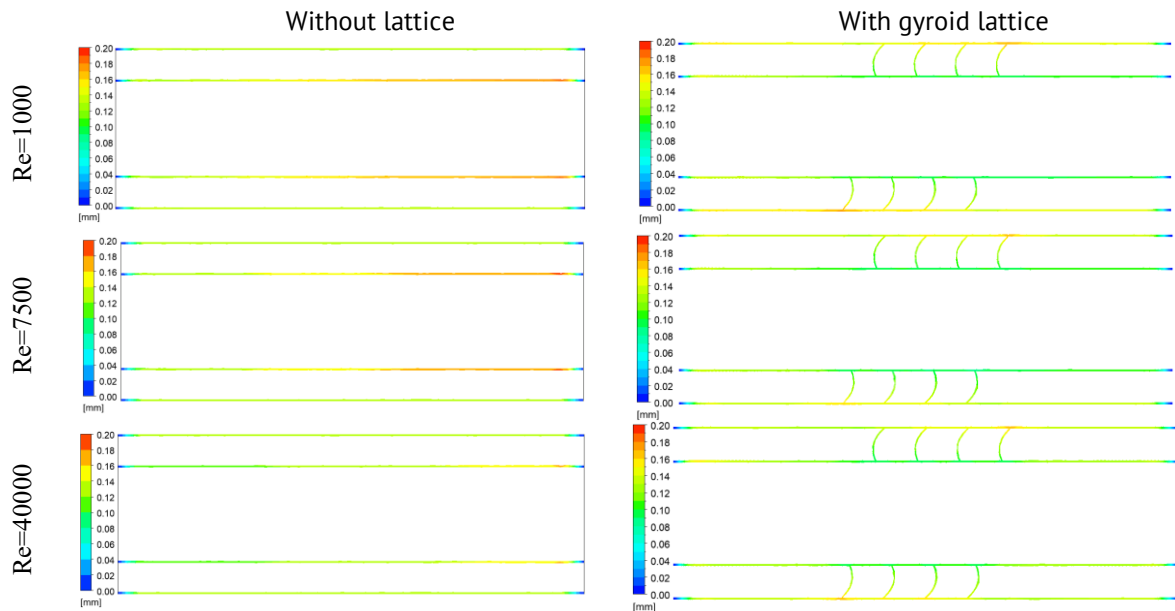
Fig. 8. Diagrams of the total displacement in the heat exchanger sections for different flows (cross-section): (a) without and (b) with gyroid lattice

For greater clarity of the differences in the results, the data were processed and presented in the form of graphs.

Figure 9 shows a graph of the dependence of the number of average stresses and average deformations in the heat exchange sectors for different flow regimes.

(a)   (b)
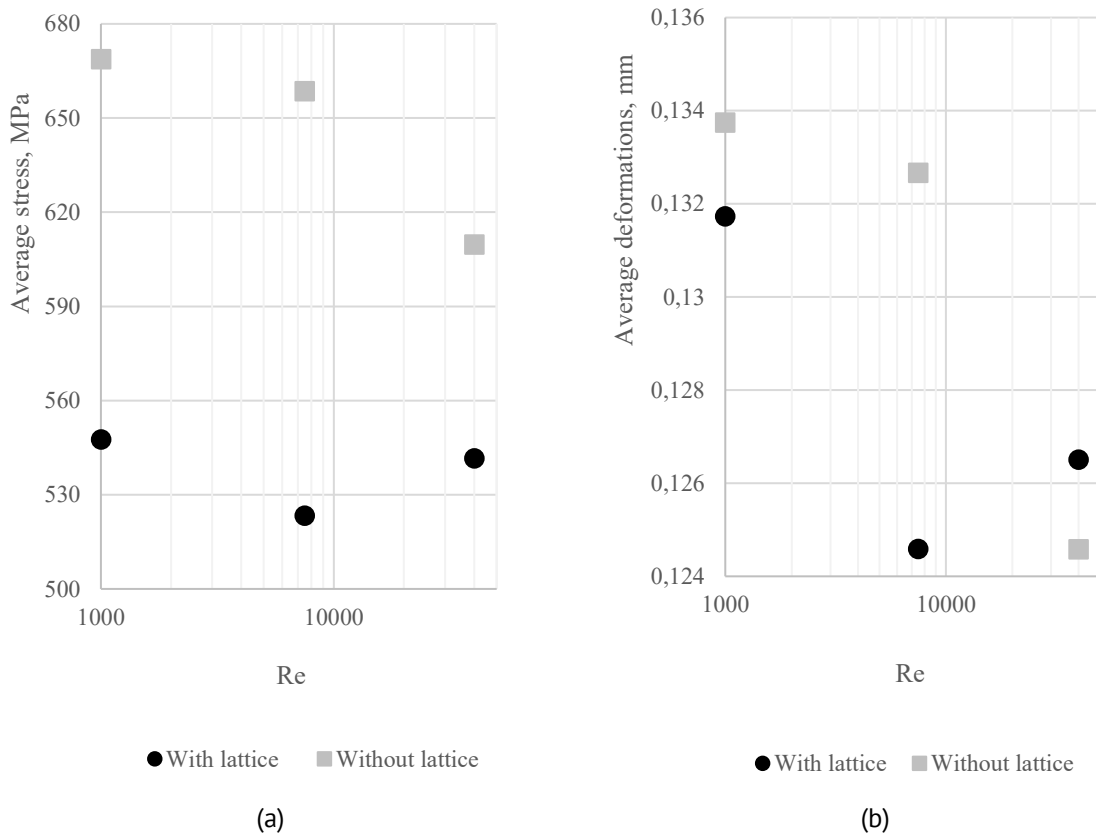
Fig. 9. A graph of the dependence of the average stress (a) and average deformations (b) in the heat exchanger sections depending on the number of *Re*

From the obtained data, it can be observed that the stresses vary depending on the different impacts of the flow on the walls of the heat exchanger. It should be noted that the stresses of the heat exchanger section with a lattice structure were lower, as expected; however, at higher Re values, this difference was significantly reduced. This is primarily due to the fact that the structure is affected by static pressure from the flow side. The change in static pressure is described by Bernoulli's law and is related to the change in both dynamic pressure and hydrostatic pressure:

$$P_{total} = P_{static} + \frac{\rho v^2}{2} + \rho g h = \text{const.} \tag{4}$$

The main element of the structure, represented as a lattice structure located in the outer loop, had a significant influence on the change in the flow pattern. This is due to the conversion of the potential energy of the pressure into kinetic energy, which significantly affects the change in flow velocity. According to Bernoulli's law, the condition of constancy of the total pressure must be observed, which is expressed as the change in the dynamic component of the pressure and leads to a decrease in the static component of the total pressure. It is important to note that the mode parameters of the compared designs of the heat exchangers are identical at the inlet boundaries, that is,

the total pressure is the same. Hence, it follows that the design with a gyroidal lattice accepts a lower load value as a result of lowering the static pressure caused by an increase in the dynamic component of the pressure (velocity) of the flow inside the heat exchanger. The velocity diagrams are presented in the previous study [30].

Analyzing the graph shown in Fig. 9, it can be seen that the values of the average stresses for the heat exchanger with the TPMS lattice are lower than those for the heat exchanger without the lattice. However, it can be observed from the graph that the values of the average stresses for the heat exchanger without a lattice monotonically decrease as the Reynolds number increases. On the contrary, for the heat exchanger with a lattice structure, this trend is not followed, and there is an extremum point after which the values of the average stresses start to increase. This can be explained by the fact that the flow regime, which is realized in the heat exchanger with a gyroid in addition to the impact of the flow on the structure, has an additional impact in the form of flow fluctuations in its parameters. Fluctuations are absolute peaks relative to the average values. In a heat exchanger with a lattice, there is a more pronounced fluctuation of the flow over the entire size of the channel compared to a smooth channel, where there are smoother changes in the flow parameters, which are concentrated mainly in the near-wall area.

The graph of the dependence of the mean strain values shows a similar dependence as that of the mean stress values. The dependencies presented in the graph are directly correlated with the stress values presented in Fig. 9. This indicated the physicality of the calculated results.

Plots of the changes in the average stresses in the cross-section for the heat exchanger sectors along their lengths for different Re numbers are presented in Fig. 10. The dotted line indicates the sector with a lattice gyroid structure. From these plots, it is clear that the stresses decreased owing to the addition of the lattice structure.

By evaluating the stress values of the presented heat exchanger sections, it can be observed that the average stresses for the Reynolds numbers of 1000 and 7500 regimes are lower when using a lattice structure along the entire length. This can be explained by the fact that part of the load is taken up by the lattice, thus minimizing the stress on the outer and inner walls. In these plots, the stresses absorbed by the TPMS lattice were expressed as a sharp drop in the stress value in the sector with it. However, by analyzing the values of the average stresses for the case with a Reynolds number of 40000, an increase in the number of average stresses in the section without the lattice is observed. The explanation of such behavior of the systems can also be additional aerodynamic influences from the flow side.

In addition to the effect of the lattice structure on the structural strength of the heat exchanger, the effect of the lattice structure on the frequency response was evaluated. Any construction has an infinite number of forms of natural vibration.

The natural frequency of the vibration depends on the stiffness and mass of the structure. Thus, the vibration frequency equation for the structures can be represented as follows:

$$\omega = \alpha\sqrt{K/m,} \tag{5}$$

where K is the structural rigidity, m is the mass, α is the empirical coefficient.
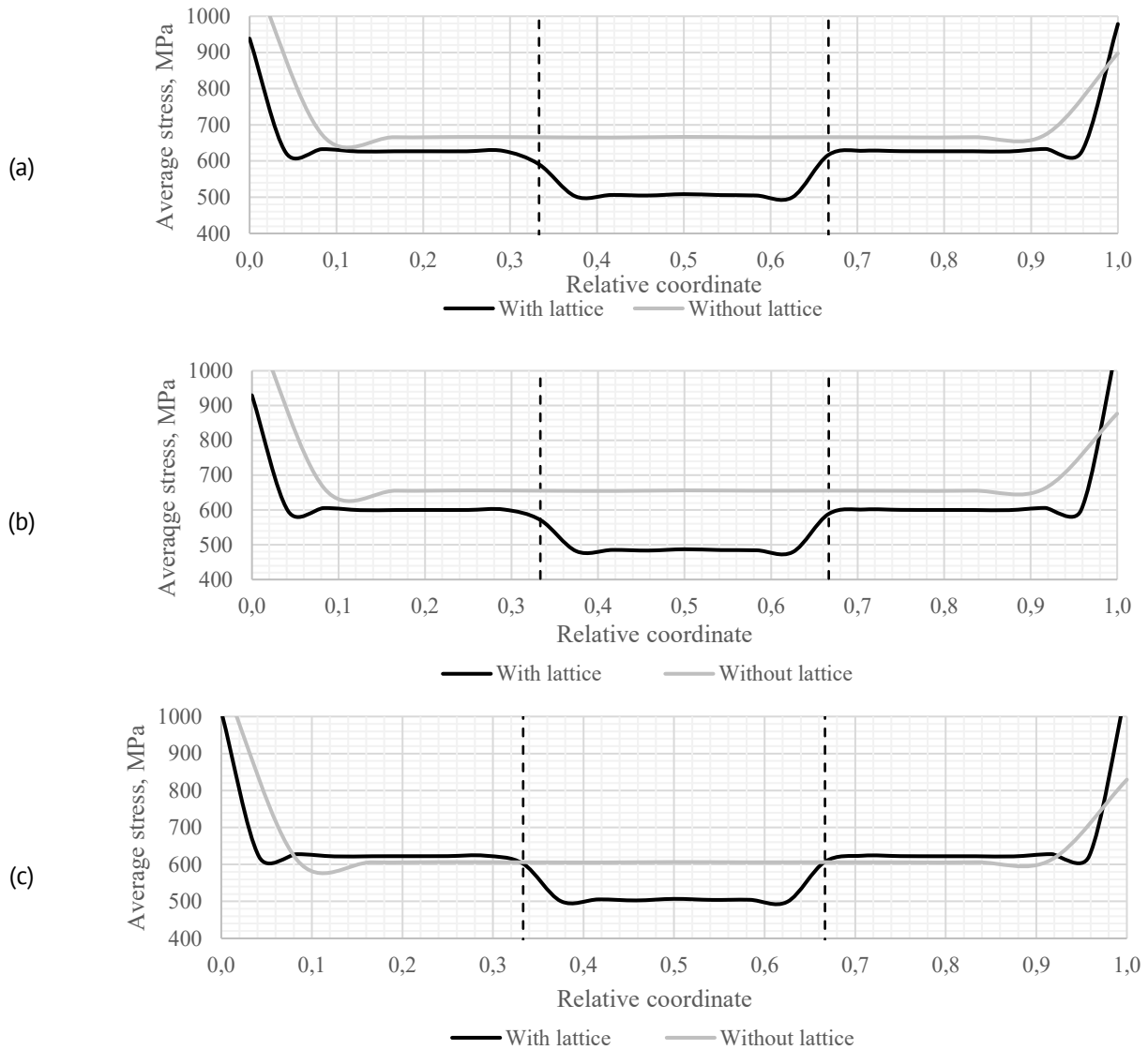
Fig. 10. Graphs of changes in average stresses in the cross section for heat exchanger sectors along their length: (a) *Re* = 1000, (b) *Re* = 7500, (c) *Re* = 40000

The results of the frequency analysis obtained in the process of modeling the operating conditions of the heat exchanger sections showed a significant increase in the natural frequencies of vibrations owing to the increase in the rigidity of the structure. Natural frequencies and forms of vibrations depend on the shape of the object in question, the material from which it is made, and the conditions of fixation. In this case, it turns out that the mass of the heat exchanger section increased with the addition of the lattice structure, which in turn negatively affected the vibration resistance properties of the object (natural frequencies were reduced). However, this structure is also a stiffener, which has a positive effect on the rigidity of the structure and therefore the vibration resistance properties of the heat exchanger section.

Increasing the natural frequencies of the structure is necessary to prevent resonant phenomena that can lead to the damage or destruction of the structure. Resonance occurs when the frequency of the external load coincides with the natural frequencies of the system. This leads to significant fluctuations that can exceed permissible limits and cause

serious damage. To avoid resonance, it is necessary to increase the natural frequencies of the structure above the range of the possible external load frequencies. Figure 11 shows the histogram of natural frequencies for both heat exchanger designs.
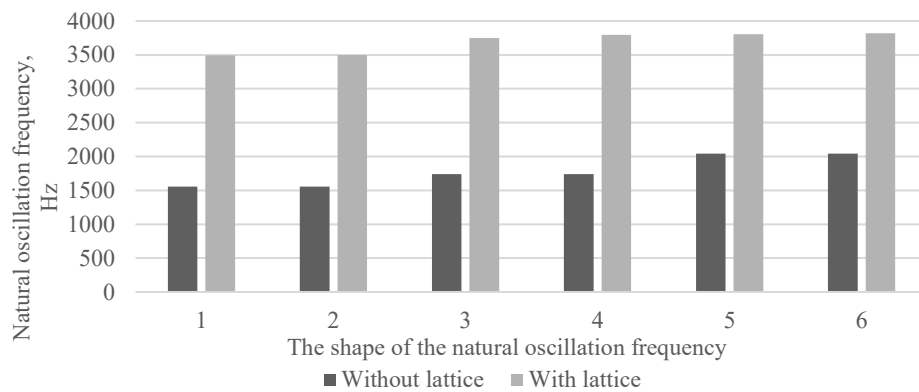
Fig. 11. Histogram of natural frequency values for various forms of vibrations

Based on the calculated data shown in Fig. 11, it can be seen that the natural frequencies of the heat exchanger section with the embedded grating are much higher than those of the smooth section. This indicates that despite the increase in mass and its negative effect on the frequency response, the increase in stiffness of the structure had a more significant effect on the frequency response, which ultimately improved the dynamic strength of the heat exchanger.

Conclusions

Summing up this article on the study of the effect of lattice structures on the strength of the heat exchanger, it was found that:

1. The positive effect of lattice structures on heat transfer in heat exchangers has been revealed. It has been established that the use of lattice structures improves the processes of heat and mass transfer, which is confirmed by numerical calculations and experimental data (Fig. 4).

2. A decrease in average stresses in the heat exchanger has been established when using lattice structures. According to finite element calculations, lattice structures can reduce average stresses by 10–20 % for flows with low Reynolds numbers, which increases the static strength of the heat exchanger.

3. The limitations of the use of lattice structures are determined. It is established that in regimes with high Reynolds numbers, the influence of lattice structures becomes negative due to an increase in stress values caused by increased flow fluctuations. This opens up prospects for optimizing the geometric parameters of lattice turbulators to improve the efficiency of heat transfer.

4. An increase in the rigidity and frequency characteristics of a heat exchanger with lattice structures has been revealed. Frequency analysis showed that the introduction of lattice structures increases the natural frequencies of the first six oscillation forms by 86–125 %, which contributes to an increase in the dynamic strength of the heat exchanger.

5. The expediency of using lattice structures to increase the service life of heat exchangers is shown. Increasing natural frequencies minimizes dangerous low-frequency deformations, which reduces the risk of structural failure during prolonged operation.

6. Further investigation of the empirical dependences of the heat transfer parameters on the characteristics of the lattice is recommended. It is proposed to use numerical methods to optimize the geometry of lattice structures in order to increase their efficiency and reliability in heat exchangers.

The aggregate of the above points forms an overall academic assessment establishing a comprehensive relationship between the use of lattice designs, heat transfer intensification and improved strength performance of heat exchangers. The results, validated by numerical simulations and frequency analysis, demonstrate practical value in optimizing heat exchangers for regimes with different Reynolds numbers. The study contributes to the theory of heat transfer and strength calculations, offering new engineering approaches and forming the basis for further development of empirical dependencies of heat transfer parameters on the characteristics of grids, which has prospects for improving the energy efficiency and durability of equipment.

References

1. Usman A, Khan AN. Failure analysis of heat exchanger tubes. *Engineering Failure Analysis.* 2008;15(1–2): 118–128.
2. Otegui JL, Fazzini PG. Failure analysis of tube-tubesheet welds in cracked gas heat exchangers. *Engineering Failure Analysis.* 2004;11(6): 903–913.
3. Zhao J, Zhu Y, Liu X, Jiang R, Ding B, Chen Y. Root cause analysis of a cracked primary heat exchanger in a gas wall-mounted boiler. *Engineering Failure Analysis.* 2023;153: 107583.
4. Sunandrio H, Suhartono HA, Prawoto Y. Overheated pipe due to scale: Field failure investigation and finite element analysis. *Case Studies in Engineering Failure Analysis.* 2017;8: 36–48.
5. Xu S, Wang C, Wang W. Failure analysis of stress corrosion cracking in heat exchanger tubes during start-up operation. *Engineering Failure Analysis.* 2015;51: 1–8.
6. Liu L, Ding N, Shi J, Xu N, Guo W, Wu CML. Failure analysis of tube-to-tubesheet welded joints in a shell-tube heat exchanger. *Case Studies in Engineering Failure Analysis.* 2016;7: 32–40.
7. Addepalli S, Eiroa D, Lieotrakool S, François AL, Guisset J, Sanjaime D, Kazarian M, Duda J, Roy R, Phillips P. Degradation Study of Heat Exchangers. *Procedia CIRP.* 2015;38: 137–142.
8. Careri F, Khan RHU, Todd C, Attallah MM. Additive manufacturing of heat exchangers in aerospace applications: a review. *Applied Thermal Engineering.* 2023;235: 12137.
9. Niknam SA, Mortazavi M, Li D. Additively manufactured heat exchangers: a review on opportunities and challenges. *Int J Adv Manuf Technol.* 2021;112: 601–618.
10. Oh SH, An CH, Seo B, Kim J, Park CY, Park K. Functional morphology change of TPMS structures for design and additive manufacturing of compact heat exchangers. *Additive Manufacturing.* 2023;76: 103778.
11. Popovich AA, Sufiiarov VS, Borisov E V., Polozov IA, Masaylo D V. Design and manufacturing of tailored microstructure with selective laser melting. *Materials Physics and Mechanics.* 2018;38(1): 1–10.
12. Du Plessis A, Razavi N, Benedetti M, Murchio S, Leary M, Watson M, Bhate D, Berto F. Properties and applications of additively manufactured metallic cellular materials: A review. *Progress in Materials Science.* 2022;125: 100918.
13. Borovkov AI, Maslov LB, Zhmaylo MA, Tarasenko FD, Nezhinskaya LS. Finite element analysis of elastic properties of metamaterials based on triply periodic minimal surfaces. *Materials Physics and Mechanics.* 2024;52(2): 11–29.
14. Attarzadeh R, Rovira M, Duwig C. Design analysis of the "Schwartz D" based heat exchanger: Anumerical study. *International Journal of Heat and Mass Transfer.* 2021;177: 121415.
15. Liu Z, Gong H, Gao J, Liu L. Topological design, mechanical responses and mass transport characteristics of high strength-high permeability TPMS-based scaffolds. *International Journal of Mechanical Sciences.* 2022;217: 107023.
16. de Aquino DA, Maskery I, Longhitano GA, Jardini AL, del Conte EG. Investigation of load direction on the

compressive strength of additively manufactured triply periodic minimal surface scaffolds. *The International Journal of Advanced Manufacturing Technology.* 2020;109: 771–779.

17. Cai Z, Liu Z, Hu X, Kuang H, Zhai J. The effect of porosity on the mechanical properties of 3D-printed triply periodic minimal surface (TPMS) bioscaffold. *Bio-Design and Manufacturing.* 2019;2: 242–255.

18. Hu B, Wang Z, Du C, Zou W, Wu W, Tang J, Ai J, Zhou H, Chen R, Shan B. Multi-objective Bayesian optimization accelerated design of TPMS structures. *International Journal of Mechanical Sciences.* 2023;244: 108085.

19. Feng G, Li S, Xiao L, Song W. Mechanical properties and deformation behavior of functionally graded TPMS structures under static and dynamic loading. *International Journal of Impact Engineering.* 2023;176: 10454.

20. Yu S, Sun J, Bai J. Investigation of functionally graded TPMS structures fabricated by additive manufacturing. *Materials & Design.* 2019;182: 108021.

21. Reynolds BW, Fee CJ, Morison KR, Holland DJ. Characterisation of Heat Transfer within 3D Printed TPMS Heat Exchangers. *International Journal of Heat and Mass Transfer.* 2023;212: 124264.

22. Baobaid N, Ali MI, Khan KA, Abu Al-Rub RK. Fluid flow and heat transfer of porous TPMS architected heat sinks in free convection environment. *Case Studies in Thermal Engineering.* 2022;33: 101944.

23. Tang W, Zou C, Zhou H, Zhang L, Zeng Y, Sun L, Zhao Y, Yan M, Fu J, Hu J, Li Z, Liu Z, Wang T, Zhang Z. A novel convective heat transfer enhancement method based on precise control of Gyroid-type TPMS lattice structure. *Applied Thermal Engineering.* 2023;230(B): 120797.

24. Yeranee K, Rao Y, Xu C, Zhang Y, Su X. Turbulent Flow Heat Transfer and Thermal Stress Improvement of Gas Turbine Blade Trailing Edge Cooling with Diamond-Type TPMS Structure. *Aerospace.* 2024;11(1): 37.

25. Alteneiji M, Ali MIH, Khan KA, Abu Al-Rub RK. Heat transfer effectiveness characteristics maps for additively manufactured TPMS compact heat exchangers. *Energy Storage and Saving.* 2022;1(3): 153–161.

26. Mahmoud D, Tandel SRS, Yakout M, Elbestawi M, Mattiello F, Paradiso S, Ching C, Zaher M, Abdelnabi M. Enhancement of heat exchanger performance using additive manufacturing of gyroid lattice structures. *International Journal of Advanced Manufacturing Technology.* 2023;126: 4021–4036.

27. Chen F, Jiang X, Lu C, Wang Y, Wen P, Shen Q. Heat transfer efficiency enhancement of gyroid heat exchanger based on multidimensional gradient structure design. *International Communications in Heat and Mass Transfer.* 2023;149: 107127.

28. Qian C, Wang J, Zhong H, Qiu X, Yu B, Shi J, Chen J. Experimental investigation on heat transfer characteristics of copper heat exchangers based on triply periodic minimal surfaces (TPMS). *International Communications in Heat and Mass Transfer.* 2024;152: 107292.

29. Wang J, Qian C, Qiu X, Yu B, Yan L, Shi J, Chen J. Numerical and experimental investigation of additive manufactured heat exchanger using triply periodic minimal surfaces (TPMS). *Thermal Science and Engineering Progress.* 2024;55: 103007.

30. Pulin A, Laptev M, Kortikov N, Barskov V, Roschenko G, Alisov K, Talabira I, Gong B, Rassokhin V, Popovich A, Novikov P. Numerical Investigation of Heat Transfer Intensification Using Lattice Structures in Heat Exchangers. *Energies.* 2024;17(13): 3333.

About Author

Anton G. Pulin 🆔 Sc
Engineer (Peter the Great St. Petersburg Polytechnic University, Saint-Petersburg, Russia)

Mikhail A. Laptev 🆔 Sc
Assistant (Peter the Great St. Petersburg Polytechnic University, Saint-Petersburg, Russia)

Kirill A. Alisov 🆔
Laboratory Assistant (Peter the Great St. Petersburg Polytechnic University, Saint-Petersburg, Russia)

Viktor V. Barskov 🆔 Sc
Doctor of Technical Sciences
Director of the Institute of Energy (Peter the Great St. Petersburg Polytechnic University, Saint-Petersburg, Russia)

Viktor A. Rassokhin [iD] Sc

Doctor of Technical Sciences
Chief Project Engineer (Peter the Great St. Petersburg Polytechnic University, Saint-Petersburg, Russia)

Bowen Gong [iD]

Assistant (Peter the Great St. Petersburg Polytechnic University, Saint-Petersburg, Russia)

Valentin S. Kotov Sc

Senior Lecturer (Peter the Great St. Petersburg Polytechnic University, Saint-Petersburg, Russia)

Gleb A. Roshchenko [iD]

Engineer (Peter the Great St. Petersburg Polytechnic University, Saint-Petersburg, Russia)

Anton M. Balakin [iD]

Engineer (Peter the Great St. Petersburg Polytechnic University, Saint-Petersburg, Russia)

Mark Golubtsov [iD]

Laboratory Assistant (Peter the Great St. Petersburg Polytechnic University, Saint-Petersburg, Russia)

Ivan R. Nurkov [iD]

Laboratory Assistant (Peter the Great St. Petersburg Polytechnic University, Saint-Petersburg, Russia)

Mehdi Basati Panah [iD]

Senior Lecturer (Peter the Great St. Petersburg Polytechnic University, Saint-Petersburg, Russia)

Modeling of working cycles of thermomechanical actuators based on shape memory alloys at repeated actuation

F.S. Belyaev [1✉] (iD), A.E. Volkov [2] (iD), D.F. Gorbachenko [2], M.E. Evard [2] (iD)

[1] Institute for Problems of Mechanical Engineering RAS, St. Petersburg, Russia

[2] St. Petersburg State University, St. Petersburg, Russia

✉ belyaev_fs@mail.ru

ABSTRACT
The microstructural model of the mechanical behavior of shape memory alloys was applied to describe the operation of a thermomechanical torsion actuator with a TiNi alloy working body and an elastic counterbody. The calculated dependences of a recovery strain, maximum stress in a cycle, and irreversible deformation on the cycle number were plotted for the working body of the actuator. It is shown that from cycle to cycle there is an accumulation of irreversible deformation, the rate of which gradually decreases. As a consequence, both the value of a recovery strain and the value of the stresses developed by the actuator decrease, which together leads to a decrease in the work output. The influence of the stiffness of the elastic counterbody on the specific work produced in the cycle was investigated. It is shown that the produced work depends non-monotonically on the stiffness of the counterbody and there is an optimal stiffness at which this work is maximized.

KEYWORDS
shape memory alloys • actuator • microstructural modeling • plastic deformation • TiNi

Introduction

Currently, actuators with working bodies made of shape memory alloys (SMA) are being actively developed and manufactured [1–16]. One of the main sources of interest in such actuators is the strict requirements for the weight of the product in modern aircraft, spacecraft, and various robotic systems. SMA-based actuators allow achieving a weight gain of up to 80 % compared to similar electric and hydraulic actuators [11]. In addition, SMA-based actuators are highly reliable, have high rates of developed forces, are quiet in operation, have a simple design, and have a small number of moving parts. At the same time, SMAs can be equally well used in large actuators that develop significant forces, as well as in microactuators.

The operation of a thermomechanical actuator with SMA working bodies is based on the implementation of the shape memory effect – the restoration of deformation during heating. Accordingly, when the working body cools, the actuator must return to its initial state. The restoration of the initial deformation occurs due to the effect of transformation plasticity, which is realized when an external load is applied during

cooling. Thus, the working cycle consists of two stages: the "cocking" stage, when the working body accumulates deformation and the actuation stage, when the deformation of the working body is restored. Actuator designs can be different, but we can distinguish between double-sided actuators capable of developing forces in two opposite directions, and single-sided actuators, with a working stroke in one direction. Double-sided actuators usually use two working bodies made of SMA, which alternately perform a working stroke, simultaneously cocking each other [14–16]. But more often, single-sided actuators are used, the design of which usually includes a SMA working body, which performs useful work when heated, and an elastic counterbody, which restores the initial deformation of the working body when cooled due to the stored elastic energy.

Despite the many advantages of SMA-based actuators, they have some drawbacks. The main drawback is the instability of the functional properties of SMA. Multiple implementation of the actuator's working cycle leads to the accumulation of irreversible deformation, a change in the characteristic temperatures of martensitic transformations, a decrease in the magnitude of the recoverable deformation and the developed forces [17]. This phenomenon manifests in all SMAs, the scale of changes depends on many factors, such as the alloy composition, the type of transformation, preliminary thermomechanical treatment, the magnitude of the acting load during the transformation, etc. [18–22]. Instability of properties can lead to a decrease in the useful work produced in the actuator's working cycle or to its incomplete operation.

Successful design of SMA-based actuators requires reliable tools of calculating the features of their mechanical behavior, including the instability of SMA properties. In known studies [15,16,23,24], simplified approaches and simple models are used to describe the behavior of the working element, which only allow one to approximately determine the actuator characteristics. On the other hand, there are microstructural models that can describe all the functional properties of SMA [25–28]. This class of models has a high predictive power and is capable of describing changes in SMA properties under repeated thermomechanical effects. But these models are not simple and transparent enough, and using them to solve specific problems requires additional efforts. In this regard, the purpose of this work was to study the possibility of using a microstructural model to describe the operation of a thermomechanical actuator based on SMA.

Microstructural model

To describe the mechanical behavior of SMA, the microstructural model developed earlier by the authors [28–32] was used in the present work. The representative volume considered within its framework corresponds to the material point of the material. The microstructural model implies the existence of several structural levels, which, in order to better describe the alloy behavior, should reflect the actual microstructure of the material. In the proposed model, it is considered that the representative volume consists of grains with different orientations of the crystallographic axes, which, in turn, consist of volumes occupied by austenite and/or orientational variants of martensite.

According to the Reuss hypothesis, the deformation of the representative volume is calculated by orientational averaging of the deformations of the grains that compose it:

$$\varepsilon = \sum_{\omega} f(\omega)\varepsilon^{gr}(\omega), \tag{1}$$

where ω is the orientation of crystallographic axes, $f(\omega)$ is the volume fraction of grains with orientation ω, and $\varepsilon^{gr}(\omega)$ is the deformation of these grains. The grain deformation can be represented as the sum of contributions of individual deformation mechanisms:

$$\varepsilon^{gr} = \varepsilon^E + \varepsilon^T + \varepsilon^{Ph} + \varepsilon^{MP}, \tag{2}$$

where ε^E is elastic deformation determined by Hooke's law, ε^T is temperature deformation due to thermal expansion, ε^{Ph} is phase deformation, ε^{MP} is microplastic deformation.

To describe the phase deformation, the model introduces internal variables Φ_n such that Φ_n/N is the volume fraction of the n-th martensite variant, where N is the number of possible martensite variants. The grain phase deformation ε^{Ph} is calculated by averaging over all martensite variants:

$$\varepsilon^{Ph} = \frac{1}{N} \sum_{n=1}^{N} \Phi_n D^n, \tag{3}$$

where D^n is the Bain strain tensor for the n-th variant of martensite.

The martensitic transformation condition is as follows:

$$F_n = \pm F^{fr}, \tag{4}$$

where F_n is the generalized thermodynamic force causing the growth of the n-th variant of martensite, F^{fr} is the dissipative force preventing the movement of interphase boundaries and responsible for the presence of temperature-phase hysteresis, the "+" sign corresponds to the direct transformation, and "-"to the reverse one.

The growing martensitic crystal, due to the incompatibility of its deformation with the austenitic matrix, creates internal stresses causing microplastic deformation. When calculating this microplastic deformation, the main assumption is that the microplastic deformation generated by the growth of a certain martensite variant is proportional to the deviator of the Bain deformation of this variant:

$$\varepsilon^{MP} = \frac{1}{N} \sum_{n=1}^{N} \kappa \varepsilon_n^{mp} dev(D^n), \tag{5}$$

where ε_n^{mp} is the scalar measure of microplastic deformation associated with the growth of the n-th martensite variant, κ is the scale factor for microplastic deformation.

The conditions for the onset of microplastic yield are similar to those for plastic yield in the one-dimensional case, taking into account kinematic and isotropic hardening, where the role of stress is played by the generalized thermodynamic force F_n^p, and the thermodynamic forces F^y and F_n^ρ correspond to kinematic and isotropic hardening:

$$\left| F_n^p - F_n^\rho \right| = F^y, \quad \left(F_n^p - F_n^\rho \right) dF_n^p > 0, \tag{6}$$

the generalized thermodynamic force causing microplastic deformation is calculated as follows:

$$F_n^p = \mu \sum_{m=1}^{N} A_{mn}(\Phi_m - b_m), \tag{7}$$

where b_m is the density of oriented defects, A is the matrix defining the interaction of martensite variants described in detail in [33,34], and the coefficient μ is calculated as follows:

$$\mu = -\frac{q_0(M_s - M_f)}{T_0(1 - 2\alpha)}, \tag{8}$$

$$T_0 = \frac{M_s + A_f}{2}, \tag{9}$$

where q_0 is the latent heat of transformation, M_s and M_f are the temperatures of the beginning and end of direct martensitic transformation, A_f is the temperature of the end of reverse transformation, T_0 is the thermodynamic equilibrium temperature of the phases (austenite and martensite), α is the interaction coefficient of martensite variants.

Deformation defects resulting from microplastic yielding can be divided into two groups: oriented defects, which create long-range stress fields, and scattered defects. To calculate the densities of oriented defects b_n and scattered defects f, the following evolution equations are proposed:

$$\dot{b}_n = \dot{\varepsilon}_n^{mp} - \frac{1}{\beta^*}|b_n|\dot{\varepsilon}_n^{mp}H(b_n\dot{\varepsilon}_n^{mp}), \tag{10}$$

$$\dot{f} = \sum_{m=1}^{N}|\dot{\varepsilon}_m^{mp}| + r_1(f - f_0)\Phi^{gr}H(-\Phi^{gr}), \tag{11}$$

where H is the Heaviside function, β^* is the maximum density of oriented defects in grain, r_1 is the recovery coefficient of scattered defects, f_0 is the equilibrium value of scattered defects.

In order to obtain a closed system of equations that allows the calculation of all internal variables, it is necessary to introduce hardening laws. In the model, it is considered that scattered defects impede the movement of dislocations and thereby create isotropic hardening, and pile-ups of oriented defects, generating internal stress fields, create kinematic hardening. Linear dependences are proposed to relate hardenings to defect densities:

$$F_n^{\rho} = a_{\rho}b_n, \tag{12}$$

$$F^y = a_y f, \tag{13}$$

where a_{ρ} and a_y are the kinematic and isotropic hardening coefficients, respectively.

Simulation results

The object of the study was a torsion actuator with a TiNi alloy working body and an elastic counterbody. In order for the actuator's working body to recover deformation and generate stress upon heating, it needs to be given an initial strain. In the simulated experiments, the sample was pre-strained in the martensitic state to 7 % and connected to an elastic counterbody of a given stiffness after unloading. Then, heating up to 450 K caused the working stroke of the actuator (deformation recovery and stress increase), and cooling to 300 K caused cocking (increase in strain and decrease in stress). In the strain-stress coordinates, a linear trajectory corresponds to the working stroke and cocking. The slope of this line is determined by the stiffness of the counterbody. The scheme of preparation of the actuator working body and its functioning is shown in Fig. 1.

To verify the ability of the presented model to describe the behavior of SMA under thermomechanical actuator conditions, numerical experiments corresponding to real experiments from [17] for a single-sided actuator with working element made of TiNi alloy and elastic counterbody were carried out. In the model, a particular alloy is defined
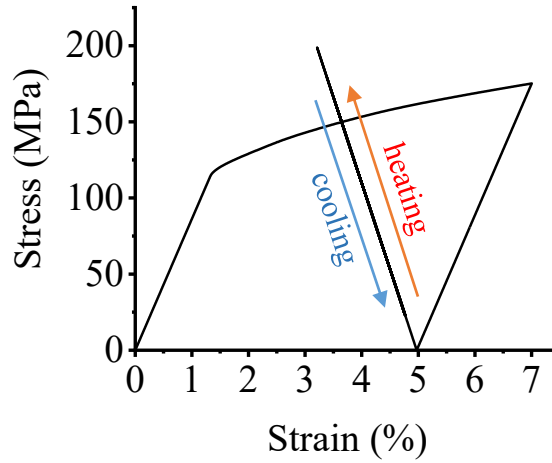
Fig. 1. The scheme of initial preparation of the actuator working body and its functioning under thermocycling
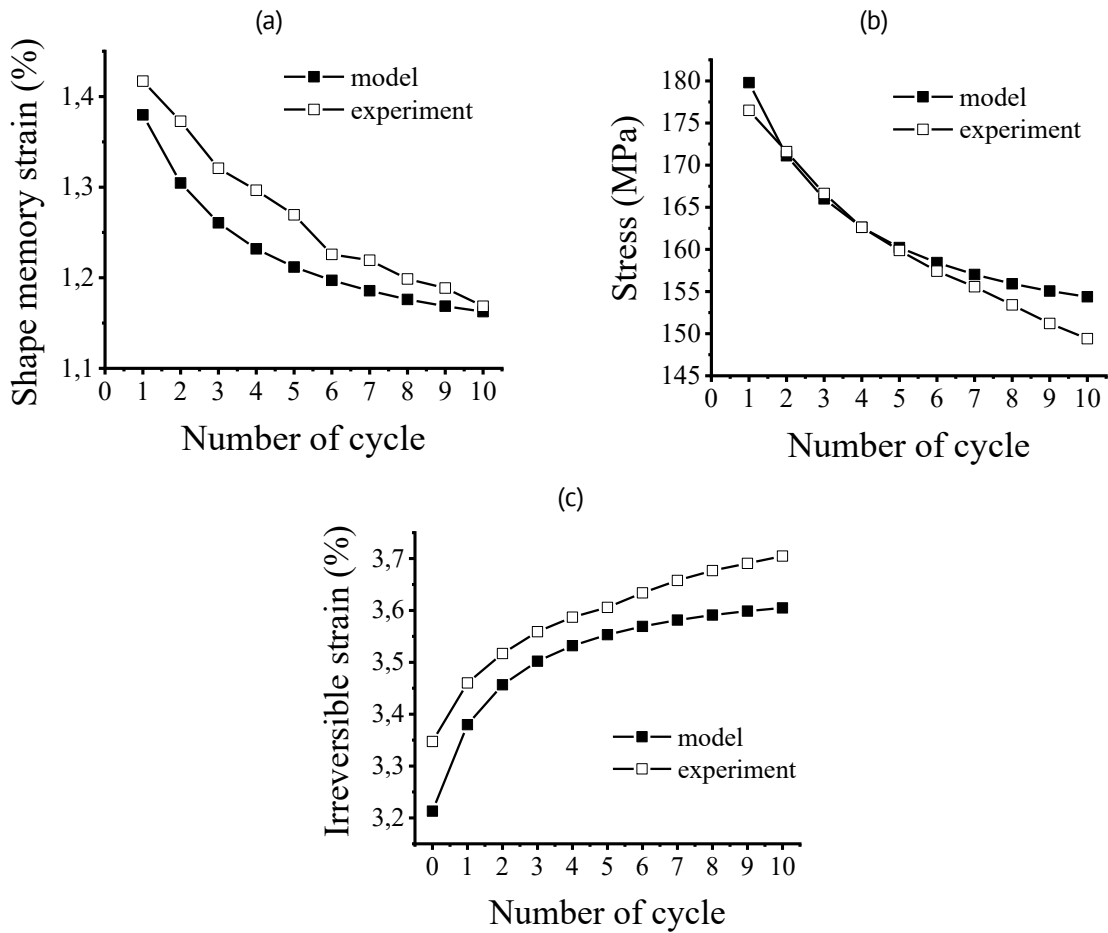
Fig. 2. The evolution of a recovery strain (a) stresses developed by the actuator (b) and accumulated residual strain (c) at thermocycling for the actuator with a counterbody stiffness of 11.3 GPa

by a corresponding set of material constants. For the calculations, characteristic temperatures and latent heat of martensite transformations were taken directly from [17], a temperature of the thermodynamic equilibrium was calculated by Eq. (9), a number of martensite variants corresponds to B2↔B19' martensitic transformation realized in TiNi

alloys, other constants were fitted to best describe the change in the working cycle parameters of the actuator with a counterbody stiffness of 11.3 GPa at the first ten actuations. The considered cycle parameters included: a recovery strain i.e. strain recovered by heating (Fig. 2(a)), maximum stresses developed by the actuator (Fig. 2(b)), accumulated residual strain (Fig. 2(c)). In Fig. 2, it can be seen that the selected constants allowed the model to describe well the evolution of the considered parameters of the actuator working cycle for the first ten operations. The list of material constants used for modeling is presented in Table 1.

Table 1. Material constants for TiNi alloy

Material constant	Symbol	Value
Number of martensite variants	N	12
Latent heat (enthalpy) of the direct martensitic transformation, MJ/m^3	q_0	-160
Characteristic temperatures of martensite transformation, K	M_f	310
	M_s	332
	A_s	340
	A_f	363
Temperature of the thermodynamic equilibrium, K	T_0	347.5
interaction coefficient of martensite variants	α	0.2
Microplastic strain scaling factor	κ	1
Coefficient of isotropic hardening, MPa	a_y	1
Coefficients of kinematic hardening, MPa	a_ρ	10
Maximum value of the oriented defects density	β^*	0.6
Initial value of scattered defects	f_0	0
Scattered defects recovery coefficient	r_1	0
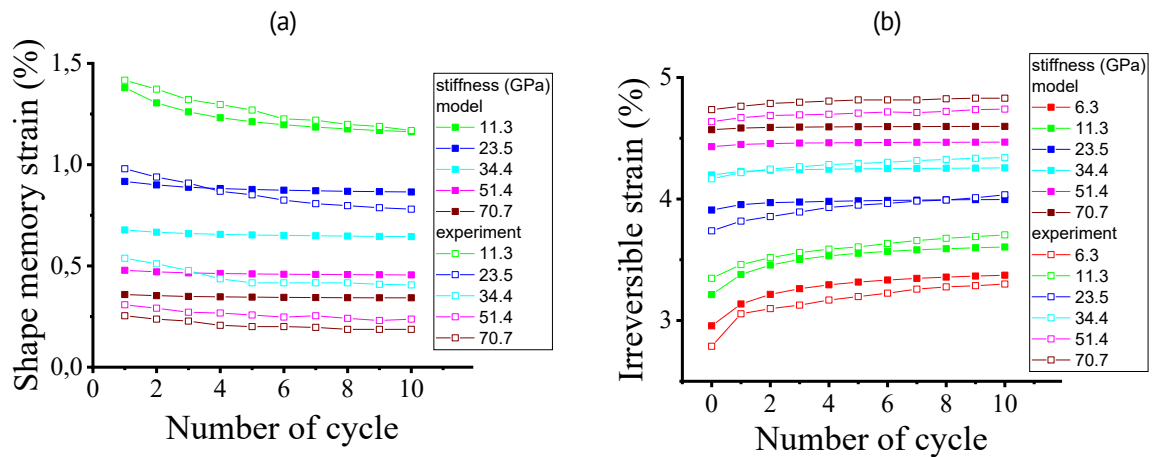
Fig. 3. The evolution of a recovery strain (a) and accumulated residual strain at thermocycling

To verify the predictive power of the model, numerical experiments were performed for other counterbody stiffnesses. Figure 3 shows a comparison of the calculated and experimental strain dependences of the shape memory effect and the accumulated residual strain for the first ten cycles. Figure 3(a) demonstrates that the model predicts very well the evolution of a recovery strain up to stiffness 23.5 GPa. For larger values of the counterbody stiffness there are some numerical discrepancies, but nevertheless there

is a good qualitative agreement. Similar results were obtained for irreversible deformation (see Fig. 3(b)), good agreement is observed up to a stiffness of 34.4 GPa, and for larger values there is a quality compliance. Thus, the model with a single set of material constants allows obtaining good results for stiffnesses close to 11.3 GPa (for which the constants were selected), and for the rest it gives a qualitative agreement.

According to experimental data [17], a significant portion of the residual strain appears during the preparation of the working element (preliminary deformation and first heating – cycle 0 in Fig. 3(b)), and then it gradually increases from cycle to cycle. It is also noted that with high counterbody stiffness, more irreversible deformation accumulates during the preparation process, but then it grows insignificantly. Since the accumulation of irreversible deformation leads to a decrease in a recovery strain, then with high stiffness values it also exhibits greater stability. These features of the operation of actuators with different counterbody stiffness can be described using the proposed model.

To determine the efficiency of the actuator, the amount of specific work produced during heating must be estimated. It can be calculated by the equation:

$$A = \frac{\tau^r \gamma^{sm}}{2},$$
(14)

where γ^{sm} is the a recovery strain and τ^r is the stresses developed by the actuator.

The calculation of the influence of the counterbody stiffness on a recovery strain and the stresses developed by the actuator are shown in Figs. 4(a) and 4(b), respectively. It can be seen that a recovery strain decreases with increasing counterbody stiffness, while the stresses developed by the actuator increase. Since the specific work of the actuator is proportional to both of these quantities, the antidirectionality of the dependencies makes the choice of the optimal counterbody stiffness non-obvious. It can also be noted that thermal cycling leads to a decrease in both the recovered strain and the developed stresses regardless of the stiffness of the counterbody. Therefore, it can be concluded that the specific work of the actuator will gradually decrease during the operation of the actuator.
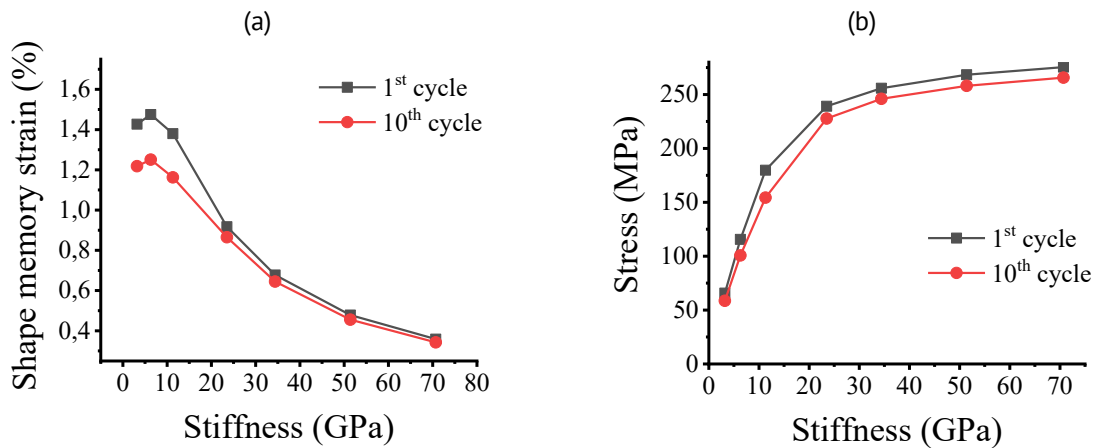
Fig. 4. The dependences of a recovery strain (a) and stresses developed by the actuator (b) on stiffness of counterbody for first and tenth cycle

A series of numerical experiments were carried out to find out the optimum stiffness to obtain the highest specific work. The calculated data presented in Fig. 5(a) qualitatively correspond to similar experimental data [17], which are presented in Fig. 5(b). As can be seen in Fig. 5(a) the specific work of the actuator changes non-monotonically as the stiffness of the counterbody increases. There is an optimal stiffness in the range of 10-15 GPa. As mentioned above changes occurring in the alloy during thermal cycling negatively affect the work produced by the actuator, but they practically do not change the optimum stiffness (see Fig. 5(a)).
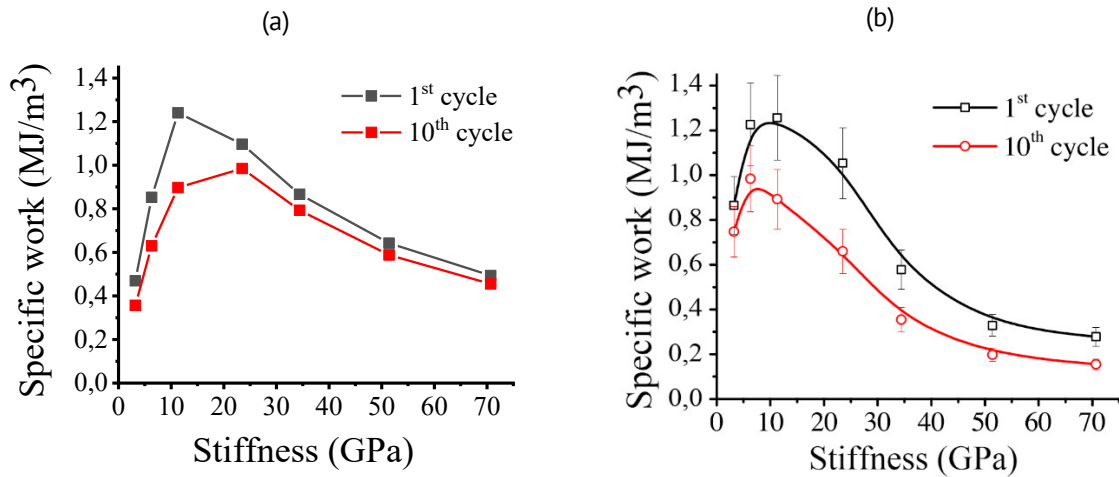
Fig. 5. The dependence of specific work on stiffness of counterbody for first and tenth cycle, simulation (a) and experiment [17] (b)

The existence of a maximum of the work produced is an interesting result and is explained in [17] as follows. The useful work depends on the magnitudes of the recovered strain and the developed stresses, but when the working element is heated during the working stroke, these magnitudes are related. In the absence of counteraction, when the developed stresses equal to zero, the largest recoverable strain is achieved. The highest reactive stresses are achieved under condition of absolutely constraint displacements, i.e. when the recoverable strain is zero. It follows that, in both extreme cases, the work produced by the SMA element is equal to zero. However, in the intermediate cases, there are both recoverable strain and reactive stresses and accordingly the actuator produces positive work. Hence, there is possible to find the optimal combination of developed stresses and recoverable deformations (determined by the stiffness of the counterbody) which provide the maximum work output.

Conclusions

The presented microstructural model is able to quantitatively describe and predict the deformation behavior of SMA under the operating conditions of the thermomechanical actuator. It makes it possible to describe the evolution of the actuator working cycle parameters at multiple actuations and the peculiarities of the working element behavior at different counterbody stiffnesses. Results of numerical experiments are in good agreement with experimental data.

The model allows to calculate the performance of the actuator in the first cycle and after multiple actuations. It also makes it possible to describe the non-monotonic variation of the specific work as a function of the counterbody stiffness and thus can be used to optimize the actuator working cycle.

References

1. Mohd Jani J, Leary M, Subic A, Gibson MA. A review of shape memory alloy research, applications and opportunities. *Materials & Design*. 2014;56: 1078-1113.

2. Butera F, Coda A, Vergani G. Shape memory actuators for automotive applications. In: *Proc. of the Intern. Conf. "Nanotec IT newsletter"*. 2007. p.12–16.

3. Hartl DJ, Lagoudas DC. Aerospace applications of shape memory alloys. *J. of Aerospace Engineering*. 2007;221(4): 535–552.

4. Kheirikhah MM, Rabiee S, Edalat ME. A Review of Shape Memory Alloy Actuators in Robotics. In: Ruiz-del-Solar J, Chown E, Plöger PG. [eds.] *RoboCup 2010: Robot Soccer World Cup XIV. RoboCup 2010. Lecture Notes in Computer Science, Vol. 6556*. Berlin: Springer; 2011. p.206–217.

5. Yadav SK, Bobade RS. Shape Memory Alloy Actuators: A Review. *International Journal for Research in Applied Science and Engineering Technology*. 2019;7(V): 799–802.

6. Gangil N, Siddiquee AN, Maheshwari S. Towards applications, processing and advancements in shape memory alloy and its composites. *Journal of Manufacturing Processes.* 2020;59: 205–222.

7. Liu Q, Ghodrat S, Huisman G, Jansen KMB. Shape memory alloy actuators for haptic wearables: A review. *Materials & Design*. 2023;233: 112264.

8. Hamid QY, Wan Hasan WZ, Azmah Hanim MA, Nuraini AA, Hamidon MN, Ramli HR. Shape memory alloys actuated upper limb devices: A review. *Sensors and Actuators Reports*. 2023;5: 100160.

9. Lu Y, Xie Z, Wang J, Yue H, Wu M, Liu Y. A novel design of a parallel gripper actuated by a large-stroke shape memory alloy actuator. *International Journal of Mechanical Sciences*. 2019;159: 74–80.

10. Xu J, Kimura Y, Tsuji K, Abe K, Shimizu T, Hasegawa H, Mineta T. Fabrication and characterization of SMA film actuator array with bias spring for high-power MEMS tactile display. *Microelectronic Engineering*. 2020;227: 111307.

11. NASA. *NASA tests new alloy to fold wings in flight*. Available from: https://www.nasa.gov/centers/armstrong/feature/nasa-tests-new-alloy-to-fold-wings-in-flight.html

12. Ostropiko ES, Razov AI. Functional properties of TiNi conical workingelements in the holding and release device. *Cybern. Phys.* 2018;7: 216–219.

13. Ostropiko E, Razov A, Cherniavsky A. Investigation of TiNi shape memory alloy for thermosensitive wire drive. *MATEC Web Conf.* 2015;33: 03021.

14. Yang J, Zhang Y, Gu X, Li J, Fang P, Yang X, Wang J, Zhu J, Zhang W. Bi-direction and flexible multi-mode morphing wing based on antagonistic SMA wire actuators. *Chinese Journal of Aeronautics*. 2024;37(12): 373–387.

15. Pei YC, Wang XY, Yao ZY, Wang BH, Liao Z, Lu H. The driving characteristics of bidirectional SMA wire actuators - Theoretical modeling and experimental testing. *Sensors and Actuators A: Physical*. 2024;372: 115328.

16. Priadko AI, Pulnev SA, Nikolaev VI, Rogov AV, Shmakov AO, Golyandin SN, Chikiryaka AV. Investigation of single crystal Cu-Al-Ni alloy bending force elements for linear motors. *Materials Physics and Mechanics*. 2016;29(2): 158–165.

17. Sibirev A, Belyaev S, Resnina N. The influence of counter-body stiffness on working parameters of NiTi actuator. *Sensors and Actuators A: Physical*. 2021;319: 112568.

18. Belyaev S, Resnina N, Zhuravlev R. Deformation of Ti-51.5 at.%Ni alloy during thermal cycling under different thermal-mechanical conditions. *Journal of Alloys and Compounds*. 2013;577: S232–S236.

19. Furuya Y, Park YC. Thermal cyclic deformation and degradation of shape memory effect in Ti-Ni alloy. *Nondestructive Testing and Evaluation*. 1992;8–9(1–6): 541–554.

20. Hamilton RF, Sehitoglu H, Efstathiou C, Maier HJ. Mechanical response of NiFeGa alloys containing second-phase particles. *Scripta Materialia*. 2007;57: 497–499.

21. Morgan NB, Friend CM. A review of shape memory stability in NiTi alloys. *J. Phys. IV France.* 2001;11(PR8): Pr8-325-Pr8-332.

22. Sehitoglu H, Wu Y, Patriarca L. Shape memory functionality under multi-cycles in NiTiHf. *Scripta Materialia*. 2017;129: 11–15.

23. Averkin AI, Yakushev PN, Trofimova EV, Zograf GP, Timashov RB, Pulnev SA, Kustov SB, Nikolaev VI. Shape memory deformation recovery features in Cu-Al-Ni single crystals. *Materials Physics and Mechanics.* 2015;22(1): 64–68. (In Russian)

24. Jani JM, Huang S, Leary M, Subic A. Numerical modeling of shape memory alloy linear actuator. *Comput Mech.* 2015;56: 443–461.

25. Chemisky Y, Duval A, Patoor E, Ben Zineb T. Constitutive model for shape memory alloys including phase transformation, martensitic reorientation and twins accommodation. *Mechanics of Materials.* 2011;43(7): 361–376.

26. Yu C, Kang G, Song D, Kan Q. Effect of martensite reorientation and reorientation-induced plasticity on multiaxial transformation ratchetting of super-elastic NiTi shape memory alloy: New consideration in constitutive model. *International Journal of Plasticity.* 2015;67: 69–101.

27. Song D, Yu C, Zhang C, Kang G. Superelasticity degradation of NiTi shape memory alloy in wide ranges of temperature and loading level: Experimental observation and micromechanical constitutive model. *International Journal of Plasticity*, 2023;161: 103487.

28. Belyaev FS, Volkov AE, Evard ME. Microstructural modeling of fatigue fracture of shape memory alloys at thermomechanical cyclic loading. *AIP Conference Proceedings.* 2018;1959: 070003.

29. Belyaev FS, Evard ME, Volkov AE. Simulation of the plastic deformation of shape memory alloys considering shear anisotropy on the slip plane. *Materials Physics and Mechanics.* 2023;51(1): 61–67.

30. Resnina NN, Ivanov AM, Belyaev FS, Volkov AE, Belyaev SP. Simulation of recoverable strain variation during isothermal holding of the Ni51Ti49 alloy under various regimes. *Letters on Materials.* 2023;13(1): 33–38.

31. Volkov AE, Belyaev FS, Volkova NA, Vukolov EA, Evard ME, Rebrov TV. The effect of martensite stabilization in titanium nickelide after various methods of pre-deformation: simulation with a single set of constants. *Materials Physics and Mechanics*. 2024;52(4): 91–99.

32. Belyaev FS, Volkov AE, Vukolov EA, Evard ME, Kudrina KV, Starodubova MS. Influence of latent heat and heat exchange conditions on tension behavior of shape memory alloy specimen. *Materials Physics and Mechanics.* 2024;52(5): 18–28.

33. Belyaev FS, Volkov AE, Evard ME, Volkova NA. A Microstructural model of SMA with Microplastic Deformation and Defects Accumulation: Application to Thermocyclic Loading. *Materials Today: Proceedings.* 2015;2(3): S583–S587.

34. Volkov AE, Belyaev FS, Evard ME, Volkova NA. Model of the Evolution of Deformation Defects and Irreversible Strain at Thermal Cycling of Stressed TiNi Alloy Specimen. *MATEC Web of Conferences.* 2015;33: 03013.

About Authors

Fedor S. Belyaev 🆔 Sc
Candidate of Physical and Mathematical Sciences
Senior Researcher (Saint Petersburg State University, St. Petersburg, Russia); Senior Researcher (Institute for Problems in Mechanical Engineering of the Russian Academy of Sciences, St. Petersburg, Russia)

Aleksandr E. Volkov 🆔 Sc
Doctor of Physical and Mathematical Sciences
Professor (Saint Petersburg State University, St. Petersburg, Russia)

Daniil F. Gorbachenko
Student (St. Petersburg State University, St. Petersburg, Russia)

Margarita E. Evard 🆔 Sc
Candidate of Physical and Mathematical Sciences
Associate Professor (Saint Petersburg State University, St. Petersburg, Russia)

Effect of Ti reinforcement on the thermal behaviour of AZ91/Ti composites

N. Kumar[1] ✉ iD, A. Bharti [2] iD, A. Rony[1] iD, R.A. Kapgate[1] iD

[1] Sanjivani College of Engineering, Kopargaon, India

[2] Motilal Nehru National Institute of Technology Allahabad, Prayagraj, India

✉ kumarnaveenmkcoe@sanjivani.org.in

ABSTRACT
Despite magnesium's high strength-to-weight ratio and eco-friendly nature, its limited industrial applications due to low corrosion and wear resistance have prompted extensive research into enhancing these properties. Magnesium matrix composites have been developed with various reinforcements, including B_4C, SiC, carbon nanotubes, graphite, and titanium (Ti). Among these, Ti is particularly promising as it improves wear resistance while preserving mechanical strength and ductility. In this study, the influence of Ti volume fraction on the thermal properties of AZ91/Ti composites fabricated via powder metallurgy is explored. Results revealed a reduction in thermal conductivity up to 6 % Ti content (6 W/m·K), attributed to Ti's lower thermal conductivity compared to magnesium. However, the Mg + 8% Ti composite exhibited enhanced thermal conductivity (10.51 W/m·K), but mechanical properties degraded. After analysis of physical, mechanical, and thermal tests, it is concluded that 6 % Ti volume fraction is the optimum choice for balancing mechanical performance in Mg/Ti composites. This research contributes valuable insights for tailoring Mg/Ti composites to specific engineering needs, offering a potential solution to the challenge of wear resistance in magnesium-based materials.
KEYWORDS
AZ91 Mg alloy • powder metallurgy • titanium • composites • thermal conductivity • thermal diffusivity

Introduction

Magnesium has garnered significant attention across various industries owing to its remarkable attributes, notably its high strength-to-weight ratio, surpassing that of other common metallic structural materials such as aluminum, copper, and iron [1–3]. Furthermore, magnesium is hailed for its eco-friendly nature. However, despite its commendable low density and high biocompatibility, the widespread industrial applications of magnesium remain limited due to its inherent shortcomings, primarily its low resistance to corrosion and wear [4,5]. To address this limitation, researchers worldwide have diligently focused on the development of magnesium matrix composites with superior corrosion and wear resistance [6,7].

Magnesium alloys were chosen over aluminum or copper alloys for their superior strength-to-weight ratio and specific properties crucial for wear and strength applications, including lightweight design, corrosion resistance, and mechanical performance. These characteristics align with the specific requirements of electronic devices applications such as laptop and mobile body.

To enhance the wear resistance of magnesium, ceramic and carbonaceous reinforcements have been employed, which have indeed shown promising results [8,9]. However, the introduction of ceramic reinforcements, while bolstering wear resistance, is often accompanied by a reduction in toughness and thermal conductivity [10,11]. On the other hand, the addition of carbonaceous reinforcements enhances strength and wear resistance, but agglomeration issues and thermal concerns persist [12,13]. To surmount these challenges, the introduction of metallic reinforcements, specifically aluminum (Al) and titanium (Ti), into the magnesium matrix has become a focal point for researchers [14−16]. These metallic reinforcements not only augment strength and wear resistance but also provide enhanced ductility and improved thermal conductivity [17−20].

The present research endeavors to delve into the impact of Ti reinforcement on the thermal behavior of AZ91/Ti composites, which have been meticulously fabricated using the powder metallurgy technique [21−24]. This method was chosen over alternative composite fabrication techniques due to its advantageous features, including high material utilization, minimal scrap generation, and reduced machining requirements [25−28]. In the context of the growing concern regarding heat dissipation in electronic devices, this study aims to shed light on the potential of AZ91/Ti composites to address this issue effectively, further enhancing the overall functionality of electronic devices.

Materials and Methods

In this study, two crucial materials played a pivotal role in the creation of composite materials tailored for electronic device applications. The matrix material selected was magnesium alloy AZ91, which was acquired in powder form from Parshwamani Metals, located in Mumbai, India. This magnesium powder, characterized by irregular particle shapes, exhibited an average particle size of approximately 50 μm. The supplier indicated a purity level of about 99 % for the magnesium powder. Additionally, titanium (Ti) was chosen as the reinforcing material, and this too was sourced in powdered form from the same supplier. The titanium powder displayed similar irregular particle morphology, albeit with a slightly smaller average particle size of about 30 μm and was also reported to maintain an impressive purity level of around 99 %, as provided by the supplier.

The rationale behind the selection of titanium as the reinforcement material is grounded in the advantageous properties it brings to the composite. Notably, titanium possesses exceptionally low solid solubility when combined with magnesium. This attribute is particularly advantageous since it precludes the formation of tertiary hard phases within the composite. Significantly, the inclusion of titanium in the composite is geared towards a substantial enhancement of its strength, a critical factor for electronic device applications such as laptop and mobile body. Equally important is the fact that while increasing the strength of the composite, the introduction of titanium does not compromise the material's ductility. This pivotal characteristic ensures that the composite retains its ability to deform plastically without fracturing under load, which is essential in the context of electronic device applications. Considering the specific challenges and demands associated with electronic devices, the judicious selection of magnesium alloy AZ91 as the matrix material and titanium as the reinforcing component forms the cornerstone of this research. The aim is to create composite materials that not

only possess enhanced strength but also exhibit superior thermal characteristics, well-aligned with the requirements for effective heat management in electronic devices.
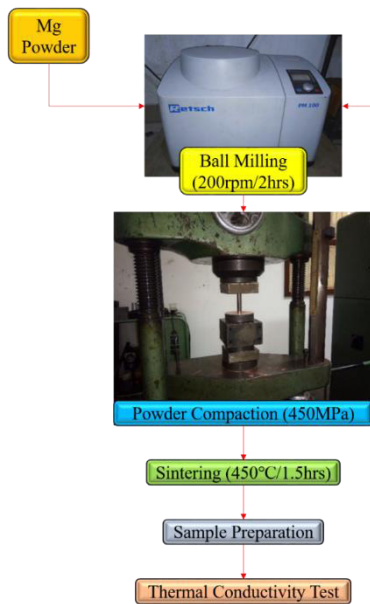
Fig. 1. Flow diagram of powder metallurgy process
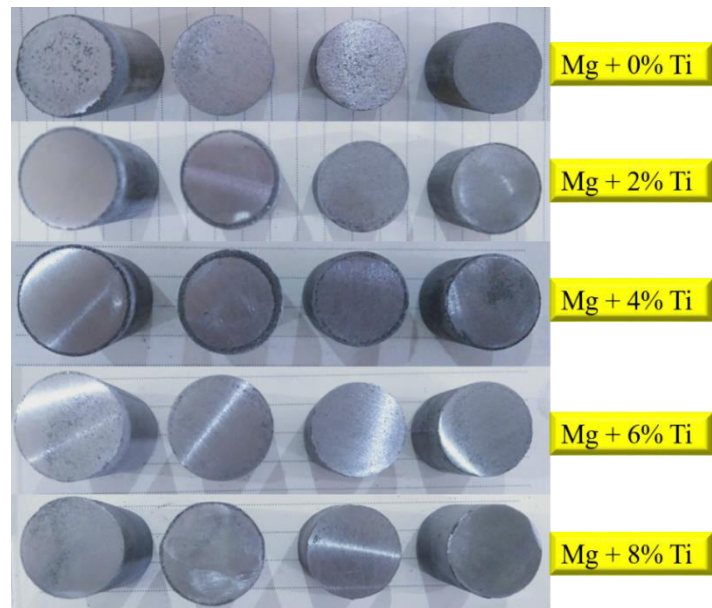
Fig. 2. A photograph of sintered Mg alloy and Mg/Ti composites

The fabrication of Mg/Ti composites was carried out via a well-structured powder metallurgy technique, as outlined in Fig. 1 [29–32]. To investigate the influence of varying volume fractions of matrix and reinforcement materials, five distinct sample types were meticulously prepared, as detailed in Table 1. The selection of the volume percentage of titanium was based on established findings in the existing literature.

Table 1. Sample specifications

Sample	Composition
Mg	100 vol.% Mg + 0 vol.% Ti
Mg + 2% Ti	98 vol.% Mg + 2 vol.% Ti
Mg + 4% Ti	96 vol.% Mg + 4 vol.% Ti
Mg + 6% Ti	94 vol.% Mg + 6 vol.% Ti
Mg + 8% Ti	92 vol.% Mg + 8 vol.% Ti

The production process commenced by accurately weighing the requisite quantities of the purchased matrix material (Mg) and reinforcement material (Ti) powders based on the predetermined volume fractions. This weighing was executed with precision using an electronic weighing balance. Subsequently, the meticulously weighed powders were combined and subjected to mechanical blending in a planetary ball milling machine. This milling process operated at 200 revolutions per min (rpm) for a duration of 2 h, maintaining a ball-to-powder weight ratio of 10:1.

Following the completion of the ball milling step, the blended powders were further processed. They were compacted under a uniaxial split-die configuration using a universal testing machine, applying a compaction pressure of 450 MPa. The outcome of

this compaction step was the production of green compacts, serving as the initial stage of the composite material.

Subsequently, the green compacts underwent sintering within a muffle furnace, executed under a controlled nitrogen environment. The sintering process was conducted at a temperature of 450 °C, with a sintering duration of 90 min. Fig. 2 provides a visual representation of the sintered samples.

After the completion of the sintering process, the samples were allowed to cool in the furnace to reach room temperature. Once cooled, thermal conductivity test samples were precisely cut from the sintered compacts using wire-cut electrical discharge machining (EDM). This systematic methodology was rigorously applied to ensure the consistent and precise production of Mg/Ti composites for subsequent analysis and testing.

In light of the paramount importance of high thermal conductivity in materials employed for applications such as braking systems, electronic devices, and automotive components, comprehensive thermal conductivity assessments were conducted on all five distinct sample types. These tests were executed at the Mechanical Engineering Department of the esteemed Indian Institute of Technology, Kanpur.

The thermal conductivity tests were meticulously conducted using a Thermal Constants Analyzer, specifically the TPS 500 model, incorporating a hot disc apparatus. This analytical approach operates on the fundamental principle of the Transient Plane Method.

With a focus on precision and reliability, these tests were instrumental in quantifying the thermal conductive properties of the composite materials. This information is vital for understanding how effectively these composites can dissipate heat, which holds critical implications for their suitability in applications like braking systems and electronic gadgets.

The results and in-depth discussions stemming from the thermal conductivity testing are elaborated upon in the subsequent section. These findings provide valuable insights into the thermal behavior of the Mg/Ti composites, shedding light on their potential for enhancing heat dissipation rates in applications demanding efficient thermal management.

To identify the various phases, present within both the crystalline powders and the prepared composites, X-ray diffraction (XRD) examinations were conducted. These analyses were performed utilizing a high-precision X-ray diffractometer, specifically the Rigaku MiniFlex 600, which is available at the Applied Sciences Department of the Indian Institute of Information Technology, Allahabad, India.

The XRD measurements were carried out under controlled conditions to ensure accuracy. The scan speed was set at 0.2 sec per step, with a step size of 0.01°, and the scan range encompassed an angular range from 10 to 80°. An operating voltage of 40 kV was employed to facilitate the analysis.

This XRD analysis is fundamental in characterizing the structural composition of the materials under investigation, enabling the identification of distinct phases and crystalline structures present in both the raw powders and the composite materials. The results derived from this examination serve as a critical foundation for understanding the material's properties and its potential performance in various applications.

Results and Discussion

The XRD patterns of all five sintered samples are vividly depicted in Fig. 3, offering a detailed examination of the structural composition of the Mg/Ti composites and revealing crucial phase transitions.
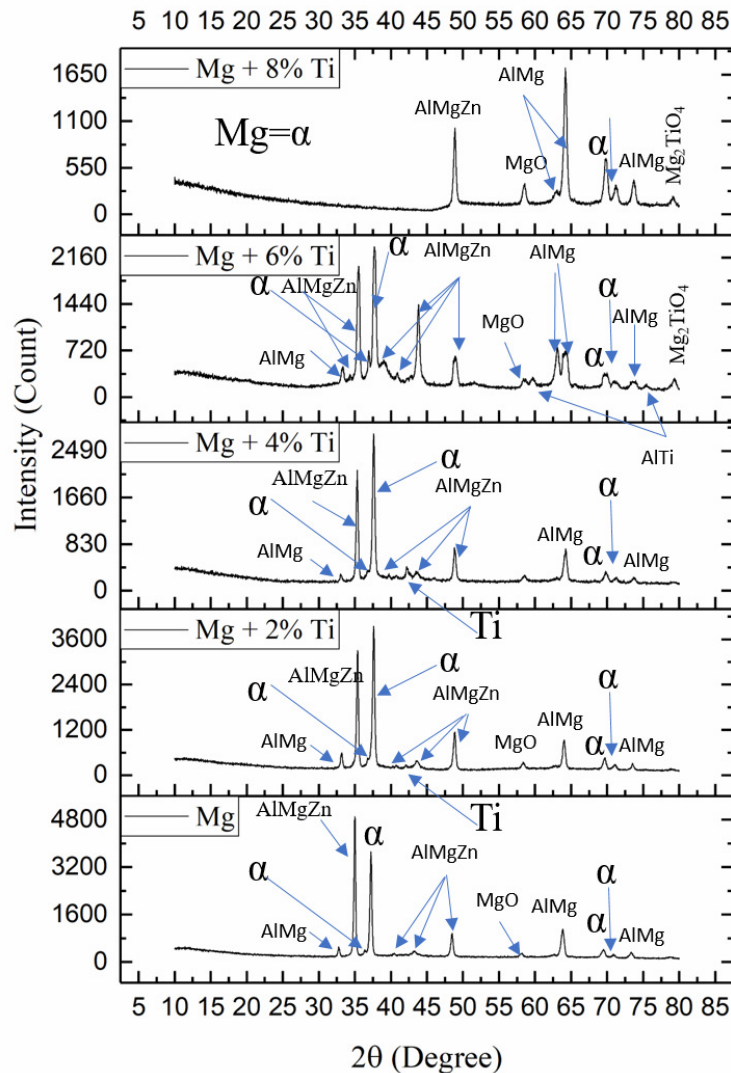
Fig. 3. The matched XRD patterns of sintered Mg alloy and Mg/Ti composites

An intriguing observation is the consistent reduction in the intensity of the highest peak as the titanium (Ti) content increases. This decrease in intensity is attributed to the concurrent emergence of secondary phases within the composites, indicative of complex structural transformations.

Remarkably, the presence of magnesium oxide (MgO) was common across all samples (composites and unreinforced magnesium samples). This observation indicates that an oxidation process occurred during the sintering phase, impacting the material's structural composition.

Notably, the XRD pattern of the Mg/8%Ti composite exhibits distinct characteristics, setting it apart from the other composite samples. It portrays a unique structural

arrangement, possibly due to reaction of Mg with Ti in the presence of oxygen. Reaction initiated after 6 vol. % of Ti and its effect was notable in case of 8 vol. % Ti sample.

The presence of free titanium (Ti) in all Mg/Ti composites, except Mg/8%Ti, signifies that Ti remained unreacted with the magnesium matrix. This unreacted Ti is evident through the distinctive XRD patterns. In case of Mg/8%Ti, Mg reacted with titanium and oxygen to form complex. Kumar et al. [29] have studied the effect of Ti volume fraction on the physical and mechanical properties of Mg/Ti composites. Ti and other phases are shown in optical micrographs.

Moreover, the $MgTiO_4$ phase was identified, which was confirmed during the X'Pert HighScore peak matching exercise. This finding signifies a chemical reaction between Ti and Mg, resulting in the formation of the $MgTiO_4$ phase. This reaction led to the dissolution of the high-intensity magnesium peak and the emergence of novel phases.

Furthermore, as the Ti volume fraction exceeded 6 %, the intensity of the AlMg phase, located within the 2θ range of 63-65°, significantly increased. This increase was coupled with the dissolution of other high-intensity peaks within the 30 to 45° range. Additionally, peak shifting was observed, reflecting heightened lattice strain as the Ti volume fraction increased.
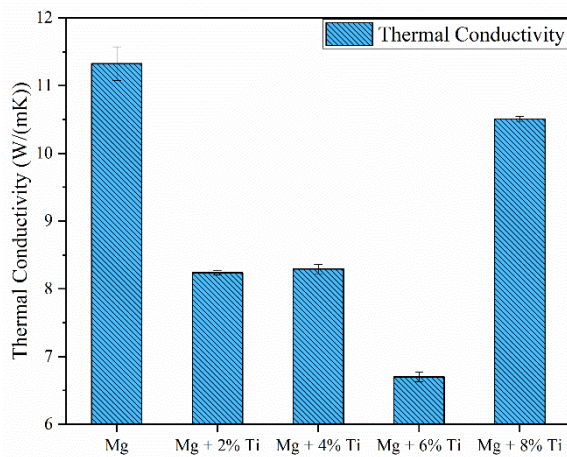
Fig. 4. Variation in thermal conductivity of Mg/Ti composites with increase in Ti volume fraction
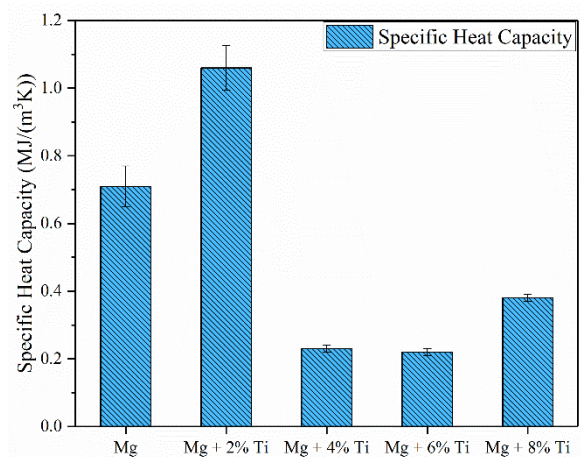
Fig. 5. Variation in specific heat capacity of Mg/Ti composites with increase in Ti volume fraction
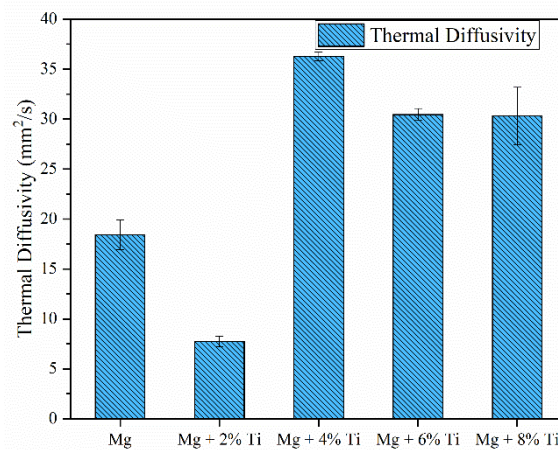
Fig. 6. Variation in thermal diffusivity of Mg/Ti composites with increase in Ti volume fraction

The thermal conductivity data, as depicted in Fig. 4, provides valuable insights into the influence of varying titanium (Ti) content on the thermal behavior of the Mg/Ti composites. Notable trends in the results can be elucidated to better understand the observed variations.

The initial phase of the thermal conductivity evaluation reveals a consistent reduction as the volume fraction of titanium within the composite increases. This decrease in thermal conductivity is particularly pronounced up to 6 vol. % Ti. The underlying mechanism behind this decline can be attributed to the distinct thermal conductivities of the constituent materials. Magnesium exhibits a relatively high thermal conductivity, approximately 72 W/m·K, while titanium, in contrast, has a substantially lower thermal conductivity of around 17 W/m·K [23]. Consequently, the introduction of titanium, especially in minor quantities, serves as a diluent within the composite, effectively lowering the overall thermal conductivity. This behavior stems from the dominant influence of the lower thermal conductivity of titanium.

However, an intriguing departure from this initial trend is observed when the Mg/Ti composite is reinforced with 8 vol. % Ti. Here, the thermal conductivity of the composite surpasses that of the Mg/Ti composite reinforced with 6 vol. % Ti. This unanticipated upturn in thermal conductivity can be attributed to complex changes occurring within the composite [17]. The X-ray diffraction (XRD) patterns provide crucial insights, indicating the dissolution of primary phases in magnesium and the emergence of new phases. These structural transformations likely contribute to the altered thermal properties, resulting in an increase in thermal conductivity. The formation of these new phases may possess thermal conductivities that differ from the original constituents, thereby influencing the composite's overall thermal behavior.

The presented data in Fig. 5 illustrates the variation in specific heat capacity with increasing titanium (Ti) volume fraction within the Mg/Ti composites. The results reveal certain noteworthy aspects that require elucidation.

One apparent observation is the significant variability in the specific heat capacity values as the Ti volume fraction increases. This substantial variation can be primarily attributed to the presence of uneven porosity within the samples (Kumar et al. [29] have studied the effect of Ti volume fraction on the density and porosity of Mg/Ti composites). The uneven distribution of porosity can significantly affect the heat capacity measurements, leading to inconsistent results.

From a theoretical perspective, it is anticipated that the specific heat capacity should exhibit an increasing trend with a rise in Ti volume fraction. This expectation is grounded in the fundamental properties of the constituent materials. Titanium (Ti) is known to possess a higher heat capacity (approximately 2.34 MJ/m³K) compared to that of magnesium (about 1.9 MJ/m³K) [21]. Therefore, as the volume fraction of Ti increases, it should theoretically contribute to a higher heat capacity in the composite material.

However, the observed fluctuations in specific heat capacity suggest that factors such as uneven porosity, sample heterogeneity, or other structural complexities might be influencing the results. Further investigations and potentially refined sample preparation techniques may be necessary to provide more consistent and reliable specific heat capacity data within the Mg/Ti composites.

The examination of thermal diffusivity, as delineated in Fig. 6, provides crucial insights into the material's ability to conduct and store heat as the titanium (Ti) volume fraction within the Mg/Ti composites increases. This variation can be better comprehended by considering the influence of thermal conductivity and specific heat capacity, which were discussed earlier.

It is essential to remember that thermal diffusivity encapsulates the rate at which heat can propagate through a material, contingent upon the interplay of thermal conductivity, density, and specific heat capacity. Generally, a higher thermal conductivity facilitates more efficient heat transfer, while greater specific heat capacity indicates the material's capacity to retain thermal energy.

The conspicuous, abrupt variation in thermal diffusivity as Ti content increases can be delineated through the prism of thermal conductivity and specific heat capacity. With the augmentation of Ti content, specifically from pure Mg to Mg + 2% Ti, a substantial reduction in thermal diffusivity is evident. This initial decrease can be attributed to the lower thermal conductivity of titanium, as discussed earlier. The inclusion of Ti acts as a diluent in the composite, impeding the efficient transmission of heat.

Progressing from Mg + 2% Ti to Mg + 4% Ti, there is a noteworthy upturn in thermal diffusivity. This transition likely stems from complex factors, such as evolving microstructure and alterations in thermal properties induced by the introduction of Ti. As a result, heat is able to propagate more effectively within the composite, resulting in higher thermal diffusivity.

From Mg + 4% Ti to Mg + 8% Ti, the thermal diffusivity displays a relatively stable pattern. This constancy indicates that the material's composition and structural characteristics stabilize as the Ti content reaches higher percentages. In this range, the materials exhibit consistent heat propagation characteristics.

Conclusions

In this study, Mg/Ti composites were successfully fabricated and analyzed to investigate the effect of Ti reinforcement on thermal behavior. Key findings and implications include:
1. Insights gained from the fabrication and investigation of Mg/Ti composites provide valuable understanding of their thermal behavior.
2. A consistent reduction in thermal conductivity was observed with increasing Ti content up to 6%, attributed to the lower thermal conductivity of titanium compared to magnesium.
3. The Mg/8%Ti composite exhibited enhanced thermal conductivity due to the dissolution of primary phases and formation of new phases, as confirmed by XRD patterns.
4. The observed trade-off between improved thermal properties and compromised mechanical characteristics emphasizes the importance of balancing material composition.
5. These findings highlight the potential for tailoring the heat transfer properties of Mg/Ti composites to meet specific engineering requirements.
6. This research contributes to advancing the understanding and application of Mg/Ti composites in various engineering and technological contexts.

References

1. Musfirah AH, Jaharah AG. Magnesium and Aluminum Alloys in Automotive Industry. *Journal of Applied Sciences Research.* 2012;8(9): 4865–4875.

2. Blawert C, Hort N, Kainer KU. Automotive applications of Magnesium and its alloys. *Indian Inst Met.* 2004;57(4): 397–408.

3. Gunes I, Uygunoglu T, Erdogan M. Effect of Sintering Duration on Some Properties of Pure Magnesium. *Powder Metall Met Ceram.* 2015;54: 156–165.

4. Kulekci MK. Magnesium and its alloys applications in automotive industry. *Int J Adv Manuf Technol.* 2008;39: 851–865.

5. Cai H, Guo F. Study on microstructure and strengthening mechanism of AZ91-Y magnesium alloy. *Materials Research Express.* 2018;5(3): 036501.

6. Kandpal BC. Production Technologies of Metal Matrix: A review. *International Journal of Research in Mechanical Engineering & Technology.* 2014;4(2): 27–32.

7. Nie KB, Wang XJ, Hu XS, Xu L, Wu K. Microstructure and tensile properties of micro-SiC particles reinforced magnesium matrix composites produced by semisolid stirring assisted ultrasonic vibration. *Materials Science and Engineering A.* 2011;528(29-30): 8709–8714.

8. Goh CS, Wei J, Lee LC, Gupta M. Development of novel carbon nanotube reinforced magnesium nanocomposites using the powder metallurgy technique. *Nanotechnology.* 2006;17(1): 7–12.

9. Kumar N, Bharti A, Tripathi H. Investigation of Microstructural and Mechanical Properties of Magnesium Matrix Hybrid Composite. In: Biswal B, Sarkar B, Mahanta P. (eds) *Advances in Mechanical Engineering.* Springer: Singapore; 2020. p.661–669.

10. Wang HY, Jiang QC, Wang Y, Ma BX, Zhao F. Fabrication of TiB 2 particulate reinforced magnesium matrix composites by powder metallurgy. *Materials Letters.* 2004;58(37–28): 3509–3513.

11. Guleryuz LF, Ozan S, Uzunsoy D, Ipek R. An Investigation of The Microstructure and Mechanical Properties of B4C Reinforced PM Magnesium Matrix Composites. *Powder Metallurgy and Metal Ceramics.* 2012;51: 456–462.

12. Ghasali E, Alizadeh M, Niazmand M, Ebadzadeh T. Fabrication of magnesium-boron carbide metal matrix composite by powder metallurgy route: Comparison between microwave and spark plasma sintering. *Journal of Alloys and Compounds.* 2016;697: 200–207.

13. Kumar D, Bharti A, Azam SM, Kumar N, Tripathi H. Investigations of Mechanical Properties of Copper Matrix Hybrid Composite. In: Biswal B, Sarkar B, Mahanta P. (eds) *Advances in Mechanical Engineering.* Singapore: Springer; 2020. p. 671–676.

14. Yu H, Zhou H, Sun Y. Microstructures and mechanical properties of ultrafine-grained Ti/AZ31 magnesium matrix composite prepared by powder metallurgy. *Advanced Powder Technology.* 2018;29(12): 3241–3249.

15. Kumar N, Bharti A, Saxena KK. A re-investigation: Effect of powder metallurgy parameters on the physical and mechanical properties of aluminium matrix composites. *Materials Today: Proceedings.* 2021;44: 2188–2193.

16. Kumar N, Bharti A, Dixit M, Nigam A. Effect of Powder Metallurgy Process and its Parameters on the Mechanical and Electrical Properties of Copper-Based Materials: Literature Review. *Powder Metallurgy and Metal Ceramics.* 2020;59: 401–410.

17. Rajesh S, Rajakarunakaran S, Pandian RS. Modeling and Optimization of Sliding Specific Wear and Coefficient of Friction of Aluminum Based Red Mud Metal Matrix Composite Using Taguchi Method and Response Surface Methodology. *Materials Physics and Mechanics.* 2012;15(2): 150–166.

18. Soleymani S, Abdollah-Zadeh A, Alidokht SA. Microstructural and Tribological Properties of Ultra Fine Grained Hybrid Composite Produced by Friction Stir Processing. *Materials Physics and Mechanics.* 2013;17(1): 6–10.

19. Shanmughasundaram P. Statistical Analysis on Influence of Heat Treatment, Load and Velocity on the Dry Sliding Wear Behavior of Aluminium Alloy 7075. *Materials Physics and Mechanics.* 2015;22(2): 118–124.

20. Li X, Ma G, Jin P, Zhao L, Wang J, Li S. Microstructure and mechanical properties of the ultra-fine grained ZK60 reinforced with low content of nano-diamond by powder metallurgy. *Journal of Alloys and Compounds.* 2019;778: 309–317.

21. Selvamani ST, Premkumar S, Vigneshwar M, Hariprasath P, Palanikumar K. Influence of carbon nanotubes on mechanical, metallurgical and tribological behavior of magnesium nanocomposites. *Journal of Magnesium and Alloys.* 2017;5(3): 326–335.

22. Turan ME, Sun Y, Akgul Y, Turen Y, Ahlatci H. The effect of GNPs on wear and corrosion behaviors of pure magnesium. *Journal of Alloys and Compounds.* 2017;724: 14–23.

23. Mahallawy NA. AZ91 Magnesium Alloys: Anodizing using Environmental Friendly Electrolytes. *Journal of Surface Engineered Materials and Advanced Technology.* 2011;1: 62–72.

24. Bolzoni L, Navas EMR, Gordo E. Quantifying the properties of low-cost powder metallurgy titanium alloys. *Materials Science and Engineering A.* 2017;687: 47–53.

25. Burke P, Kipouros GJ. Development of Magnesium Powder Metallurgy AZ31 Alloy Using Commercially Available Powders. *High Temp. Mater. Proc.* 2011;30(1–2): 51–61.

26. Yusoff M, Hussain Z. Effect of Compaction Pressure on Microstructure and Properties of Copper-based Composite Prepared by Mechanical Alloying and Powder Metallurgy. *Advanced Materials Research.* 2013;795: 343–346.

27. Yu C, Cao P, Jones MI. Titanium Powder Sintering in a Graphite Furnace and Mechanical Properties of Sintered Parts. *Metals.* 2017;7(2): 67.

28. Rajadurai M, Annamalai AR. Effect of Various Sintering Methods on Microstructures and Mechanical Properties of Titanium and Its Alloy (Ti–Al–V–X): A Review. *Russian Journal of Non-Ferrous Metals.* 2017;58: 434–448.

29. Kumar N., Bharti A., Saxena K.K. Effect of Ti Reinforcement on the Physical and Mechanical Properties of AZ91/Ti Composites. *Indian Journal of Engineering and Materials Sciences.* 2021;28: 602–607.

30. Kumar N., Bharti A., Chauhan A.K. Effect of Ti Reinforcement on the Wear Behaviour of AZ91/Ti Composites Fabricated by Powder Metallurgy. *Materials Physics and Mechanics.* 2021;47: 600–607.

31. Kumar N., Bharti A. Optimization of powder metallurgy process parameters to enhance the mechanical properties of AZ91 magnesium alloy. *Materials Physics and Mechanics.* 2022;48(3): 315–327.

32. Kumar N., Bharti A. Optimization of powder metallurgy process parameters to recycle AZ91 magnesium alloy. *Materials Physics and Mechanics.* 2021;47(6): 968–977.

About Authors

Naveen Kumar 🆔 Sc

PhD, Assistant Professor (Sanjivani College of Engineering, Kopargaon, India)

Ajaya Bharti 🆔 Sc

PhD, Associate Professor (Motilal Nehru National Institute of Technology Allahabad, Prayagraj, India)

Aiswarya Rony 🆔

M. Tech, Assistant Professor (Sanjivani College of Engineering, Kopargaon, India)

Rajendrakumar Kapgate 🆔

PhD, Assistant Professor (Sanjivani College of Engineering, Kopargaon, India)

Study on n-TiB₂ particulates reinforced Al7075 nano composite for soil nail applications: mechanical, wear, and fracture characterizations

M. Gangadharappa [1] ✉, **H.R. Geetha** [2], **N.K. Manjunath** [3], **G.L. Umesh** [4],

M.M. Shivakumar [3] (iD)

[1] Visvesvaraya Technological University, Belagavi, Karnataka, India

[2] KR Pet Krishna Government Engineering College, KR Pet, Karnataka, India

[3] BMS College of Engineering, Bengaluru, Karnataka, India

[4] Bangalore Institute of Technology, Bengaluru, Karnataka, India

✉ gangahitu2011@gmail.com

ABSTRACT

Stir casting was used to produce Al7075/n-TiB₂ composites with three distinct n-TiB₂ weight percentages: 1, 1.5, 2 and 2.5 %. The mechanical and tribological characteristics of Al7075/n-TiB₂ composites have been investigated in dry sliding situations. Evenly distributed dispersion of n-TiB₂ particulates and the strong interfacial interaction among the matrix as well as reinforcement are confirmed by the microstructural characterization. Composites with 1, 1.5, 2 and 2.5 % reinforced n-TiB₂ show the better mechanical properties when compared to base alloy. Fracture research revealed that n-TiB₂ reinforced aluminum matrix composites and non-reinforced aluminum alloy exhibited ductile expression in the form of dimples. Dry sliding wear assessments have been performed using pin-on-disc instruments. We measured the wear loss of the nano composites and found that the cumulative wear loss variation with n-TiB₂ is linear for each composite. According to the SEM examination of worn-out surfaces, oxidative wear is responsible for specimens that fall within the prescribed stress and sliding distance. The experiment demonstrates that wear loss decreases linearly with an increase in the weight percentage of titanium diboride nanoparticles. The obtained results show that the fabricated nano composites exhibit improved hardness of 14 %, tensile strength of 9 % and wear resistance of 20 % when compared to the base alloy.

KEYWORDS

Al7075 • n-TiB2 • microstructure • mechanical properties • wear behavior • fracture surface

Introduction

Aluminum alloys are becoming more and more popular for structural applications, especially in the automotive and aerospace industries, due to their high specific power, low density, high conductivity, and high strength to weight ratio, all of which have a positive economic impact [1]. Metal matrix composites with an aluminum basis are

commonly utilized due to their high modulus, strength-to-weight ratio, stiffness, corrosion resistance, and wear resistance. These composites have superior mechanical characteristics than conventional metals and alloys [2]. Frequently utilized ceramics for reinforcement include of SiC, TiC, Al_2O_3, and B_4C. These can be utilized as long fibers, tiny whiskers, irregular or irregular, or as particles [3]. Liquid composites are used to create aluminum metal matrix composites (AMMCs). Due to its unique features, TiB_2 stands out when compared to ordinary ceramic reinforcements due to its higher thermodynamic stability, higher hardness, and low density. Due to its many advantages over the ex-situ process, researchers have been concentrating on the development of aluminum-TiB_2 in situ composites with metal matrix in recent years. Better in-situ production of Al alloys is made possible by the exothermic reaction and increased wettability of TiB_2 with aluminum, which results in a better interface bonding and less variation in the thermophysical features of the two during heating. Ceramics with poor wettability have higher porosity, bad mechanical characteristics, and uneven dispersion [4]. Researcher [5] studied Cu-Sn alloy with 7.5 wt. % of Si_3N_4 particles reinforced composites fabricated by using conventional stir casting method. It is stated that Cu-Sn alloy with 7.5 wt. % of silicon nitride particles reinforced composites showed lesser densities as compared to the base Cu-Sn alloy. The wear resistance of Cu-Sn alloy increased with the incorporation of Si_3N_4 particles. Several investigations into the mechanical properties and strengthening techniques of TiB_2/A356 composites have been conducted; the results indicate significant improvements in tensile strength [6]. Al7475 alloy was used to make composites with 2, 4, 6, 8 and 10 wt. % of B_4C particles. By incorporating particles into the matrix, the density of Al alloy composites was lowered. Al7475 alloy with B_4C composites exhibited superior tensile properties at room and elevated temperatures as compared to the base alloy [7]. Researcher [8] studied effect of nanosized Al_2O_3 and Al_2O_3-SiC on mechanical, wears and fracture surface of Al7075 composites for soil anchoring applications. It was concluded that, in contrast to Al7075 alloy, hybrid MMCs enhanced tensile strength and superior hardness. The obtained results indicate that highest hardness of 78 VHN and tensile strength of 126 MPa were achieved for developed hybrid composites. According to Zulkamal et al. [9], the semi-solid A356 alloy's wear resistance was enhanced, and its microstructure was rectified with the inclusion of TiB_2 particles. Low cycle fatigue studies on in-situ TiB_2/A356 composites were carried out by Deepak et al. [10], who discovered that TiB_2 particles significantly affected the composites' hardness, tensile strength, structure, and fatigue life. The microstructure, type of reinforcement, percentage of interfacial bonding, average load, sliding distance, and sliding-speed are the main factors influencing the mechanical and tribological characteristics of composites. Among all these characteristics, particle size has a favorable impact on the composites' performance. According to literature survey, a large number of researchers have studied various grades of aluminum, but comparatively few have studied the impact of n-TiB_2 wt. % on Al7075 alloy. The novelty of the research is to investigate the mechanical and wear properties of newly developed n-TiB_2 reinforced Al7075 composites and analyze the surface morphology. Overall, the results showed that Al composites reinforced with nanosized TiB_2 particles could be good materials where wear-resistant and high-strength components are crucial, especially in the civil-structures, aerospace, and automotive engineering industries.

Materials and Methods

Stir casting produced a homogeneous distribution, which improved the characteristics of aluminum composites. Therefore, the stir casting method was used for the current study's hybrid MMC manufacturing. Bright extruded rods of Al7075 and n-TiB₂ particles were employed to make these composites. Table 1 displays the weight percentage of Al7075's chemical makeup.

Table 1. Chemical composition of Al7075 alloy (wt. %)

Content	Al	Cu	Mg	Si	Fe	Mn	Ni	Pb	Sn	Ti	Zn	Cr
wt.%	Rem	1.480	2.306	0.059	0.256	0.052	0.052	0.023	0.012	0.052	5.424	0.280

The Al7075 (base alloy) was first melted by using graphite crucible at 750 °C [11,12]. Subsequently, the molten melt was mixed with 30–50 nm sized n-TiB₂ (1, 1.5, 2, and 2.5 %) particulates that had been preheated to 450 °C. During the stirring operation, the pre-heated reinforcement particles were mixed with the base alloy. Inert gases were extracted from the molten aluminum metal matrix using a degassing tablet. Melting the slurry required 60 sec of stirring at 150 rpm, and then it was put into a pre-heated mold. The as-cast samples were taken out of the mold once they had set. As-cast and nano-composites were both machined to prepare the test samples using CNC machining. The relevant ASTM standards were followed in the preparation of test specimens for wear and mechanical testing. Hybrid MMC samples were polished using diamond paste and different-sized grit sheets to produce a clean surface finish in preparation for microstructural analysis. After using Keller's reagent to etch these specimens, they were left to dry in the open. The produced hybrid MMCs were examined for microstructure using Nikon E-200 optical microscope. The developed hybrid MMCs were exposed to microhardness testing using a Vickers Micro Hardness testing apparatus in compliance with E92-ASTM guidelines. Specimens with diameters and thicknesses of 20 mm each were used to evaluate the hardness. For thirty seconds, a constant 5 kg load was applied by using diamond shape indenter. Tensile testing was carried out utilizing a 450 KN weight on a Universal Testing Machine (UTM) in compliance with ASTM E8 requirements (gauge length is 50 mm and gauge dia is 10 mm). Tensile strength values varied by less than 10 %, according to the results, which were based on average values of three test samples with similar compositions. The pin-on-disc test apparatus was used in accordance with ASTM G99 guidelines to measure wear loss (30 mm length and 6 mm dia). The mean values, with variances of less than 10 %, were considered after three wear test specimens with comparable compositions were analyzed.

The prepared composites' densities were determined by applying the Archimedes principles, and theoretical densities were calculated by applying the rule of mixture in accordance with the percentage of reinforcement weight, as indicated in this equation [13]:

$$\rho_c = \rho_m V_m + \rho_r V_r, \tag{1}$$

where ρ_c is the composite density, ρ_m is the matrix density, ρ_r is the reinforcement density, V_m is volume fraction of mass, V_r is the volume fraction of reinforcement.

One of the crucial physical characteristics that will significantly affect the composite's mechanical and tribological qualities is porosity. The primary factors influencing the

porosity for the composites are mechanical alloying, sintering temperature, and compaction pressure. The porosity percentages of the resulting composites were computed using [14]:

$$Porosity = \frac{Theoretical\ density - Experimental\ density}{Theoretical\ density} \cdot 100. \qquad (2)$$

Figure 1 shows the framework of the present research investigation.
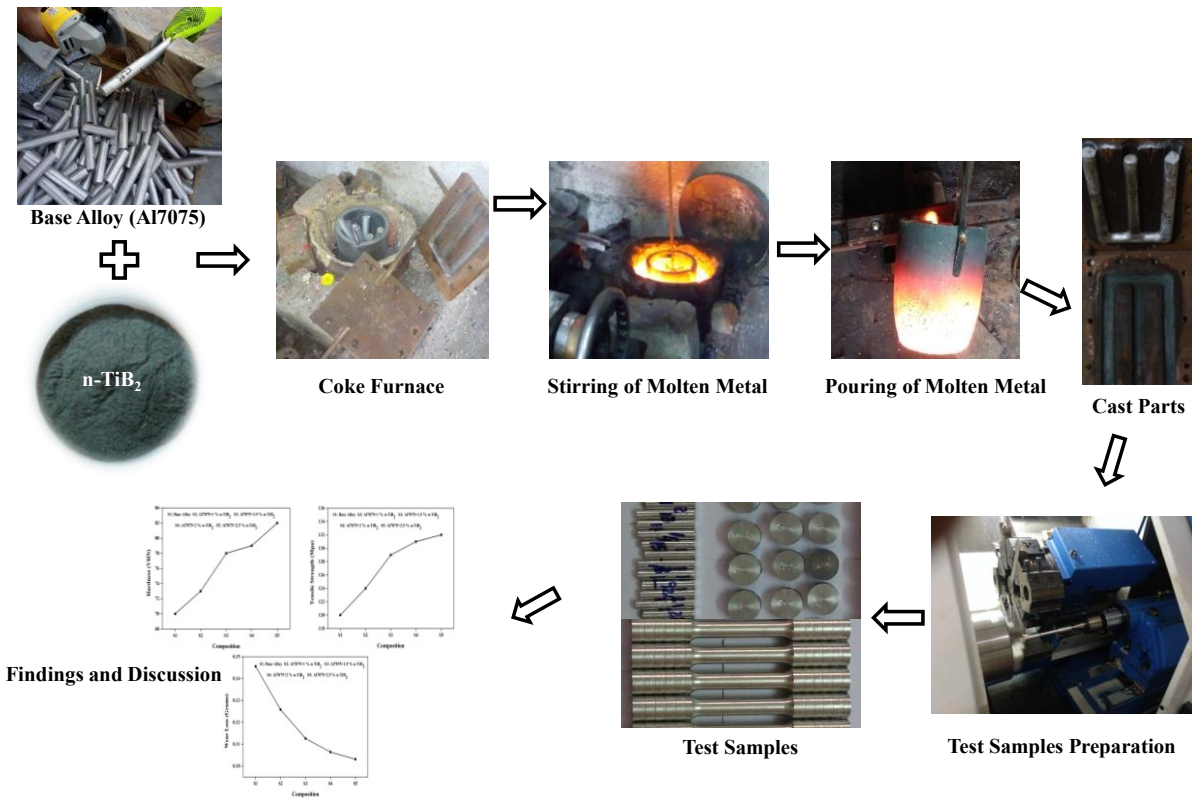
Fig. 1. Framework of the present research investigation

Findings and Discussion

Micro-structural Investigation

A matrix material's reinforcing particle distribution is examined via microstructural analysis. The mechanical and wear characteristics of Al7075/n-TiB$_2$ nanocomposite are analyzed by microstructural characteristics. The optical microstructure pictures of base alloy and developed nanocomposites are displayed in Fig. 2.

The micro structural pictures of all the samples show an equal distribution of small-pored n-TiB$_2$ particles. Since liquid metallurgy method was used to produce the specimens, porosity cannot be totally removed. It is also evident from microstructural pictures that cluster formation increases as % of n-TiB$_2$ increases from 1 to 2.5. The existence of more n-TiB$_2$ clusters is one of the primary reasons for the improved mechanical and wear features. The uniform dispersion of n-TiB$_2$ nanoparticles in the base matrix strengthens the interfacial-bond between the reinforcement element and the base matrix, which explains the improved mechanical and wear properties of the 2.5 wt. % n-TiB$_2$ composite. The number of n-TiB$_2$ particles increases with the nucleation sites

because it provides additional barriers to the fractures in the grains that cause the change of the grain structure [15,16].
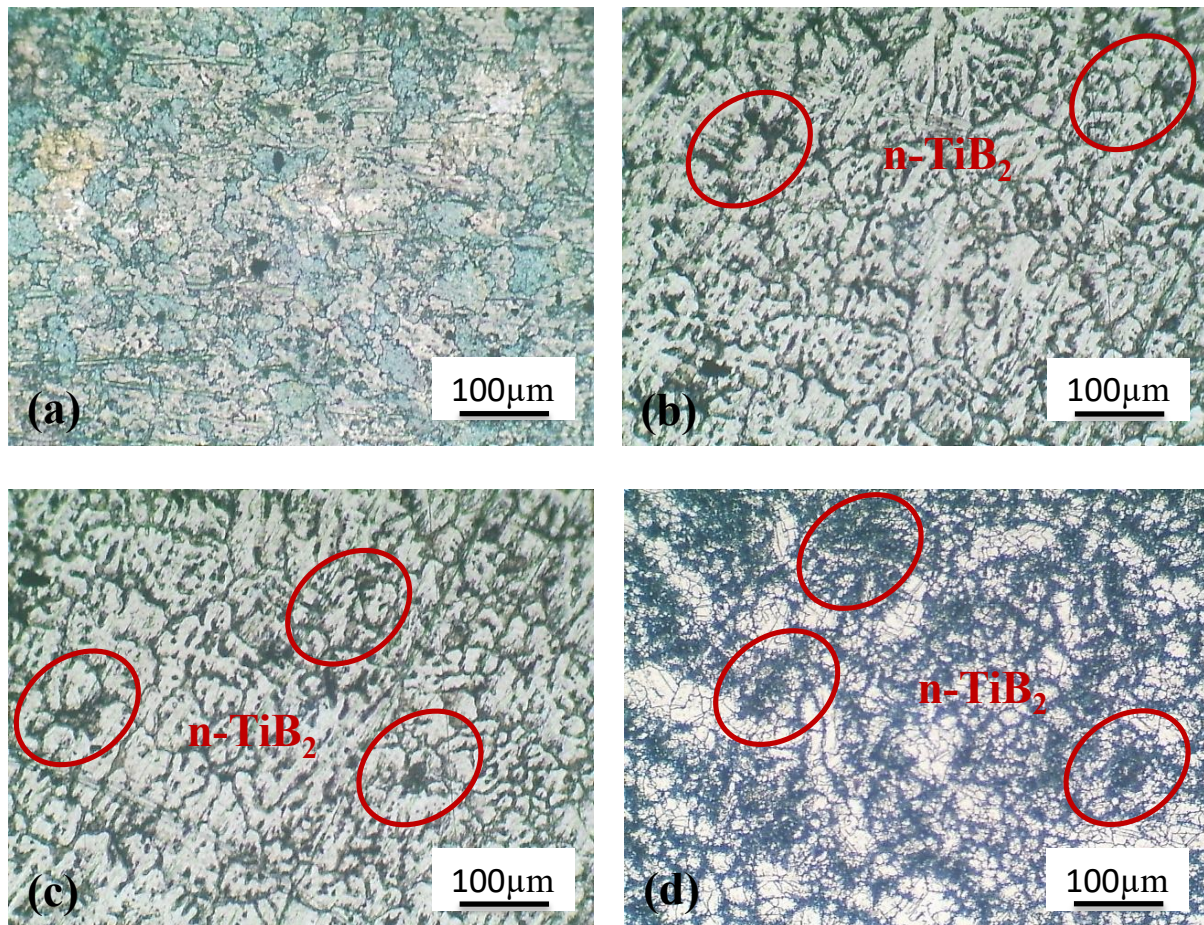
Fig. 2. Microstructure of (a) Base alloy, (b) 1.5 % n-TiB₂ composites, (c) 2 % n-TiB₂ composites and (d) 2.5 % n-TiB₂ composites

Energy dispersive X-ray spectroscopy study

Energy dispersive X-ray spectroscopy (EDS) analysis was performed on the fabricated nano MMCs samples in order to assess the chemical compositions of the Al7075/n-TiB₂ composite. The results are shown in Fig. 3. The analysis unequivocally demonstrates that
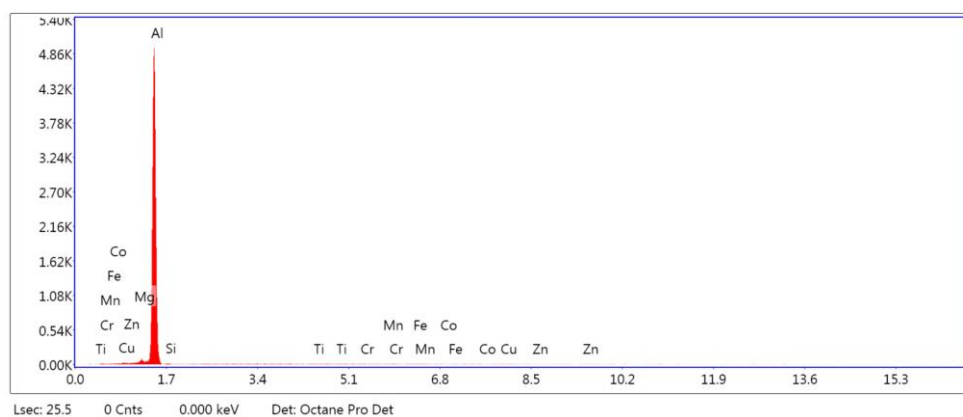
Fig. 3. EDS analysis of Al7075+2.5 % n-TiB₂

Al, Mn, Cu, Co, Ti, and other elements occur over a range of peaks. The result displays the EDS study's "Ti" peak. It provides proof that developed nano MMCs contain TiB_2 particles [17].

Density and porosity

The Archimedes method for determining density uses the fact that the apparent weight of an object submersed in liquid is lighter that the object's weight in air by the weight of the volume of liquid that the object displaces. Figure 4 illustrates the variation in the porosity and the density of Al7075/n-TiB$_2$ composites.
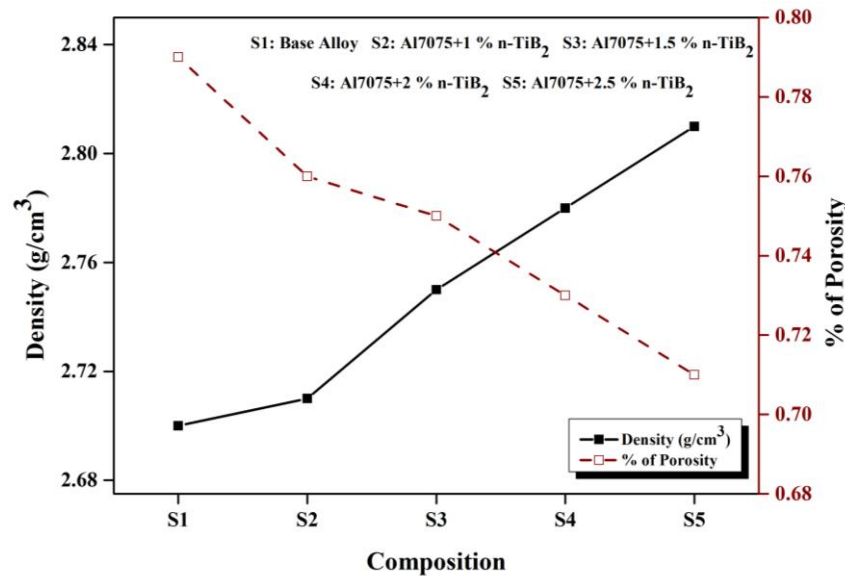
Fig. 4. Effect of n-TiB$_2$ on Density and porosity

Theoretical and experimental density values for Al7075/n-TiB$_2$ composites show a nearly similar trend and are nearly in agreement with one another. Density levels rise with the reinforcement addition. This increment of density values may be the cause of the high n-TiB$_2$ (hard) particle density [18]. The lower porosity of all the composites shows that reinforcement and matrix material have a strong interfacial bond. High compacting pressure and the temperature of sintering are the two primary factors that can impact the porosity within a composite [19,20].

Hardness

Figure 5 displays the hardness of the Al7075/n-TiB$_2$ composites. It is found that the 2.5 wt. % n-TiB$_2$ composite has far higher hardness values than the other composites. The produced composites' increased hardness could be credited to many factors [21]. First off, the n-TiB$_2$ particulates have a higher hardness than matrix alloy, and this hardness is enhanced by the reinforcements' homogeneous distribution throughout the matrix. Second, adding robust hard particles refines the grains of the aluminum alloy, which raises the dislocation density at the matrix-reinforcement interfaces and raises the produced composites' hardness values. Ultimately, the mass of the produced composites increases with increasing in reinforcement content, and this densification improves the

composites' hardness [22]. When the n-TiB$_2$ wt. % rose from 0 to 2.5, the hardness values improved from 70 to 84 VHN.
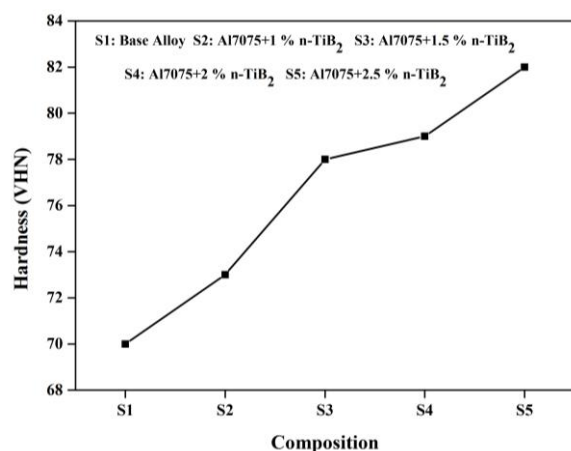
Fig. 5. Effect of n-TiB$_2$ on hardness
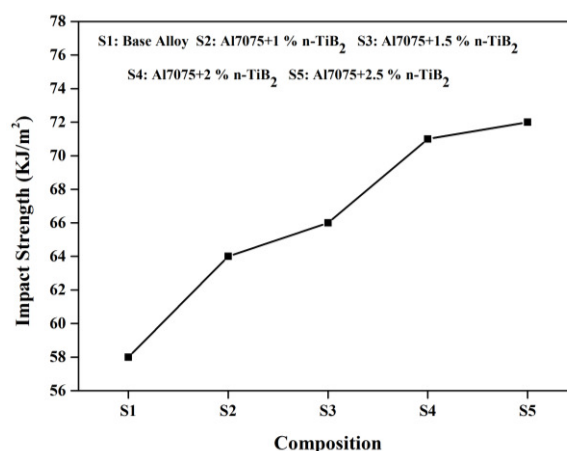
Fig. 6. Effect of n-TiB$_2$ on toughness

Toughness

The sample's energy absorption during an abrupt load was determined by an impact test procedure that adhered to the ASTM D256 standard. In this test, the amount of energy in a material upon break can be determined using the strength value. The impact strength of the composites is determined using the Charpy impact test. The strength variation of toughness for Al7075/n-TiB$_2$ composites with varying reinforcements is displayed in Figure 6. The n-TiB$_2$ composite with 2.5 wt. % showed higher impact strength than the others. The uniform dispersion of n-TiB$_2$ particulates in the matrix and strong interfacial bonding are the reasons for the high ductility. The main cause of the lower impact strength reported by most composites is the existence of pores and microcracks.

Tensile strength

Figure 7 shows that as the weight percentage of n-TiB$_2$ content increased, the hybrid composites' tensile strength increased as well. The reported outcomes are consistent with what has been seen in the majority of hard particle reinforced micro MMCs [23]. Other studies [24,25] detailed the strengthening mechanisms and connected them to the enhanced load-sustaining capability of the resulting composite, which was attained by increasing the wt. % of hard nano particulates and enhancing the resistance to the dislocation or movement of the particles.

Strength increased as a result of the generated nano MMCs' resistivity to dislocations, and the tension strength was increased even more by including additional n-TiB$_2$ particles into the MMCs. The hard particle's characteristics made the material stronger. The ultimate strength was increased by hard nanoparticles rather than dislocations. Several additional researchers reported similar findings [26]. A higher concentration of n-TiB$_2$ resulted in an improvement in the ultimate tensile strength, which is commonly ascribed to a decreased degree of porosity along with a more even distribution of reinforcement of hard particles. This fact is supported by the results obtained from most hard particles reinforced nano composites. The micro MMCs solidified

more quickly as a result of the matrix's level of reinforcement. This is usually caused by the complexity that results from the inclusion of strong nanoparticles, which obstructs dislocation motions across the base matrix [27].
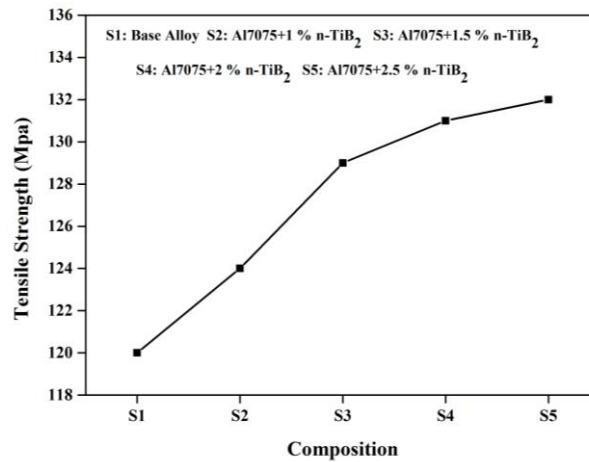
Fig. 7. Effect of n-TiB$_2$ on tensile strength

Figure 8 shows the stress-strain curves for the alloy and nanocomposites. These curves' primary characteristics are that as particle content rises, tensile strength increases as fracture strain decreases. When compared to the nanocomposites, the base alloy is shown to have the largest plastic strain and to show the least resistance of plastic deformation due to its relatively lower flow stress. It is noted that, in comparison to the base alloy, all of the nanocomposites exhibit greater strength. This is because the nanoparticles have been strengthened and the grains have been refined. The mismatch strengthening and elevated load bearing brought on by the nano-sized particles are typically responsible for the increase in strength in nano-MMCs. It is deduced that this might be because of variations in the CTE between the reinforcements and the matrix. The dislocation's mobility within the matrix is impeded by the hard nanoparticles, which is why the durability of the nano-MMCs is found to be greater compared to base matrix. During tensile tests, the hard ceramic nanoparticles' ability to trap dislocations resulted in an increase in the nanocomposites' tensile strength [28,29].
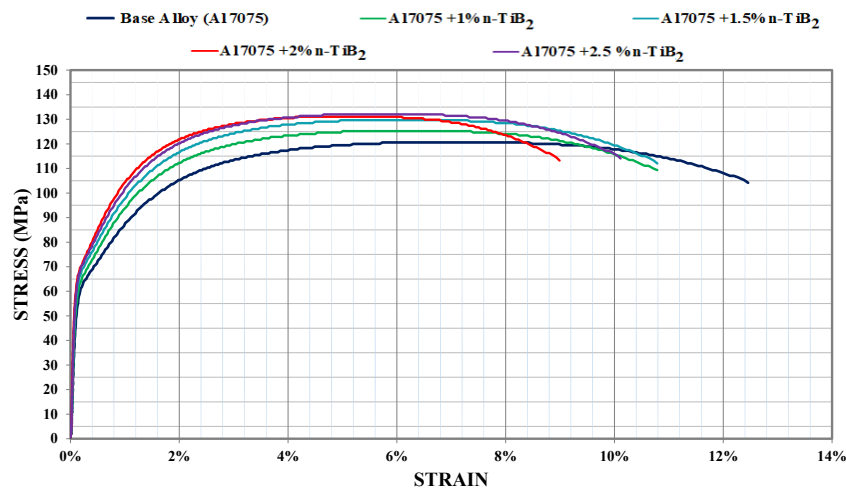
Fig. 8. Effect of n-TiB$_2$ nanoparticles concentration on stress-strain curves

When tension load was applied, higher weight percentage of reinforcements caused significant debonding at the matrix-reinforcement material contact point, which reduced ductility. Tensile fractured surface of the as-cast and 2.5 % n-TiB$_2$ reinforced MMC specimen are depicted in Fig. 9. The development of small pores on shattered material surfaces was the reason for the extreme ductility observed in MMC manufacture. In comparison to nanocomposites, as-cast elements with fractured surfaces showed more dimple shapes, suggesting superior ductile strength. The addition of n-TiB$_2$ particles caused the failure type to change from ductile to brittle, according to fractography investigations. This displacement is indicated by the dimples on the surface fractured specimen and the deformed area. More hard reinforcements resulted in more microcracks, indicating that the material was less ductile. The architecture of fractured surfaces frequently exhibited a higher density of voids and cracks. Because of their presence in the soft matrix, the robust particles created a triaxial stress state that ultimately led to void formation. This implies that there is a strong relation between the reinforcement being used and the matrix material, and that the size and shape of the reinforcements have an impact on bonding. Linear relationship observed between the dimple diameters and the composite's strength. Tensile sample fracture surfaces revealed details about the composition of nanoparticles at the interface. Hard nanoparticle pullout and fracture were two of the fracture processes that decreased ductility. The outward propagation of cracks from their centers was enhanced by voids at the particle and matrix interfaces [30,31].
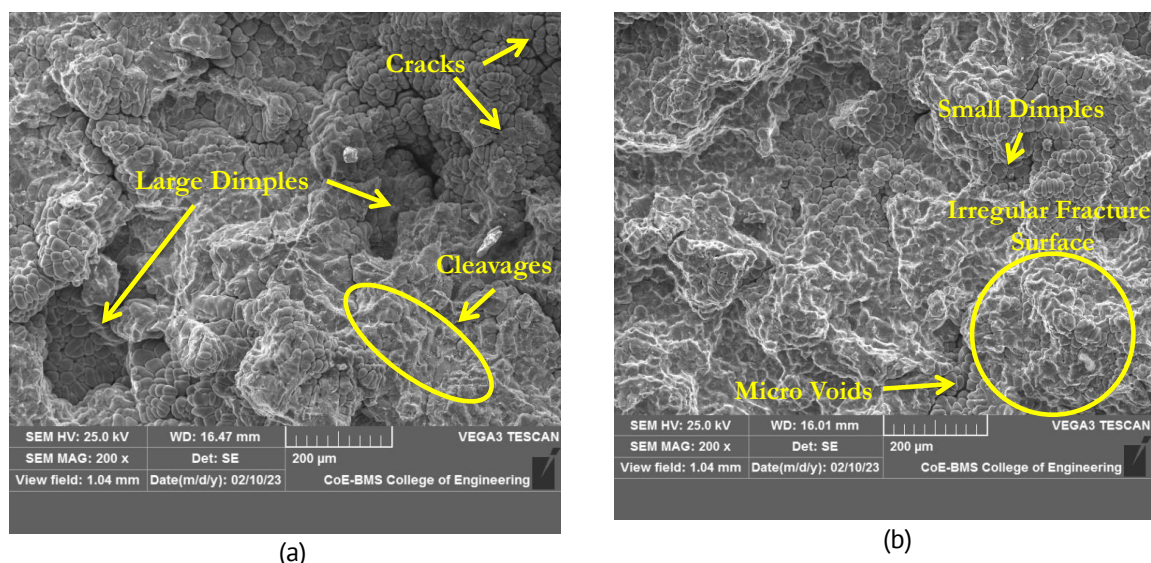
Fig. 9. Fracture surface of (a) base alloy and (b) 2.5 % n-TiB$_2$ composites

Wear loss

In the present investigation, all the wear test samples were tested with a constant load of 10 N, sliding speed of 500 rpm and sliding distance of 1000 m have been considered. Figure 10 shows the wear rates for both the Al matrix alloy and the Al/n-TiB$_2$ MMCs. The amount of n-TiB$_2$ that exists in reinforced composites has been found to increase the transition load. It was also observed that the composite had a lower wear rate than the base metal. The wear resistance that the composite samples given by releasing n-TiB$_2$ into the surface that contacts them during sliding is most likely the cause of this.

Alpas and Zhang [32] examined the sliding wear characteristics of Al-Si alloys reinforced with TiB$_2$ particles. It was concluded that TiB$_2$ reinforcement greatly improves wear resistance based on their studies.
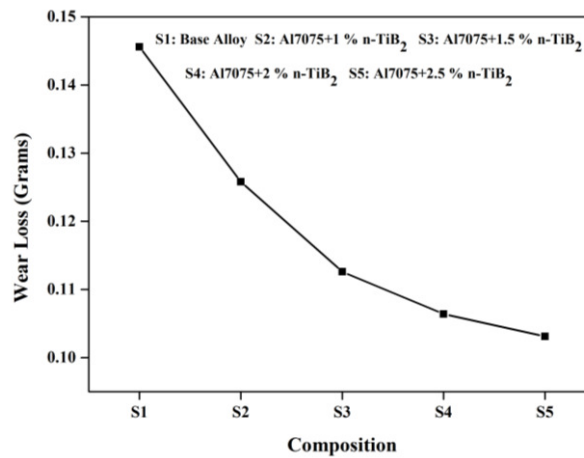
Fig. 10. Effect of n-TiB$_2$ on wear loss

| (a) | (b) |
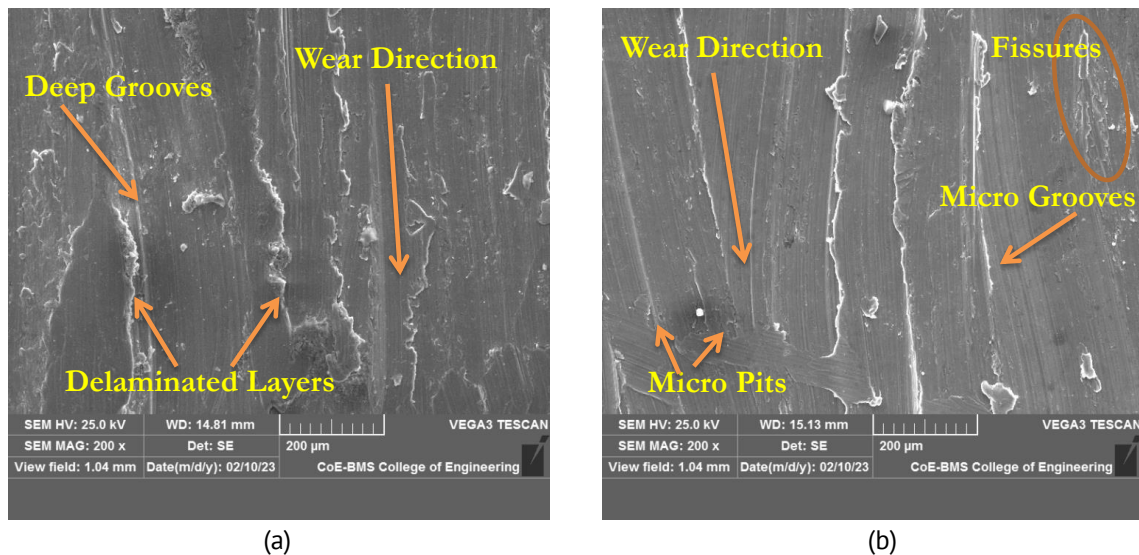
Fig. 11. SEM micrographs of worn surfaces of (a) base alloy and (b) 2.5 % n-TiB$_2$ composites

A thin film forms between the surfaces that meet when sliding wear causes n-TiB$_2$ particles to shear and stick to the metal surface with the principal axis parallel to the sliding direction. Moreover, the n-TiB$_2$ hard film can bear stress within low load circumstances without breaking or turning plastic due to its incredibly limited ductility. Research has repeatedly demonstrated that wear rate as well as surface damage may be decreased if material used at the counter contact is prevented from plastically deforming. The n-TiB$_2$ strong film in composites efficiently reduces the wear rates while sustaining high loads [33]. Therefore, the pace at which the sheared reinforcing layers stick to the sliding surfaces determines how well the n-TiB$_2$ particulates in the composite materials can slow down wear. The test samples' sliding wear tracks were inspected using scanning electron microscopy (SEM). SEM analyses of the wornout surfaces provided evidence about how hard particles affected the produced composites' wear characteristics.

Wornout surface of the as-cast and 2.5 % n-TiB$_2$ reinforced MMC sample are depicted in Fig. 11, where they display worn surfaces as depicted in SEM images.

These pictures show different-sized grooves on the wornout surfaces, most likely caused by worn debris particles acting as secondary abrasive bodies. Hard particulates within the alloy prevented plastic deformation, resulting in the forming of these grooves and small patches on the worn surfaces [34]. The n-TiB$_2$ particles significantly increased wear resistance by facilitating the development of a protecting effect on the surface under the applied load. The beneficial effects of n-TiB$_2$ particulates on the wear characteristics of MMCs have been shown by this investigation. The n-TiB$_2$ particles that were put into the counterface and test samples caused micro-ploughing on the MMCs' contact surfaces. SEM pictures of the fabricated nano composites in Fig. 11(b) reveal substantially less debris and more consistent sliding wear tracks. When compared to as-cast alloys, nano composites exhibit greater wear resistance due to their increased density and superior interfacial adhesion between the particles and base matrix. There was less wear loss because the steel discs could not penetrate the composite materials due to the presence of ceramic particles [35].

Conclusions

This work investigated the effects of n-TiB$_2$ weight percentage on both the tribological and mechanical characteristics of Al7075/TiB$_2$ composite. The following are the principal findings.

One of the most effective methods for fabricating Al7075/n-TiB$_2$ composites is stir casting. When producing nano composites with strong matrix-reinforcement bonding, a uniform dispersal of the reinforcement was attained. The developed composites' density values increased linearly as the wt. % of n-TiB$_2$ particles increased. Addition of n-TiB$_2$ particulates improved hardness of developed nano composites. Results show that composites reinforced by 2.5 wt. % of n-TiB$_2$ was found to be the hardest with hardness of 82 VHN. Tensile strength increased when the weight of n-TIB$_2$ particles increased with 132 MPA, the maximum tensile robustness was observed for 2.5 % of the nano composites reinforced with n-TIB$_2$. The obtained results show that the fabricated nanocomposites exhibit improved hardness of 14 %, tensile strength of 9 % and wear resistance of 20 % when compared to the base alloy. Fracture research exposed that n-TiB$_2$ reinforced aluminum matrix composites and unreinforced aluminum alloy exhibited ductile expression in the form of dimples. The equiaxed dimples and low depth were found in the particle-reinforced aluminum matrix composite. Compared to the Al/n-TiB$_2$ reinforced composites, the unreinforced aluminum alloy had a greater wear rate. In the developed nano composites, the wear rate decreased as n-TiB$_2$ concentration increased.

References

1. Agarwal S, Angra S, Singh S. A review on the mechanical behaviour of aluminium matrix composites under high strain rate loading. *Materials Physics and Mechanics.* 2023;51(6): 1–13.

2. Medvedev AE, Atroshchenko VV, Selivanov AS, Bogdanov AR, Gorbatkov MV, Logachev YV, Lobachev VS. Influence of various friction stir processing (FSP) schemes on the microstructure and properties of AD31 aluminium alloy busbar. *Materials Physics and Mechanics.* 2024;52(1): 95–107.

3. Gowrishankar TP, Sangmesh B. Role of heat treatment on mechanical and wear characteristics of Al-TiC composites. *Materials Physics and Mechanics.* 2024;52(1): 108–117.

4. Mohd Joharudin NF, Abdul Latif N, Mustapa MS, Badarulzaman NA. Effects of Untreated and Treated Rice Husk Ash (RHA) on Physical Properties of Recycled Aluminium Chip AA7075. *International Journal of Integrated Engineering.* 2020;12(1): 132–137.

5. Adaveesh B, Prabhushankar GV, Nagaral M. Tribological and tensile behaviour of Si_3N_4 reinforced Cu-Sn matrix composites. *Materials Physics and Mechanics.* 2023; 51(4): 11–22.

6. Ravikumar N, Reddappa HN, SureshR. Study on mechanical and tribological characterization of Al_2O_3/SiCp reinforced aluminum metal matrix composite. *Silicon.* 2018;10: 2535–2545.

7. Chandrasekhar GL, Vijayakumar Y, Nagaral M, Rajesh A, Manjunath K, Kaviti RVP, Auradi V. Synthesis and tensile behavior of Al7475-nano B_4C particles reinforced composites at elevated temperatures. *Materials Physics and Mechanics.* 2024;52(3): 44–57.

8. Ravikumar M, Naik R, Vinod BR, Chethana KY, Rammohan YS. Study on nanosized Al2O3 and Al2O3-SiC on mechanical, wear and fracture surface of Al7075 composites for soil anchoring applications. *Materials Physics and Mechanics.* 2023;51(6): 24–41.

9. Zulkamal NAM, Nasir LMM, Anasyida AS. Microstructure and wear properties of T6 heat treated semisolid A356-TiB_2 composite, *J. Phys. Conf. Ser.* 2018;1082: 012065.

10. Deepak Kumar S, Jha SK, Karthik D, Mandal A. Fatigue analysis of A356-TiB_2 (5 wt. %) in-situ nano composites, *Materials Today Proceedings.* 2019;18(3): 774–779.

11. Samal P, Surekha B, Vundavilli PR. Experimental investigations on microstructure, mechanical behavior and tribological analysis of AA5154/SiC composites by stir casting. *Silicon.* 2021;17(7): 3317–3328.

12. Ononiwu NH, Ozoegwu CG, Ifeanyi JG, Nwachukwu VN, Akinlabi ET. The influence of sustainable reinforcing particulates on the density, hardness and corrosion resistance of AA 6063. *Frattura ed Integrità Strutturale.* 2022;16(61): 510–518.

13. Kumar N, Gautam G, Gautam RK, Mohan A, Mohan S. Synthesis and characterization of TiB_2 reinforced aluminium matrix composites: a review. *J Inst Eng (India) Ser D.* 2016;97: 233–253.

14. Surya MS, Prasanthi G. Effect of silicon carbide weight % and number of layers on microstructural and mechanical properties of Al7075/SiC functionally graded material. *Silicon.* 2022;14(4): 1339–1348.

15. Dwivedi SP, Sahu R. Effects of SiC Particles Parameters on the Corrosion Protection of Aluminum-based Metal Matrix Composites using Response Surface Methodology. *Jordan Journal of Mechanical and Industrial Engineering.* 2018;12(4): 313–321.

16. Ali M, Falih S. Synthesis and Characterization of Aluminum Composites Materials Reinforced with TiC Nano-Particles. *Jordan Journal of Mechanical and Industrial Engineering.* 2014;8(5): 257–264.

17. Sreenivasa Iyengar SR, Sethuramu D, Ravikumar M. Study on micro-structure, hardness and optimization of wear characteristics of Al6061/TiB2/CeO2 hot-rolled MMCs using Taguchi method. *Frattura ed Integrità Strutturale.* 2023;65: 178–193.

18. Dey D, Bhowmik A, Biswas A. Effect of SiC content on mechanical and tribological properties of Al2024-SiC composites. *Silicon.* 2022;14(1): 1–11.

19. Daniel AA, Murugesan S, Manojkumar, Sukkasamy S. Dry sliding wear behaviour of aluminium 5059/SiC/MoS_2 hybrid metal matrix composites. *Materials Research.* 2017;20(6): 1697–1706.

20. Ononiwu NH, Ozoegwu CG, Jacobs I, Nwachukwu VN, Akinlabi ET. The influence of sustainable reinforcing particulates on the density, hardness and corrosion resistance of AA 6063. *Frattura ed Integrità Strutturale.* 2022;61(61): 510–518.

21. Kumar V, Angra S, Singh S. Influence of rare earth elements on aluminium metal matrix composites: A review. *Materials Physics and Mechanics.* 2023;51(2): 1–20.

22. Agarwal S, Angra S, Singh S. A review on the mechanical behaviour of aluminium matrix composites under high strain rate loading. *Materials Physics and Mechanics.* 2023;51(6): 1–13.

23. Chawla N, Shen YL. Mechanical behavior of particle reinforced metal matrix composites. *Advanced Engineering Materials.* 2001;3(6): 357–370.

24. Bhowmik A, Dey D, Biswas A. Characteristics study of physical, mechanical and tribological behaviour of SiC/TiB₂ dispersed aluminium matrix composite. *Silicon.* 2022;14(3): 1133–1146.

25. Faisal N, Kumar K. Mechanical and tribological behaviour of nano scaled silicon carbide reinforced aluminium composites. *Journal of Experimental Nanoscience.* 2018;13(1): S1–S13.

26. Akbari MK, Baharvandi HR, Shirvanimoghaddam K. Tensile and fracture behavior of nano/micro TiB₂ particle reinforced casting A356 aluminum alloy composites. *Materials & Design.* 2015;66: 150–161.

27. Wang H, Li Y, Xu G, Li J, Zhang T, Lu B, Yu W, Wang Y, Du Y. Effect of nano-TiC/TiB2 particles on the recrystallization and precipitation behavior of AA2055-TiC+TiB2 alloys. *Materials Science and Engineering: A.* 2023;871: 144927–144927.

28. Wang H, Zheng H, Hu M, Ma Z, Liu H. Synergistic effect of Al2O3-decorated reduced graphene oxide on microstructure and mechanical properties of 6061 aluminium alloy. *Scientific Reports.* 2024; 14: 16213.

29. Ravikumar M, Reddappa HN, Suresh R, Babu ER, Nagaraja CR. Study on micro - nano sized Al₂O₃ particles on mechanical, wear and fracture behavior of Al7075 metal matrix composites. *Frattura ed Integrità Strutturale.* 2021;58: 166–178.

30. Rajasekaran NR, Sampath V. Effect of In-Situ TiB₂ particle addition on the mechanical properties of AA 2219 Al alloy composite. *Journal of Minerals & Materials Characterization & Engineering.* 2011;10(6): 527–534.

31. Sridhar Raja KS, Hemanandh J, Mohan Krishna J, Muni Sai Preetham R. Effect of TiB2 on mechanical properties and microstructural of aluminium composite. In: Arockiarajan A, Duraiselvam M, Raju R. (eds.) *Advances in Industrial Automation and Smart Manufacturing. Lecture Notes in Mechanical Engineering.* Singapore: Springer; 2021. P.697–703.

32. Zhang J, Alpas AT. Wear regimes and transitions in Al₂O₃ particulate reinforced aluminium alloys. *Materials Science and Engineering: A.* 1993;161(2): 273–284.

33. Sreenivasan A, Paul Vizhian S, Shivakumar ND, Muniraju M, Raguraman M. A study of microstructure and wear behaviour of TiB₂/Al metal matrix composites. *Latin American Journal of Solids and Structures.* 2011;8(1): 1–8.

34. Ganesh K, Hemachandra Reddy K, Sudhakar Babu S, Ravikumar M. Study on microstructure, tensile, wear, and fracture behavior of A357 by modifying strontium (Sr) and calcium (Ca) content. *Materials Physics and Mechanics.* 2023;51(2): 128–139.

35. Ravikumar M, Hanumanthe G, Umesh GL, Raghavendra S, Darshan SM, Shivakumar MM, Santhosh S. An Experimental Investigation on Effect of B4C/CeO2 Reinforcements on Mechanical, Fracture Surface and Wear Characteristics in Al7075 Hybrid Metal Matrix Composites. *International Journal of Integrated Engineering.* 2024;16(5): 100–113.

About Authors

M. Gangadharappa
PhD, (Visvesvaraya Technological University, Belagavi, Karnataka, India)

H.R. Geetha
Master Technology, Assistant Professor (K R Pet Krishna Government Engineering College, K R Pet, Karnataka, India)

N.K. Manjunath
Master Engineering, Assistant Professor (BMS College of Engineering, Bangaluru, Karnataka, India)

G.L. Umesh
PhD, Assistant Professor (Bangalore Institute of Technology, Bangalore, Karnataka, India)

M.M. Shivakumar 🆔
Master Technology, Assistant Professor (BMS College of Engineering, Bangaluru, Karnataka, India)

Effect of rotational speed on various performance measures in friction stir lap weld of aluminium alloy 6061 using numerical simulation approach

A. Yadav ✉ **ⓘD, A. Jain, R. Verma**

National Institute of Technology Kurukshetra, Kurukshetra, India

✉ amit.insan77@gmail.com

ABSTRACT
The quality of a friction stir weld is significantly influenced by the choice of appropriate weld parameters, with rotational speed being one of the key factors. This study aims to examine these elements' influence on physical characteristics of velocity, viscosity, and torque. The performance measures being evaluated include the assessment of maximum weld interface velocity, minimum weld interface viscosity and tool-workpiece interface torque. This study utilises a computational fluid dynamics model to examine the influence of various rotational speeds on the aforementioned performance indicators. The workpiece selected for this study is an Aluminium Alloy 6061, while the tool employed is a truncated conical pin tool featuring a conical shoulder in a lap joint configuration. The study reveals that with an increase in rotational speed from 500 to 2900RPM, maximum weld interface velocity exhibits an increase with decreasing slope. As the rotational speed increases, the minimum weld interface viscosity decreases with decreasing slope. It is also found that tool-workpiece interface torque decreases with approximately constant slope with increasing rotational speed (500 to 2900RPM), meaning a linear decreasing trend. The findings of this investigation are validated through a comparative analysis with previously published data. With this information and the resulting conclusions, friction stir welders can deepen their understanding of how rotational speed affects welding quality.

KEYWORDS
friction stir welding • computational fluid dynamics • fluent • finite volume method

Introduction

The friction stir welding (FSW) technique was initially developed in 1991 and subsequently patented by the prestigious organization known as The Welding Institute (TWI) [1]. The purpose of this invention was to achieve robust and durable structures by welding materials with limited welding capabilities, specifically aluminium alloys. This issue is of great importance to various industries, particularly the aerospace sector, as conventional methods are inadequate for welding aluminium alloys or joining incompatible materials like aluminium and magnesium alloys.

During FSW, a rotating tool is gradually inserted into the workpiece until the shoulder comes into contact with the workpiece, as shown in Fig. 1. This position is upheld until the necessary temperature is attained due to the generation of heat through friction and plastic deformation. In order to accomplish the necessary weld, the tool is displaced along the weld line. The term advancing side (AS) is used to describe the side of a rotating tool that has identical direction as the tangential velocity and traverse speed

(TRS). The retreating side (RS) refers to the side of a rotating tool that has a vectorial sense opposite to the tangential velocity and TRS [2]. The workpiece section located ahead of tool is known as leading side, and the section located behind tool is known as trailing side.

Since its inception, a substantial body of research has been dedicated to investigating the impacts of various elements in the FSW process [3–8]. Certain factors are machine-specific, while others, such as spinning velocity and pin geometry, are inherent to the tool [9–15]. Each of these variables influences the transfer of heat and the movement of material, which subsequently has an effect on the microstructure and quality of the weld [16,17]. This study aims to assess the impact of rotational speed (ROS) on various performance measures for aluminium alloy 6061 (AA6061) lap welds using a truncated conical pin with conical shoulder (TCPCS) tool. The variables of interest include maximum weld interface temperature (Max. WIT), maximum weld interface velocity (Max. WIV), minimum weld interface viscosity (Min. WIVis), and tool-workpiece interface torque (TWIT). This study employs the finite volume technique (FVM) of computational fluid dynamics (CFD) as an efficient and time-effective approach [11].
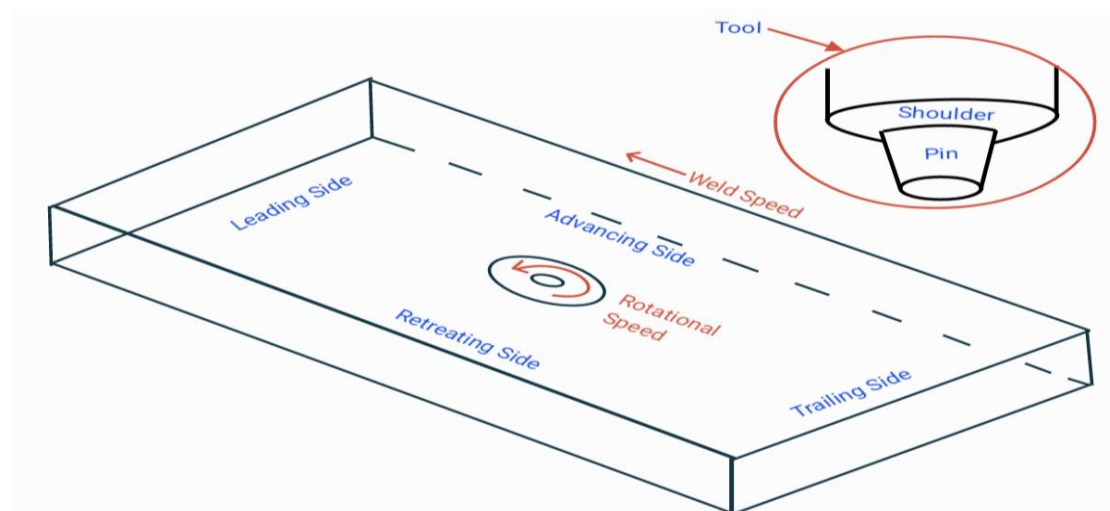
Fig. 1. Schematic representation of the FSW process

Multiple researchers have conducted investigations on FSW. Nandan et al. [12–14]. utilised the three dimensional visco-plastic model for butt joints in stainless steel-SS304, AA6061, and mild steel-1018, respectively. The instrument's combined rotational and linear movement revealed a notable imbalance in the temperature distribution surrounding it. In [15], it was conducted a study where they developed a three-dimensional thermo-mechanical model to examine the temperature and material flow in the butt weld of AA6061-T6. Augmenting the ROS while reducing the welding speed results in an intensified stirring motion, hence improving the weld's quality. To avoid defects, the ROS should increase proportionally with the welding speed [15]. J. Zhang et al. [11]. developed a computational fluid dynamics model in FLUENT® to analyse the temperature distribution and material flow characteristics of an AA6061-T6 lap joint under the influence of a conical tool. The model does not consider the effect of tool tilt. The findings suggest that the shoulder surface area is primarily responsible for the

Effect of rotational speed on various performance measures in friction stir lap weld of aluminium alloy 6061 using numerical simulation approach

116

majority of heat generation, accounting for 88 % of the total. On the other hand, the regions of the pin's side surface and pin's bottom surface barely account for 10.48 and 1.52 %, respectively. The occurrence of intense material movement is primarily limited to the area near the tool, where material located on tool's front is driven towards RS and then gathers at tool's back [11]. Jain, Pal, and Singh [16] created a model to forecast the forces, spindle torque, temperature, and plastic strain that occur during the butt-welding process of two AA2024-T4 metals. The rise in heat generation rate, as indicated by the temperature distribution, leads to a decrease in forces and spindle torque as the ROS increases. In addition, the conical shape of the pin resulted in a higher material velocity compared to its cylindrical version while requiring less effort during the plunging process Shi and Wu [17] created a transient model to accurately assess the dynamic changes in heat-generation, temperature-distribution, and material-flow during the butt FSW process of AA2024. They also examined how these factors are influenced by process parameters, including TRS and tool ROS. It has been observed that the tool torque rises when the TRS increases, providing that the ROS remains constant. An inverse relationship was seen when the rotating speed increased, assuming that the temperature and pressure remained constant. Hasan [18] conducted a study where he used FSW to simulate the butt joint of AZ31 magnesium alloy. Results showed that the maximum temperature drops as the TRS increases while the ROS remains constant. Roubaiy et al. [19] examined how different welding parameters affect the mechanical properties of a butt joint made by FSW using aluminium 5083-H116. As the ROS increases (assuming the TRS remains constant), the tensile strength and joint efficiency rise while the absorbed energy drops. Conversely, a contrasting effect on TRS was noticed, but the ROS remained unchanged [19]. Nirmal and Jagadesh [20] conducted a study on the percentage elongation, yield strength, and ultimate tensile strength of a dual-phase titanium alloy using FSW on butt joints. The study revealed that when the ROS increases (assuming the TRS remains constant), the yield stress, ultimate tensile stress, and tensile strength also increase, while the percentage elongation drops. An inverse relationship was seen as the TRS increased, assuming the ROS remained constant [20]. Andrade et al. [21] examined the torque and temperature FSW of aluminium alloys belonging to series AA2xxx, AA5xxx, AA7xxx, and AA8xxx. It has been observed that when the ROS increases (assuming the torque sensitivity remains constant), the torque drops but the peak temperature increases. In contrast, there was a reported increase in TRS, assuming that the rotating speed remained constant. Furthermore, it was noted that an increase in workpiece thickness correspondingly leads to an increase in torque. An augmentation in shoulder diameter leads to a corresponding augmentation in peak torque and temperature [21]. H. J. Zhang et al. [22] performed FSW on AA6061 with rotation speeds varying from 1,000 to 6,000 RPM. The study reveals that as the ROS increases (while keeping the TRS constant), the peak temperature also increases. Yadav et al. [23] conducted a study on the tool tilt effect for AA6061 using a tapered cylindrical pin to analyse its impact on heat and material flow. It was discovered that the temperature drops as the tilt angle increases [23].

The literature review indicates that no previous study has examined the impact of different ROS on velocity, viscosity, and torque for AA6061. Specifically, this study focuses on the use of a TCPCS tool for a lap joint. The current study investigates the impact of

different ROSs (ranging from 500 to 2900 RPM) on several performance parameters, including maximum weld interface velocity, minimum weld interface viscosity, and tool-workpiece interface torque. Solidworks® 2017 is utilised for the purpose of geometric modeling, whereas the CFD programme FLUENT® is employed specifically for FVM modeling [24]. The effect of changing ROS is evaluated by analysing these performance indicators. The novelty of this work will be elucidated in the next section:

This study examines the impact of tilt angle and slip in lap weld. The impact of the shoulder's side surface on heat generation is also taken into account. An analysis is conducted on the performance metrics of the lap weld's weld surface. Prior studies have examined the maximum temperature attained within a workpiece. The range of ROS is dictated by the recrystallization and solidus temperatures of the workpiece formed at the weld surface. This comprehensive study examines the impact of all significant input elements on the geometry of FSWs and the tool used, as well as their influence on many performance metrics.

Numerical modeling

As a result of the intricate nature of the practical arrangement, a cost and time-efficient technique of numerical modelling is utilised [13,25]. This particular portion provides a numerical model for friction stir lap weld of AA6061 using a TCPCS tool. It includes the necessary assumptions, boundary-conditions, material-parameters and model validation.

Description of model

Utilising numerical modeling allows for the efficient and effortless visualisation of temperature distribution, material movement, as well as stress and strain analysis [11]. It offers valuable understanding into the operation of the process. The impact of different ROS on velocity, viscosity, and torque was analysed using the commercial CFD FLUENT® software. Figure 2 illustrates the simulation model. AA6061 plates are utilised. The dimensions of each plate are 200 × 100 ×5 mm^3. When joined in a lap arrangement, the measurements are 200 × 100 × 10 mm^3 [11]. The parameters for the FSW technique are provided in Table 1. The selection of these characteristics is based on a thorough evaluation of the pertinent literature [17,18].

Table 1. Process parameters employed

Process parameter	Value
Diameter of shoulder, mm	25
Conical angle of shoulder, °	2
Tilt angle, °	0.25
Pin length, mm	5
Root diameter of pin, mm	8
Tip diameter of pin, mm	6
Traverse speed, m/s	0.05
Plunge depth, mm	0.375
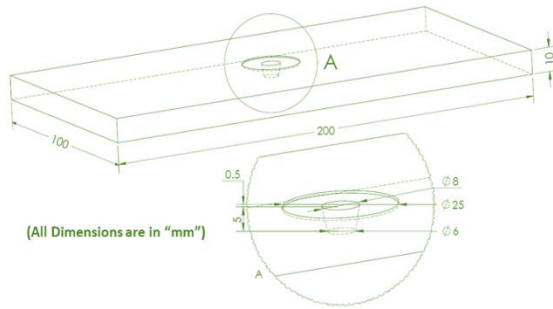
Fig. 2. Model's schematic sketch
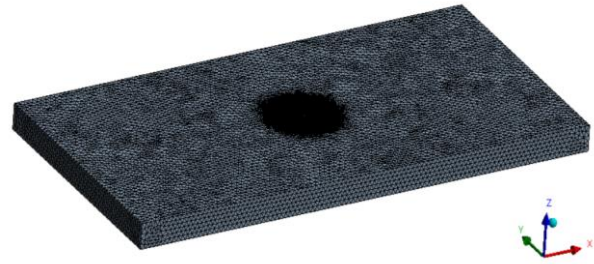
Fig. 3. Mesh used

The Realisable k-epsilon viscous model is employed to simulate the flow of material in a transient state. Mesh with tetrahedron-cells is utilised, with fine mesh at the interface between the tool and the workpiece, as depicted in Fig. 3. The present work adheres to the following assumptions.

The process is a quasi-steady process, meaning that the rate of heat generation remains constant. Plasticized material is classified as non-Newtonian, incompressible, and visco-plastic. The material is presumed to exhibit the characteristics of a non-Newtonian fluid, where its viscosity is influenced by both temperature and strain rate. There is a condition of partial slip between the tool and the workpiece. The upper, bottom, and side surfaces of the workpiece have a free slip condition. The outlet boundary assumes a value of zero pressure.
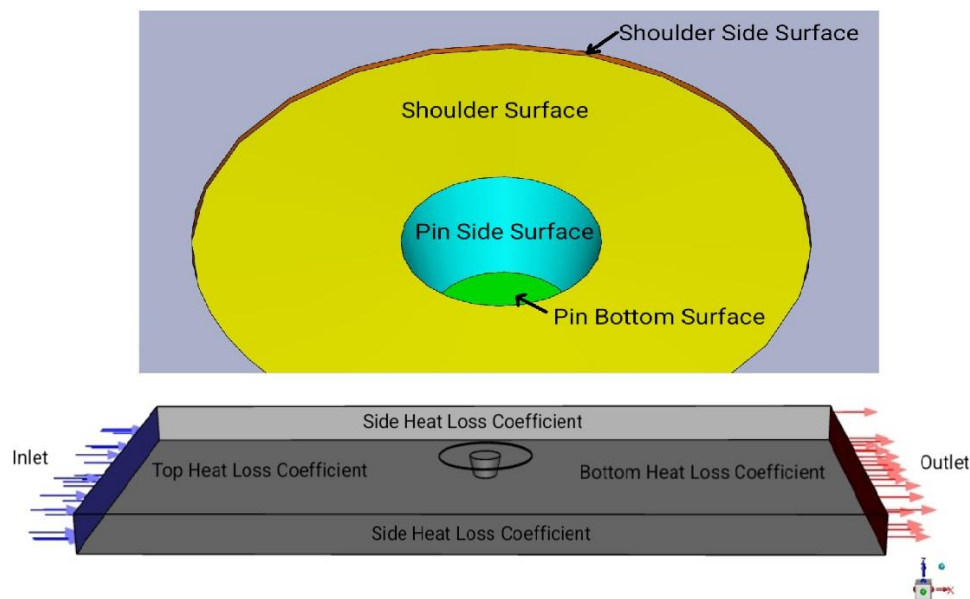
Fig. 4. Model's parts and boundary conditions

Boundary conditions and material properties. In order to make precise predictions about welding, it is crucial to employ realistic boundary conditions [18]. Figure 4 displays the parts and boundaries imposed on the model.

The inlet boundary condition of flow is defined as follows:

$$u = u_{weld}, \; v = 0, \; w = 0, \tag{1}$$

where welding velocity is represented by u_{weld}, whereas the velocity intensities in the X, Y, and Z directions are represented by u, v, and w, respectively.

The tool periphery velocity, which is the combined effect of the tool's angular velocity and the welding speed, is provided below:

$$u_i = \omega r sin\theta - u_{weld}, v_i = \omega r cos\theta, w_i = 0. \tag{2}$$

The value of r is such that $r_1 < r < r_3$. The variables u_i, v_i and w_i denote vectors of velocity in the X, Y, and Z directions. The index notation "i" means a specific location on tool's surface where the tool's combined ROS and the TRS are determined. r_1 represents the radius of tool shoulder; r_3 represents the radius of pin bottom; θ is the angle between the horizontal direction vector from the tool axis to any point on the cylindrical surface. In the weld direction, θ is equal to zero.

Tool periphery velocity when tool tilt angle (ξ) and contact state variable (δ) are considered are represented [13]:

$$u_i = (1 - \delta)((\omega r sin\theta) \cos \xi - u_{weld}), \tag{3}$$
$$v_i = (1 - \delta)\omega r cos\theta, \tag{4}$$
$$w_i = (1 - \delta)(\omega r sin\theta) \sin \xi, \tag{5}$$
$$\delta = 0.9\left(0.31 e^{\omega r/1.87} - 0.026\right). \tag{6}$$

The viscosity (ɳ) is determined using below equations [26−28]:

$$\eta = \frac{\sigma}{3\bar{\varepsilon}}, \tag{7}$$

$$\sigma \text{ (flow stress)} = \frac{1}{\beta} \ln\left\{ \left(\frac{Z}{A}\right)^{\frac{1}{n}} + \left(1 + \left(\frac{Z}{A}\right)^{\frac{2}{n}}\right)^{\frac{1}{2}} \right\}, \tag{8}$$

$$Z \text{(Zener Hollomon parameter)} = \bar{\varepsilon} e^{\left(\frac{Q}{RT}\right)}, \tag{9}$$

$$\bar{\varepsilon} \text{ (strain rate)} = \left(\frac{2}{3} \varepsilon_{ij} \varepsilon_{ij}\right)^{\frac{1}{2}}, \tag{10}$$

where T represents temperature (K), A, β, and n are constants that describe the material properties, Q is an activation energy that does not depend on temperature, R is the gas constant. These equations are implemented through the use of user defined functions (UDF). Table 2 provides the material-constants and properties of AA6061 [29].

Table 2. Material-constants and properties for aluminium alloy 6061

Parameter	Value
Material-constants:	
A, s^{-1}	2.41×10^8
n	3.55
Q, J·mol^{-1}	1.45×10^5
B, MPa	0.045
Material density ρ, kg·m^{-3}	2700
Gas constant R, J·K^{-1}·mol^{-1}	8.314

The heat created during the FSW process is distributed over many regions. The tool's contacting surface with the workpiece is partitioned into three sections: bottom shoulder surface (SS), pin side surface (P_{SS}), and pin bottom surface (P_{BS}) (Fig. 4). The SS is subdivided into two sections: shoulder with conical surface (S_{CS}) and shoulder with flat surface (S_{FS}). All these sections exhibit partial sticking-sliding contact. The heat produced by different sources is provided below:

$$Q_{total} = \delta Q_{sticking} - (1 - \delta)Q_{sliding}. \tag{11}$$

The symbol δ represents the contact state variable. When the slip coefficient (δ) is equal to zero, heat is only generated through friction. When the value of δ is equal to 1 (indicating a stick), all heat is produced only through the deformation of the plastic material [30].

The assumed maximum yielding shear stress is:

$$\tau_b = \frac{\sigma_s}{\sqrt{3}},\tag{12}$$

where σ_s represents the material's yield stress at its melting point temperature [31].

The δ at S_{CS} has been assigned a value of 0.35 [11]. The heat-flux (W/m^2) at this section is:

$$q_{S_{CS}} = \frac{[\delta_{CSS}\tau_b + (1-\delta_{CSS})\mu P]2\omega[(r_1^3 - r_2^3)(1+\tan\alpha')]}{3(r_1^2 - r_2^2)}.\tag{13}$$

At P_{SS}, δ is equal to 0.5 [11]. The heat-flux (W/m^2) at this section is:

$$q_{P_{SS}} = \frac{2\delta_{PSS}\omega\tau_b(r_2^3 - r_3^3)\cos\alpha}{3(r_2^2 - r_3^2)} + \frac{2(1-\delta_{PSS})\mu P\omega(r_2^3 - r_3^3)}{3(r_2^2 - r_3^2)}\tag{14}$$

At P_{BS}, δ has a value of 0.35 [11]. The heat-flux (W/m^2) at this section is:

$$q_{P_{BS}} = \frac{2\omega r_3(\delta_{PBS}\tau_b + (1-\delta_{PBS})\mu P)}{3},\tag{15}$$

where μ (0.4) is coefficient of friction [11], P is plunge pressure (Pa), ω is ROS (rad/s) and α' is cone angle of shoulder ($\alpha' = 0$ for S_{FS})). A plunging pressure of 12 MPa is taken here [11].

The specific-heat (C_p) equation for AA6061 is shown below [13]:

$$C_p = 929 - 0.627T + 1.481 \times 10^{-3}T^2 - 4.33 \times 10^{-8}T^3.\tag{16}$$

The thermal-conductivity (k) equation for AA6061 is shown below [13]:

$$k = 25.22 + 0.3978T + 7.358 \times 10^{-6}T^2 - 2.518 \times 10^{-7}T^3.\tag{17}$$

The boundary condition for heat exchange between the top surface of the workpiece and the environment is convective as well as radiative heat transfer [13]. The heat exchange between the bottom and side surfaces of the workpiece is conductive (due to contacts of jigs and fixtures) and convective heat transfer, respectively. All these heat exchanges are converted to convective form as shown below [13]:

$$k\frac{\partial T}{\partial z} = h_t(T - T_0),\tag{18}$$

$$k\frac{\partial T}{\partial z} = h_b(T - T_0),\tag{19}$$

$$k\frac{\partial T}{\partial z} = h_s(T - T_0).\tag{20}$$

where h_t, h_b and h_s are coefficients of heat dissipation at workpiece's top, bottom and side surface, respectively. T_0 is the environmental temperature (300 K).

In this study, h_b = 150 W/m^{2}K, and h_t = h_s = 80W/m^{2}K. The external emissivity of workpiece top surface is 0.09 [32].

Model validation

Validation of current model is done with the work by J. Zhang et al. [11]. They created a 3D CFD model in FLUENT® to understand the temperature-field and material-flow behaviour of an AA6061-T6 lap joint subjected to a conical tool (neglecting tool tilt effect). In the present study, the above work is replicated, and upon validating the current methodology and procedure, additional fixed input parameters (tilt angle and plunge depth) are introduced. The temperature distribution and material flow velocity data

closely correspond to those reported data. Figure 5 compares the present and validated studies' temperature distributions. Thus, numerical-modeling methods are satisfactory.

(a)

(b)
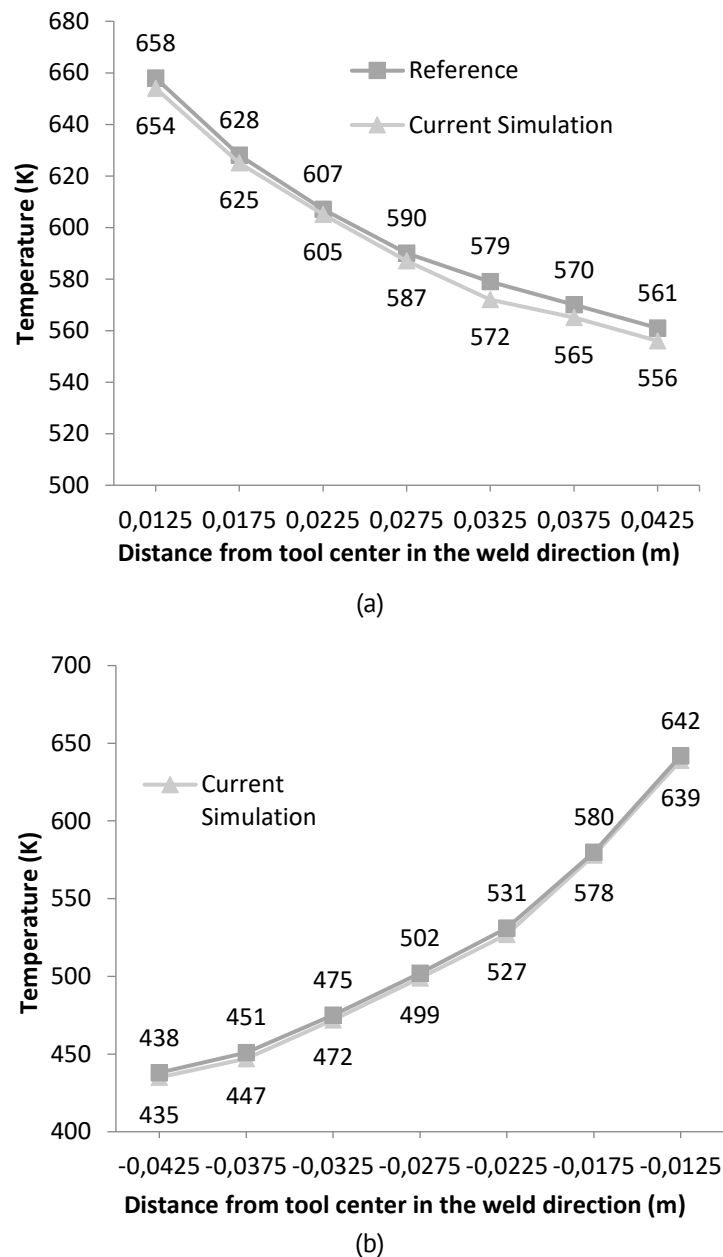
Fig. 5. Comparison of weld temperature for present study and reference study [11]: (a) temperature at workpiece's top surface on trailing side, (b) temperature at workpiece's top surface on leading side

Results and Discussion

This part of the article presents ROS's influence on maximum velocity, minimum viscosity and torque as performance measures. The range of ROS is selected from 500 to 2900 RPM range as below 500 RPM ROS, temperature at weld surface (surface joining two weld plates in lap joint) reaches below its recrystallization temperature (0.5 melting point temperature) for alloys, i.e., 462.5 K and above 2900 RPM ROS, temperature of workpiece increases above its solidus temperature (855 K for AA6061).

Effect of rotational speed

To study the effect of ROS on maximum weld interface velocity, minimum weld interface viscosity and tool-workpiece interface torque, all other input parameters such as TRS, tilt angle and plunge depth are kept at their average value of 0.05 m/s, 0.25° and 0.375 mm, respectively. Table 3 summarizes considered performance measures as varying ROS is varied from 500 to 2900 RPM.

Table 3. Effect of rotational speed on maximum weld interface velocity, minimum weld interface viscosity and tool-workpiece interface torque as performance measures

Rotational speed, RPM	Max. weld interface velocity, m/s	Min. weld interface viscosity, Kg/(ms)	Tool-workpiece interface torque, Nm
500	0.1438	696164	45.6
900	0.2234	174093	40.22
1300	0.2962	75616	35.41
1700	0.3615	46734	32.06
2100	0.4185	36169	29.68
2500	0.4662	29048	27.04
2900	0.5038	23901	26.04
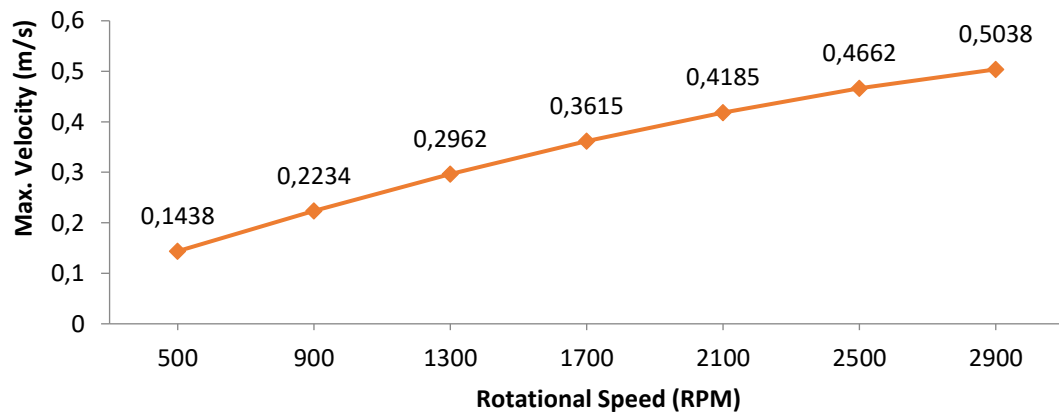
Fig. 6. Effect of tool rotational speed on maximum weld interface velocity (material flow) during FSW

Figure 6 shows the effect of ROS on maximum weld interface velocity. The value of maximum weld interface velocity increases but with a decreasing slope on increasing ROS from 500 to 2900 RPM. The reason for this behaviour is explained as follows. From Eqs. (3)–(5), it is known that resultant velocity is dependent on tool peripheral velocity in the axial directions (x, y and z). This resultant velocity governs maximum velocity performance measure. From Eqs. (3)–(5), it is found that peripheral tool velocity in axial directions is dependent on ROS (ω) and contact state variable (δ), provided all other parameters (traverse speed, tilt angle, etc.) remains constant. The value of contact state variable varies between 0 and 1. This contact state variable is further dependent on ROS, as shown by Eq. (6). Tool peripheral velocity in the axial direction is directly proportional to ROS, and contact state variable is exponentially directly dependent on ROS (meaning

contact state variable is inversely dependent on maximum velocity performance measure, Eq. (6)).

The effect of ROS on minimum weld interface viscosity is shown in Fig. 7. It indicates that as ROS increases, minimum weld interface viscosity decreases with decreasing slope. This is due to the fact that at low ROS and at constant traverse speed, tilt angle and plunge depth, the heat flux generation is minimum. This results in a low strain rate and lower temperature, which in turn results in higher viscosity at a low ROS (Eqs. (7)–(10)). As the ROS increases, the temperature and strain rate increase, resulting in lower viscosity. The critical viscosity above which no significant plastic flow takes place is typically around $5 \cdot 10^6$ Pa/s for AA6061 [13].
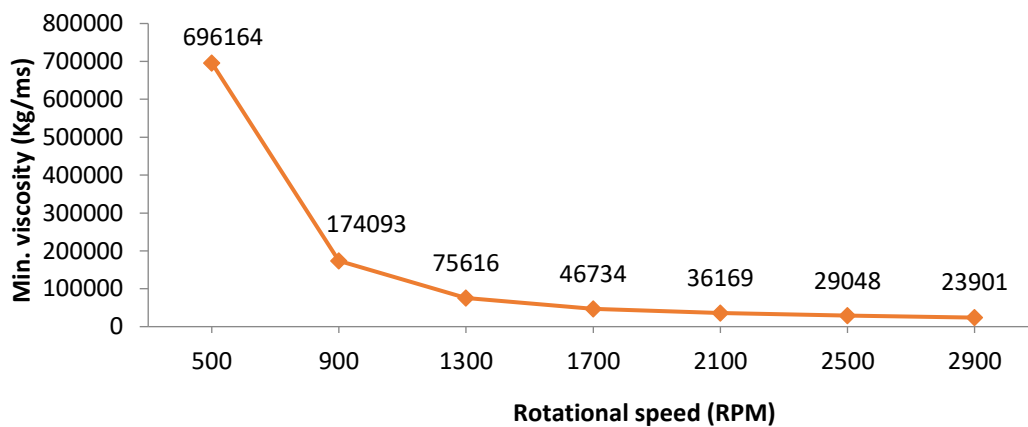
Fig. 7. Effect of tool rotational speed on maximum weld interface velocity

Figure 8 shows the effect of ROS on tool-workpiece interface torque. It indicates that torque decreases with approximately constant slope with increasing the ROS (200 to 2000 RPM), meaning a linear decreasing trend. This is due to the fact that as viscosity decreases with increasing ROS at constant traverse speed, torque at the tool-workpiece interface decreases due to softening of the material.
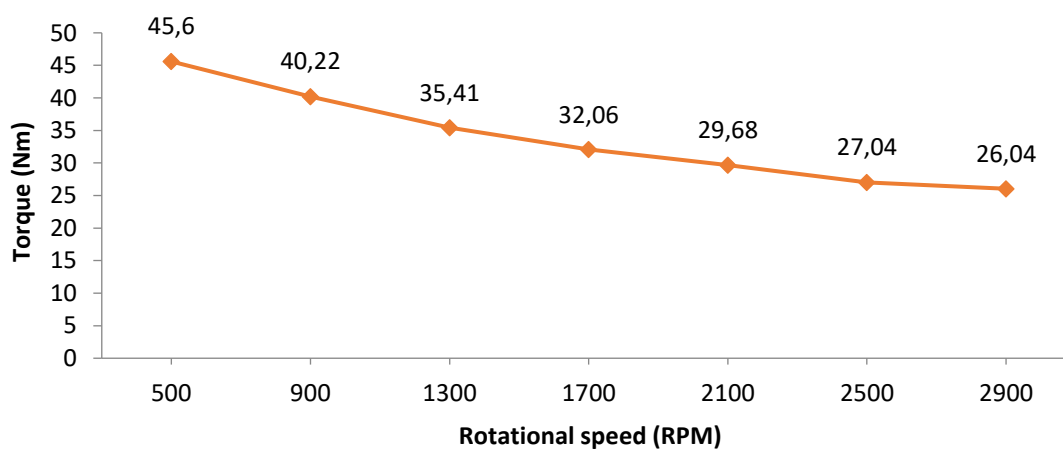
Fig. 8. Effect of tool rotational speed on tool-workpiece interface torque

Effect of rotational speed on various performance measures in friction stir lap weld of aluminium alloy 6061 using numerical simulation approach

124

Conclusions

This investigation studies the effect of varying ROS on maximum weld interface velocity, minimum weld interface viscosity and tool-workpiece interface torque as performance measures. The following conclusions are drawn from the study:

1. with an increase in ROS from 500 to 2900 RPM, maximum weld interface velocity increases but with a decreasing slope;
2. with increase in ROS, minimum weld interface viscosity decreases with decreasing slope. A significant drop in minimum viscosity occurs between 500 and 1300 RPM;
3. tool-workpiece interface torque decreases with the approximately constant slope with increasing ROS (500 to 2900RPM), meaning a linear decreasing trend.

References

1. Schillings Tsang. Friction welding. In: Welding, Brazing, and Soldering. *ACM Internatinal.* 1993. p.315-317.
2. Nandan R, DebRoy T, Bhadeshia HKDH. Recent advances in friction-stir welding - Process, weldment structure and properties. *Prog. Mater. Sci.* 2008;53(6): 980–1023.
3. Zhang XX, Wu LH, Andrä H, Gan WM, Hofmann M, Wang D, Ni DR, Xiao BL, Ma ZY. Effects of welding speed on the multiscale residual stresses in friction stir welded metal matrix composites. *Journal of Materials Science & Tech.* 2019;35: 824–832.
4. Buffa G, Campanile G, Fratini L, Prisco A. Friction stir welding of lap joints: Influence of process parameters on the metallurgical and mechanical properties. *Mater Sci Eng A.* 2009;519: 19–26.
5. Keivani R, Bagheri B, Sharifi F, Ketabchi M, Abbasi M. Effects of pin angle and preheating on temperature distribution during friction stir welding operation. *Trans Nonferrous Met Soc China.* 2013;23(9): 2708–2713.
6. Shi L, Wu CS, Liu HJ. The effect of the welding parameters and tool size on the thermal process and tool torque in reverse dual-rotation friction stir welding. *Int J Mach Tools Manuf.* 2015;91: 1–11.
7. Kadian AK, Puri G, Das S, Biswas P. Effect of tool geometry and process parameters on the material flow of friction stir welding. In: *5th International and 26th All India Manufacturing Technology, Design and Research Conference (AIMTDR 2014).* Assam, India: IIT Guwahati; 2014. p.12–14.
8. Zhang S, Shi Q, Liu Q, Xie R, Zhang G, Chen G. Effects of tool tilt angle on the in-process heat transfer and mass transfer during friction stir welding. *Int J Heat Mass Transf.* 2018;125: 32–42.
9. Sun Z, Wu CS, Kumar S. Determination of heat generation by correlating the interfacial friction stress with temperature in friction stir welding. *J Manuf Process.* 2018;31: 801–811.
10. Zhai M, Wu CS, Su H. Influence of tool tilt angle on heat transfer and material flow in friction stir welding. *J Manuf Process.* 2020;59: 98–112.
11. Zhang J, Shen Y, Li B, Xu H, Yao X, Kuang B, Gao J. Numerical simulation and experimental investigation on friction stir welding of 6061-T6 aluminum alloy. *Mater Des.* 2014;60: 94–101.
12. Nandan R, Roy GG, Lienert TJ, Debroy T. Numerical modelling of 3D plastic flow and heat transfer during friction stir welding of stainless steel. *Sci. Technol. Weld Join.* 2006;11(5): 526–537.
13. Nandan R, Roy GG, Debroy T. Numerical simulation of three dimensional heat transfer and plastic flow during friction stir welding. *Metall. Mater. Trans. A.* 2006;37(4): 1247–1259.
14. Nandan R, Roy GG, Lienert TJ, Debroy T. Three-dimensional heat and material flow during friction stir welding of mild steel. *Acta Mater.* 2007;55(3): 883–895.
15. Zhang Z, Zhang HW. Numerical studies on controlling of process parameters in friction stir welding. *J. Mater. Proc. Tech.* 2009;209(1): 241–270.
16. Jain R, Pal SK, Singh SB. A study on the variation of forces and temperature in a friction stir welding process : A finite element approach. *J. Manuf. Process.* 2016;23: 278–286.
17. Shi L, Wu CS. Transient model of heat transfer and material flow at different stages of friction stir welding process. *J Manuf Process.* 2017;25: 323–339.
18. Hasan AF. CFD modelling of friction stir welding (FSW) process of AZ31 magnesium alloy using volume of fluid method. *J. Mater. Res. Technol.* 2019;8(2): 1819–1827.
19. Roubaiy AOA, Nabat SM, Dl A. ScienceDirect An Investigation into Friction Stir Welding of Aluminium

Alloy 5083-H116 Similar Joints. *Mater Today Proc.* 2020;22: 2140–2152.

20. Nirmal K, Jagadesh T. Materials Today : Proceedings Numerical simulations of friction stir welding of dual phase titanium alloy for aerospace applications. *Mater Today Proc.* 2021;46: 4702-4708.

21. Andrade DG, Leitão C, Dialami N, Chiumenti M, Rodrigues DM. Modelling torque and temperature in friction stir welding of aluminium alloys. *Int J Mech Sci.* 2020;182: 105725.

22. Zhang HJ, Sun SL, Liu HJ, Zhu Z, Wang YL. Characteristic and mechanism of nugget performance evolution with rotation speed for high-rotation-speed friction stir welded 6061 aluminum alloy. *J Manuf Process.* 2020;60: 544–552.

23. Yadav A, Jain A, Verma R. Effect of tilt angle for conical pin tool with a conical shoulder on heat transfer and material flow using numerical simulation in friction stir welding. *Materials Physics and Mechanics.* 2023;51(3): 126–145.

24. Kumar A, Bansal SN, Chandraker R. Computational modeling of blast furnace cooling stave based on heat transfer analysis. *Materials Physics and Mechanics.* 2012;15(1): 46–65.

25. Arora A, Nandan R, Reynolds AP, DebRoy T. Torque, power requirement and stir zone geometry in friction stir welding through modeling and experiments. *Scr Mater.* 2009;60(1): 13–16.

26. Thomas WM, Johnson KI, Wiesner CS. Friction stir welding-recent developments in tool and process technologies. *Adv Eng Mater.* 2003;5(7): 485–490.

27. Sheppard T, Wright DS. Determination of flovv stress: Part 1 constitutive equation for aluminium alloys at elevated temperatures. *Metals Technology.* 1979;6(1): 215–223.

28. Sheppard T, Jackson A. Constitutive equations for use in prediction of flo\N stress during extrusion of alurniniul11alloys. *Materials Science and Technology.* 1997;13(3): 203–209.

29. Tello KE, Gerlich AP, Mendez PF. Constants for hot deformation constitutive models for recent experimental data. *Sci Technol Weld Join.* 2010;15(3): 260–266.

30. Hamilton C, Dymek S, Sommers A. A thermal model of friction stir welding in aluminum alloys. *Int. J. Mach. Tools Manuf.* 2008;48(10): 1120–1130.

31. Neto DM, Neto P. Numerical modeling of friction stir welding process: A literature review. *Int. J. Adv. Manuf. Technol.* 2013;65(1–4): 115–126.

32. Yang CL, Wu CS, Lv XQ. Numerical analysis of mass transfer and material mixing in friction stir welding of aluminum/magnesium alloys. *J Manuf Process.* 2018;32: 380–394.

About Authors

Amit Yadav iD Sc
Researcher (National Institute of Technology Kurukshetra, Kurukshetra, India)

Ajai Jain Sc
PhD, Professor (National Institute of Technology Kurukshetra, Kurukshetra, India)

Rajiv Verma Sc
PhD, Professor (National Institute of Technology Kurukshetra, Kurukshetra, India)

Periodic system of fullerenes from the mathematical standpoint

A.I. Melker [1], M.A. Krupina [2] ✉ iD

[1] St. Petersburg Academy of Sciences on Strength Problems, St. Petersburg, Russia

[2] Peter the Great St. Petersburg Polytechnic University, St. Petersburg, Russia

✉ ndtcs@inbox.ru

ABSTRACT
The types of classification for fullerenes' property are considered. It accumulates empirically found the horizontal and vertical symmetry of fullerenes which give a preliminary classification. Two different symmetries are united into a common symmetry producing the periodic system of fullerenes. This system may be considered as the topological lattice in the topological space of the points corresponding to the fullerenes. The system gives the general classification of fullerenes on the basis of symmetry.
KEYWORDS
carbon • fullerene • graph • growth • isomer • periodic system • topology

Classification, Appearance and Development

Property

The term classification (*Lat* classis – class + facere – do, execute) is defined as the act or process of arranging people or things (such as plants, animals, books in libraries, etc.) into groups in the dependence on their common features [1–3]. Historically the term is originated from the sixth Roman tsar Servius Tullius, (578-534 B.C.) who divided the Roman people into six classes according with their property, the sixth class having nothing [4].

Libraries

The classification of books has appeared simultaneously with libraries. The world's first genuine library was arranged by the Assyrian tsar Ashshurbanipal (668 - 626 B.C.) who has carried on many campaigns [5–8]. After the victories, he driven a chariot harnessed by four captive tsars in his capital Ninevia (the north of the modern Iraq). Contrary to his ancestors, he was rather well educated; he wielded three languages, including dead language Sumerian, liked reading and history, and even wrote poetry. In his big palace there were special rooms for the library. The manuscripts were on astronomy, geography, history, literature, law, trades and myths. The huge library contained more than 30 thousand of clay plates, each plate being 40 cm in the high. They contained 400 lines of cuneiform (*Lat* cuneus – wedge) signs on both sides. In the end of text there were given the elements of bibliographical description: heading, plate's number, the first words of the next plate, and the name of owner or copyist. The plates were kept in boxes. It's

interesting to note that the word *library* originated from the Latin word *librarium* what means a box for manuscripts or books.

Education

The book and knowledge classification was developing in parallel with education. The Roman system of education included seven fields of knowledge, so called seven crafts or "the seven liberal arts". Pupils studied trivium (1-st cycle: grammatics, dialectics, rhetoric) and quadrivium (2-d cycle: arithmetic, music, geometry, astronomy). The Latin both words mean crossing of three or four roads [4]. That standard education program was conserved in the middle-age schools of Europe, except of the principal addition – theology [9]. In due time, the schools had developed or were united into Universities [10]. However, the classified education has been carefully conserved [11].

In 1340 the professors of juridical faculty (Sorbonne) have adopted a resolution that any student should begin his education having a comprehensive knowledge of seven liberal arts. "We believe that if there is no base, it's no allowed to make a superstructure and that not by a breach of the sequence of degrees, but the rise to higher posts and sciences must be done gradually and timely. Since grammatics, logic, physics and other primary sciences are the way and base to other, more higher knowledge, we establish and prescribe that nobody is allowed to pretend to the degree of bachelor of cannon law at the juridical faculty in Paris, if he is not enough strong in primary knowledge".

To the end of the fifteen century the books were classified in accordance with the existing four faculties of the Universities, theological, philosophical, juridical and medical.

Real philosophy

The development of technique and natural sciences in West Europe in XVI-XVII centuries had led to the conclusion that the previous classification of knowledge is too narrow [12]. Some philosophers and writers, especially Michel Eyquem de Montaigne (1533-1592) and Francis Bacon (1561–1626), contradicted to speculative philosophy the knowledge based on experience which is connected with human nature [13–17]. In the beginning of the seventeenth century Sir Francis Bacon (1561–1626) had suggested classifying knowledge with respect to the ability of human spirit [15–17]. According to Bacon, memory originates history, imagination produces poetry and mind creates philosophy.

It should be mentioned that both philosophers were well educated; they knew foreign and ancient classical languages. Michel Montaigne studied law, at one time was a member of Bordeaux's parliament and later was elected the mayor of that city; he maintained friendly relations with Henri Bourbon, the future King Henri IV (1589-1610). Montaigne lived in the stormy period of Huguenot Wars (1562-1598). "In 1571 being 38 years old, tired by public duties, I decided to spend the rest of life devoting it to the Muses". In 1580, he traveled one year across Europe visiting Germany, Switzerland and Italy; in 1588 he was put for a short time into the Bastille. Montaige had exerted great influence on the intellectuals in many countries; in Russia he was highly appreciated by Pushkin, Herzen, Tolstoy and Gorky [14].

Francis Bacon succeeded to "practically philosophical outlook on things created by Montaigne" [14]. He studied at the Trinity College (Cambridge), then was incorporated in the English embassy in Paris, and due to his diplomatic work visited Germany, Spain, Poland, Denmark and Sweden [15]. Returning to England, Bacon had entered the Juridical Corporation where he studied jurisprudence and philosophy. As a jurist he took part in many trials concerning financial cases of the state. He was noticed and the new King Jacob I (1603-1625) at first knighted him and then he successively became Lord Keeper of the Great Seal, Lord Chancellor and Peer of England. In 1621, Bacon was accused of bribery; he had pleaded guilty, and although the penalty, heavy fine and Tower, was softened, his career had finished. Five years later he had died. According to his will, large sums were given to Oxford and Cambridge Universities for establishing the chairs of real philosophy.

It is interesting to note that Bacon is known especially because of the suggestion that he may have written some or all of Shakespeare's plays [3]. Francis Bacon (1561–1626) and William Shakespeare (1564-1616) leaved in one and the same time.

Branches of knowledge

The first complete classification of sciences on the base of the sequence of human cognition was created by André Marie Ampère (1775–1836) [18–20]. "In 1829 I prepared the course in general and experimental physics at French college. Two questions were appeared [20]:

1. General physics, what does it mean? What is the exact feature that differ it from other sciences?

2. What are the different fields of physics which can be considered as separate sciences or the parts of a more common science? "

To answer these questions, André Marie Ampère had distinguished the four stages of the knowledge corresponding to the evolution of science development: direct observation (auto-optical point of view), studying what is hidden in an object (cryptoristic point of view, from κρυπτος – secret + οριζω – determine), studying the changing of an object (troponomic point of view, from τροπη – turn + νομος – custom, law) ,discovering the reasons and consequences (cryptologic point of view).

"Such is the natural sequence of human cognition". The four standpoints can be united in two main ones. The first and second produce an elementary theory of an object; the third and fourth form a highest theory where the subjects are studied taking into account correlation and mutual connection.

Taking this principle as a base, Ampère had assumed that general physics can be divided into four groups: experimental physics (the first stage, auto-optical standpoint), chemistry (the second stage, cryptoristic standpoint), mathematical physics (the third stage, troponomic standpoint) and atomology (the forth stage, cryptologic standpoint).

On this concept, Ampère at first had considered physics and then other sciences. As a result, in 1832 he had created "The natural classification of sciences". Ampère distinguished the orders of sciences. The science of the first order unites all the knowledge referring to one object. It can be divided into two sciences of the second order which correspond to the main points of view, elementary and high. In their turn, each of

these sciences can be divided into two sciences of the third order referring to one of the four stages of human cognition. "Just a man has received some number of notions about any object; he tries to arrange them in a definite order for using them better. Such is the origin of classifications".

The existing sciences contained only a part of all the possible 128 sciences of the third order classified by Ampère, and he had predicted new sciences, giving them mostly Greek names. Thus he foresaw the appearance of medical physics but he is known especially because of predicting the science of the third order – cybernetics (from κυβερνητικη scilicet τεχνη). The ancient Greeks used that word as sea-craft, but Ampère accepted meaning of the word as management generally. It was done a hundred years before the appearance of cybernetics by Norbert Wiener (1894–1964).

"Thousands of people pronounce the word 'ampere' knowing nothing about that man. While his mortal remains had turned to dust, his name became the common property of mankind" (M. Berthelot, 1827–1907). André Marie Ampère (1775–1836) was born in Lion, in the family of a rich liberal merchant. When he learned to read, he began to eat up all the books being in the large library of his farther and in the Lion city library. At the age of twelve, he became proficient in differential calculus; at that he learned Latin, to read Euler and Bernoulli in the original, later he learned ancient Greek and Italian. At the age of fourteen, he studied all the twenty volumes of the Encyclopedia by Denis Diderot (1713–1783) and Jean le Rond d'Alembert (1717–1783). Having no teachers and not going to any school, he was well trained gaining wisdom by experience. In 1793 his farther was executed by Jacobeans, and for more than one year he was in mental disorder. After that Ampère successively indulged in botanic and poetry (since 1795, verses in French and Latin), mathematics (1802), chemistry (1816, he had done the first classification of chemical elements), physics (1820, he created new science - electrodynamics). Last years he engaged in systematization of flora and fauna, and all the knowledge.

Classification of fullerenes

Periodic system of fullerenes

In 2017, we created the periodic system of fullerenes, based on symmetry principles. It consists of horizontal series and vertical columns (groups) [21–30]. The horizontal series form the Δn periodicities, where the fullerene structure changes from threefold symmetry to sevenfold through four, five and sixfold ones. The vertical columns include the fullerenes of one and the same symmetry s, the mass difference of perfect fullerenes for each column being equal to a double degree of symmetry $\Delta m=2s$. The first version of the system contained the series beginning with $\Delta n=6$, later the series $\Delta n=2, 4$ were added. The full version is given below. We suppose the fullerenes of one and the same column have similar physical and chemical properties.

Two columns of three fold symmetry differ by the shape of their apices. The fullerenes of S-symmetry column have two sharp apices, the third order symmetry axis going through them; those of T-symmetry have two truncated apices, the third order axis going through the centers of equilateral apices triangles (Table 1).

Table 1. Periodic system of fullerenes

Series \ Columns	Symmetry of fullerenes				
	3-fold S ($\Delta m=6$)	3-fold T ($\Delta m=6$)	4-fold ($\Delta m=8$)	5-fold ($\Delta m=10$)	6-fold ($\Delta m=12$)
$\Delta n=2$	**C_2**	**C_6**	**C_8**	**C_{10}**	**C_{12}**
$\Delta n=4$	**C_8**	**C_{12}**	**C_{16}**	**C_{20}**	**C_{24}**
$\Delta n=6$	**C_{14}** C_{16} C_{18}	**C_{18}** C_{20} C_{22}	**C_{24}** C_{26} C_{28} C_{30}	**C_{30}** C_{32} C_{34} C_{36} C_{38}	**C_{36}** C_{38} C_{40} C_{42} C_{44} C_{46}
$\Delta n=8$	**C_{20}** C_{22} C_{24}	**C_{24}** C_{26} C_{28}	**C_{32}** C_{34} C_{36} C_{38}	**C_{40}** C_{42} C_{44} C_{46} C_{48}	**C_{48}** C_{50} C_{52} C_{54} C_{56} C_{58}
$\Delta n=10$	**C_{26}** C_{28} C_{30}	**C_{30}** C_{32} C_{34}	**C_{40}** C_{42} C_{44} C_{46}	**C_{50}** C_{52} C_{54} C_{56} C_{58}	**C_{60}** C_{62} C_{64} C_{66} C_{68} C_{70}
$\Delta n=12$	**C_{32}** C_{34} C_{36}	**C_{36}** C_{38} C_{40}	**C_{48}** C_{50} C_{52} C_{54}	**C_{60}** C_{62} C_{64} C_{66} C_{68}	**C_{72}** C_{74} C_{76} C_{78} C_{80} C_{82}
$\Delta n=14$	**C_{38}** C_{40} C_{42}	**C_{42}** C_{44} C_{46}	**C_{56}** C_{58} C_{60} C_{62}	**C_{70}** C_{72} C_{74} C_{76} C_{78}	**C_{84}** C_{86} C_{88} C_{90} C_{92} C_{94}
$\Delta n=16$	**C_{44}** C_{46} C_{48}	**C_{48}** C_{50} C_{52}	**C_{64}** C_{66} C_{68} C_{70}	**C_{80}** C_{82} C_{84} C_{86} C_{88}	**C_{96}** C_{98} C_{100} C_{102} C_{104} C_{106}
$\Delta n=18$	**C_{50}**	**C_{54}**	**C_{72}**	**C_{90}**	**C_{108}**

Theory of sets and fullerenes. Topological symmetry

From the standpoint of mathematics [29], the series and columns are sets. The notion 'set' or 'totality' is considered as one of the simplest mathematical notions. It is not defined and is explained by means of examples. For example, we may say 'a set of books' composing a library. At that the books are the elements of the set. To determine a set, it is necessary to point out such property of the set elements, what all the elements have and only they. In our case we may consider the fullerenes of one and the same column as the set $\Delta n=2m$.

For the sets it's possible to perform different operations. We need such operation as *crossing of two sets*, i.e. the set of elements being common to both sets. Joining the sets of series and columns into one set (the periodic systems of fullerenes) we have obtained the *crossing of those two sets*, i.e. the fullerenes being common to both sets. In our case they are regular (perfect) fullerenes; they are denoted by *bold symbols*. In doing so, we have obtained the possibility to mark out the regular part of the fullerene set, or the *ordered subset* which elements are the fullerenes of a regular shape. Other fullerenes compose the *subset of imperfect fullerenes*. However there is a curtain order in this subset, i.e. the imperfect fullerenes produce *partially ordered subset*.

By analogy with physics of crystals, consider what it means. In crystal physics there are such notions as a short-range and long-range order. In real crystals, the long-range order is impossible because defects violate a translational symmetry [28]. Nevertheless the long-range order is observed experimentally; however diffraction lines differ from theoretical δ–functions. The lines become broader and lower throughout the height, but they conserve a sequence, in other words they have a fixed place. Such real long-range order is known as a *topological* one (τοπος – place).

By analogy with physics of real crystals, we assume that imperfect fullerenes are originated in due to the appearance of extra carbon dimers which play the part of defects. In real crystals the number of defects is much less than the number of the atoms forming a

crystal lattice. Likewise, in imperfect fullerenes the number of the extra dimers that distort the structure is many fewer than the number of regular atoms (It's clear from the periodic system). For this reason, the symmetry violation takes place only in a local region around the defect (extra dimer) but in the most part of a fullerene the symmetry is conserved. We have named such symmetry of imperfect fullerenes *topological symmetry* [22].

Topology and fullerenes

In the sentences above we used the adjectives (the part of speech being the indicator of a subject), *topological* long-rang order, *topological* symmetry. What does the noun, *topology*, mean? In mathematics, topology is defined as its part in which the idea of continuity of space and time is studied [29]. The formal definition of space and time is based on the notion of a set. The space is defined as the set of the elements (points) in which some relations between the points are fixed, these relation being similar to common space relations.

Historically the first mathematical space is the 3-dimensional Euclid space *(Ευκλειδης, IV–III Ages B.C.)*, which corresponds with the real space approximately. The general notion of space is the result of generalization and modification of the Euclid geometry. The set of mathematical functions, the set of states of a physical system, the set of polyhedrons make up the spaces where the points are functions, states, polyhedrons. These sets are understood as spaces if there defined the *relations between the points*, e.g. the distances and properties which depend on them. For example, the distance between the states is defined as the difference of energies of the states. A *figure* is defined as an arbitrary set of points.

The *general relation* in any set is the *relation of belonging*: a point belongs to a set; a set is a part of another. If only these relations are taken into account, the set has no geometry and therefore it is not a space. However, if to separate some *special figures* (special sets of points), the laws of point connection with these figures create the geometry of space. The laws are named axioms. In particular, the Euclid geometry is created through the axioms of belonging, one of which looks like: through any two points it is possible to draw a line and only one. Here the special figure is the line.

As a special set, one can choose instead of points their neighborhood. At that, under the action of connection laws there appears a sort of space, so called *topological space*. All sorts of objects are studied in that space. This version of geometry is the most general geometry, and it is named *topology*.

Consider some examples. A special case of the more general topological space is a metric space which is generated by some metrics. A metrics (μετρον – measure) is the distance between two points of a set. The number scale, Euclid space of any dimensions, phase space of states of a physical system, all of them is an example of the metric spaces.

The topological spaces are classified into different types. These classes had appeared under the influence of different branches of mathematics and other sciences, which have different aims and they are unlike to each other, e.g. the sets of functions and polyhedrons. The latter is defined as the set built in a regular manner from elementary figures such as line segments, triangles, tetrahedrons, prisms etc.

The main problem of topology is considered to be revealing and studying topological properties of spaces or *topological invariants*, i.e. the properties of figures which are conserved during any continuous similar mapping one topological space into other. In particular, the number of measurements of a figure (dimensionality) is a topological invariant. We assume that topological long-rang order and topological symmetry are also topological invariants.

Coordinates, topology and periodic system of fullerenes

In 1637, René Descartes (*Cartesius, 1596 - 1650*) had published "Geometry", which incorporated into algebra all the classical geometry and later was named analytic geometry [29,31]. Nine years he studied at collège la Flèche, one of the best French educational institutions established by Jesuits by approbation of King Henri IV (1589-1610), who gave them his family castle 'château Nef'. Descartes studied at first Latin, ancient Greek, grammatics, dialectics, rhetoric, theology and scholasticism. The last three years were devoted to philosophy which embodied logics, ethics, physics, mathematics and Aristotle's metaphysics. Descartes highly appreciated the quality of education in Jesuit's college.

In 1615, he entered the Poitiers University for studying law and medicine. Having become a bachelor, he thirteen years traveled across Europe, visiting Italy, Poland, Denmark, Germany, Czechia and the Netherlands. It was the stormy period of Thirty Years' War (1618-1648). Descartes had served in three Armies: Dutch, Bavarian and Hungarian. Beginning with 1628, he had lived twenty years in the Netherlands devoting himself to science. In 1649, he arrived to Stockholm, having accepted the invitation of Queen Christina, who wanted to establish Sweden Academy of Sciences. The unusual severe climate led to pneumonia and some months later he had died.

Descartes was an adherent of real philosophy, but contrary to his forerunners, he was not only well educated in the humanities, but well educated in natural philosophy. He had searched a general method of reasoning. Whereas Montaigne and Bacon evolved the real philosophy on the base of inductive reasoning, Descartes developed deductive reasoning. "In those times the only science on nature, which had a systemized building, was mechanics [31]. A key to understanding mechanics could be given by mathematics." Thus the development of the real philosophy led to mathematics. "Taking in account that among the all seeking the truth only the mathematicians had managed to find precise and evident proofs, I did not doubt that it was necessary to begin with mathematics" [17].

Cartesian coordinates. Descartes' geometry contained the method of coordinates what lay in the following. We take two straight lines *Ox* and *Oy* intersecting at point *O* and perpendicular to each other. The indefinite straight line *Ox* is known as the *axis of the abscissas* or the *x-axis*; the indefinite straight line *Oy* is called the *axis of the ordinates* or the y-*axis*; point *O* is called the *origin of the coordinates* (abscisio – cut off, ordinatus – ordered, co – jointly). The lines *Ox* and *Oy* together with origin *O* make the Descartes' system of coordinates.

The position of any point *M* in this system is defined in the following manner. Let us assume M_x and M_y to be the projections of this point onto the axes of the coordinates,

the values of segments OM_x and OM_y being numbers *x* and *y*; they are known as the Cartesian coordinates. The point *M* is denoted as *M (x, y)*.

Topological lattice. It is a set of topological-space points having *whole coordinates* with respect to some system of coordinates [29]. In essence, the periodic system of fullerenes is the lattice of a definite plane of a topological space. Here the space points having whole coordinates are the knots of the lattice. A point *M* is the fullerene C_m of mass *m*, an abscissa *x* is the whole coordinate *s* (the order of symmetry) and an ordinate y is the whole even coordinate Δn.

The abscissa *s* takes the value 3S, 3T, 4, 5, 6 and 7; the ordinate Δn = 2, 4, 6, 8, 10, 12, 14, 16, 18. At that, the mass of the point *M* (the mass of fullerene C_m) can be calculated with the following formula: *m=s×Δn*. The one exception is represented by the points having the abscissas *s=3S*; here the formula takes the form: *m=s×Δn - 4*. The point *M* together with the coordinates can be written as C_m *(s, Δn)*. For the fullerenes of the third order symmetry, it is necessary to add argument S or T, for example, C_{32} (3S, 12) and C_{36} (3T, 12). In principle, one may include into the arguments of the point of topological space other values, e.g. energy. In such a form, the periodic system of perfect fullerenes was presented in [21] without evidence for its topological nature.

In the case of the complete periodic system of fullerenes, which embodies perfect and imperfect fullerenes, the situation becomes more complex. Here it is necessary to include into the topological lattice not only the knots but isolated points what correspond to imperfect fullerenes. These points are located on the coordinate lines parallel to the axis of the ordinates. For example, the coordinate line going through the abscissa *s=3S* has the following knots: **C_2, C_8, C_{14}, C_{20}, C_{26}, C_{32}, C_{38}, C_{44}, C_{50}**.

Two points should be added in each interval between the knots (perfect fullerenes). As a result, the coordinate line takes additional points located between the knots: **C_2, C_8, C_{14},** C_{16}, C_{18}**, C_{20},** C_{22}, C_{24}**, C_{26},** C_{28}, C_{30}**, C_{32},** C_{34}, C_{36}**, C_{38},** C_{40}, C_{42}**, C_{44},** C_{46}, C_{48}**, C_{50}.**

In a similar manner, it should be dealt with the fullerenes of other symmetry. In the general case, the number of added points in each interval between the knots is equal to *s-1*.

Graph representation. The periodic system of fullerenes can be also presented as a graph, if to connect some points of the topological lattice with arcs. If to specify direction to these arcs, we obtain an orientable graph. For example, let us connect the points of the number axis, such as **C_{26}**→C_{28}→C_{30}→**C_{32}**. Then we obtain the finite-arc sequence which is called a route [30]. In our case, the route reflects the growth of the fullerene in the interval (**C_{26}, C_{32})** through embedding carbon dimers. If to connect all the points corresponding to the fullerenes having one and the same mass, but different symmetry, we obtain the *route of isomers*. Inputting the routes into the periodic system of fullerenes allows lead well-directed investigations.

Conclusion

Empirically found horizontal and vertical symmetry allows give a preliminary classification of fullerenes. Two different symmetries are united into a common symmetry producing the periodic system of fullerenes. This system may be considered as the

topological lattice in the topological space of the points corresponding to the fullerenes. The system gives the general classification of fullerenes on the basis of symmetry.

References

1. Lyokhin IV, Petrov FN. (eds.) *Dictionary of Foreign Words*. Moscow: GIINS; 1954. (In Russian)

2. Prokhorov YuV. (ed.) *New illustrated encyclopedic dictionary*. Moscow; 2000. (In Russian)

3. *Longman Dictionary of English Language and Culture*. UK: Longman Group Limited; 1992.

4. Dvoretsky IH. *Latin-Russian Dictionary*. Moscow: Russian Language; 2000. (In Russian)

5. Mikhailov AI, Cherny AI, Gilyarevsky RS. *Fundamentals of Computer Science*. Moscow: Nauka; 1968. (In Russian)

6. Mishulin AV. (ed.) *History of the ancient world*. Moscow: GUPI Min. Pros. RSFSR; 1950. (In Russian)

7. *World history in 24 volumes. V. 3, Age of Iron*. Minsk; Modern Writer, 2000. (In Russian)

8. Ryzhov K. *Monarchs of the ancient world*. Moscow: Veche; 2010. (In Russian)

9. Alphan L. *Great Empires of the Barbarians*. Moscow: Veche; 2006, (In Russian)

10. Melker AI. *Noophysics (Science and Scientists)*. St. Petersburg: St. Petersburg Academy of Sciences on Strength Problems; 2006. (In Russian)

11. Stepanova VE, Shevelenko AYA. *History of the Middle Ages, part II*. Moscow: Enlightenment; 1974. (In Russian)

12. Semenov VF. *History of the Middle Ages*. Moscow: Enlightenment; 1975. (In Russian)

13. Montaigne M. *Experiments, books one and two*. St. Petersburg; Crystal; 1998. (In Russian)

14. Montaigne M. *Experiments, boor three.* St. Petersburg; Crystal; 1998. (In Russian)

15. Vasilyeva EK, Pernatyev YS. *100 famous sages*. Kharkov; Folio; 2008. (In Russian)

16. Smirnov SG. *Problem book on the history of science*. Moscow: Science – Interperiodica; 2001. (In Russian)

17. Kudryavtsev PS. *Course on the history of physics*. Moscow: Enlightenment; 1974. (In Russian)

18. Arago F. *Biographies of famous astronomers, physicists and geometers, volume II, III*. Moscow: Research Center Regular and Chaotic Dynamics; 2008. (In Russian)

19. Golin GM. *Classics of Physical Science*. Minsk; Higher School; 1981. (In Russian)

20. Povarov GN. *Ampere and cybernetics*. Moscow: Soviet Radio; 1977. (In Russian)

21. Melker AI, Krupina MA. How the periodic table of fullerenes was born. *Nonlinear Dynamics and Applications*. 2022;28: 200-209.

22. Melker AI, Krupina MA. It's a long, long way to the periodic table of fullerenes. In: *Perspective Materials, Vol. 10*. Togliatti, Russia: Togliatti State University; 2023. p.154-240. (In Russian)

23. Melker AI, Krupina MA, Matvienko AN. Nucleation and growth of fullerenes having three-fold T-symmetry. *Frontier Materials and Technologies.* 2022;2: 383-394.

24. Melker AI, Krupina MA, Matvienko AN, Nucleation and growth of fullerenes and nanotubes having four-fold symmetry. *Materials Physics and Mechanics.* 2021;47(1): 315-343.

25. Melker AI, Krupina MA, Matvienko AN, Nucleation and growth of fullerenes and nanotubes having five-fold symmetry. *Materials Physics and Mechanics.* 2022;49(1): 51-72.

26. Melker AI, Krupina MA, Matvienko AN. Isomers of fullerenes C_{58} and C_{60}. *Nonlinear Phenomena in Complex Systems.* 2024;**27**(2): 1-18.

27. Melker AI, Krupina MA. Periodic system of fullerenes: the column of six-fold symmetry. *Materials Physics and Mechanics.* 2024;52(5): 127–147.

28. Melker AI, Krupina MA, Zabrodkin EO. Changing symmetry during the growth of fullerenes originated from the nuclei of six-fold symmetry. *Materials Physics and Mechanics.* 2024;52(5): 148–160.

29. Prokhorov YuV. *Mathematical encyclopedic dictionary.* Moscow; 1988. (In Russian)

30. Kosevich AM. *Physical mechanics of real crystals*. Kyiv; Naukova Dumka; 1981. (In Russian)

31. Stroik DYa. A brief outline of the history of mathematics. Moscow: Nauka; 1984. (In Russian)

32. Basaker R, Saaty T. *Finite graphs and networks*. Moscow: Nauka; 1974. (In Russian)

About Authors

Alexander I. Melker Sc

Doctor of Physical and Mathematical Sciences
Professor (St. Petersburg Academy of Sciences on Strength Problems, St. Petersburg, Russia)

Maria A. Krupina 🆔 Sc

Candidate of Physical and Mathematical Sciences
Associate Professor (Peter the Great St. Petersburg Polytechnic University, St. Petersburg, Russia)

Production techniques and properties of particulate reinforce metal matrix composites: a review

S. Agarwal ✉ (iD), **S. Singh** (iD)

National Institute of Technology Kurukshetra, Haryana, India

✉ saumy_61900049@nitkkr.ac.in

ABSTRACT
The production techniques intended for synthesizing the metal matrix composites (MMCs) with particle-sized reinforcements are summarized and also the influence of reinforcement particles on various properties of MMCs is discussed. Stir casting is one of the largely used production practice for such MMCs as it is economical but there is some compromise with quality of composite due to agglomeration of reinforcement particles within the matrix phase. Such problem does not occur when MMCs are fabricated using ultrasonic stir casting process, squeeze casting and powder metallurgy technique. Tensile strength and hardness of MMCs were improved by 9 to 110 % and by 5 to 120 %, respectively, by adding reinforcement (0.5% to 30%). Wear rate and corrosion rate were decreased from 5.5 to 3.7 mm^3/km and 0.0396 to 0.0178 mm/yr, respectively. But some properties like ductility, % elongation, toughness and impact strength of the composite are compromised due to the brittle nature of the reinforcement.
KEYWORDS
metal matrix composites • reinforcements • mechanical properties • stir casting • powder metallurgy

Introduction

In aerospace and automotive industry there are always a requirement of high strength, low weight and high toughness material. Strength and toughness also have inverse relationship. So, how to get such a material? The answer is composites. Composites possess such type of exceptional combination of mechanical properties and other properties also. Two or more materials with distinct chemical compositions and phases make up a composite [1]. The matrix-phase of the composite transfers the load to the reinforcement whereas the reinforcement-phase of the composite sustains the load and provide the strength required to the composite [2]. For classification of composites refer to Fig. 1. Aluminium, copper, magnesium and titanium are most commonly used matrix materials in fabrication of metal matrix composites (MMCs) whereas the reinforcement material can either be metal or non-metals like ceramics and organic materials [3,4]. Various kinds of reinforcement materials that are used in MMCs are summarized in Table 1. Using coated graphite (Gr) particles as reinforcement and Aluminium metal as the matrix, the first MMCs were created in the mid-1960s [5]. The weight percentage of matrix material in MMCs is typically greater than that of reinforcement material. With addition of reinforcement material, various material properties of MMCs can be tailored [6] like tensile strength, hardness, wear resistance, corrosion resistance, impact

strength etc. The reinforcement material can either be in form of small particles, whiskers or fibers [7].

The main focus in this review is on the MMC with particle-sized reinforcements (or PMMCs) as they are cost-effective in terms of procurement and production cost. In these types of composites, the reinforcement material is in the form of small particles i.e. there is no long dimension [8]. Due to cost restrictions, MMCs find their usage mainly in structural and engineering related industries such as automobile industry, aerospace industry, ship-building industry, and sports industry where the product requires good strength with minimal density or weight [9]. MMCs are used in Boeing aircrafts (787, 777) and fighter jets (F-16). Door access panels, fuel lid cover, and rotor blades sleeve are made of MMCs. MMCs also find their applications in drive shafts, brake discs, and cylinder walls in an automobile. Sports products like track shoes, tennis rackets, and golf sticks can also be made using MMCs [10,11].

The problems with conventional processing of MMCs are agglomeration of particles, low density, low wettability between matrix and reinforcement material and thermal instability due to different coefficient of thermal expansion [12,13]. To overcome such issues various alternative fabrication methods are developed and also few modifications are made into the conventional processes like two-step stir casting process or ultrasonic-assist stir casting process [14]. These various types of production techniques of PMMCs, their process parameters along with the influence of particle-sized reinforcements on the properties of the fabricated composites are discussed in this paper through numerous past research articles.
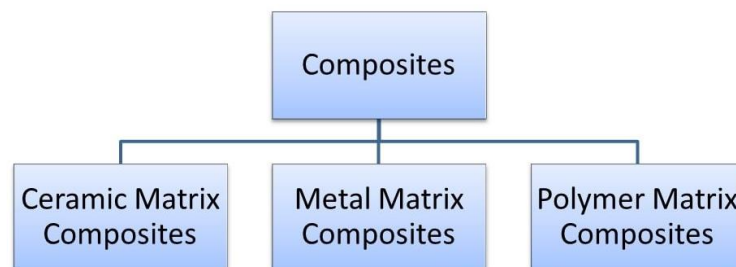
Fig. 1. Classification of composites based on matrix material

Table 1. Different reinforcement materials used in MMCs

Reinforcement Types		Examples
Ceramic	Borides	TiB_2, ZrB_2 [15,16]
	Carbides	SiC, TiC, WC, B_4C [17–20]
	Nitrides	Si_3N_4, BN [21,22]
	Oxides	Al_2O_3, ZrO_2, Cr_2O_3, TiO_2 [23–25]
	Carbon allotropes	Graphite, graphene, fullerene, CNT, carbon fibres, MWCNT [26–30]
Organic		Flyash, ricehusk, red mud [31–34]

Production techniques of particle-reinforced metal matrix composites

The production techniques for the particle-reinforced metal matrix composites (PMMCs) are illustrated in Fig. 2. Stir casting and squeeze casting are the most commonly used liquid-state techniques for the synthesis of MMCs, whereas powder metallurgy is preferred among the various solid-state techniques [35]. In this review paper discussions will be on stir casting, squeeze casting and powder metallurgy (PM) techniques along with recent modifications made by researchers.

Fig. 2. Different types of production techniques for MMCs

Stir casting

One of the frequently used fabrication techniques for casting MMC with ceramic reinforcements was commenced in 1968 by S. Ray [36,37]. It is an economical process and provides better density to the composite as compared to that of solid-state techniques like powder metallurgy [38]. The stir casting setup can be seen in Fig. 3, where the composite is formed by mixing reinforcement (particles or fibres) into the liquid melt pool (matrix phase) with the help of a mechanical stirrer that is electrically fitted. The sti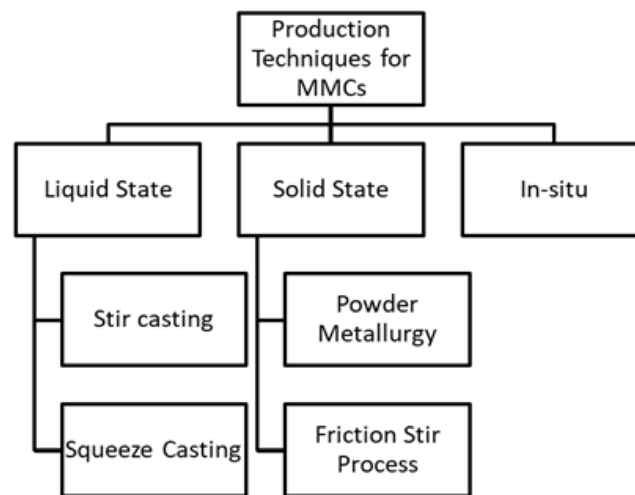rring action helps in improving the wettability between ceramic reinforcement and liquid metal [39]. In order to reduce blow holes and porosity in the casted composites, shielding is done using Argon or Nitrogen gas. Degassing agents such as Hexachloroethane (C_2Cl_6) or creating a vacuum condition can also remove trapped gases in the melt pool [40–42].

In 2018, Faisal and Kumar [43] fabricated an Aluminium matrix composite (AMC) with Silicon carbide (SiC) nanoparticles using a conventional stir casting approach. Aluminium alloy AA2219 was melted at 800°C and preheated SiC was added with wt. % varying from 0.5 to 2.5 %. Changes in the mechanical properties and tribological properties were observed with the change in SiC content. Mohanavel et al. (2018) [44] stir casted AA6082/Al_2O_3 nano-MMCs with reinforcement wt. % varying up to 3 %. The furnace temperature was 850 °C and the melt mixture was stirred for 20 minutes. Madhusudhan et al. (2017) [23] developed AA7068/ZrO_2 (upto 8 %) MMCs using stir casting route. C_2Cl_6 was added to the melt mixture to remove the air and other gases, i.e.

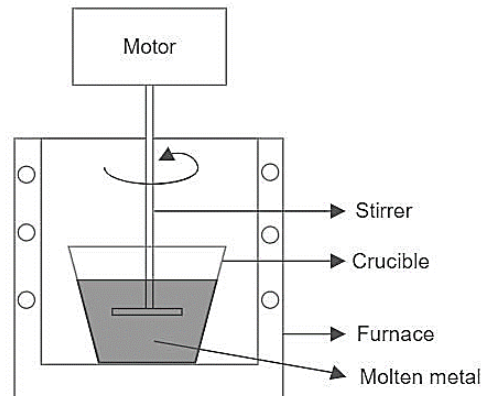improve permeability. The mixture was stirred at 200 rpm for the homogeneous mixing of particles in the pool.

Fig. 3. A simple schematic of stir casting set-up

The problem with stir casted composites is that with an increase in reinforcement volume there is the increased agglomeration of particles within the matrix [45]. This occurrence can be a result of a decrease in wettability between particles which could reduce interfacial bonding between them that could lead to debonding of particles. The reason behind poor wettability can be the weak adhesion between the particles due to the layer of contaminants and the presence of oxide films on melt surface can hinder wettability between the liquid metal and ceramic particles which causes agglomeration at interfaces [46]. The scanning electron microscopy (SEM) test result of the fabricated AMC through stir casting route by Sharma et al. (2015b) [47] revealed the clustering of reinforcement particles in the aluminium matrix when wt. % of graphite was increased up to 12 %.

The wettability could be improved either with a coating of the reinforcement particles or with the addition of some dopants like magnesium (Mg) [48]. Few modifications in the conventional stir casting method could improve mixing of reinforcement particles preventing the formation of a cluster of particles such as using an ultrasonic probe, two-step casting, hot extrusion etc. [49,50].

In 2020, Purohit et al. [51] used ultrasonic probe assist stir casting followed by hot forging to fabricate MMC with an Aluminium alloy Al6061 as matrix and nano-Al_2O_3 (2 to 3 %) powder as reinforcement. The distribution of reinforcement particles in casted composites and hot forged, as observed through SEM test, was uniform which was further improved with heat treatment. Hashim et al. (2001) [52] did extensive research on improving the wettability between reinforcement and matrix materials. It was improved by the addition of filler material such as Mg upto 1 % by weight and also by stirring the mixture at a semi-solid state. Singh & Goyal (2016) [45] fabricated a hybrid AMC with SiC and B_4C (5 to 20 %) as reinforcements. To enhance the wettability and bonding between the two phases, Mg powder was added. Al/SiC based MMC was manufactured by Kaushik & Singhal (2018) [53] using a modified two-step stir casting procedure accompanied by mixing of 1 wt. % Mg powder. Satisfactory mixing of particles was observed till 7 wt. % of SiC reinforcement particles.

With Ultrasonic assist stir casting, manufacturing of the metal matrix composites with different metal matrix materials (like magnesium, titanium, copper etc.) becomes easier as compared to the conventional stir casting technique [54]. In 2010, Z.H. Wang et al. [55] produced Mg/SiC nano-MMC using ultrasonic stir casting technique where matrix material was Magnesium alloy AZ91. Qi et al. [56] produced Ti/TiC (10 to 20 %) composites through stir casting process, where electromagnetic stirring of melt pool was done in order to produce homogeneous mixing of TiC particles within the liquid titanium melt.

Brief information about the matrix and reinforcement material and process parameters used by various researchers in the stir casting procedure can be found in Table 2.

Table 2. Materials and process parameters used in stir casting

Matrix	Reinforcement	Process parameters	Remarks
LM4 [15]	$(TiB_2)_P$	800 °C and 500 rpm	$(TiB_2)_P$ were preheated at 600°C
AZ91 [57]	$(SiC)_P$ and Gr	680 °C	An aluminite coated stirrer was used.
Al6061 [58]	$(TiB_2)_P$	750 °C and 450 rpm	The melt was stirred in semi-solid form.
LM6 [59]	$(ZrO_2)_P$	850 °C and 950 rpm	Stirring was done with drill machine at 950 rpm for 15 minutes.
Al6061 [60]	$(ZrO_2)_P$	700-800 °C and 350 rpm	NH_4Cl and Mg were added for degassing and improvement in wettability.
Al6063-T4 [61]	$(TiO_2)_P$	850 °C and 450 rpm	Stirring was done with graphite mixer at 450 rpm for 4 minutes.
Al2219 [62]	$(TiC)_P$	750 °C and 300 rpm	C_2Cl_6 was added for degassing.
Al6101 [63]	Gr	800 °C and 550 rpm	Composites were heat treated as per T6 std.
Al+4.5%Cu [64]	$(Al_2O_3)_P$	1000 °C and 30 min	Exothermic reaction took place which formed Al-Cu phases
Al7075 [65]	$(Al_2O_3)_P$ and Gr	850 °C and 500 rpm	Spiral shaped stirrer was used and composites were heat treated afterwards.
Al6061 [66]	$(Al_2O_3)_P$	800 °C and 200 rpm	C_2Cl_6 was added for degassing.

Squeeze casting

In this method, MMC is formed by applying high pressure to the mixture of molten metal and reinforcement particles [67]. In this method, either the liquid mixture of metal matrix and ceramic or organic reinforcement are compressed together to the solid form (direct casting) or the molten metal is made to infiltrate the preform made of reinforcement material by applying pressure (indirect casting) [68]. An indirect route is generally preferred for casting MMCs with ceramic reinforcements. In comparison to stir casting, squeeze casting does not require a riser and runner thereby material wastage is reduced to the bare minimum. Also, there is improvement in the wettability between particles along with less probability of agglomeration at interfaces and low porosity due to applied pressure [69–71].

In 2020, Patil et al. [72] fabricated an Al-4.5%Cu matrix composite reinforced with Al_2O_3 fibres (10, 20 and 30 %) using the Squeeze Casting method. The alloy was melted at 750 °C and it was pressed against the preform at a pressure varying from 70–100 MPa.

Feng et al. (2008) [69] developed the hybrid composite with Aluminium borate whiskers (ABOw) and Tungsten oxide particles (WO_{3p}) as reinforcement materials and 99.6 % pure Aluminium as the matrix, using the Squeeze casting method. The pressure applied was 80 MPa. The hybrid preforms of WO_{3p} and ABOw were made using silica gel as a binder. Homogeneous mixing of both the reinforcements was observed in the hybrid composite. Gurusamy et al. (2014) [67] analysed the mechanical behaviour of the Al/10%SiC MMC developed using the Squeeze casting process, as a function of melt and die temperatures. The pressure used was 100 MPa. From the SEM test of the samples with varied melt temperatures, it was evident that the agglomeration of the particles was more at low melt temperatures and it was less at higher melt temperatures. The optimum die temperature at which the yield and impact strength were maximum was 350 °C.

Succinct information about the materials and process parameters (alloy melt temperature and pressure applied) used in squeeze casting by some of the previous researchers can be found in Table 3.

Table 3. Materials and process parameters used in squeeze casting

Matrix	Reinforcement	Process parameters	Remarks
LM6 [31]	Flyash	800 °C and 3 MPa	The stir-squeeze procedure was followed.
A356 [73]	$(SiC)_P$	800 °C, pressure: 0, 30 to 130 MPa	Low porosity, high density and better distribution of particles at high pressures above 50 MPa.
Al4032 [74]	$(SiC)_P$	750-800 °C and 100 MPa	Uniform distribution of SiC.
Al6061 [70]	$(SiC)_P$	800 °C and 100 MPa	Homogeneous distribution of reinforcement.
Al7075 [75]	$(Al_2O_3)_P$	750 °C and 125 MPa	Stir-squeeze route was used.

Powder metallurgy

It is a frequently used solid-state fabrication technique where both the matrix and reinforcement materials are in form of small particles or powder. The complete procedure for the PM technique can be seen in Fig. 4. The powders are mixed and ball milled in the required ball to powder (BPR) ratio. The mixture is then pressed with high pressure to form a green compact which then is then sintered at elevated temperatures [76]. It is a costly method but there is no wettability problem between reinforcement and matrix material, unlike the stir casting method. It also provides better distribution of particles as compared to the stir casting method [77].

Fig. 4. Steps in PM technique

In 2014, Ashwath and Xavior [78] developed an Al2900 matrix composite with SiC, Al_2O_3 and Graphene as reinforcement materials (10 to 20 %) using the PM route. The powders were all mixed and ball milled followed by compaction at 650 MPa and sintering at a temperature of 550 °C for 10 to 15 min. Al-based composites were manufactured with 0.5 to 4.5 % TiO_2 reinforcement by Nassar and Nassar (2017) [79] with help of the PM method where the powders were first ball-milled and then compacted at a pressure of 100 MPa. Sintering was done for the compacted samples at a temperature of 450 °C in the protective environment of Argon.

With some further treatment like extrusion and heat treatment after developing MMC through the Powder metallurgy technique, the hardness of composite and mixing of reinforcement particles can be improved [80]. Al-Cu/SiC composite was synthesized by Z. Wang et al. (2010) [77] using the powder metallurgy method followed by hot extrusion. Al-Cu and SiC powders were first ball milled at a BPR ratio of 4:1 followed by compaction at a pressure of 200 MPa. The compacted mixture was sintered at 420 and 570 °C and was then hot extruded. There was an improvement in the homogeneous mixing of reinforcement particles due to extrusion.

Aluminium metal matrix is mostly preferred when fabricating any MMC using conventional stir casting process but through the Powder Metallurgy process, different matrix materials can be used [81]. Some modifications can also be made in the steps of PM process for manufacturing different types of MMCs [28]. Magnesium powders usually get burnt during ball milling so the composite powders are mixed and stirred within the solvent like ethanol. The powders are then dried in vaccum followed by compaction and sintering process to create a sample of Mg based MMC [82].

Table 4. Materials and process parameters used in PM technique

Matrix	Reinforcement	Process parameters (pressure, sintering temp., atmosphere etc.)
Ti powder [18]	$(B_4C)_P$	60 MPa, 1450 °C, Sintering time: 60 min
Ti powder [24]	$(ZrO_2)_P$	700 MPa, 1100 °C, Argon, BPR- 10:1
Mg powder [25]	$(TiO_2)_P$	960 MPa, Sintering at 500 and 400 °C, hot extrusion with a ratio 16:1
Mg powder [28]	$(Fullerene)_P$	Compaction at 50 MPa and 540 °C, Sintering at 540 °C for 60 min using Argon gas for shielding.
Mg powder [82]	$(Cu)_P$ and Graphene nanoplatelets (GNP)	600 MPa, 630 °C, Argon, hot extrusion with ratio 5:1
Al powder [83]	$(SiC)_P$ and $(B_4C)_P$	150 MPa, 610 °C, Nitrogen
Al powder [84]	$(Al_2O_3)_P$	250 MPa, 600 °C, Inert, Sintering time: 300 min.
Ti powder [85]	$(AlSiCoFeNi)_P$	1000 MPa, Sintering at 600,700,800 and 900°C, Vaccum
Al powder [86]	$(Al_2O_3)_P$	500-600 °C, Argon, BPR- 10:1, Sintering time: 30-90 min.

Song et al. (2019) [76] studied the consequences of carbon-fibre powder (upto 0.8 %) on the tribological properties of the Copper MMC fabricated by the PM method. For uniform and homogeneous mixing, the powders were mixed continuously for 8 h. Then the mixture was cold pressed at 50 MPa followed by a sintering process at a temperature of about 1000 °C at 0.5 MPa. El-Tantawy et al. (2018) [22] fabricated Nickel-Copper Matrix Composite with Boron Nitride nanoparticles (1 to 5 %) as reinforcement using powder metallurgy technique. Copper and nickel powders were made from the

atomization method. A very small percentage of paraffin wax (0.5 %) mixed in acetone was used as a binding agent. Uniform and homogeneous distribution of boron nitride particles was found in the sintered composite. A summary of a few of the previous researches on MMCs processed using PM is given in Table 4.

Alternative techniques for processing MMCs

There are a few other techniques apart from the above three for manufacturing of MMCs such as friction stir processing (FSP) method, disintegrated melt deposition, mechanical alloying, compo-casting method, in-situ method etc.

In 2011, Ghosh and Saha [87] studied the wear behaviour of the aluminium MMC with silicon carbide (10 to 30 %) as reinforcement which was fabricated using Direct Metal Laser Sintering (DMLS) method. Dinaharan et al. (2020) [88] developed titanium-reinforced (upto 21 %) Mg-based MMC using the FSP technique. Process parameters like the number of tool passes, traverse speed of tool and volume fraction of titanium particles were altered for obtaining the uniform distribution of reinforcement and the optimum value of tensile strength.

Some of the alternate techniques are mentioned in Table 5 used in the past researches for synthesizing of MMCs.

Table 5. Alternative production techniques

Process used	Matrix	Reinforcement
Friction stir processing [89]	Al6063	(Quartz)$_P$
Disintegrated melt deposition [90]	Pure Mg	(Fly ash waste)$_P$
Investment casting [91]	Ti alloy	B_4C
Spark plasma sintering [92]	Pure Al powder	SiC_P
Compo-casting [93]	Al6061	Flyash

Effects of reinforcement particles on the properties of the MMCs

With the introduction of reinforcements, there will be few changes in the mechanical, physical and tribological properties of the MMC compared to that of monolithic metals or their alloys. Some changes are beneficial and unwanted. Few of the properties of MMCs are mentioned below:

Tensile Strength

The strength of material under the action of tensile forces is known as tensile strength. High values of tensile strength mean that the material can perform its intended function at high loading condition. It improves with the introduction of reinforcement particles as they act as barrier to the dislocation movement which increases the value of stress required for same amount of plastic deformation [55]. Reddy et al. [94] produced Al 5052 based hybrid composites using SiC and TiC particulate reinforcements. The tensile strength of hybrid MMCs were improved from 119 to 142 MPa (19.3 % increase in strength). MMCs were produced by adding Al_2O_3 to pure Mg using PM method [95]. Tensile strength was increased by 26 % (from 168 to 211 MPa) when compared to base alloy. Comparative tensile strength of different base alloys and their MMCs are demonstrated

through bar graph in Fig. 5. Table 6 shows the summarized tensile strength data for various MMCs observed by past researchers.
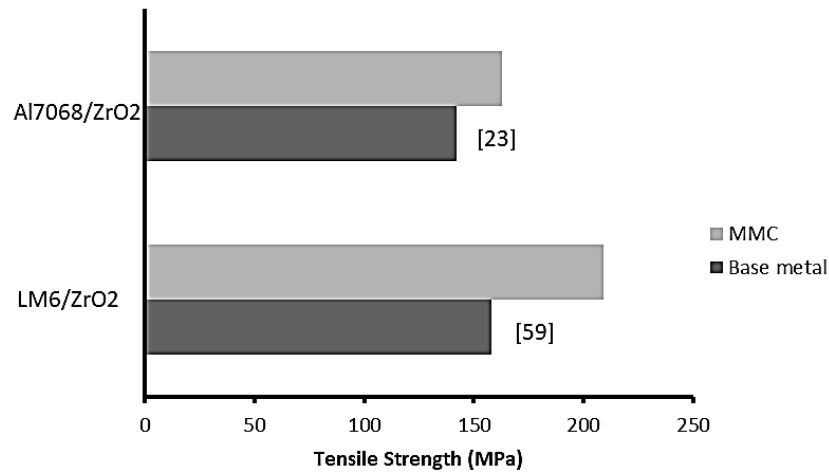

Fig. 5. Tensile strength of base metal and MMC. Based on [23,59]

Table 6. Summarized Tensile strength data for various MMCs

MMC	Method	Tensile strength, MPa	
		Base Alloy	**MMC**
Al6063/B$_4$C/marble dust/Gr/glass fibre [6]	Stir casting	180	249
Al6061/ZrO$_2$/Gr [38]	Stir Casting	128	166.3
AZ91C/SiC [41]	Stir casting	84	178
Al2219/SiC [43]	Stir Casting	80	87
AZ91D/SiC [54]	Ultrasonic Stir casting	133	191
Mg/Cu/GNP [82]	Powder Metallurgy	164	260
AZ31B/Ti [88]	Friction stir processing	226	283
Ti/B$_4$C [91]	Investment casting	785	1029
Mg/Al$_2$O$_3$ [95]	Powder Metallurgy	168	211
Ti/SiC [96]	Spark plasma sintering	504 ± 18	726 ± 10

Hardness

It is the resistance to indentation or scratch. Strength and hardness are correlated with each other. The ceramic reinforcements are hard and brittle in nature thus addition of even a small amount of reinforcement material improves the hardness of composites significantly [97]. The hardness value for Al7075/h-BN MMCs manufactured by Kuldeep et al. [40] was improved up to 68 BHN at 3 % h-BN. The improvement in hardness was attributed to the increase in dislocation density. Yoganandam et al. (2020) [81] analysed the mechanical properties of TMC developed using powder metallurgy method and found the rise in the values of hardness up to 5.24 % (53.97 to 56.80 BHN) with continuous mixing of boron carbide powder as reinforcement. Mg-based MMCs were manufactured with 5 % Al$_2$O$_3$ and 0-8 % SiC [98]. The hardness was increased by 16.47 % (64.53 to 75.16 HV). The hardness was increased due to grain refinement and precipitate hardening. Comparison of hardness between base metal and fabricated MMCs is

illustrated in Fig. 6. Table 7 shows the summarized hardness data for various MMCs observed by past researchers.
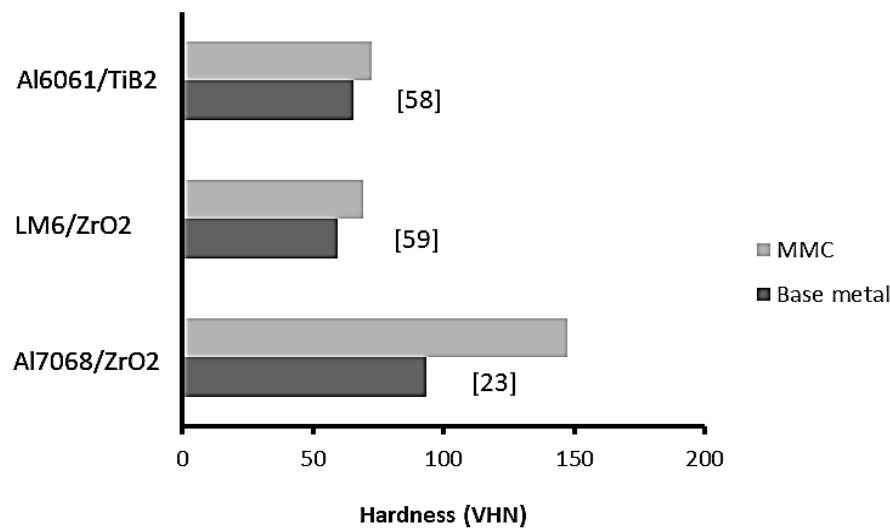

Fig. 6. Vicker's hardness comparison between base metal and MMC. Based on [23,58,59]

Table 7. Summarized Hardness data for various MMCs

MMC	Method	Hardness	
		Base Alloy	MMC
Al6063/B$_4$C/marble dust/Gr/glass fibre [6]	Stir casting	76 HV	88 HV
Ti/ZrO$_2$ [24]	Powder metallurgy	290 HV	570 HV
Mg/TiO$_2$ [25]	Powder metallurgy	52.41 HV	63.89 HV
LM6/flyash [31]	Squeeze casting	57.5 BHN	64 BHN
AZ91D/SiC [54]	Ultrasonic stir casting	63.5 HV	73.2 HV
Al6063/quartz [89]	Friction stir processing	62 HV	135 HV
Mg/flyash [90]	Disintegrated melt deposition	47±2 HV	112±7 HV
Al6061/SiC/Jute ash [99]	Stir casting	48 HV	66 HV

Ductility and toughness

Toughness is the measure of ability of material to absorb energy. It is high for ductile materials. With introduction of brittle reinforcement material, ductility and toughness of MMC usually decreases. The percentage elongation also decreases with increase in reinforcement quantity in the matrix of composite [45]. Deng et al. (2014) [100] manufactured magnesium based MMC with SiC particles (2, 5 and 10 %) as reinforcement and found that percentage elongation was decreased from 15 to 0.5 % with increase in SiC particles up to 10 % into the metal matrix. Mg-MMCs were produced using Vaccum stir casting with 15 % SiC added into AZ91C Mg alloy [41]. Elongation % was decreased to 1.1 from 7.2 % as a result of hard SiC particles which hindered the plastic slip movement. Aigbodion and Hassan (2007) [101] noted the decrease in the impact energy (from 17 to 10 J) of the fabricated Aluminium MMC with rise in the volume of SiC reinforcement particles upto 25 %. The elongation% was also reduced to 1.5 in 25 % SiC-MMC from 6 % in base alloy. Roseline et al. [102] developed Al/ZrO$_2$ MMCs and the

decrease in the impact energy from 5 to 3.56 J was reported. The percent elongation for MMCs was compared with the base matrix in Fig. 7.
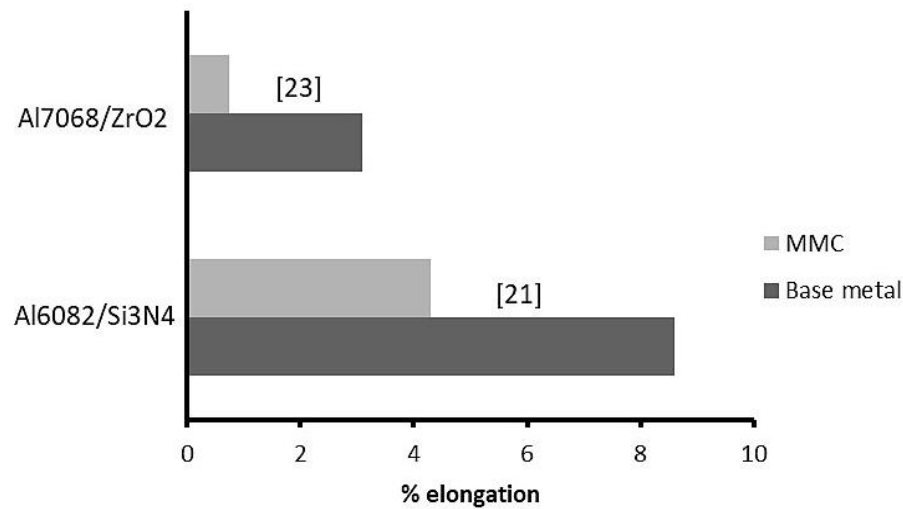

Fig. 7. Percentage elongation of Base metal and MMC. Based on [21,23]

Corrosion and wear resistance

All materials fail either due to excessive wear or under the corrosive atmosphere irrespective of loading condition. So, it's necessary to know wear and corrosion behaviour of MMCs so that their useful life can be predicted. With improvement in hardness, the resistance to wear also get enhanced [103,104]. Some materials like graphite acts as solid lubricant when added into the composite thereby improving resistance to wear to some degree [105]. To analyse wear resistance, dry sliding wear test is performed as per ASTM G99 standard [99]. With addition of reinforcements, even the corrosion resistance of developed MMCs gets improved as reinforcement materials do not corrode easily compared to the pure metals [106].

In 2017, Harti et al. [62] fabricated the Aluminium based MMCs with TiC (2, 4 and 6 %) as reinforcement to enhance the wear resistance of synthesized composites as compared to that of the monolithic metal. The dry sliding wear test was performed at different loads (0.5 to 2 kg) and speeds (600–900 rpm). The 6 % SiC-based MMC has least wear rate of $2 \times 10^{-5} \, cm^3/m$. Similar enhancement in the wear resistance property was found in copper based MMCs when investigated by Ali et al. (2020) [107] with addition of 4 % ZrO_2 and 4 % graphite (Gr) as reinforcement phases. The minimum wear of 122 μm was found for hybrid MMC with 4%ZrO_2 and 4% Gr at 1 kg load and 300 rpm. Change in wear rate with increase in reinforcement is evident from Fig. 8 [57], where the wear rate of Magnesium based MMCs was decreased as reinforcement weight percent was increased from 1 to 3%. Table 8 shows the summarized wear data for various MMCs observed by past researchers. From the review of these past research works, it is evident that the wear rate gets affected by the applied load, sliding distance and sliding speed. Adhesion, abrasion, ploughing and delamination are common phenomena that occur during the dry sliding wear test of MMCs samples [108–115].
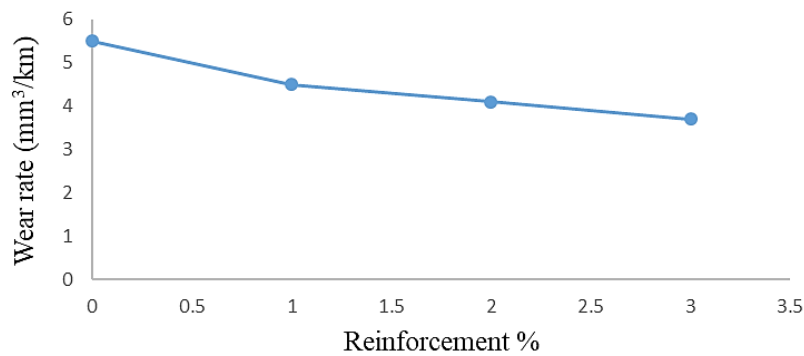
Fig. 8. Change of wear with reinforcement weight percent. Based on [57]

Table 8. Summarized wear data for different MMCs

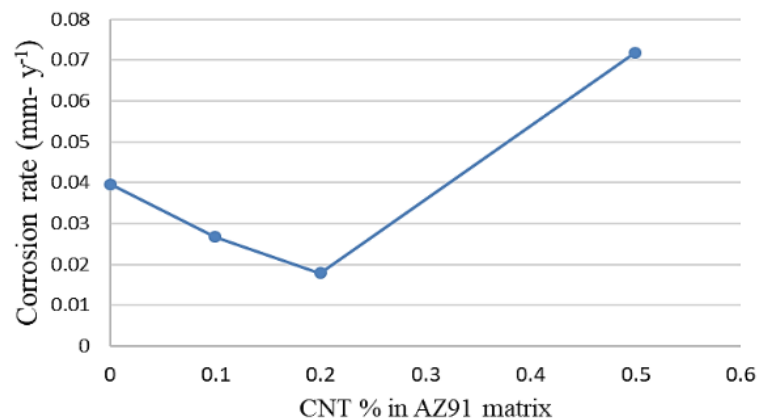| Matrix material	Reinforcement	Wear	
		Base Alloy	MMC
LM30 [108]	18% Al_2SiO_5	$35 \times 10^{-3} mm^3/min$	$15 \times 10^{-3} mm^3/min$
A356 [109]	SiC+ MoS_2	0.038 mg/m	0.013 mg/m
Al6061 [110]	3% CeO_2+3% GNPs	0.85 mm^3/Nm	0.7 mm^3/Nm
Al [111]	0.1% GNPs	$3.4 \times 10^{-4} mm^3/Nm$	$1.2 \times 10^{-4} mm^3/Nm$
Al [112]	15%TiB_2	$55 \times 10^{-3} mm^3/km$	$6 \times 10^{-3} mm^3/km$
Mg [113]	0.5% ZnO	$3.3 \times 10^{-5} gm/m$	$2.3 \times 10^{-5} gm/m$
AZ91 [114]	0.15%MWCNT+0.15% GNPs	0.002 mm^3/m	0.0005 mm^3/m
Mg [115]	2% SiC	0.0212 gm/m	0.011 gm/m

Fig. 9. Change of corrosion rate with reinforcement weight percent. Based on [29]

In 2020, Say et al. [29] studied the corrosion resistance property of magnesium matrix composites, which were reinforced with 0.1 to 0.5 % carbon nanotubes (CNTs), using Potentiodynamic scanning (PDS) tests (Fig. 9). The minimum corrosion rate (0.0178 mm-y^{-1}) was found for AZ91-based MMC reinforced with 0.2 wt. % of CNTs. An immersion test showed increased corrosion in AZ91D-ZrO_2 composites after 72 h, but it decreased after 168 h [116]. The corrosion rate for MMC was reduced to 0.23 from 1.05 mm-y^{-1} for base alloy (approximately 78 % reduction). This is due to the fine dispersion of the reinforcement, which reduced corrosion potential. Kumar et al. [106] studied the corrosion behaviour of Al6061/CeO2 MMCs at different temperatures from room temperature to 75 °C where the

samples were immersed for 180 h. The corrosion was increased with increasing temperature but decreased with exposure time possibly due to anodic stabilization. Zakaria [117] performed the corrosion test on Al/SiC composites as per ASTM G31 standard using 3.5 wt. % aqueous solution at temperatures 25, 50 and 75 °C. The corrosion rate (CR) after immersion duration of 120 h for base alloy was 0.205 mm-y^{-1} and by increasing the SiC wt. % up to 15 % the CR was decreased to 0.173 mm-y^{-1} with fewer amount of pits formation. At high temperatures, CR was found to be higher due to formation of intermetallics (Al_4C_3) at the interface. Figiel et al. [118] tested Ti-based MMCs for their corrosion resistance with TiC micro (1, 10 and 20 %) and nano-powders (1, 10 and 20 %) as reinforcements. The corrosion resistance (R_{pol}) and corrosion current density (I_{cr}) for base alloy were 9.19×10^3 Ω/cm^2 and 3.19 $\mu A/cm^2$, respectively. The best corrosion resistance was observed in sample with 10 % nano-TiC powder where values of R_{pol} and I_{cr} were 43.95×10^3 Ω/cm^2 and 1.02 $\mu A/cm^2$, respectively.

Conclusions

Processing techniques of particle-reinforced MMC, influence of the particle-sized reinforcement on various properties of MMCs as well as application of MMCs were discussed briefly in the previous segments by reviewing numerous research papers. The following conclusions are made:

1. PMMCs have wide range of applications: automobile parts, aircrafts bodies, sports equipment;
2. stir casting, squeeze casting and powder metallurgy are commonly used methods for production of PMMCs;
3. the conventional stir casting method has its limitations like an agglomeration of reinforcement particles caused due to wetting problem between matrix and reinforcement particles;
4. agglomeration problems can be reduced to an extent by some modifications like adding Mg powder, using ultrasonic-assisted stir casting or squeeze casting method;
5. porosity can be reduced by using Argon gas shielding and also by adding C_2Cl_6 into melt can result in degassing;
6. the powder metallurgy process can manufacture a variety of MMCs and is not limited to just AMCs;
7. mixing of ceramic particles like SiC, Alumina, ZrO_2, B_4C etc., tends to enhance the low strain properties like hardness, UTS, and yield strength (up to 100 %) along with wear resistance and corrosion resistance of the MMCs as a result of increase in dislocation density, precipitation hardening and grain refinement; but at the same time, ductility and impact strength reduces due to the brittle nature of the reinforcement.

References

1. Agarwal S, Angra S, Singh S. A review on the mechanical behaviour of aluminium matrix composites under high strain rate loading. *Materials Physics and Mechanics*. 2023;51(6): 1–13.
2. Deshmukh S, Joshi G, Ingle A, Thakur D. An overview of Aluminium Matrix Composites: Particulate reinforcements, manufacturing, modelling and machining. *Materials Today: Proceedings*. 2021;46: 8410–8416.

3. Kumar D, Singh S, Angra S. Effect of reinforcements on mechanical and tribological behavior of magnesium-based composites: a review. *Materials Physics and Mechanics.* 2022;50(3): 439–458.

4. Agarwal S, Singh S. Investigation of Microstructural and Tensile behaviour of stir-casted Al5052-based Composites with nano-reinforcements. *Journal of Polymer and Composites.* 2024;12(2): 1–7.

5. Ye HZ, Liu XY. Review of recent studies in magnesium matrix composites. *Journal of Materials Science.* 2004;39(20): 6153–6171.

6. Kashyap S, Tripathi H, Kumar N. Mechanical Properties of Marble Dust Reinforced Aluminum Matrix Structural Composites Fabricated By Stir Casting Process. *Materials Physics and Mechanics.* 2022;48(2): 282–288.

7. Sharma DK, Mahant D, Upadhyay G. Manufacturing of metal matrix composites: A state of review. *Materials Today: Proceedings.* 2019;26: 506–519.

8. Hirmaz MS. Composites Classification and Manufacturing Operations: A Review. *International Journal Of Advance Research, Ideas, And, Innovations In Technology.* 2017;3(3): 1708–1713.

9. Kumaraswamy J, Anil KC, Veena TR, Purushotham G, Sunil Kumar K. Investigating the Mechanical Properties of Al 7075 Alloy for Automotive Applications: Synthesis and Analysis. *Evergreen.* 2023;10(3): 1286–1295.

10. Rohatgi P, Schultz B, Gupta N, Daoud A. Solidification During Casting of Metal-Matrix Composites. *Casting.* 2018;15: 390–397.

11. Miracle DB. Metal matrix composites - From science to technological significance. *Composites Science and Technology.* 2005;65(15-16): 2526–2540.

12. Casati R, Vedani M. Metal matrix composites reinforced by Nano-Particles—A review. *Metals.* 2014;4(1): 65–83.

13. Dwivedi SP, Maurya M, Chauhan SS. Mechanical, physical and thermal behaviour of SiC and MgO reinforced aluminium based composite material. *Evergreen.* 2021;8(2): 318–27.

14. Kala H, Mer KKS, Kumar S. A Review on Mechanical and Tribological Behaviors of Stir Cast Aluminum Matrix Composites. *Procedia Materials Science.* 2014;6: 1951–1960.

15. Poria S, Sahoo P, Sutradhar G. Tribological Characterization of Stir-cast Aluminium-TiB2 Metal Matrix Composites. *Silicon.* 2016;8(4): 591–599.

16. Mohanavel V, Ravichandran M, Suresh Kumar S. Tribological and mechanical properties of Zirconium Di-boride (ZrB2) particles reinforced aluminium matrix composites. *Materials Today: Proceedings.* 2020;21: 862–864.

17. Jacob Dhas DSE, Velmurugan C, Wins KLD, BoopathiRaja KP. Effect of tungsten carbide, silicon carbide and graphite particulates on the mechanical and microstructural characteristics of AA 5052 hybrid composites. *Ceramics International.* 2019;45(1): 614–621.

18. Vadayar KS, Rani SD, Prasad VVB. Effect of Boron Carbide Particle Size and Volume Fraction of TiB-TiC Reinforcement on Fractography of PM Processed Titanium Matrix Composites. *Procedia Materials Science.* 2014;6: 1329–1335.

19. Maurya M, Maurya NK, Bajpai V. Effect of SiC reinforced particle parameters in the development of aluminium based metal matrix composite. *Evergreen.* 2019;6(3): 200–206.

20. Srivastava AK, Maurya M, Saxena A, Maurya NK, Dwivedi SP. Statistical optimization by response surface methodology of process parameters during the cnc turning operation of hybrid metal matrix composite. *Evergreen.* 2021;8(1): 51–62.

21. Sharma P, Sharma S, Khanduja D. Production and some properties of Si3N4 reinforced aluminium alloy composites. *Journal of Asian Ceramic Societies.* 2015;3(3): 352–359.

22. El-Tantawy A, Daoush WM, El-Nikhaily AE. Microstructure and properties of BN/Ni-Cu composites fabricated by powder technology. *Journal of Experimental Nanoscience.* 2018;13(1): 174–187.

23. Madhusudhan M, Naveen GJ, Mahesha K. Mechanical Characterization of AA7068-ZrO2 reinforced Metal Matrix Composites. *Materials Today: Proceedings.* 2017;4(2): 3122–3130.

24. Abd-Elwahed MS, Ibrahim AF, Reda MM. Effects of ZrO2 nanoparticle content on microstructure and wear behavior of titanium matrix composite. *Journal of Materials Research and Technology.* 2020;9(4): 8528–8534.

25. Pc E, Radhakrishnan G, Emarose S. Investigation into Physical, Microstructural and Mechanical Behaviour of Titanium dioxide Nanoparticulate Reinforced Magnesium Composite. *Materials Technology.* 2020;36(10): 1–10.

26. Gaharwar D, Jha SK, Bhuyan BK. Fabrication of a Hybrid Metal Matrix Composite of Al 6082, SiC, Graphite and Mg. *Evergreen.* 2023;10(2): 1080–1083.

27. Kumar P, Sharma V, Kumar D, Akhai S. Morphology and Mechanical Behavior of Friction Stirred Aluminum Surface Composite Reinforced with Graphene. *Evergreen.* 2023;10(1): 105–110.

28. Turan ME, Sun Y, Akgul Y. Improved wear properties of magnesium matrix composite with the addition of fullerene using semi powder metallurgy. *Fullerenes Nanotubes and Carbon Nanostructures.* 2018;26(2): 130–136.

29. Say Y, Guler O, Dikici B. Carbon nanotube (CNT) reinforced magnesium matrix composites: The effect of CNT ratio on their mechanical properties and corrosion resistance. *Materials Science and Engineering A.* 2020;798: 139636.

30. Ghasali E, Alizadeh M, Pakseresht AH, Ebadzadeh T. Preparation of silicon carbide/carbon fiber composites through high-temperature spark plasma sintering. *Journal of Asian Ceramic Societies.* 2017;5(4): 472–478.

31. Prasad KNP, Ramachandra M. Determination of Abrasive Wear Behaviour of Al-Fly ash Metal Matrix Composites Produced by Squeeze Casting. *Materials Today: Proceedings.* 2018;5(1): 2844–2853.

32. Dwivedi SP, Maurya M, Maurya NK, Srivastava AK, Sharma S, Saxena A. Utilization of groundnut shell as reinforcement in development of aluminum based composite to reduce environment pollution: A review. *Evergreen.* 2020;7(1): 15–25.

33. Sathi BR, Gurugubelli SN, Babu HN. The Effect of ECAP on Structural Morphology and Wear Behaviour of 5083 Al Composite Reinforced with Red Mud. *Evergreen.* 2023;10(2): 774–781.

34. Yadav R, Dwivedi SP, Dwivedi VK. Effect of Casting Parameters on Tensile Strength of Chrome Containing Leather Waste Reinforced Aluminium Based Composite using RSM. *Evergreen.* 2022;9(4): 1031–1038.

35. Chak V, Chattopadhyay H, Dora TL. A review on fabrication methods, reinforcements and mechanical properties of aluminum matrix composites. *Journal of Manufacturing Processes.* 2020;56: 1059–1074.

36. Ali M. Review of stir casting technique and technical challenges for ceramic reinforcement particulate and aluminium matrix composites. *Epitoanyag - Journal of Silicate Based and Composite Materials.* 2020;72(6): 198–204.

37. Kant S, Singh Verma# A. Stir Casting Process in Particulate Aluminium Metal Matrix Composite: A Review. *International Journal of Mechanics and Solids.* 2017;9(1): 973–1881.

38. Pandiyarajan R, Maran P, Marimuthu S, Ganesh KC. Mechanical and tribological behavior of the metal matrix composite AA6061/ZrO2/C. *Journal of Mechanical Science and Technology.* 2017;31(10): 4711–4717.

39. Baisane V, Sable Y, Dhobe M, Sonawane P. Recent development and challenges in processing of ceramics reinforced Al matrix composite through stir casting process: A Review. *International Journal of Engineering and Applied Sciences.* 2015;2(10): 11–16.

40. Kuldeep B, Ravikumar KP, Pradeep S. Effect of hexagonal boron nitrate on microstructure and mechanical behavior of Al7075 metal matrix composite producing by stir casting technique. *International Journal of Engineering, Transactions A: Basics.* 2019;32(7): 1017–1022.

41. Gui MC, Han JM, Li PY. Microstructure and mechanical properties of Mg-Al9Zn/SiCp composite produced by vacuum stir casting process. *Materials Science and Technology.* 2004;20(6): 765–771.

42. Adityawardhana Y, Syahrial AZ, Adjiantoro B. Characteristic of AA 7075-Reinforced Nano-SiC Composites Produced by Stir-Squeeze Casting and Open Die Cold Forging as An Armor Material Candidate. *Evergreen.* 2023;10(2): 722–730.

43. Faisal N, Kumar K. Mechanical and tribological behaviour of nano scaled silicon carbide reinforced aluminium composites. *Journal of Experimental Nanoscience.* 2018;13: S1–13.

44. Mohanavel V, Suresh Kumar S, Mariyappan K, Ganeshan P, Adithiyaa T. Mechanical behavior of Al-matrix nanocomposites produced by stir casting technique. *Materials Today: Proceedings.* 2018;5(13): 26873–26877.

45. Singh G, Goyal S. Microstructure and mechanical behavior of AA6082-T6/SiC/B4C-based aluminum hybrid composites. *Particulate Science and Technology.* 2018;36(2): 154–161.

46. Hashim J, Looney L, Hashmi MSJ. The wettability of SiC particles by molten aluminium alloy. *Journal of Materials Processing Technology.* 2001;119(1–3): 324–328.

47. Sharma P, Sharma S, Khanduja D. A study on microstructure of aluminium matrix composites. *Journal of Asian Ceramic Societies.* 2015;3(3): 240–244.

48. Aswad MA, Awad SH, Kaayem AH. Study on Iraqi Bauxite ceramic reinforced aluminum metal matrix composite synthesized by stir casting. *International Journal of Engineering, Transactions A: Basics.* 2020;33(7): 1331–1339.

49. Dwivedi SP, Maurya NK, Maurya M. Assessment of hardness on AA2014/eggshell composite produced via electromagnetic stir casting method. *Evergreen.* 2019;6(4): 285–294.

50. Shorowordi KM, Laoui T, Haseeb ASMA, Celis JP, Froyen L. Microstructure and interface characteristics of B4C, SiC and Al2O3 reinforced Al matrix composites: A comparative study. *Journal of Materials Processing Technology.* 2003;142(3): 738–743.

51. Purohit R, Qureshi MMU, Jain A. Forming behaviour of aluminium matrix nano Al2O3 composites for automotive applications. *Advances in Materials and Processing Technologies.* 2020;6(2): 324–335.

52. Hashim J, Looney L, Hashmi MSJ. The enhancement of wettability of SiC particles in cast aluminium matrix composites. *Journal of Materials Processing Technology.* 2001;119(1–3): 329–335.

53. Kaushik N, Singhal S. Wear conduct of aluminum matrix composites: A parametric strategy using Taguchi based GRA integrated with weight method. *Cogent Engineering.* 2018;5(1): 1467196.

54. Jia XY, Liu SY, Gao FP, Zhang QY, Li WZ. Magnesium matrix nanocomposites fabricated by ultrasonic assisted casting. *International Journal of Cast Metals Research.* 2009;22(1–4): 196–199.

55. Wang ZH, Wang XD, Zhao YX, Du WB. SiC nanoparticles reinforced magnesium matrix composites fabricated by ultrasonic method. *Transactions of Nonferrous Metals Society of China.* 2010;20(3): s1029–s1032.

56. Qi JQ, Chang Y, He YZ, Sui YW, Wei FX, Meng QK, Wei ZJ. Effect of Zr, Mo and TiC on microstructure and high-temperature tensile strength of cast titanium matrix composites. *Materials and Design.* 2016;99: 421–426.

57. Girish BM, Satish BM, Sarapure S, Somashekar DR, Basawaraj. Wear behavior of magnesium alloy az91 hybrid composite materials. *Tribology Transactions.* 2015;58(3): 481–489.

58. Suresh S, Moorthi NSV. Process development in stir casting and investigation on microstructures and wear behavior of TiB2 on A16061 MMC. *Procedia Engineering.* 2013;64: 1183–1190.

59. Karthikeyan G, Jinu GR. Experimental investigation on mechanical and wear behaviour of aluminium LM6 / ZrO2 Composites Fabricated by Stir Casting Method. *Journal of the Balkan Tribological Association.* 2015;21(3): 539–556.

60. Khalili V, Heidarzadeh A, Moslemi S, Fathyunes L. Production of Al6061 matrix composites with ZrO2 ceramic reinforcement using a low-cost stir casting technique: Microstructure, mechanical properties, and electrochemical behavior. *Journal of Materials Research and Technology.* 2020;9(6): 15072–15086.

61. Jaber MH, Aziz GA, Mohammed AJ, AL-AlKawi HJ. Electrical conductivity, magnetic and fatigue properties of aluminum matrix composites reinforced with nano-titanium dioxide (TiO2). *Nanocomposites.* 2020;6(2): 47–55.

62. Harti JI, Prasad TB, Nagaral M, Jadhav P, Auradi V. Microstructure and Dry Sliding Wear Behaviour of Al2219-TiC Composites. *Materials Today: Proceedings.* 2017;4(10): 11004–11009.

63. Sharma P, Paliwal K, Garg RK, Sharma S, Khanduja D. A study on wear behaviour of Al/6101/graphite composites. *Journal of Asian Ceramic Societies.* 2017;5(1): 42–48.

64. Patil V, Kulkarni SN. Characterization of Mechanical Properties of Aluminium Alloy Metal Matrix Composites. *International Journal of Engineering Research and Technology.* 2014;3(12): 771–776.

65. Baradeswaran A, Elaya Perumal A. Study on mechanical and wear properties of Al 7075/Al2O 3/graphite hybrid composites. *Composites Part B: Engineering.* 2014;56: 464–471.

66. Bharath V, Nagaral M, Auradi V, Kori SA. Preparation of 6061Al-Al2O3 MMC's by Stir Casting and Evaluation of Mechanical and Wear Properties. *Procedia Materials Science.* 2014;6: 1658–1667.

67. Gurusamy P, Prabu SB, Paskaramoorthy R. Influence of processing temperatures on mechanical properties and microstructure of squeeze cast aluminum alloy composites. *Materials and Manufacturing Processes.* 2015;30(3): 367–373.

68. Dhanashekar M, Senthil Kumar VS. Squeeze casting of aluminium metal matrix composites - An overview. *Procedia Engineering.* 2014;97: 412–420.

69. Feng YC, Geng L, Zheng PQ, Zheng ZZ, Wang GS. Fabrication and characteristic of Al-based hybrid composite reinforced with tungsten oxide particle and aluminum borate whisker by squeeze casting. *Materials and Design.* 2008;29(10): 2023–2026.

70. Reihani SMS. Processing of squeeze cast Al6061-30vol% SiC composites and their characterization. *Materials and Design.* 2006;27(3): 216–222.

71. Kalkanlı A, Yılmaz S. Synthesis and characterization of aluminum alloy 7075 reinforced with silicon carbide particulates. *Materials and Design.* 2008;29: 775–780.

72. Patil V, Janawade S, Kulkarni SN, Biradar A. Studies on mechanical behavior and morphology of alumina fibers reinforced with aluminium-4.5% copper alloy metal matrix composites. *Materials Today: Proceedings.* 2021;46(1): 99–106.

73. Gurusamy P, Balasivanandha Prabu S. Effect of the squeeze pressure on the mechanical properties of the squeeze cast Al/SiCp metal matrix composite. *International Journal of Microstructure and Materials Properties.* 2013;8(4–5): 299–312.

74. Zhang Q, Wu G, Chen G, Jiang L, Luan B. The thermal expansion and mechanical properties of high reinforcement content SiCp/Al composites fabricated by squeeze casting technology. *Composites Part A: Applied Science and Manufacturing.* 2003;34(11): 1023–1027.

75. Muraliraja R, Arunachalam R, Al-Fori I, Al-Maharbi M, Piya S. Development of alumina reinforced aluminum metal matrix composite with enhanced compressive strength through squeeze casting process. *Proceedings of the Institution of Mechanical Engineers, Part L: Journal of Materials: Design and Applications.* 2019;233(3): 307–314.

76. Song Y, Fan J, Wu S, Liu J, Zhang C, Li Y. Effect of carbon-fibre powder on friction and wear properties of copper-matrix composites. *Materials Science and Technology.* 2020;36(1): 92–99.

77. Wang Z, Song M, Sun C, Xiao D, He Y. Effect of extrusion and particle volume fraction on the mechanical properties of SiC reinforced Al-Cu alloy composites. *Materials Science and Engineering A.* 2010;527(24–25): 6537–6542.

78. Ashwath P, Anthony Xavior M. The effect of ball milling & reinforcement percentage on sintered samples of aluminium alloy metal matrix composites. *Procedia Engineering.* 2014;97: 1027–1032.

79. Nassar AE, Nassar EE. Properties of aluminum matrix Nano composites prepared by powder metallurgy processing. *Journal of King Saud University - Engineering Sciences.* 2017;29(3): 295–299.

80. Montealegre Melendez I, Neubauer E, Angerer P, Danninger H, Torralba JM. Influence of nano-reinforcements on the mechanical properties and microstructure of titanium matrix composites. *Composites Science and Technology.* 2011;71(8): 1154–1162.

81. Yoganandam K, Mohanavel V, Vairamuthu J, Kannadhasan V. Mechanical properties of titanium matrix composites fabricated via powder metallurgy method. *Materials Today: Proceedings.* 2020;33(7): 3243–3247.

82. Rashad M, Pan FS, Asif M, Ullah A. Improved mechanical properties of magnesium-graphene composites with copper-graphene hybrids. *Materials Science and Technology.* 2015;31(12): 1452–1461.

83. Bodukuri AK, Eswaraiah K, Rajendar K, Sampath V. Fabrication of Al–SiC–B4C metal matrix composite by powder metallurgy technique and evaluating mechanical properties. *Perspectives in Science.* 2016;8: 428–431.

84. Ahmad KR, Lee WJ, Zaki RM, Noor MM, Wahid MFM, Shamsudin SR, Jamaludin SB. The Microsructure and Properties of Aluminium Composite Reinforced with 65 μm Alumina Particles via Powder Metallurgy. In: *ICoSM.* 2007. p.165–167.

85. Satyanarayanaraju CHV, Dixit R, Miryalkar P, Karunanidhi S, AshokKumar A, NagaLakshmi J, et al. Effect of heat treatment on microstructure and properties of high entropy alloy reinforced titanium metal matrix composites. *Materials Today: Proceedings.* 2019;18: 2409–2414.

86. Rahimian M, Ehsani N, Parvin N, Baharvandi H reza. The effect of particle size, sintering temperature and sintering time on the properties of Al-Al2O3 composites, made by powder metallurgy. *Journal of Materials Processing Technology.* 2009;209(14): 5387–5393.

87. Ghosh SK, Saha P. Crack and wear behavior of SiC particulate reinforced aluminium based metal matrix composite fabricated by direct metal laser sintering process. *Materials and Design.* 2011;32(1): 139–145.

88. Dinaharan I, Zhang S, Chen G, Shi Q. Development of titanium particulate reinforced AZ31 magnesium matrix composites via friction stir processing. *Journal of Alloys and Compounds.* 2020;820: 153071.

89. Joyson Abraham S, Chandra Rao Madane S, Dinaharan I, John Baruch L. Development of quartz particulate reinforced AA6063 aluminum matrix composites via friction stir processing. *Journal of Asian Ceramic Societies.* 2016;4(4): 381–389.

90. Nguyen QB, Sharon Nai ML, Nguyen AS, Seetharaman S, Wai Leong EW, Gupta M. Synthesis and properties of light weight magnesium-cenosphere composite. *Materials Science and Technology.* 2016;32(9): 923–929.

91. Wang J, Guo X, Qin J, Zhang D, Lu W. Microstructure and mechanical properties of investment casted titanium matrix composites with B4C additions. *Materials Science and Engineering A.* 2015;628: 366–373.

92. Zhang J, Shi H, Cai M, Liu L, Zhai P. The dynamic properties of SiCp/Al composites fabricated by spark plasma sintering with powders prepared by mechanical alloying process. *Materials Science and Engineering A.* 2009;527(1–2): 218–224.

93. David Raja Selvam J, Robinson Smart DS, Dinaharan I. Microstructure and some mechanical properties of fly ash particulate reinforced AA6061 aluminum alloy composites prepared by compocasting. *Materials and Design.* 2013;49: 28–34.

94. Venkateshwar Reddy P, Suresh Kumar G, Satish Kumar V, Veerabhadra Reddy B. Effect of Substituting SiC in Varying Proportions for TiC in Al-5052/TiC/SiC Hybrid MMC. *Journal of Bio- and Tribo-Corrosion.* 2020;6(1): 1–11.

95. Wong WLE, Karthik S, Gupta M. Development of hybrid Mg/Al 2O 3 composites with improved properties using microwave assisted rapid sintering route. *Journal of Materials Science.* 2005;40(13): 3395–3402.

96. Liu Y, Dong L, Lu J, Huo W, Du Y, Zhang W, et al. Microstructure and mechanical properties of SiC nanowires reinforced titanium matrix composites. *Journal of Alloys and Compounds.* 2020;819: 152953.

97. Patil DS, Bhoomkar MM. Investigation on Mechanical Behaviour of Fiber-Reinforced Advanced Polymer Composite Materials. *Evergreen.* 2023;10(1): 55–62.

98. Karthick E, Mathai J, Michael Tony J, Marikkannan SK. Processing, Microstructure and Mechanical Properties of Al2O3 and SiC Reinforced Magnesium Metal Matrix Hybrid Composites. *Materials Today: Proceedings.* 2017;4(6): 6750–6756.

99. Coyal A, Yuvaraj N, Butola R, Tyagi L. An experimental analysis of tensile, hardness and wear properties of aluminium metal matrix composite through stir casting process. *SN Applied Sciences.* 2020;2(5): 1–10.

100. Deng KK, Wang XJ, Wu K. Microstructure and tensile properties of magnesium matrix composite: Effected by volume fraction of micron SiCp. *Materials Research Innovations.* 2014;18: S4505–S4509.

101. Aigbodion VS, Hassan SB. Effects of silicon carbide reinforcement on microstructure and properties of cast Al-Si-Fe/SiC particulate composites. *Materials Science and Engineering A.* 2007;447(1–2): 355–360.

102. Roseline S, Paramasivam V, Jayabal S. Evaluation of structure and mechanical properties of zirconia reinforced aluminium matrix composites. *Journal of Computational and Theoretical Nanoscience.* 2018;15(3): 830–838.

103. Reddy PV, Prasad PR, Krishnudu DM, Goud EV. An Investigation on Mechanical and Wear Characteristics of Al 6063/TiC Metal Matrix Composites Using RSM. *Journal of Bio- and Tribo-Corrosion.* 2019;5(4): 1–10.

104. Kumar H, Kumar V, Kumar D, Singh S. Wear Behavior of Friction Stir Processed Copper-Cerium Oxide Surface Composites. *Evergreen.* 2023;10(1): 78–84.

105. Pandiyarajan R, Maran P, Marimuthu S, Prabakaran MP. Investigation on mechanical properties of ZrO2, C and AA6061 metal matrix composites. *Advances in Materials and Processing Technologies.* 2020;8(1): 178–186.

106. Kumar D, Singh S, Angra S. Morphology and Corrosion Behavior of Stir-Cast Al6061-CeO2 Nanocomposite Immersed in NaCl and H2So4 Solutions. *Evergreen.* 2023;10(1): 99–104.

107. Ali Z, Muthuraman V, Rathnakumar P, Gurusamy P, Nagaral M. Investigation on the tribological properties of copper alloy reinforced with Gr/Zro2 particulates by stir casting route. *Materials Today: Proceedings.* 2020;33(7): 3449–3453.

108. Sharma S, Nanda T, Pandey OP. Effect of particle size on dry sliding wear behaviour of sillimanite reinforced aluminium matrix composites. *Ceramics International.* 2018;44(1): 104–114.

109. Alidokht SA, Abdollah-zadeh A, Assadi H. Effect of applied load on the dry sliding wear behaviour and the subsurface deformation on hybrid metal matrix composite. *Wear.* 2013;305(1–2): 291–298.

110. Kumar D, Singh S, Angra S. Dry sliding wear and microstructural behavior of stir-cast Al6061-based composite reinforced with cerium oxide and graphene nanoplatelets. *Wear.* 2023;516–517: 204615.

111. Şenel MC, Gürbüz M, Koç E. Mechanical and tribological behaviours of aluminium matrix composites reinforced by graphene nanoplatelets. *Materials Science and Technology.* 2018;34(16): 1980–1989.

112. Sreenivasan A, Paul Vizhian S, Shivakumar ND, Muniraju M, Raguraman M. A study of microstructure and wear behaviour of TiB2/Al metal matrix composites. *Latin American Journal of Solids and Structures.* 2011;8(1): 1–8.

113. Selvam B, Marimuthu P, Narayanasamy R, Anandakrishnan V, Tun KS, Gupta M, et al. Dry sliding wear behaviour of zinc oxide reinforced magnesium matrix. *Materials & Design.* 2014;58: 475–481.

114. Turan ME, Zengin H, Sun Y. Dry Sliding Wear Behavior of (MWCNT + GNPs) Reinforced AZ91 Magnesium Matrix Hybrid Composites. *Metals and Materials International.* 2019;26: 541–550.

115. Kaviyarasan K, Soundararajan R, Seenuvasaperumal P, Sathishkumar A, Kumar JP. Experimental investigation of dry sliding wear behaviour on ceramic reinforced magnesium composite by powder metallurgy technique. *Materials Today: Proceedings.* 2019;18: 4082–4091.

116. Vaira Vignesh R, Padmanaban R, Govindaraju M, Suganya Priyadharshini G. Investigations on the corrosion behaviour and biocompatibility of magnesium alloy surface composites AZ91D-ZrO2 fabricated by friction stir processing. *Transactions of the Institute of Metal Finishing.* 2019;97(5): 261–270.

117. Zakaria HM. Microstructural and corrosion behavior of Al / SiC metal matrix composites. *Ain Shams Engineering Journal.* 2014;5(3): 831–838.

118. Figiel P, Garbiec D, Biedunkiewicz A, Biedunkiewicz W, Kochmański P, Wróbel R. Microstructural, corrosion and abrasive characteristics of titanium matrix composites. *Archives of Metallurgy and Materials.* 2018;63(4): 2051–2059.

About Authors

Saumy Agarwal iD Sc

*Research Scholar (National Institute of Technology Kurukshetra, Haryana, India)*

Satnam Singh iD Sc

PhD, Assistant Professor (National Institute of Technology Kurukshetra, Haryana, India)

Investigation of aluminum metal matrix composite fabrication processes: a comparative review

P. Kumar [1] ⓘ, D. Kumar [1]✉ ⓘ, K. Kaur [2] ⓘ, R. Chalisgaonkar [3] ⓘ, S.S. Singh [4] ⓘ

[1] Maharishi Markandeshwar University, Mullana-Ambala, India

[2] Dev Polytechnic College, Ambala, India

[3] Medi-Caps University, Indore, India

[4] Poornima University, Jaipur, India

✉ dinesh_kumar@mmumullana.org

ABSTRACT
Aluminum alloys are widely used in industry because of their superior mechanical qualities and high specific strength-to-weight ratio. Al-matrix composites (AMC) may identify the newly synthesized material because it has the mechanical properties of pure aluminum alloys with reinforcement from a variety of ceramics. Matrix materials have included aluminum alloys, with ceramic reinforcements including aluminum oxide (Al_2O_3), magnesium oxide (MnO), graphene nanoplatelets (GNPs), boron carbide (B_4C), silicon carbide (SiC), graphite (Gr), fly ash (FA), etc. The best, most practical, and most cost-effective way to create the composites is by the stir casting process. The review focuses on the two-step stir-casting process for AMCs production. Reinforcement pre-heating temperature, injection rate, porosity, wettability, stirrer structure, stirring time and speed, purge, pouring temperature, solidification rate, and mold temperature are examined to optimize the casting process. Optimal conditions include preheating particles at 200–500°C for 30–60 min, maintaining a feeding rate of 8–10 mg/min, stirring speeds of 700–800 rpm for 10–40 min, and using a 30-degree to 60-degree impeller-blade angle. Emerging trends suggest enhancements such as microwave heating, ultrasonic probe usage, inert environment incorporation, and electromagnetic stir casting for improved wettability and uniformity.
KEYWORDS
aluminum alloys • composites • reinforcements • ceramics • stir-casting

Introduction

Partially reinforcing a matrix of aluminum creates a strong structural material with widespread use in aerospace and automotive applications [1]. Al-matrix composites (AMCs) are a class of materials with desirable qualities achieved by reinforcing ductile metallic alloys with hard particles [2]. These materials have superior mechanical properties, including a higher significant modulus of elasticity, higher specific strength with reduced weight densities, greater operational temperature, and better durability against wear [3]. Most tasks associated with the automotive, electrical, and aerospace sectors found an AMC material to be a superior substitute to current conventional aluminum alloys [4]. Particulate AMCs are notable because of their enhanced damping capacity, machinability, resistance to friction and seizure, and low thermal expansion coefficient, among other characteristics [5]. AMCs are manufactured in a way that allows

for a wide range of reinforcing element and base matrix changes during the melt-stirring process. Maximizing Young's modulus, yield strength, and tensile strength while keeping toughness to a minimum should be the fabrication targets for ultralight material composites [6]. Instead of employing monolithic alloys, researchers have investigated the prospect of increasing resistance to fracture and heat shock at elevated levels by modifying production parameters like melt stirring and solidification rate [7]. Composites deteriorate in their ability to withstand heat, corrosion, and wear as time passes. In order to better understand and enhance the performance of AMCs, numerous researchers have conducted tensile strength [8], compressive strength [9], impact resistance [10], dry sliding wear [11], and fracture tests [12], as well as metallurgical tests such as scanning electron microscope (SEM), transmission electron microscope (TEM), optical microscope (OM), X-ray spectroscopy (XRS), and X-ray diffraction (XRD), etc. [13]. It has been decided to concentrate on the stir-casting approach for the fabrication of AMCs due to it being a very inexpensive melt-stirring technology currently available [14]. The main benefit of this manufacturing process is that, in comparison to other methods, it is easy to implement, has few limitations, and can be used to make a wide variety of shaped components in huge quantities [15]. Figure 1 shows the historic development of the AMCs.

Fig. 1. Historic development of the AMCs

The objective of this paper involves understanding and optimizing the methods used to create these composites. Stir casting stands out as an innovative and practical method for making aluminum metal matrix composites (AMCs) in the ever-changing world of materials engineering. This innovative method uses mechanical agitation to evenly distribute reinforcing elements in an aluminum matrix, improving mechanical qualities and performance. This research explores the stir casting technique and shows its promise as a flexible and cost-effective way to make sophisticated composite materials for varied industrial applications. This study seeks to open new materials science and engineering frontiers by nuancedly exploring its principles, methods, and problems.

Matrix and reinforcement particles

Matrix

The choice of matrix alloy for stir casting aluminum matrix composites (AMCs) depends on several factors including desired mechanical properties, corrosion resistance, thermal

stability, and cost considerations. Some common aluminum alloys used as matrix materials (Fig. 2) in stir casting include:

1. Al-SiC alloy (e.g., 6061, 4032): these alloys offer good castability, mechanical properties, and corrosion resistance. They are commonly used in automotive and aerospace applications.

2. Al-Cu alloys (e.g., 2024, 7075): these alloys offer high strength and excellent fatigue resistance. They are widely used in aerospace, automotive, and structural applications.

3. Al-Mg alloys (e.g., 5083, 5052): these alloys offer good weldability, corrosion resistance, and moderate strength. They are commonly used in marine and structural applications.

4. Al-Zn alloys (e.g., 7075, 7050): these alloys offer high strength-to-weight ratios and good fatigue resistance. They are often used in aerospace and sporting goods applications.

5. Al-Ni alloys (e.g., 2124): these alloys offer high strength and excellent fracture toughness. They are used in aerospace applications where high strength and toughness are required.

6. Al-Li alloys: these alloys offer significant weight savings compared to traditional aluminum alloys due to the low density of lithium. They are used in aerospace applications where weight reduction is critical.
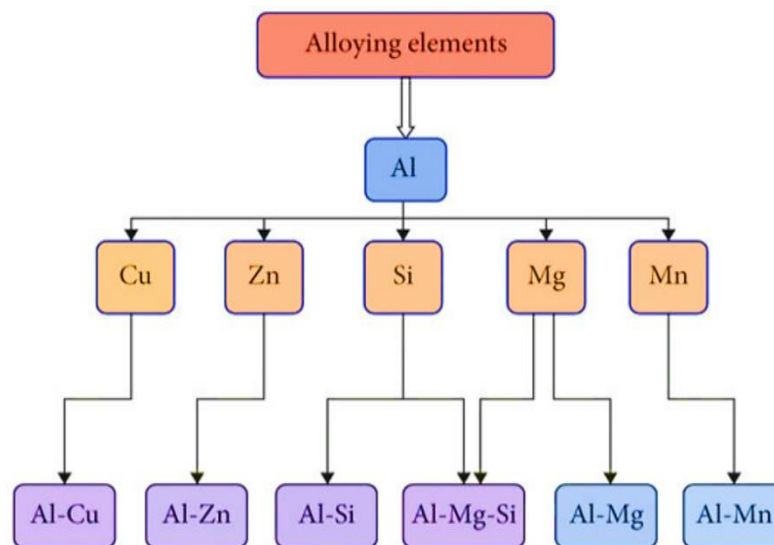

Fig. 2. Aluminum metal matrix composites

When selecting a matrix alloy for stir casting AMCs, it's essential to consider the compatibility between the matrix alloy and the reinforcement material, as well as the processing conditions required for stir casting.

Reinforcement

The manufacturing process is very sensitive to the choices made in the processing variables. Many scientists have synthesized composites using many organic (coconut shell ash (CSA) [16], fly ash (FA) [17], etc.) and non-organic reinforcements, such as Mg [18],

SiC [19], TiC [20], Al$_2$O$_3$ [21], WC [22], B$_4$C [23], TiO$_2$ [20], and many more as shown in Fig. 3. The reinforcement size, shape, and behaviour are critical processing parameters in the fabrication of aluminium-based advanced composite materials. AMCs with lower particle sizes display improved mechanical characterizations, although reinforcement size is the most influential component overall. Candiani et al. [24] developed a stir-casting technique for the synthesis of AA 6061-Al$_2$O$_3$ composites. Al$_2$O$_3$ particles were inserted at a depth of 5–20% in AA-6061 to create composites with somewhat uniform dispersion. The micro-hardness and tensile strength of the specimens showed an increase with increasing weight content in this investigation. Through the use of a stir casting technique, binary ceramic reinforced composites based on AA6061/SiC/Fly-ash were manufactured. 10 wt. % of SiC and FA-based particles were utilized for reinforcement, whereas the percentages of fly ash in the matrix ranged from 0 to 2.5 to 5 to 7.5 to 10 wt. %. Both particles were evenly distributed throughout the composite matrix alloys throughout the synthesis process for AA6061/10%SiC/7.5. The tensile strength and microhardness of composites made with fly ash have increased, while the percentage of fly ash used in their construction has decreased [25]. Stir casting was used to fabricate AA-2014-based composite reinforcing molybdenum disulfide (MoS$_2$), boron nitride (BN), and graphite (Gr). Reinforced ceramics composed of 4 wt. % BN, 4–8 wt. % MoS$_2$, and 6 wt. % Gr has found use. The hardest possible Vickers microhardness value was achieved by composite material, with a 28 % increase in hardness above the basic matrix (AA 2014) [26]. Many scientists have found that using mono-, binary-, multiple-, or tri-reinforcement in the ceramic's manufacturing through the melt stirring approach improves the material's AMC performance [27–29]. There is a clear difference in performance between binary or single-reinforced AMCs and multi-reinforced composites [20].
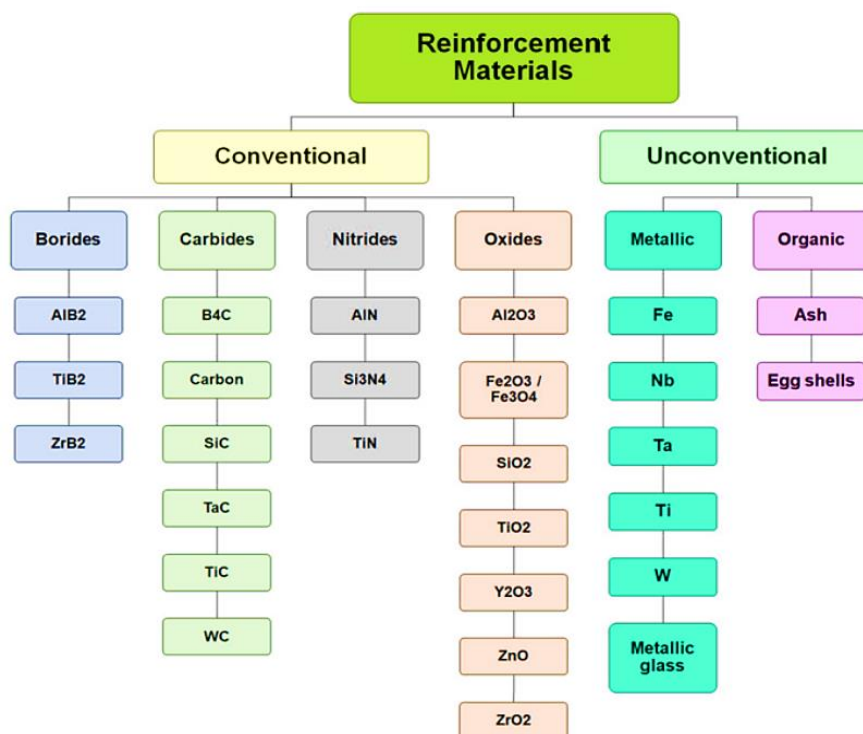

Fig. 3. Various organic and inorganic materials used as reinforcement

Experimental setup

AMC Fabrication Processes

Fabrication processes for aluminium metal matrix composites (AMCs) as shown in Fig. 4, encompass various methods such as stir casting, powder metallurgy, squeeze casting, infiltration, spray deposition, mechanical alloying, direct metal deposition, extrusion, hot pressing, each offering unique advantages and challenges tailored to specific application requirements [30–32].
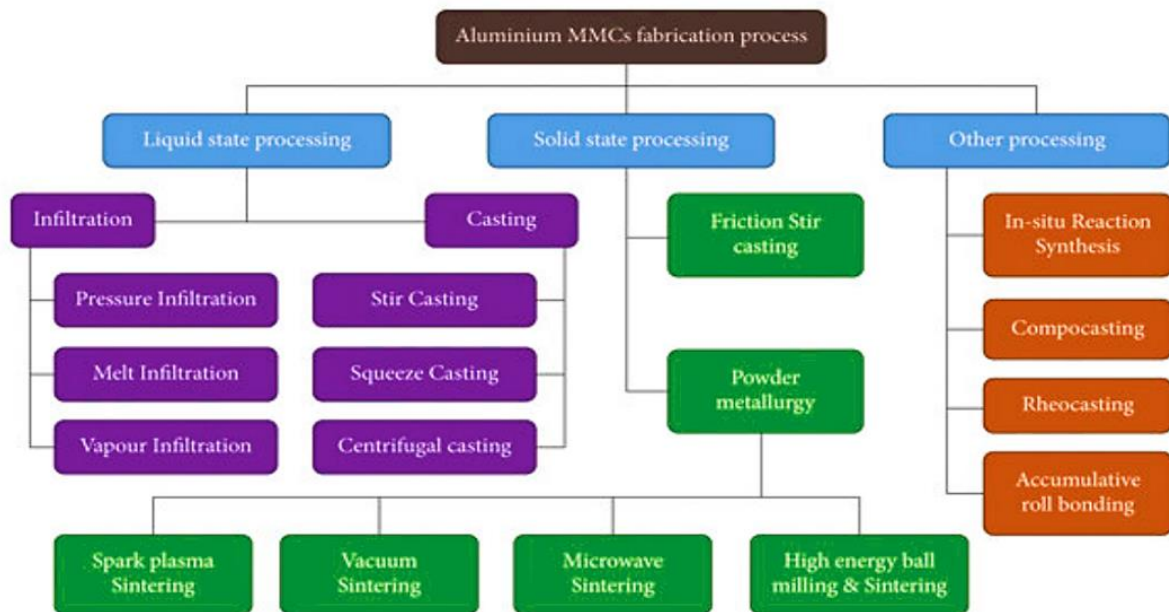

Fig. 4. AMCs fabrication process

Stir casting

Stir casting is a popular and cost-effective way to make aluminium metal matrix composites. Melting aluminium in a furnace crucible at 700–800 °C starts the process. After melting aluminium, a mechanical stirrer forms a vortex in which warmed reinforcing particles like SiC or Al_2O_3 are slowly added. Preheating the particles prevents molten aluminium from cooling too quickly and improves wetting and bonding. To ensure particle dispersion, stirring is done for a defined time. After mixing, a degassing agent may release trapped gases, lowering porosity. After mixing, the composite is put into a prepared mold and cooled to harden. Machining or heat treatment may obtain the desired dimensions and qualities [33–36].

Powder Metallurgy

Fabrication of aluminium metal matrix composites using powder metallurgy is accurate and adaptable. The procedure starts with aluminium powder and SiC or Al_2O_3 reinforcing particles. These components are combined, commonly in a ball mill, to distribute reinforcement evenly throughout the aluminium matrix. A die is used to compress the blended powder mixture under high pressure to generate a "green" compact that

maintains the intended component shape. A temperature below aluminium's melting point is used to sinter this compact. A dense composite material is formed when particles connect during sintering [37–42].

Squeeze casting

Liquid metal forging, or squeeze casting, is an innovative production technique for aluminium metal matrix momposites (AMCs). Aluminium being melted in a furnace. After melting, aluminium is placed into a prepared mold with reinforcing material like ceramic particles or fibers. After pouring, a hydraulic press forces the molten metal to fill mold holes and thoroughly permeate reinforcing material. High-pressure application continues until the metal hardens, creating a thick composite with low porosity and good matrix-reinforcement bonding. High pressure removes gasses and refines the microstructure, improving composite mechanical characteristics. After solidification, the mold is opened and the cast item is expelled for machining or heat treatment [43–46].

Infiltration

Infiltration is a complex technique for making aluminium metal matrix composites (AMCs) by infusing molten aluminium into a porous reinforcing material like ceramic particles or fibers. After preparing and moulding the preform, it is warmed to reduce moisture and improve wettability. The mold is subsequently filled with molten aluminium, frequently with external pressure or a vacuum, to guarantee thorough penetration into the preform's pores. Pressure or vacuum overcomes molten aluminium's surface tension, enabling deep penetration and minimizing voids. After the metal completely penetrates the preform, the composite cools and solidifies [47–50].

Friction stir process

A new solid-state joining and processing method called friction stir processing (FSP) improves the microstructure and mechanical characteristics of aluminium metal matrix Composites (AMCs). FSP generates frictional heat by plunging a specialized spinning tool with a pin and shoulder into the material. The tool may move over the surface because localized heat softens the material without melting it. The tool stirs the material, breaking down and dispersing reinforcing particles in the aluminium matrix. Intense plastic deformation and mixing refine microstructures, distribute reinforcements homogeneously, and increase mechanical qualities including strength and fatigue resistance [51–54].

Stir casting process

In recent years, stir casting has emerged as a prominent method for fabricating aluminium metal matrix composites (AMCs), owing to its simplicity, cost-effectiveness, and versatility. This paper aims to provide a comprehensive overview of the stir-casting process, elucidating its principles, methodologies, advantages, and challenges.

According to the usual approach, liquid, solid, and semi-solidroutes are the categories that have been used to classify AMC production techniques [55]. The

production of AMCs has been accomplished by using methods (Fig. 4) such as powdered metal metallurgy, liquid manufacturing, squeeze-casting, and spraying deposition, amongst others, which have been used by a number of researchers [56]. Stir-casting routes are preferred over other methods of production because of their simplicity and effectiveness in making AMCs [57]. Melt stirring motion is used in the stir-casting process to distribute reinforcing components throughout the matrix. S. Ray's early research on stir-casting of composites mostly included the fabrication of composite material using aluminium alloy as a matrix material reinforcing alumina particles. AMCs have been manufactured using a stir-casting amalgamation process [58]. Melting and stirring of molten material casting is the most efficient and cost-effective of the well-established methods of producing AMCs [59]. Base alloys are melted into a graphite crucible furnace and then stirred beyond their melting point as part of the stir-casting technique [60]. Casting the AMCs entails adding warmed particles to a molten slurry, stirring it continually for a certain amount of time, and then pouring the material into moulds of choice [61]. The melting of pure aluminium alloy requires heating higher than its liquidus point [62]. Additionally, it undergoes cooling to an intermediate concentrated slurry and is stored in a semi-solid state [63].

This is the stage when the preheated particles are combined with the molten liquid. Once again, the slurry is brought to a condition of perfect liquidity by heating, and then it is well mixed [64]. To get the right distribution of particles in the castingmould, AMCs are prepared in a certain way that prevents the solidification of the melt while yet allowing the suspended ceramic particles to remain in place [65]. The ultimate distribution of particulates within the solid casting is influenced by various factors related to material properties and method limitations [66]. These factors include the temperature at which the material is pre-heated, the rate at which reinforcing material is introduced, the extent to which the particulates are wetted by the molten material, the presence of porosity, the speed and duration of stirring, stirrer design, the use of chemical agents for degassing, and the rate at which solidification occurs along with the preheating temperature of the mould [67].

Results and Discussions

The purpose of this research is to describe the causes and limitations that impact stir casting throughout the two-step stirring process [68]. When making AMCs composites, reinforcement contents of up to 30 % by volume may be made via stir casting [69]. One primary concern in the stir casting process is the settling of particles during the process of heating and the process of solidification of the substances in metallic moulds [70]. This issue has to be resolved with the use of a stir-casting route as shown in Fig. 5.

Reinforcement thermal stabilization temperature and particle injection rate

The particles are subjected to preheating at an optimal temperature in order to minimize the presence of undesirable gases originating from reinforcements in addition to the aluminium alloy [71]. Additionally, this preheating process serves to improve the bonding between the particles, hence enhancing the wetting behaviour of reinforcement particulates with base materials. Casting composites may be difficult due to the non-

uniform dispersion of the particles and the resulting poor mechanical characteristics. Typically, particles are heated between 200 and 500 °C for 30–60 min [72]. The gaseous moisture in the reinforcement is removed. The optimal reinforcement injection rate plays a critical role in achieving optimal casting performance for advanced metal castings (AMCs) since increasing the feeding rate leads to the production of agglomerates of solid particles. Research conducted by scientists has shown that maintaining a consistent feeding rate within the range of 8–10 mg/min throughout the length of stirring yields excellent results [73].
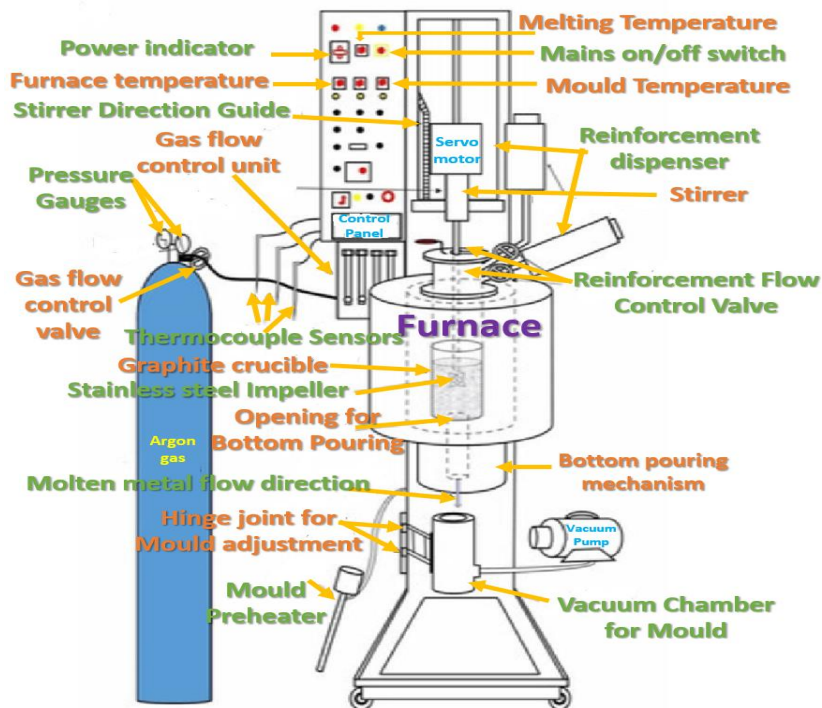
Fig. 5. Stir casting machine and its components

Void fraction and wetting behavior

Wettability describes the ability of a molten metal to spread and adhere to the surface of reinforcement particles, promoting uniform distribution and strong interfacial bonding. A high degree of wettability facilitates the wetting of reinforcement particles by the molten metal, leading to improved mechanical properties and enhanced homogeneity. Throughout the stirring process, the contact angle and interfacial surface tension have a substantial impact on the surface's wettability [74]. A lower contact angle suggests that the components are more wettable to one another. It is essential to take these aspects into account in order to produce the best possible wettability between the components [75]. A drop in mechanical properties might result from a lower wettability. When making composites using the melt stirring technique, porosity becomes a major concern [76]. Composites' mechanical performance degrades as their porosity increases.

Structure of a stirrer

A mechanical stirrer with blades may be used to create a vortex in a molten liquid, which allows particles to be added and distributed evenly [77]. For effective mixing, it is essential to optimize the design of the stirrer blades. To create an efficient vortex and encourage material homogeneity, mechanical stirrers might have two, three, or even more blades [78]. It is well-known, however, that composites made via mechanical stirring processes are best handled by single-step impellers. The formation of a vortex occurred as a consequence of the stirring process, which facilitated the transfer of particulate matter into the molten alloys [79]. This led to the creation of a homogenous dispersion of aluminium matrix composites (AMCs). Consequently, the careful determination of an appropriate impeller-blade angle is a crucial factor in achieving favourable axial flow and the angle of 30° has been identified as the most effective in promoting the uniform dispersion of particles while minimizing undesired agglomerations [80]. In some instances, blade angles of 45° and 60° have been seen to provide a consistent distribution in the manufactured samples [81].

Time and speed of stirring

As a matter of wettability, the speed at which the mixture is stirred is a crucial limiting factor. Most researchers have found that stirring speeds in the range of 700–800 rpm, at a cost of about 10 min, yield the most appropriate results [82]. The rotational speeds play a determining role in the formation of the vortex, leading to the distribution of particulates inside the reinforcement and matrix material liquid mixture. Enhanced mechanical characterizations of synthesized materials may be attained by comprehensive agitation over a suitable duration [83]. Particles' suitable mixing rate is another difficulty that is strongly affected by aided factors such as stirrer blade design, stirring speed, and duration, and so becomes a problem to be optimized [84].

Purge

To remove air bubbles and other inclusions from molten materials, purging or degassing is performed, and chemicals like tetra-chloro-ethane and sodium hexa-chloro-aluminate are added to improve wettability [85]. Nevertheless, more investigation is required to determine the effectiveness of the decontamination action.

Casting temperature

The temperature at which the molten metal is poured has a significant role in the solidification process. It is crucial to sufficiently increase the pouring temperature to guarantee that the metal flows smoothly and to prevent the formation of structures with coarse grains [86]. There is a significant level of responsibility associated with the excellence of casting. In order to prevent the entrapment of gases, it is essential that the pouring rate of molten materials remains consistent and homogeneous [87]. The measurement of the distance between the mould and the crucible is a critical factor that significantly impacts the quality of the casting process.

Solidification rate

The process of directional solidification in the context of melting materials of AMCs serves to decrease the likelihood of wear and tear [88]. The pace at which solidification occurs is primarily influenced by the degree to which the form and size of the mould are compatible. Similarly important to casting quality is the mould's proximity to the crucible [89].

Temperature of mould

Preheating the permanent mould is a great way to avoid porosity, the most detrimental flaw in AMC casting [90]. Metal moulds provide significant improvements over sand moulds, and they may be customized to meet the needs of the manufacturer in terms of thickness (at least 25 mm) as well as overall size and weight [91]. In addition, the use of metallic moulds would enhance the mechanical characterizations of the cast aluminium matrix composites (AMCs) [92]. Furthermore, many types of coating materials are used to enhance the die life of AMCs. Coatings such as silicate and graphite in water may be applied using spraying them within the moulds [93–96].

Emerging trends

1. Improving the mechanical performance of synthesized AMCs requires overcoming certain difficulties that arise during the melt stirring process and producing improved castings.
2. During the stir casting process, ensuring that the reinforcing particles are evenly dispersed is an important issue that arises. The dispersion of particulates inside composites is influenced by many factors, including the density of the materials (both matrix and reinforcement), the size (macro, micro, and nano) of the particulates, the degree of viscosity of the heated substance, and the right use of the stirring rate and stirring duration. These factors all contribute to achieving a uniform and homogenous dispersion.
3. The two-step stir casting technique was shown to provide the most favourable outcomes when ideal factors such as stirring speed, stirring duration, and federate were carefully controlled. Additionally, it was advised to use a three pitched-blade stirring impeller for this procedure.
4. The typical stir casting technique is often used in the industry. However, there are opportunities for improvement in the design of this process. One such enhancement is the use of an ultrasonic probe during the stir casting process. This modification may result in improved wettability and more uniform mixing of particle phases in the molten mixture.
5. The use of an inert environment in bottom-poured stir-casting has been extensively investigated by several researchers. This approach uses a setup that incorporates an inert atmosphere and bottom-pouring additives to prevent the occurrence of unwanted chemical reactions induced by gases. Additionally, it reduces porosity and improves the uniformity of particle matter.

6. Electromagnetic stir casting employs an electromagnetic stirrer as a viable alternative to conventional liquid stirring in order to mitigate surface flaws often seen in AMCs. In the context of electromagnetic stir-squeeze casting, the use of an ultrasonic transducer and bottom pouring connectors enhances the processing capabilities of the composites.

7. Numerous studies have used a range of optimization approaches (analysis of variance (ANOVA) [97], swarm optimizer (SO), fuzzy logic (FL), finite element method (FEM) [98], etc.), and others, to effectively manage and optimize the stir-casting process factors. The objective is to produce optimal outcomes within the given set of variables. The suggested factors have been offered to improve the mechanical characteristics of AMCs. Further research is required to investigate this subject in greater depth in the future.

8. Microwave heating has garnered increasing attention as a promising method for the fabrication of composite materials due to its ability to provide rapid and volumetric heating, precise temperature control, and energy efficiency. Microwave-assisted composite castings may also be studied in aerospace, automotive, and manufacturing. Microwave-assisted processing for industrial AMC and composite material manufacture may be studied for scalability, cost-effectiveness, and environmental sustainability [99–101].

Sustainability of stir-casting process

When evaluating the sustainability of the stir-casting process for aluminium metal matrix composites (AMMCs), several key sustainability issues are to be considered [102,103]:

1. Energy consumption. Stir casting typically requires significant energy input for melting aluminium and maintaining process temperatures. The energy intensity of the process, especially if traditional fossil fuel-based energy sources are used, can contribute to greenhouse gas emissions and environmental impact. Implementing energy-efficient practices and utilizing renewable energy sources can help mitigate these sustainability concerns.

2. Raw material usage. The sustainability of stir casting is influenced by the choice of raw materials, particularly aluminium and reinforcement particles. Aluminium extraction and processing have environmental implications, including energy consumption, resource depletion, and emissions of greenhouse gases and other pollutants. Sustainable sourcing practices, recycling of aluminium scrap, and utilization of eco-friendly reinforcement materials can help reduce the environmental footprint of AMMC production.

3. Waste generation: Stir casting can generate waste in the form of scrap metal, slag, and other by-products. Proper waste management practices, such as recycling of aluminium scrap and utilization of waste materials for other applications, can minimize waste generation and promote circular economy principles. Additionally, efforts to optimize process parameters and minimize defects can help reduce material losses and waste.

4. Emissions and pollution. The stir casting process may release emissions and pollutants into the environment, including particulate matter, volatile organic compounds (VOCs), and greenhouse gases. Controlling and mitigating these emissions through the use of pollution control technologies, such as exhaust systems and filtration devices, can help reduce environmental impact and protect air quality.

5. Occupational health and safety: Worker health and safety considerations are integral to the sustainability of any manufacturing process, including stir casting. Exposure to

molten metal, fumes, and hazardous chemicals poses risks to workers' health and well-being. Implementing appropriate safety measures, providing training and personal protective equipment (PPE), and ensuring compliance with occupational health and safety regulations are essential for safeguarding worker health and promoting sustainable practices.

6. Lifecycle assessment: Conducting a comprehensive lifecycle assessment (LCA) of the stir casting process can provide insights into its overall environmental impact, from raw material extraction and processing to end-of-life disposal or recycling. By quantifying environmental indicators such as energy consumption, greenhouse gas emissions, water usage, and waste generation, LCAs can inform decision-making and identify opportunities for sustainability improvements.

Conclusions

The fabrication of particulate-based AMCs may be done quickly and cheaply by the stir-casting approach. Researchers have shown that a homogenous distribution of the particulate, together with superior wettability and little porosity in the cast AMCs, is achieved by carefully controlling the parameters that play a vital role in the synthesis process, which involves adding particles to molten materials. The optimization of stir casting parameters is essential for achieving high-quality advanced metal matrix Composites (AMCs). Through careful control of variables such as pre-heating temperature, injection rate, stirring speed, and impeller-blade angle, significant improvements in mechanical characteristics can be attained. Key findings include:

1. reheating particles between 200 and 500 °C for 30–60 min enhances wettability and minimizes undesirable gases;

2. maintaining a consistent injection rate of 8–10 mg/min yields optimal casting performance;

3. stirring at speeds of 700–800 rpm for approximately 10–40 min facilitates the formation of a vortex and homogenous dispersion of particles;

4. an impeller-blade angle of 30–60° proves most effective in promoting uniform particle dispersion;

5. mold thickness should be at least 20-25 mm to avoid porosity;

6. emerging trends such as the use of ultrasonic probes and electromagnetic stir casting offer promising avenues for further improvement;

7. the sustainability of the stir casting process for AMCs hinges on optimizing energy usage, minimizing waste generation, and mitigating emissions while ensuring worker health and safety.

References

1. Kumar D, Angra S, Singh S. Mechanical Properties and Wear Behaviour of Stir Cast Aluminum Metal Matrix Composite: A Review. *International Journal of Engineering, Transactions A: Basics* 2022;35(4): 794–801.

2. Guo Z, Li S, Wu Q, Li N. Rare earth oxide ceo2 decorated graphene nanoplatelets-reinforced 2024 aluminum alloy matrix composites fabricated by pressure sintering process. *Applied Sciences.* 2021;11(23): 11177.

3. Ozden S, Ekici R, Nair F. Investigation of impact behaviour of aluminium based SiC particle reinforced metal-matrix composites. *Composites Part A: Applied Science and Manufacturing.* 2007;38(2): 484–494.

4. Tjong SC, Lau KC. Abrasive wear behavior of TiB2 particle-reinforced copper matrix composites. *Materials Science and Engineering: A.* 2000;282(1–2): 183–186.

5. Chak V, Chattopadhyay H, Dora TL. A review on fabrication methods, reinforcements and mechanical properties of aluminum matrix composites. *Journal of Manufacturing Processes*. 2020;56: 1059–1074.

6. Nurashikin S, Hazizan A. Preparation and properties of thermoplastic honeycomb core sandwich structure with aluminum skin. *Journal of Composite Materials.* 2011;46(2): 183–191.

7. Fang DR, Zhao SS, Lin XP, Chai T, Kuo Y, Sun H, Dong Y. Correlation between microstructure and mechanical properties of columnar crystals in the directionally solidified Mg-Gd-Y-Er alloy. *Journal of Magnesium and Alloys.* 2021;10(3): 743–755.

8. Joseph EJ, Panneerselvam K. Manufacturing and Characterization of Tungsten Particulate-Reinforced AW106 Epoxy Resin Composites. *Transactions of the Indian Institute of Metals.* 2021;74:8 17–825.

9. Huang WYW, Shang ZWF, Huang W, Zhang B. Thermal and Mechanical Properties of Graphene – Titanium Composites Synthesized by Microwave Sintering. *Acta Metallurgica Sinica.* 2016;29: 707–713.

10. Niemczewska-Wójcik M, Pethuraj M, Uthayakumar M, Majid MSA. Characteristics of the Surface Topography and Tribological Properties of Reinforced Aluminium Matrix Composite. *Materials.* 2022;15(1): 358.

11. Kumar D, Singh S, Angra S. Dry sliding wear and microstructural behavior of stir-cast Al6061-based composite reinforced with cerium oxide and graphene nanoplatelets. *Wear.* 2023;516–517: 204615.

12. Hosseinzadeh A, Yapici GG. Materials Science & Engineering A High temperature characteristics of Al2024 / SiC metal matrix composite fabricated by friction stir processing. *Materials Science & Engineering A.* 2018;731: 487–494.

13. Murashkin MYu, Zainullina LI, Motkov MM, Medvedev AE, Timofeev VN, Enikeev NA. Microstructure, mechanical properties and heat resistance of AL30 piston alloy produced via electromagnetic casting. *Materials Physics and Mechanics.* 2024;52(1): 81–94.

14. Gowrishankar TP, Manjunatha LH, Sangmesh B. Mechanical and Wear behaviour of Al6061 reinforced with Graphite and TiC Hybrid MMC 's. *Materials Research Innovations*. 2020;24(3): 179-185.

15. Baburaja K, Teja Sainadh S, Sri Karthik D, Kuldeep J, Gowtham V. Manufacturing and machining challenges of hybrid aluminium metal matix composites. *IOP Conference Series: Materials Science and Engineering.* 2017;225; 012115.

16. Gope PC. Maximum tangential stress coupled with probabilistic aspect of fracture toughness of hybrid bio-composite. *Engineering Science and Technology, an International Journal.* 2018;21(2): 201–214.

17. Hashim J, Looney L, Hashmi MSJ. Metal matrix composites: production by the stir casting method. *Journal of Materials Processing Technology* 1999;92–93: 1–7.

18. Jafarian M, Saboktakin M. A Comprehensive Study of Diffusion Bonding of Mg AZ31 to Al 5754 , Al 6061 and Al 7039 Alloys. *Transactions of the Indian Institute of Metals*. 2018;71: 3011–3020.

19. Schröter F, Ismar H, Streicher F. Numerical Determination of Damping in Metal Matrix Composites. *Mechanics of Composite Materials.* 2001;37: 43–46.

20. Kumar J, Singh D, Kalsi NS, Sharma S, Mia M, Singh J, Rahman MA, Khan AM, Rao KV. Investigation on the mechanical, tribological, morphological and machinability behavior of stir-casted Al/SiC/Mo reinforced MMCs. *Journal of Materials Research and Technology.* 2021;12: 930–946.

21. Dhakar B, Chatterjee S, Sabiruddin K. Linear reciprocating wear behaviour of plasma-sprayed Al 2 O 3 – Cr2O3 coatings at different loading and sliding conditions. *Sadhana.* 2020;42: 1763–1772.

22. Surzhenkov A, Viljus M, Simson T, Tarbe R, Saarna M, Casesnoves F. Wear resistance and mechanisms of composite hardfacings at abrasive impact erosion wear. *Journal of Physics: Conference Series.* 2017;843: 012060.

23. Vedabouriswaran G, Aravindan S. Development and characterization studies on magnesium alloy (RZ 5) surface metal matrix composites through friction stir processing. *Journal of Magnesium and Alloys*. 2018;6(2): 145–163.

24. Candiani S. Corrosion behavior of a particulate metal-matrix composite. *Corrosion*. 1999;55(4): 422–431.

25. Jauhari S, Prashantha Kumar HG, Anthony Xavior M. Synthesis and characterization of AA 6061-Graphene - SiC hybrid nanocomposites processed through microwave sintering. *IOP Conference Series: Materials Science and Engineering*. 2016;149: 012086.

26. Venkatesan SP, Muthuswamy G, Shyam Sundar R, Ganesan S, Hemanandh J. Investigation of mechanical properties of aluminum metal matrix composites with nanomaterial reinforcement. *Materials Today: Proceedings*. 2022;62: 572–582.

27. Aravind Senan VR, Anandakrishnan G, Rahul SR, Reghunath N, Shankar K V. An investigation on the impact of SiC/B4C on the mechanical properties of Al-6.6Si-0.4Mg alloy. *Materials Today: Proceedings*. 2019;26: 649–653.

28. Sharma VK, Kumar V, Joshi RS, Sharma D. Experimental analysis and characterization of SiC and RE oxides reinforced Al-6063 alloy based hybrid composites. *Int J Adv Manuf Technol.* 2020;108: 1173–1187.

29. Luo J, Liu S, Paidar M, Vignesh RV, Mehrez S. Enhanced mechanical and tribological properties of AA6061/CeO2 composite fabricated by friction stir processing. *Materials Letters.* 2022;318: 132210.

30. Prakash C, Singh S, Sharma S, Garg H, Singh J, Kumar H, Singh H. Fabrication of aluminium carbon nano tube silicon carbide particles based hybrid nano-composite by spark plasma sintering. *Materials Today: Proceedings.* 2020;21: 1637–1642.

31. Kumar D, Singh S. Enhancing friction and wear performance in hybrid aluminum composites through grey relational analysis. *Research on Engineering Structures and Materials.* 2024;10(3): 943-956..

32. Kumar D. Qualitative and quantitative interdependence of physical and mechanical properties of stir-casted hybrid aluminum composites. *Materials Physics and Mechanics.* 2023;51(6): 14–23.

33. Singh S, Kumar P, Jain SK. An experimental and numerical investigation of mechanical properties of glass fiber reinforced epoxy composites. *Advanced Materials Letters.* 2013;4(7): 567–572.

34. Shah S, Kumar P, Panda SK, Kumar S. Mixed-mode thermo elastic delamination fracture behavior of composite skin stiffener containing interface delamination. *Integrative Medicine Research.* 2019;8(6): 5941–5949.

35. Sharma P, Khanduja D, Sharma S. Dry sliding wear investigation of Al6082 / Gr metal matrix composites by response surface. *Integrative Medicine Research.* 2015;5(1): 29–36.

36. Sharma VK, Kumar P, Akhai S, Kumar V, Joshi RS. Corrosion inhibition analysis on cerium induced hydrophobic surface of Al-6061/SiC/Al2O3 hybrid composites. *Proceedings of the Institution of Mechanical Engineers, Part B: Journal of Engineering Manufacture.* 2024;238(14): 2126-2138.

37. Abhik R, Umasankar V, Xavior MA. Evaluation of Properties for Al-SiC Reinforced Metal Matrix Composite for Brake Pads. *Procedia Engineering.* 2014;97: 941–950.

38. Shaik MA, Golla BR. Two body abrasion wear behaviour of Cu–ZrB2 composites against SiC emery paper. *Wear.* 2020;450–451: 203260.

39. Seikh Z, Sekh M. Metal Matrix Composites Processed Through Powder Metallurgy : A Brief Overview. To be published in *Journal of The Institution of Engineers (India): Series D.* [preprint] 2024. Available from: https://doi.org/10.1007/s40033-024-00651-6

40. Jeyasingh KR, Balakrishnan SS. Characteristics Investigation on Aluminium / Diamond Composites Fabricated Through Powder Metallurgy. *Transactions of the Indian Institute of Metals.* 2024;77: 857–864.

41. Bahramzadeh S, Raygan S. Diamond & Related Materials Mechanical performance of CNT-reinforced aluminum matrix composite fabricated via flake powder metallurgy : Experimental modeling and molecular dynamics study. *Diamond & Related Materials.* 2024;142: 110742.

42. Zhu Y, Zhou M, Geng Y, Zhang S, Xin T, Chen G, et al. Microstructural evolution and its influence on mechanical and corrosion behaviors in a high-Al/Zn containing duplex Mg-Li alloy after friction stir processing. *Journal of Materials Science and Technology.* 2024;184: 245–255.

43. Zhang C, Liao W, Shan Z, Song W, Dong X. Materials Science & Engineering A Squeeze casting of 4032 aluminum alloy and the synergetic enhancement of strength and ductility via Al-Ti-Nb-B grain refiner. *Materials Science & Engineering A.* 2024;896: 146233.

44. Hari PGS, Raj K, Bhattacharjee B, Bhowmik A. Assessment of Microstructure and Investigation Into the Mechanical Characteristics and Machinability of A356 Aluminum Hybrid Composite Reinforced with SiCp and MWCNTs Fabricated Through Rotary Centrifugal and Squeeze Casting Processes. *Silicon.* 2024;16: 367–382.

45. Deng J, Liu G, Wang L, Liu G, Wu X. Journal of Industrial Information Integration Intelligent optimization design of squeeze casting process parameters based on neural network and improved sparrow search algorithm. *Journal of Industrial Information Integration.* 2024;39: 100600.

46. Zhao B, Xing S, Gao W, Yan G. Effect of pressure on the microstructure refinement , solidification mechanism and fracture behavior of wrought Al-Zn-Mg-Cu alloys prepared by squeeze casting. *Journal of Materials Processing Tech.* 2024;324: 118239.

47. Fu J, Zhou C, Mi G, Liu Y. Effects of diamond particle size on microstructure and properties of diamond / Al-12Si composites prepared by vacuum-assisted pressure infiltration. *China Foundry.* 2024;21, 360–368.

48. Yang X, Zhang Y, Huang J, Liu J, Chen J, Li T. Materials Science & Engineering A Interfacial microstructure evolution and mechanical properties of carbon fiber reinforced Al-matrix composites fabricated by a pressureless infiltration process. *Materials Science & Engineering A.* 2024;891: 145968.

49. Sun Y, Han Z, Kuang Z, Xia Y, Wu G, Ju B, et al. Recycling of beryllium swarf for the preparation of Be / Al composites with high mechanical properties by pressure infiltration method. *Journal of Materials Research and Technology.* 2024;29: 3967–3975.

50. Lin G, Dai J, Wang B, Zu Y, Sha J. Improving mechanical and thermal expansion properties of aluminum matrix composites reinforced by silicon carbide fiber. *Materials Letters.* 2024;366: 136553.

51. Kaya N, Çetinkaya C, Karakoç H, Ada H. Effect of process parameters of Al5083 / SiC surface composites fabricated by FSP on microstructure , mechanical properties and wear behaviors. *Materials Chemistry and Physics.* 2024;315: 128991.

52. Wang C, Zhu X, Fan Y, Liu J, Xie L, Jiang C, Xiao X, Wu P, You X. Microstructure and Properties of Aluminum – Graphene – SiC Matrix Composites after Friction Stir Processing. *Materials.* 2024;17(5): 979.

53. Ramezani NM, Davoodi B. Evaluating the influence of various friction stir processing strategies on surface integrity of hybrid nanocomposite Al6061. *Scientific Reports.* 2024;14: 8056.

54. Kareem H, Raju H, Annapoorna E, Thethi HP, Kumar L. Advancements in Aluminum-Based Composite Manufacturing : Leveraging La2O3 Reinforcement through Friction Stir Process. *E3S Web of Conf.* 2024;507: 01036.

55. Gajalakshmi K, Senthilkumar N. A Critical Review of Wear and Machinability Studies of Aluminium Metal A Critical Review of Wear and Machinability Studies of Aluminium Metal Matrix Composite. *Journal of Advanced Engineering Research.* 2018;5(1): 31–40.

56. Kumar D, Singh S, Angra S. Effect of reinforcements on mechanical and tribological behavior of magnesium-based composites : a review. *Materials Physics and Mechanics.* 2022;50(3): 439–458.

57. Petrovi J, Mladenovi S, Markovi I, Dimitrijevi S. Characterization of hybrid aluminum composites reinforced with Al2O3 particles and walnut-shell ash. *MatTech.* 2022;56(2): 115–122.

58. Gudimetla A, Lingaraju D, Sambhu Prasad S. Investigation of mechanical and tribological behavior of al 4032-sihgm mmc. *Composites Theory and Practice.* 2020;20(3–4): 142–156.

59. Kumar D, Singh S, Angra S. Morphology and Corrosion Behavior of Stir-Cast Al6061- CeO 2 Nanocomposite Immersed in NaCl and H 2 So 4 Solutions. *Evergreen.* 2023;10: 94–104.

60. Hashim FA, Abdulkader NJ. Corrosion Behavior of Recycling Al- Alloy Based Metal Matrix Composites Reinforced by Nano particles. *Kurdistan Journal of Applied Research.* 2017;2(3): 279–283.

61. Kumar D, Angra S, Singh S. High-temperature dry sliding wear behavior of hybrid aluminum composite reinforced with ceria and graphene nanoparticles. *Engineering Failure Analysis.* 2023;151: 107426.

62. Kumar D, Angra S, Singh S. Synthesis and characterization of DOE-based stir-cast hybrid aluminum composite reinforced with graphene nanoplatelets and cerium oxide. *Aircraft Engineering and Aerospace Technology.* 2023;95(10): 1604–1613.

63. Kubica M, Skoneczny WBB, Bara M. Analysis of Al2O3 Nanostructure Using Scanning Microscopy. *Scanning.* 2018;2018: 459768.

64. Fu S, Chen X, Liu P, Cui H, Zhou H, Ma F, Li W. Tribological Properties and Electrical Conductivity of Carbon Nanotube-Reinforced Copper Matrix Composites. *Journal of Materials Engineering and Performance.* 2022;31: 4955–4962.

65. Khanna N, Sharma P, Bharati M, Badheka VJ. Friction stir welding of dissimilar aluminium alloys AA 6061-T6 and AA 8011-h14: a novel study. *Journal of the Brazilian Society of Mechanical Sciences and Engineering.* 2020;42: 7.

66. Liu M, An XH, Wang BB, Liu FC, Wu LH, Xue P, Ni DR, Xiao BL, Ma ZY. Achieving high fatigue strength of large-scale ultrafine-grained copper fabricated by friction stir additive manufacturing. *Materials Letters.* 2023;346: 134531.

67. Alrobei H. Effect of different parameters and aging time on wear resistance and hardness of SiC-B4C reinforced AA6061 alloy. *Journal of Mechanical Science and Technology.* 2020;34: 2027–2034.

68. Moosa A, Awad AY. Effect of Rare Earth Addition on Wear Properties of Aluminum Alloy- Rice Husk Ash / Yttrium Oxide Hybrid Composites. *International Journal of Current Engineering and Technology.* 2016;6: 788–798.

69. Sharma A, Belokar RM, Kumar S. Dry sliding wear characterization of red mud reinforced aluminium composite. *Journal of the Brazilian Society of Mechanical Sciences and Engineering.* 2018;40: 294.

70. Zhou W, Xu ZM. Casting of SiC reinforced metal matrix composites. *Journal of Materials Processing Technology.* 1997;63: 358–363.

71. Hou M, Guo S, Yang L, Gao J, Peng J, Hu T, Wang L, Ye X. Fabrication of Fe–Cu matrix diamond composite by microwave hot pressing sintering. *Powder Technology.* 2018;338: 36–43.

72. Ali R, Zafar M, Manzoor T, Kim WY, Rashid MU, Abbas SZ, et al. Elimination of solidification shrinkage defects in the casting of aluminum alloy. *Journal of Mechanical Science and Technology.* 2022;36: 2345–2353.

73. Wang K, Lei Z, Liao Z, Tao C, Zhong Y, Wang Z, et al. Effect of the Stirring Velocity and the SiO2 Precursor Particles Feeding Rate on the Microstructure of the Al2O3/SiO2/Al Composites Prepared via Stir Casting Process. *Advanced Engineering Materials.* 2022;24: 1–14.

74. Bose S, Mandal N, Nandi T. Comparative and Experimental study on Hybrid Metal Matrix Composites using Additive Ratio Assessment and Multi-Attributive Border Approximation area Comparison methods varying the different Weight Percentage of the Reinforcements. *Materials Today: Proceedings.* 2019;22: 1745–1754.

75. Bharath V, Nagaral M, Auradi V, Kori SA. Preparation of 6061Al-Al 2 O 3 MMC's by Stir Casting and Evaluation of Mechanical and Wear Properties. *Procedia Materials Science.* 2014;6: 1658–1667.

76. Zheng RR, Wu Y, Liao SL, Wang WY, Wang WB, Wang AH. Microstructure and mechanical properties of Al/(Ti,W)C composites prepared by microwave sintering. *Journal of Alloys and Compounds.* 2014;590: 168–175.

77. Ramanathan A, Krishnan PK, Muraliraja R. A review on the production of metal matrix composites through stir casting – Furnace design, properties, challenges, and research opportunities. *Journal of Manufacturing Processes.* 2019;42: 213–245.

78. Ramachandra M, Radhakrishna K. Effect of reinforcement of flyash on sliding wear , slurry erosive wear and corrosive behavior of aluminium matrix composite. *Wear.* 2007;262(11–12): 1450–1462.

79. Babu KA, Jeyapaul R. An Investigation into the Wear Behaviour of a Hybrid Metal Matrix Composite Under Dry Sliding Conditions Using Taguchi and ANOVA Methods. *Journal of Bio- and Tribo-Corrosion.* 2022;8: 15.

80. Saravana Kumar M, Begum SR, Vasumathi M. Influence of stir casting parameters on particle distribution in metal matrix composites using stir casting process. *Materials Research Express.* 2019;6: 1065d4.

81. Zhang WY, Du YH, Zhang P. Vortex-free stir casting of Al-1.5 wt% Si-SiC composite. *Journal of Alloys and Compounds.* 2019;787: 206–215.

82. Shankar Srivastava V, Kumar Gupta T, Nigam A. Study of stirrer speed and preheat temperature on stir cast aluminium matrix composite materials - A review. *Materials Today: Proceedings.* 2021;47: 4114–4120.

83. Kumar M, Gupta RK, Pandey A. A Review on Fabrication and Characteristics of Metal Matrix Composites Fabricated by Stir Casting. *IOP Conference Series: Materials Science and Engineering.* 2018;377: 012125.

84. Aklilu G, Adali S, Bright G. Tensile behaviour of hybrid and non-hybrid polymer composite specimens at elevated temperatures. *Engineering Science and Technology, an International Journal.* 2020;23: 732–743.

85. Awasthi S, Gupta P, Pachuri P, Tyagi M, Aniruddha. Optimization of magnesium ZK60A/SiC/B4C hybrid composite fabricated by friction stir processing. *Materials Today: Proceedings.* 2022;62: 191–197.

86. Amouri K, Kazemi S, Momeni A, Kazazi M. Microstructure and mechanical properties of Al-nano/micro SiC composites produced by stir casting technique. *Materials Science and Engineering A.* 2016;674: 569–578.

87. Mozammil S, Verma R, Karloopia J, Jha PK. Investigation and measurement of porosity in Al + 4.5Cu/6wt%TiB2 in situ composite: optimization and statistical modelling. *Journal of Materials Research and Technology.* 2020;9: 8041–8057.

88. Aqida SN, Ghazali MI, Hashim J. Effect of Porosity on Mechanical Properties of Metal Matrix Composite: An Overview. *Jurnal Teknologi.* 2012;40(1): 17-32.

89. Sree Manu KM, Resmi VG, Brahmakumar M, Narayanasamy P, Rajan TPD, Pavithran C, Pai BC. Squeeze infiltration processing of functionally graded aluminum-SiC metal ceramic composites. *Transactions of the Indian Institute of Metals.* 2012;65: 747–751.

90. Kataria M, Mangal SK. Excellence of al-metal matrix composite fabricated by gas injection bottom pouring vacuum stir casting process. *Indian Journal of Engineering and Materials Sciences.* 2020;27: 234–245.

91. Jia XY, Liu SY, Gao FP, Zhang QY, Li WZ. Magnesium matrix nanocomposites fabricated by ultrasonic assisted casting. *International Journal of Cast Metals Research.* 2009;22: 196–199.

92. Amirkhanlou S, Niroumand B. Synthesis and characterization of 356-SiCp composites by stir casting and compocasting methods. *Transactions of Nonferrous Metals Society of China.* 2010;20: s788–s793.

93. Ali M. Review of stir casting technique and technical challenges for ceramic reinforcement particulate and aluminium matrix composites. *Epitoanyag - Journal of Silicate Based and Composite Materials.* 2020;72: 198–204.

94. Tan H, Wang S, Cheng J, Zhu S, Yang J. Sliding Tribological Behavior of Al-Fe-V-Si-Graphite Solid-Lubricating Composites at Elevated Temperatures. *Journal of Tribology.* 2018;140(1): 011302

95. Sharma S, Singh J, Gupta MK, Mia M, Dwivedi SP, Saxena A, et al. Investigation on mechanical, tribological and microstructural properties of Al-Mg-Si-T6/SiC/muscovite-hybrid metal-matrix composites for high strength applications. *Journal of Materials Research and Technology.* 2021;12: 1564–1581.

96. Khatkar SK, Verma R, Kharb SS, Thakur A, Sharma R. Optimization and Effect of Reinforcements on the Sliding Wear Behavior of Self-Lubricating AZ91D-SiC-Gr Hybrid Composites. *Silicon.* 2021;13: 1461–1473.

97. Reddy PV, Ramanjaneyulu P, Reddy BV, Rao PS. Simultaneous optimization of drilling responses using GRA on Al-6063/TiC composite. SN Applied Sciences. *SN Appl. Sci.* 2020;2; 431.

98. Umer U, Mohammed MK, Abidi MH, Alkhalefah H, Kishawy H. Modeling the effect of particle size while machining aluminum based metal matrix composite using an equivalent homogenous material approach. *Materials Today: Proceedings.* 2022;62: 2981–2987.

99. Kaushal S, Singh S, Gupta D. Processing strategy for high strength Ni-based hybrid composite clad on SS 316L steel through microwave heating. *Proceedings of the Institution of Mechanical Engineers, Part B: Journal of Engineering Manufacture.* 2022;236(3): 190-203.

100. Taylor P, Singh S, Gupta D, Jain V, Sharma AK. Materials and Manufacturing Processes Microwave Processing of Materials and Applications in Manufacturing Industries: A Review Microwave Processing of Materials and Applications in Manufacturing Industries: A Review. *Materials and Manufacturing Processes.* 2014;30(1): 1–29.

101. Alem SAA, Latifi R, Angizi S, Hassanaghaei F, Aghaahmadi M, Ghasali E, et al. Microwave sintering of ceramic reinforced metal matrix composites and their properties: a review. *Materials and Manufacturing Processes.* 2020;35: 303–327.

102. Bindal A, Singh S, Batra NK, Khanna R. Development of Glass / Jute Fibers Reinforced Polyester Composite. *Indian Journal of Materials Science.* 2013;2013(1): 675264.

103. Singh K, Khanna V, Singh S, Anil S, Chaudhary V, Khosla A. Paradigm of state-of-the-art CNT reinforced copper metal matrix composites: processing, characterizations, and applications. *Journal of Materials Research and Technology.* 2023;24: 8572–8605.

About Authors

Pardeep Kumar iD Sc
Ph.D., Associate Professor (Maharishi Markandeshwar University, Mullana-Ambala, India)

Dinesh Kumar iD Sc
Ph.D., Assistant Professor (Maharishi Markandeshwar University, Mullana-Ambala, India)

Kawaljeet Kaur iD
M.Sc., Assistant Professor (Dev Polytechnic College, Ambala, India)

Rupesh Chalisgaonkar iD Sc
Ph.D., Associate Professor (Medi-Caps University, Indore, India)

Shashank Shekhar Singh iD Sc
Ph.D., Assistant Professor (Poornima University, Jaipur, India)

MPM
SCIENTIFIC
JOURNAL